



Brno University of Technology  
Faculty of Mechanical Engineering  
Institute of Machine and Industrial Design

Vysoké učení technické v Brně  
Fakulta strojního inženýrství  
Ústav konstruování

# MEASUREMENT OF SHAPE AND DIMENSIONS OF FORGINGS

MĚŘENÍ TVARU A ROZMĚRU VÝKOVKŮ

**Jakub Hurník, Ing.**

Author

Autor práce

**doc. Ing. Daniel Koutný, Ph.D.**

Supervisor

Vedoucí práce

Dissertation Thesis

Dizertační práce

Brno 2022



## ABSTRACT

In the process of open-die forging, inaccuracies can appear. These inaccuracies must be measured and corrected. Passive heavy forging measurement, based on their silhouettes in images, potentially offers many advantages in this application. However, regarding forging measurement, this method showed limited accuracy in the literature and was never verified under industrial conditions. Therefore, the aim of this thesis is to examine the feasibility of this method in the industrial environment, by using advanced methods of optical measurement. Interfering effects are discussed, and original methods, working as countermeasures, are proposed. Methods are verified in both the laboratory and the industrial environment. The results suggest the effectiveness of the proposed methods; the accuracy achieved in the laboratory and industrial environment is of the same order. The error is approximately around 1 mm in a measurement volume of  $6 \times 6 \times 2$  m for the geometry of the axis and the measurement of the diameter. This result satisfies the demands of an industrial environment. However, the measurement still contains outliers, which are discussed. The knowledge obtained can be used during the development of a professional measurement system for this application. Secondly, the knowledge can be generalized to the measurement of hot objects, or objects in a complex environment, based on their silhouettes. A system for the measurement of forgings could increase the effectiveness of manufacturing and could become a part of automated forging production line in the future.

## KEYWORDS

forging, measurement, silhouettes, edge detection, axis straightness

## ABSTRAKT

V procesu výroby těžkých výkovků volným kování vznikají nepřesnosti, které je třeba měřit a korigovat. Metoda pasivního měření výkovků, na základě jejich siluet v obraze, zde potenciálně nabízí mnoho výhod. V případě měření výkovků ale v literatuře vykazuje relativně nízkou přesnost a nebyla ověřena v průmyslových podmínkách. Cílem práce je proto prozkoumat možnosti využití této metody v reálných podmínkách, které umožní pokročilé metody optického měření. Jsou diskutovány rušivé vlivy prostředí a navrhovány originální metody, jak ovlivnění zmírnit nebo mu předejít. Ty jsou ověřovány v laboratorním i v průmyslovém prostředí. Výsledky potvrzují efektivitu navržených metod; dosahovaná přesnost je stejného řádu s tou dosaženou v laboratorním prostředí. Bylo dosaženo chyby okolo 1 mm v měřicím objemu  $6 \times 6 \times 2$  m v případě měření přímosti osy a průměru výkovku. Tento výsledek postačuje požadavkům průmyslového prostředí. Nicméně, měření stále obsahuje odlehle hodnoty, jejichž výskyt je diskutován. Poznatky obsažené v této práci je možné využít při vývoji profesionálního měřicího systému pro tuto aplikaci. Sekundárně jsou pak zobecnitelné a využitelné při měření horkých objektů nebo obecně objektů v komplexním prostředí na základě jejich siluet. Systém pro měření výkovků by v budoucnu mohl přinést vyšší efektivitu výroby volně kovaných polotovarů a mohl by se stát součástí automatizované kovací linky.

## KLÍČOVÁ SLOVA

výkovek, měření, siluety, detekce hran, přímost osy

## BIBLIOGRAPHICAL REFERENCE

HURNÍK, Jakub. *Measurement of Shape and Dimensions of Forgings*. Brno, 2022, 138 p. Dissertation thesis. Brno University of Technology, Faculty of Mechanical Engineering, Institute of Machine and Industrial Design. Supervisor doc. Ing. Daniel Koutný, Ph.D.



## ACKNOWLEDGMENTS

First, I would like to thank my supervisors. I would like to thank doc. Ing. David Paloušek, Ph.D. for supervising me the first 4 years of my studies and for his support and advice. I would like to thank doc. Ing. Jan Brandejs, CSc. and doc. Ing. Daniel Koutný, Ph.D. for taking over his role for the rest of my studies. I also acknowledge my supervisor-specialist Ing. Aneta Zatočilová, Ph.D. for collaboration making possible to obtain the experimental data. Special thanks belong to my girlfriend Dott.ssa Mag. et Ing. Tereza Konečná for her support, as well as valuable advice from her field of expertise (applied mathematics, statistics). The final thanks belong mainly to my family and then to colleagues of the department (namely Ing. Martin Krčma, Ing. Arnošt Vespalec, Ing. Ondřej Červinek, Ing. Martin Malý, Ing. Ondřej Vaverka and Ing. Jan Suchý), for making a good company to work in during the long, demanding studies.

The articles *Circular coded target system for industrial applications* (published in journal *Machine Vision and Applications*) and *Multi-view camera system for measurement of heavy forgings* (published in *The International Journal of Advanced Manufacturing Technology*) are reproduced with permission from Springer Nature.

## STATEMENT

I hereby declare that I have written the PhD thesis *Measurement of Shape and Dimensions of Forgings* on my own according to the advice of my supervisors, doc. Ing. Daniel Koutný, Ph.D., doc. Ing. Jan Brandejs, CSc., and doc. Ing. David Paloušek, Ph.D., and using the sources listed in references.

.....

Author's signature



# CONTENT

<b>1</b>	<b>INTRODUCTION</b>	<b>11</b>
<b>2</b>	<b>STATE OF THE ART</b>	<b>13</b>
2.1	Close range photogrammetry	13
2.2	Interfering effects during in-process forging measurement	14
2.2.1	Thermal radiation influence	14
2.2.2	Heat haze and air lens	18
2.2.3	Camera calibration	22
2.3	Active optical forging measurement	26
2.3.1	Laser scanners	27
2.3.2	Active stereo vision	29
2.3.3	Fringe projection systems	31
2.3.4	Laser triangulation	34
2.4	Passive optical forging measurement	37
2.4.1	Passive stereovision	37
2.4.2	Measurement based on silhouettes	39
<b>3</b>	<b>ANALYSIS AND CONCLUSION OF LITERATURE REVIEW</b>	<b>45</b>
3.1	Challenges during in-process forging measurement	45
3.2	Applicable approaches	46
3.2.1	Active measurement systems	46
3.2.2	Passive measurement systems	47
3.3	Summary, areas of missing knowledge	48
<b>4</b>	<b>AIMS OF THE THESIS</b>	<b>50</b>
4.1	Main aim and the problems covered in thesis	50
4.2	Scientific question and hypotheses	51
4.3	Thesis layout	51
<b>5</b>	<b>MATERIALS AND METHODS</b>	<b>53</b>
5.1	Measurement system principle	53
5.2	Proposed methods to enhance system robustness	54
5.3	Measurement system hardware	56
5.4	Reference geometry and comparative measurement	58

5.5	Target system benchmark	58
<b>6</b>	<b>RESULTS AND DISCUSSION</b>	<b>60</b>
<b>7</b>	<b>CONCLUSIONS</b>	<b>121</b>
<b>8</b>	<b>LIST OF PUBLICATIONS</b>	<b>124</b>
8.1	Papers published in journals with impact factor	124
8.2	Papers in conference proceedings	125
	<b>REFERENCES</b>	<b>126</b>
	<b>LIST OF FIGURES AND TABLES</b>	<b>135</b>

# 1 INTRODUCTION

Forging is a manufacturing operation that is used to produce semi-finished products for high-strength mechanical parts. Heavy forgings are manufactured using open-die forging, due to their large dimensions and small-series production. These forgings are used in the energy, petrochemical and shipbuilding industry to manufacture various shafts. During open-die forging, significant deviations from the ideal forging dimensions and shape often appear. Shape deviations can be corrected directly after the forging operation. Although the costs of the production are very high, this is still often carried out based on primitive contact measurement techniques. Some geometric characteristics cannot be measured at all, including, e.g., forging axis straightness. Therefore, this important shape deviation can be corrected only based on forging press operator estimation. The evidence of low achievable accuracy is the large machining allowances, which must be applied. According to ČSN 42 9011, the allowances can exceed 20% of the total material used for forging manufacturing.

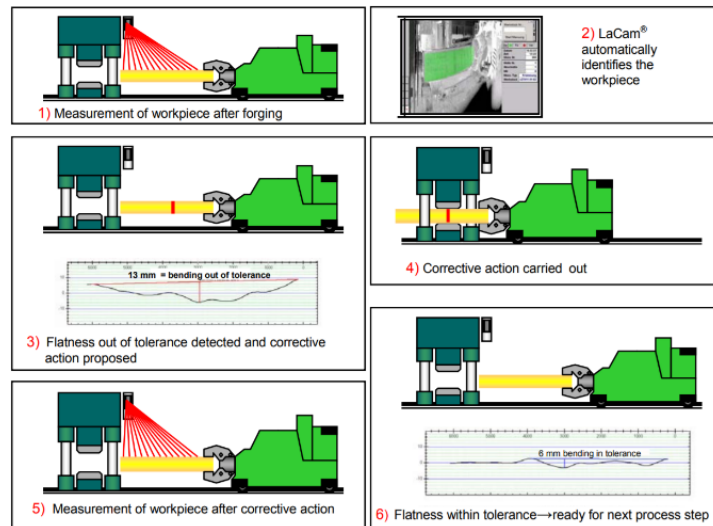


Fig. 1-1 Correction of axis straightness using LaCam® Forge by Ferrotron; 1) measurement of forging, 2) forging segmentation, 3) evaluation of axis-straightness, 4) three-point bending axis correction, 5), 6) repeated measurement [1].

The problem is that due to the specific conditions in the environment of heavy industry, common available noncontact measurement systems cannot be used. The dimensions of heavy forgings are in meters, and their forging temperature varies between 1250 – 850 ° C. There are many physical effects, which can critically affect optical measurement systems, e.g., the radiance or contrasting scales on the forging surface, dimensionally and thermally unstable environment, or air lens around the forging. There are only a few systems in the world capable of forging measurement, including, e.g., the LaCam® Forge by Ferrotron. However, these are based on the laser scanning principle, which has many disadvantages. Therefore, the research continues to find an alternative. The literature suggests many

advantages of passive, image-based measurement using forging silhouettes [2]. However, this approach showed limited accuracy during forging measurement and was never tested under industrial conditions. On the other hand, the measurement system in the literature used only basic optical measurement methods.

The aim of this thesis is to examine the possibilities of passive, image-based measurement of forgings in the process of their manufacturing, by using advanced methods of optical measurement. In this work, the measurement system, based on this principle, is proposed. The interfering effects of the industrial environment are discussed and many original methods, making this measurement method resistant to these effects, are proposed. The effectiveness of the methods was verified under both laboratory and industrial conditions and compared with the state-of-the-art. The knowledge obtained can be used to develop a professional measurement system, which would provide the feedback to the forging press operator, to accurately correct the forging shape and dimensions. This would lead to material savings on the machining allowances, and therefore energy and emissions savings. In the future, the measurement system can become a part of automated forging manufacturing line (e.g., like a concept presented in literature [3]), in accordance with industry 4.0 implementation.

## 2 STATE OF THE ART

### 2.1 Close range photogrammetry

Close-range photogrammetry is a science branch dealing with the measurement of object shape, dimensions, or location, based on the images. The result is normally its digital reconstruction (a set of points in a coordinate system). Close-range photogrammetry is used in many areas, including mechanical engineering, civil engineering, architecture, medicine, natural sciences, or crime investigation applications. Photogrammetry has a wide range of applications in the industry. The typical applications are – inspection of mechanical parts or assemblies, calibration of robot manipulators, reverse engineering, or digitization of the art creations [4].

To obtain the object location or geometry, the image formation process needs to be described from the geometric point of view. To describe the image formation process, modified central projection is normally used. The basic model is provided in Fig. 2-1:

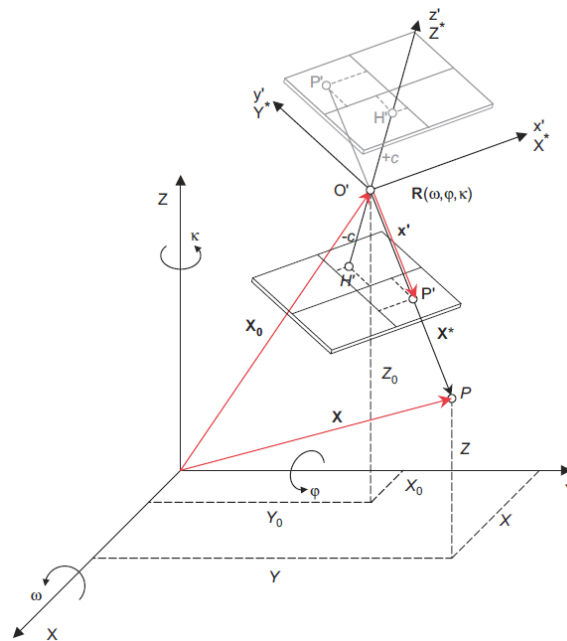


Fig. 2-1 Basic representation of central projection model (image formation) [5].

Where:

- Axis  $z'$  is the camera optical axis.
- The camera focal length is marked  $c$ .
- $H'[x'_0, y'_0]$  is the physical image centre (principal point).
- $O'$  or  $X_0[X_0, Y_0, Z_0]$  is the projection centre.
- $P[X, Y, Z]$  and  $P'[x', y']$  are the object point and the corresponding image point, respectively.

- Angles  $\omega, \varphi, \kappa$  are the rotation angles around the axes  $X, Y, Z$ .

Based on this model, “Basic equation of photogrammetry”, was derived (equation 2.1 [5]):

$$\begin{aligned} x' - x'_0 - \Delta x' &= -c \frac{r_{11}(X - X_0) + r_{21}(Y - Y_0) + r_{31}(Z - Z_0)}{r_{13}(X - X_0) + r_{23}(Y - Y_0) + r_{33}(Z - Z_0)} \\ y' - y'_0 - \Delta y' &= -c \frac{r_{12}(X - X_0) + r_{22}(Y - Y_0) + r_{32}(Z - Z_0)}{r_{13}(X - X_0) + r_{23}(Y - Y_0) + r_{33}(Z - Z_0)} \end{aligned} \quad (2.1)$$

Where  $r_{11} \dots r_{33}$  are the components of the image plane rotation matrix, derived based on the rotation angles  $\omega, \varphi, \kappa$ . The central projection model modification mainly includes the image distortion parameters  $\Delta x', \Delta y'$ , which arises from the optical system imperfections. Usually, the radial distortion is the most significant and needs to be compensated for. In the case of more accurate optical systems, tangential and affine distortion components are also included. The process of estimating these parameters is called camera calibration. Camera calibration can be carried out by imaging, for example, a planar calibration field with a regular pattern [6, 7], a 3D calibration object with known geometry [8], or a 3D calibration field created of the coded calibration targets with known location [9, 10]. A special case are the self-calibration methods, which do not need any accurate calibration scene. Instead, the methods use the correspondences between the individual images. Due to the fact that every object point in the image is measured with a small random error, the camera calibration is normally an optimization problem. On the basis of the parameters obtained, the object or the scene can be reconstructed. The main division of methods includes passive and active approaches. The difference is that active approaches reconstruct the object based on a known pattern projection.

Research in close-range photogrammetry includes the spreading of optical image-based methods to new applications. This is possible thanks to the development of computational power, digital cameras, and computational methods, based e.g., on neural networks [11, 12].

## 2.2 Interfering effects during in-process forging measurement

### 2.2.1 Thermal radiation influence

#### Passive image-based measurement systems

The passive image-based measurement takes advantage of the light present in the environment. No external light source is needed. In case of glowing-hot forgings, the

captured light is blackbody radiation, which is, due to the high forging temperature, in visible spectrum.

Dworkin et al. [13] dealt with the imaging of glowing hot forging in industrial conditions using a CCD camera. The authors showed that images are blurred, and the background is not sufficiently distinguished (Fig. 2-2). Therefore, the authors suggest using the NIR (near infrared) color filter, to improve the forging contrast. A side effect was a narrow interval of the wavelengths that needs to be focused on the camera sensor. Therefore, the obtained images were sharper. The authors sufficiently segmented the forging in the image using simple thresholding (Fig. 2-3).

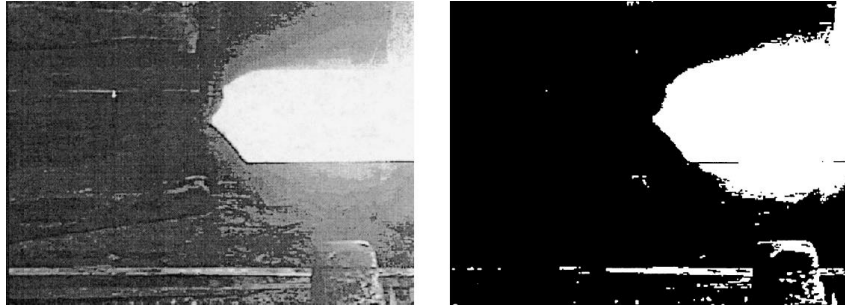


Fig. 2-2 Image without use of color filter and the result of forging segmentation using thresholding [13].

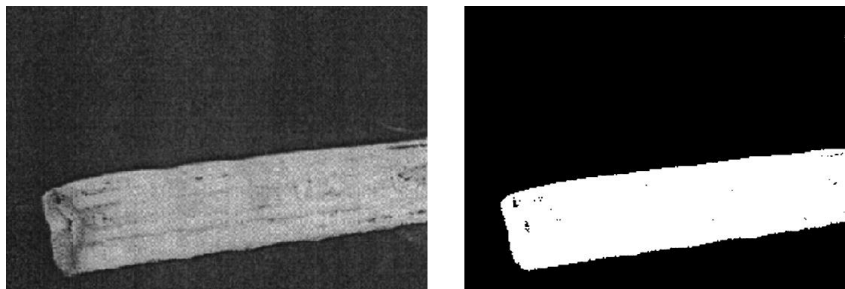


Fig. 2-3 Image taken by using NIR color filter and the result of forging segmentation using thresholding [13].

The advantage of using color filters was also shown by Bi et al. [14]. The authors studied the dependence of the forging temperature on its contrast in the laboratory environment. The specimen was a small steel cube with dimensions in centimeters, and the silhouette contrast was examined throughout the interval of common forging temperatures (800 – 1200 ° C). Four different color filters and their combinations were used – red, green, blue, and IR-cut. The sample of resulting images are provided in Fig. 2-10. Using these images, the forging contrast in this work was calculated (Fig. 2-11) based on equation 2.2:

$$\Delta V = |V_O - V_B| \quad (2.2)$$

Where  $\Delta V$  is the image contrast,  $V_O$  and  $V_B$  are the image intensities of the object and background, respectively. The conclusion was confirmation that the spectral-selective method has a strong impact on the forging contrast and, therefore, the reliability of forging

segmentation. The second finding was that different color filters are suitable for different temperature intervals.

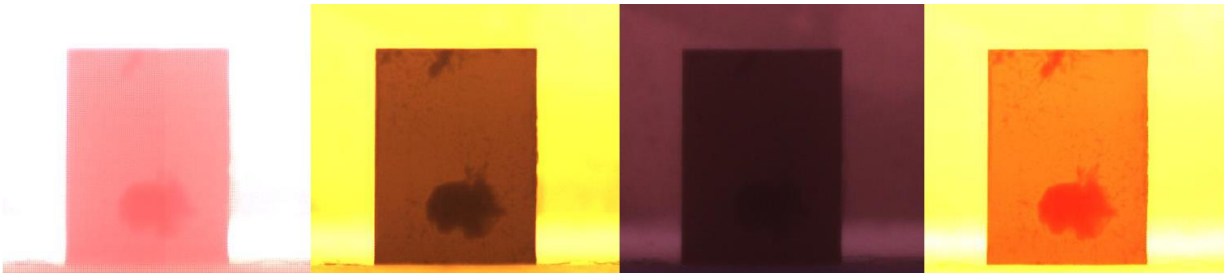


Fig. 2-4 Forging images taken by using (from left): red, green, blue, and IR-cut color filter [14].

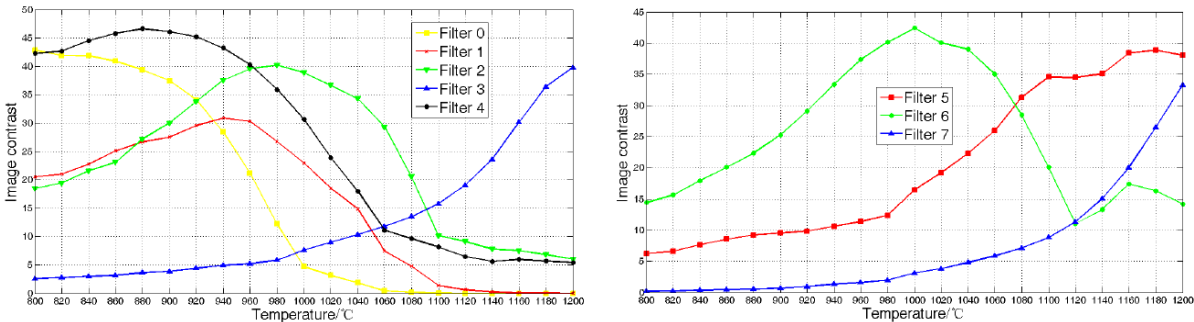


Fig. 2-5 Dependency of forging contrast on the forging temperature [14].

Hu et al. [15] dealt with the problem of forging segmentation. The authors showed that state-of-the-art image edge detectors fail in the case of segmentation of glowing hot forging in the complex environment. The reason was the contrasting scales on the forging surface, as well as the areas with lower temperature, which have lower contrast. Therefore, false positive and false negative edges appeared. The authors presented a custom forging segmentation method to solve this problem. The method was based on the Canny edge detector [16]. The modifications included pre-processing using histogram equalization, to enhance the contrast of weak edges. Furthermore, post-processing was used to suppress false edges based on their surroundings. Both procedures were integrated directly into the Canny edge detector. The comparison of the results is provided in Fig. 2-6.

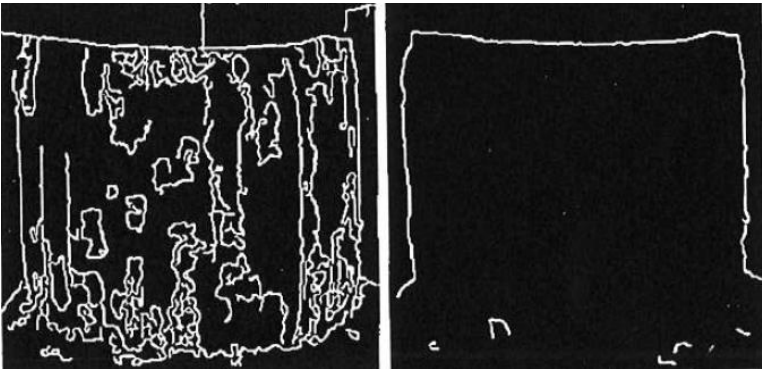


Fig. 2-6 Comparison of the forging image processed by Canny edge operator (left), and the proposed segmentation method (right) [15].

## Active image-based measurement systems

Active image-based measurement takes advantage of the light projected on the object. Therefore, contrary to passive image-based measurement systems, the philosophy is to suppress the black-body radiation of the forging, which affects the signal-to-noise ratio. The basic method for suppressing the radiation is the spectral selective method. The authors [17] examined the signal-to-noise ratio and developed a model for its prediction for a structured light-aided stereo vision system. The experimental setup is depicted in Fig. 2-7.



Fig. 2-7 Structured light aided stereo vision experimental setup [17].

The ‘signal’ included the light projected on the surface of the forging, while the ‘noise’ included the light radiated by the forging. Signal-to-noise ratio was computed as follows:

$$SNR = \frac{\int (M_p(\lambda) + M_n(\lambda)) \eta_s(\lambda) \eta_f(\lambda) d\lambda}{\int M_n(\lambda) \eta_s(\lambda) \eta_f(\lambda) d\lambda}; M_p = \phi_p \frac{\rho}{S} \quad (2.3)$$

Where  $SNR$  is the signal-to-noise ratio;  $M_p$  is the projected signal, which depends on the radiation flux  $\phi_p$ , reflectivity of the forging surface  $\rho$  (0.2 – 0.5) and the projected area  $S$ ;  $M_n$  is the noise (thermal radiation of the forging);  $\eta_s$  is the quantum efficiency of the camera sensor;  $\eta_f$  is the optical filter transmission,  $\lambda$  is the wavelength.

Based on the developed model and expected radiation-wavelength curve for the considered forging temperatures, the cameras were equipped with 440 nm low-cut filter, to mostly suppress the forging radiation (Fig. 2-8). The developed model was experimentally verified. The setup consisted of a DLP projector with a 250 W lamp (5000 lm) and two CCD cameras, the forging temperature was 1150 – 1200 °C. The lowest SNR achieved was 2.5, which was considered satisfactory. However, the effect of other potential light sources in the environment was not considered.

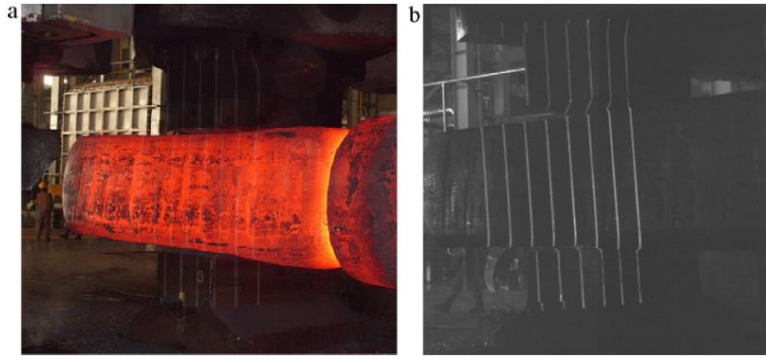


Fig. 2-8 Comparison of the measurement images without (a) and with (b) the usage of the spectral selective method [17].

## 2.2.2 Heat haze and air lens

The heat haze and air lens is the result of an inhomogeneous atmosphere in the scene. Air with different properties varies in refractive index. Studies from different fields are oriented on this topic.

Ciddor [18] examined the predictability of the refractive index of air. The context of this work was the examination accuracy of geodesic measurement and its enhancement by compensating the varying refractive index of the air. The author assumed that the refractive index is dependent on temperature, air pressure, moisture, and carbon dioxide content. The author derived an equation for the refractive index of air, based on these variables. The equation showed great agreement with the experimental measurements (error on the order of  $10^{-8}$ ) in a wide range of atmospheric conditions (temperature  $-40 - +100$  °C, pressure  $80 - 120$  kPa, moisture  $0 - 100\%$ ) and wavelengths ( $300 - 1690$  nm). However, the author emphasized the problem of measuring air conditions in practice, which becomes a limit of optical measurement accuracy.

Yamauchi [19] focused on the prediction of the behavior of the air lens. The author carried out an experiment, during which an object was measured using laser ranging principle. The layout of the experiment is provided in Fig. 2-9. The author considered the hot air over the heated plate as a cylindrical air lens. Therefore, Equation 2.4 was derived for the lens focal length  $c$ :

$$c = \frac{r_l n_1 n_0}{2(n_1 - n_0)(2n_1 - n_0)} \quad (2.4)$$

Where  $n_0$  and  $n_1$  are the refractive indexes of the surrounding air and the air forming the air lens, respectively. Variable  $r_l$  is the radius of the lens. The measurement was carried out per  $50$  °C in a temperature range of  $27 - 550$  °C.

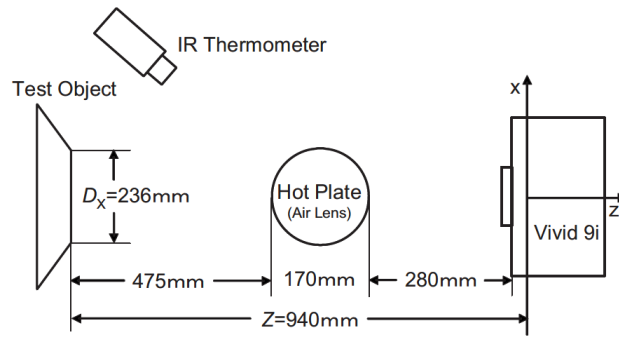


Fig. 2-9 The layout of the experiment verifying the derived air lens model (Vivid 9i is the laser range finder by Konica-Minolta) [19].

Fig. 2-10 compares the predicted transverse (in the  $x$  direction) and total (in the  $z$  direction) magnification with the experimental results. The maximum predicted magnification was 0.35% and 0.20% for the case of transverse and total respectively. The true, measured magnification was 0.08% and 0.04% for the case of transverse and total, respectively. Therefore, the experiment varied significantly from the analytical prediction. According to the author, the reason for this difference was that the air that formed the air lens had a lower temperature than the heated platform. However, the author recommended using this model to estimate the maximum possible error, which can appear during optical measurement.

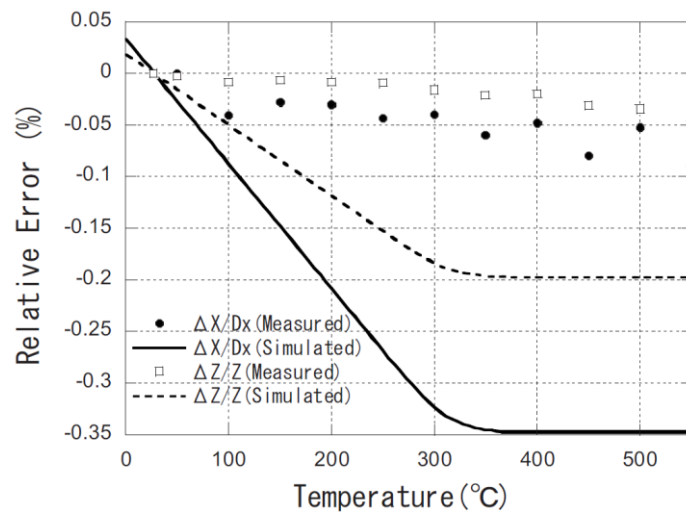


Fig. 2-10 The results of the measurement affected by air lens compared to the prediction [19].

Beermann et al. [20] created a complex simulation model of the influence of an inhomogeneous, hot atmosphere surrounding the hot object on the line scanning measurement. The model included simulations of the hot atmosphere surrounding the object, its refractive index, and the optical track between the line laser, the object, and the camera. The authors considered a 532 nm line laser and a triangulation angle of  $60^\circ$ . The detailed layout of the simulation is provided in Fig. 2-11. The object temperature considered is  $900 - 1250^\circ\text{C}$ . Only laminar air flow was considered. The refractive index of air was calculated based on the extrapolated Ciddor equation [18]. The authors also considered

various relative position of the measurement system and the object (angle  $\beta$  in Fig. 2-11). In this virtual simulated environment, the measurement error caused by the hot atmosphere was simulated using the ray tracing method.

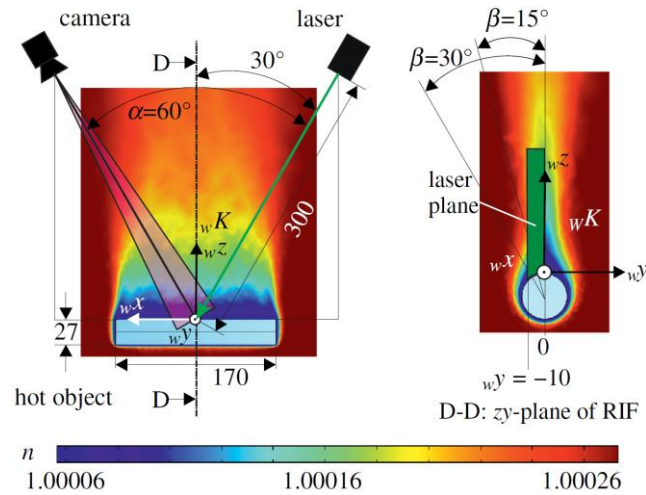


Fig. 2-11 Air lens simulation layout ( $n$  is a local refractive index of air) [20].

The results of the simulation are provided in Fig. 2-12. The authors discovered the opposing effect of refraction on the light rays, which partially compensated itself. This resulted in a smaller measurement error around  $50 \mu\text{m}$ , which was considered as satisfactory. This error did not change significantly with forging temperature. However, the error decreased with larger angle  $\beta$ . Therefore, the authors suggested avoiding the measurement of hot objects through a wide layer of the hot atmosphere above the forging. Furthermore, because of the neglect of turbulent flow, the authors suggested repeatedly measuring the object and using a mean measurement value.

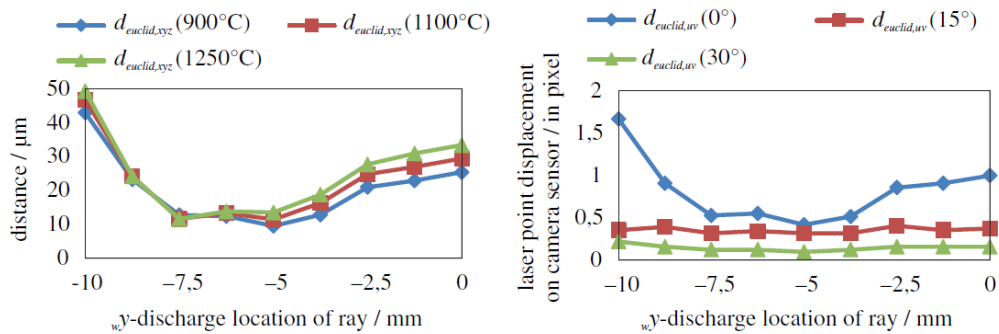


Fig. 2-12 Simulated measurement error due to air lens; left – the effect of different forging temperatures, right – the effect of different measurement device location [20].

Another study focused on the possibilities of employing this simulation method in the design of a physical compensation system for the air lens [21]. This was based on controlling the air flow in the environment using compressed air flowing from nozzles, eliminating the air lens over the hot object. The compensation system was designed for a fringe projection measurement system. The measured object was a steel rod with a length of 250 mm,

a diameter of 50 mm, and a temperature of up to 1300 K. The objective of the simulation was to estimate the needed air flow velocities. The result of the simulation is provided in Fig. 2-13. Based on the simulation, the compensator air flow velocity was chosen  $1 - 4 \text{ ms}^{-1}$  to minimize the width of a hot air layer above the forging.

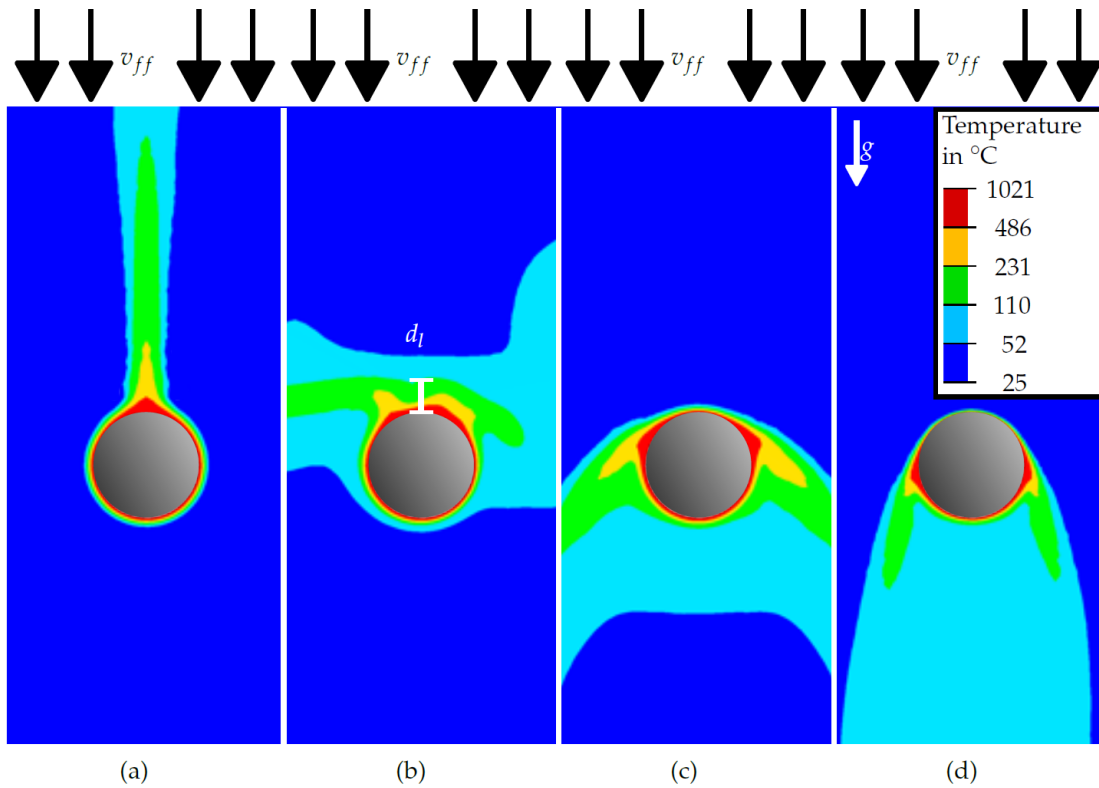


Fig. 2-13 The resulting simulated atmosphere surrounding the hot object in dependence on the compensator air flow velocity  $v_{ff}$  – (a)  $0.0 \text{ ms}^{-1}$ ; (b)  $0.2 \text{ ms}^{-1}$ ; (c)  $0.55 \text{ ms}^{-1}$ ; (d)  $1.0 \text{ ms}^{-1}$  [21].

The effect of the compensation system was experimentally verified and compared with the unaffected state. The mean object reconstruction error was examined (Fig. 2-14).

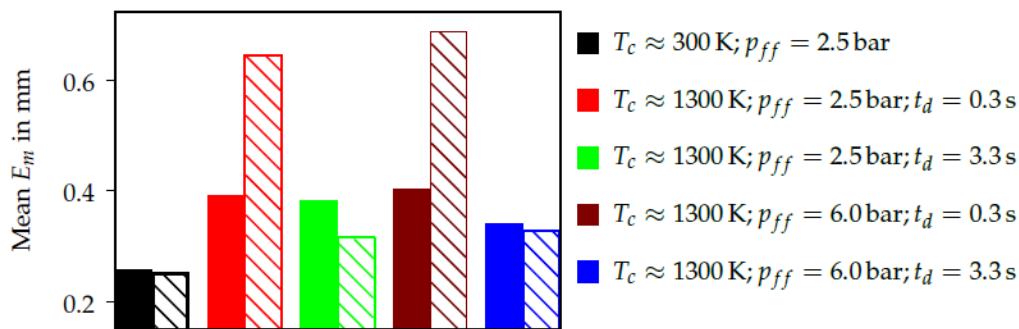


Fig. 2-14 The experimentally measured mean reconstruction error  $E_m$  in dependence on the compressed air pressure ( $p_{ff}$ ), time from flow activation of the flow to the measurement ( $t_d$ ). The hatched columns denote the measurement with activated air flow [21].

From the results, it is obvious that the hot atmosphere around the hot specimen significantly affected the reconstruction error. The compensation system helped reduce this error;

however, the error remained significantly larger than in the unaffected state. Another finding was that the compensation system caused a significant increase in measurement errors if the time between the activation of the compensation system air flow and the measurement was too short.

### 2.2.3 Camera calibration

#### Large field of view camera calibration

Most common calibration methods, based on imaging of a planar calibration field with regular pattern, are not suitable for large measurement volumes with dimensions of the order of meters, due to the large dimensions of the calibration object. Solutions based on imaging (single or multi-image) of a field of point calibration targets offer an alternative. Space resection or, in the case of self-calibration, the bundle adjustment method can be used. Based on the mathematical principles, various conditions (point distances, 3D coordinates, or other geometric constraints) can be used to determine the camera parameters.

In [10] the authors dealt with the calibration of a videogrammetric system with a  $5 \times 5$  m field of view. The system consisted of 4 high speed cameras (Fig. 2-15 on the left) and was designed to track deformable objects. The cameras were fitted with a  $1024 \times 1024$  px sensor with 20  $\mu$ m pixel size and 50 mm fixed focal length objectives. The camera calibration was based on a geometric model presented as eq. 2.1. The authors considered three-parameter radial, tangential, and affinity distortions. The multi-image calibration method was based on imaging of a large calibration object, a cross with calibration targets. The accurate coordinates of the calibration targets were measured using an industrial photogrammetric system, XJTUDP.

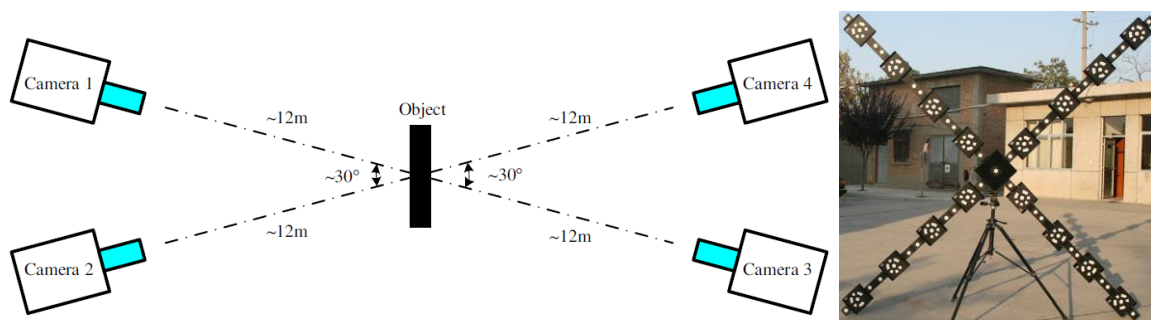


Fig. 2-15 Left – videogrammetric system camera layout; right – calibration object [10].

The cameras were calibrated with a reprojection error of less than 0.05 px. Calibration accuracy was verified based on the measurement of a professional scale bar with accurate and known length. The measurement system achieved 0.24 mm error.

Schneider et al. [9] used a hemispherical field of calibration targets with known location (Fig. 2-16) to validate mathematic geometric models for fisheye lenses, for possible

photogrammetric applications. A camera fitted with a 14 Mpx sensor and an 8 mm Nikkor lens was used. The authors showed that by using a suitable lens analytic model, a standard deviation of 0.1 px of spatial resection or bundle adjustment can be achieved.

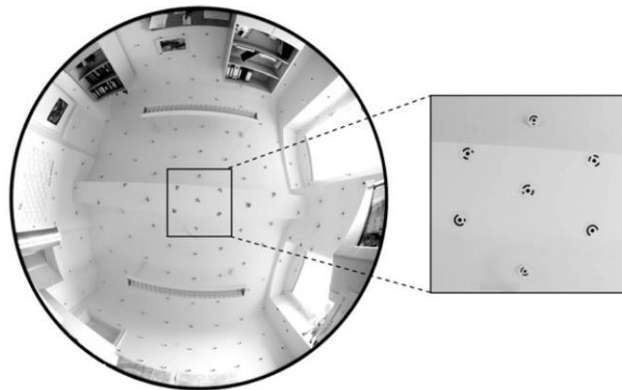


Fig. 2-16 Hemispherical calibration room for calibrating the cameras equipped with fisheye lenses [9].

### Coded calibration targets

Coded calibration targets are used to code locations in space or to find correspondences between images. Calibration target systems should be capable of reliable target identification in the image, and their library should contain a sufficient number of unique targets. There are two main types of target coding, which can be distinguished – barcode type (Fig. 2-17 a, b, c) and coding based on unique element distribution [22, 23] (Fig. 2-17 d, e). The barcode type can be distinguished to circular [8, 24–29] or square [30–34]. The square target design is advantageous for machine vision or augmented reality applications because one target codes four locations in total (the target corners). On the other hand, most common design of coded calibration targets in industrial photogrammetry, essential to calibrate the cameras, is circular coded design (Fig. 2-17 a). This (or similar) design is used by many professional photogrammetric systems, including TRITOP (GOM), XJTUDP, Aicon Photogrammetry, and others.

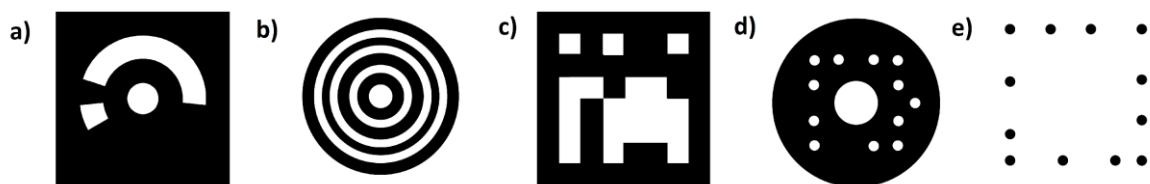


Fig. 2-17 Different designs of coded targets (schematic) – a) TRITOP (GOM); b) Calvet, 2016; c) Garrido-Jurado 2014; d) Ahn, 2001; e) Bergamasco, 2013.

There are more similar approaches to segmentation, accurate location, and recognition of circular coded targets presented in the literature [8, 24–27]. The authors used 9 – 16-bit coding (Fig. 2-18). To segment the targets, the image was binarized using thresholding or an edge operator (see, e.g., [16]). The potential centers of the targets were then sorted based on their geometric characteristics (size, shape) or contrast. Based on the known target geometry,

the target code was scanned in the image and divided into segments. The binary target code was then determined from the scanned greyscale distribution in the bit segments based on thresholding (e.g., Otsu's method [35]). Alternatively, the code was determined based on the gradients on bit transitions. The obtained code is cyclic, and its correct orientation needs to be determined (for example, cyclic code 101 includes 3 different forms – 101, 110, 011). The resulting target code was determined based on the transformation of the binary to decimal – the lowest decimal number was considered as the identification number of the target. No error correction method was implemented. Finally, the target center coordinates were calculated using, for example, the weighted centroid method. The global result is the target coordinates with their corresponding identification numbers. The described method was evaluated as fast and reliable under common conditions.

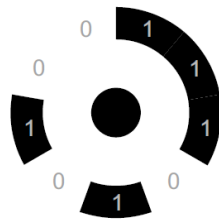


Fig. 2-18 Sample design of circular coded target often used in industrial photogrammetric applications; in the center - contrasting circle for target segmentation and location; annulus around – the unique code ring (9-bit in this case) [8].

In [29], an alternative method for the detection and recognition of circular coded targets was presented. Target center detection was carried out in the frequency domain using several oriented Gabor filters. Approximately circular objects are supposed to have non-zero response on variously oriented Gabor filters. By multiplying the results of the convolutions of variously oriented Gabor filters with the original image in the frequency domain, non-circular objects were suppressed Fig. 2-19. The image was variously scaled to capture ellipses of different dimensions. The target cyclic code was obtained by scanning the code ring, which was thresholded. The cyclic code was then compared with the codes in a lookup table to obtain the target identification code (total match was needed). The last step was the target validation. The theoretical synthetic target code was compared with the scanned thresholded code. Based on the correlation between the images, false positive targets were rejected. The presented method was compared with Aicon software on various datasets and showed similar or better results.

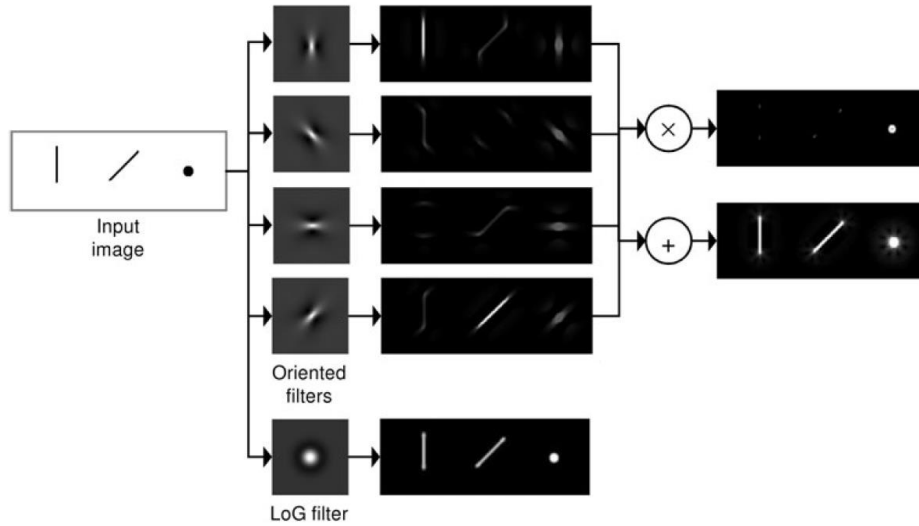


Fig. 2-19 The response of Gabor filter and Laplacian of Gaussian filter for comparison on different objects in an input image; the result of sum and multiplication of the images [29].

A coded fiducial marker system ArUco for machine vision or augmented reality applications was developed in [32]. This system was based on simple, square coded marker design (Fig. 2-20). This design included  $n$  by  $n$ -bit unique code surrounded by a contrasting border. The target system was based on the generator of target code libraries. The main idea was that usually a low number of targets is needed; therefore, the generator creates a set of codes with maximum inter-code and maximum Hamming distance in the code library. Moreover, the number of bit transitions was also optimized, to prevent the target confusion with random objects of background.



Fig. 2-20 ArUco square coded targets (5, 6, and 8-bit) [32].

In the image, the target was found based on its shape, the perspective distortion was removed, and the target was thresholded using the Otsu method [35]. The target code matrix was determined based on the pixel values in the bit regions. Target recognition included the error correction method, which allowed the system to recognize partially damaged or occluded targets and take advantage of the high Hamming distance in the target code library. This was carried out based on rotation-invariant Hamming distance between the scanned code and the codes in the target code library. The rotation invariant distance  $D$  between square codes  $m_i, m_j$  was expressed as follows (equation 2.5):

$$D(m_i, m_j) = \min_{k \in \{0,1,2,3\}} \{H(m_i, R_k(m_j))\} \quad (2.5)$$

Where  $H$  is the Hamming distance and  $R_k$  is the rotation function. If the distance was under certain limit, the target was recognized. The error correction limit was  $(\tau-1)/2$ , where  $\tau$  is the minimum rotation-invariant Hamming distance. The authors compared the developed method with available systems of calibration targets with similar design – ARTag and ARToolKitPlus. The developed target system achieved the best error correction capability. Moreover, it performed the best under Gaussian image noise among the compared systems.

The next work of the authors focused on improving the target generator, which has not achieved optimum results [33]. The goal was to achieve a higher marker distance in the target code library. The improvement included the implementation of the optimization method (mixed integer linear programming). However, the method was computationally demanding and did not significantly improve the results; therefore, the authors recommended using it only in certain applications.

Moreover, the authors dealt with improving the robustness of target detection and recognition. This was achieved using algorithms based on artificial neural networks [34]. For this purpose, the library of fifty  $6 \times 6$ -bit targets was created. Training was carried out based on 12500 synthetic images of calibration targets, varying in the amount of negative image effects – light, geometric, and noise. 210 000 images were used for the negative class. Using neural network-based methods, the robustness of the target recognition was significantly improved. However, a training procedure is needed in the case of changing the target library.

Another improvement of the target system included the development of an alternative, fast target detection and recognition algorithm [31]. This method was designed for real-time applications.

## 2.3 Active optical forging measurement

A wide review of forging 3D measurement methods, which focused on active methods, was presented in [36]. In this work, the main methods used for hot objects measurement were divided into laser scanning (or TOF, time-of-flight systems), laser triangulation technology, and multi-view stereo vision method (mainly active). The technology development on the time scale is provided in Fig. 2-21.

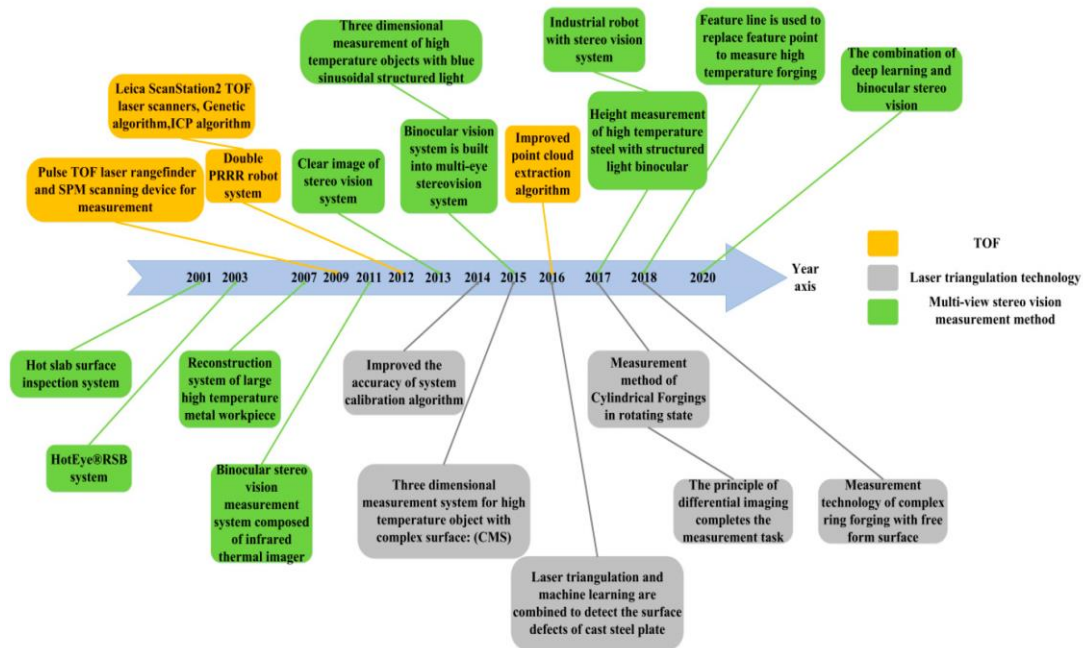


Fig. 2-21 The timeline of advances in 3D hot objects measurement [36].

### 2.3.1 Laser scanners

Z. S. Tian et al. [37] and Z. C. Du et. al. [38] applied laser scanning to the measurement of large cylindrical forgings (up to 20 m in length and 6 m in diameter). Both authors measured the length of the object its diameter. Du used a line laser scanner LMS100 2D (SICK), which was tilted in a single axis by a servo motor, Tian used an unspecified point laser scanner, which was driven in two axes. The authors also developed the method of point cloud processing (object segmentation and measurement). Both authors experimentally verified the developed measurement systems in the industrial environment. Forgings with dimensions of up to 7000 mm (Tian) and 3000 mm (Du) and a temperature of around 1000 ° C were measured. The results achieved by both authors are provided in Fig. 2-22. The measurement time ranged from several seconds (Tian) to 15 seconds (Du). The relative repeatability error obtained was, in the case of both authors, below 2%. The main finding of both studies was that the negative effects present in industrial environment do not affect laser scanning measurement.

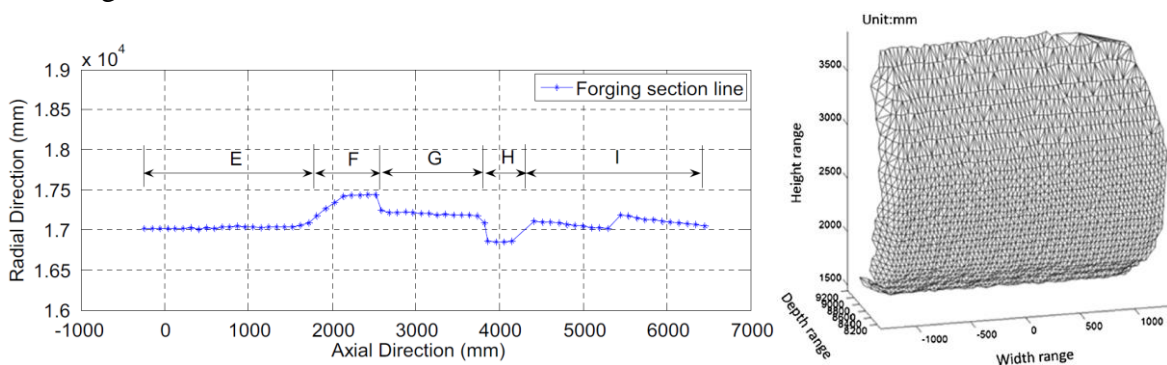


Fig. 2-22 Left – the measurement result presented by Tian [37] and Du [38].

Zhang et al. [39] used Hired Hi50 laser range finders (TOF principle, 1 mm resolution) to examine the concentricity of cylindrical parts of forging with fittings. Alternatively, the concentricity of the forging and the forging tool can be measured to determine the correct placement of the semi-finished product under the forging press. The experiment was carried out to verify the proposed method. The diameter of the semi-finished product was 900 mm and the diameter of the forging tool was 200 mm. The resulting error was less than 0.5 mm, which was considered as satisfactory.

Fu et al. [40] used a combination of a 2D laser scanner with a monocular camera for the measurement of a ring forging diameter. The diagram of the proposed system is shown in Fig. 2-23. The system was designed to measure the 3D point cloud representing the forging, which was achieved by rotating the specimen and moving the measurement device. The monocular camera measurement itself was based on the imaging of forging silhouettes. The edges in the image were found using the Roberts edge operator and filtered using median filtering. The forging radius was obtained using a pixel-to-millimeter calibration. The measurement system was based on the radius matching method. This method used the radius measured by the monocular camera system  $R$  to verify the points measured by the laser scanner. If a point measured by the laser scanner had a greater deviation from  $R$  than a certain threshold, it was rejected. The proposed system was verified under both laboratory and industrial conditions. Under industrial conditions, a ring forging with a diameter of up to 2800 mm was measured with an error under  $\pm 1$  mm.

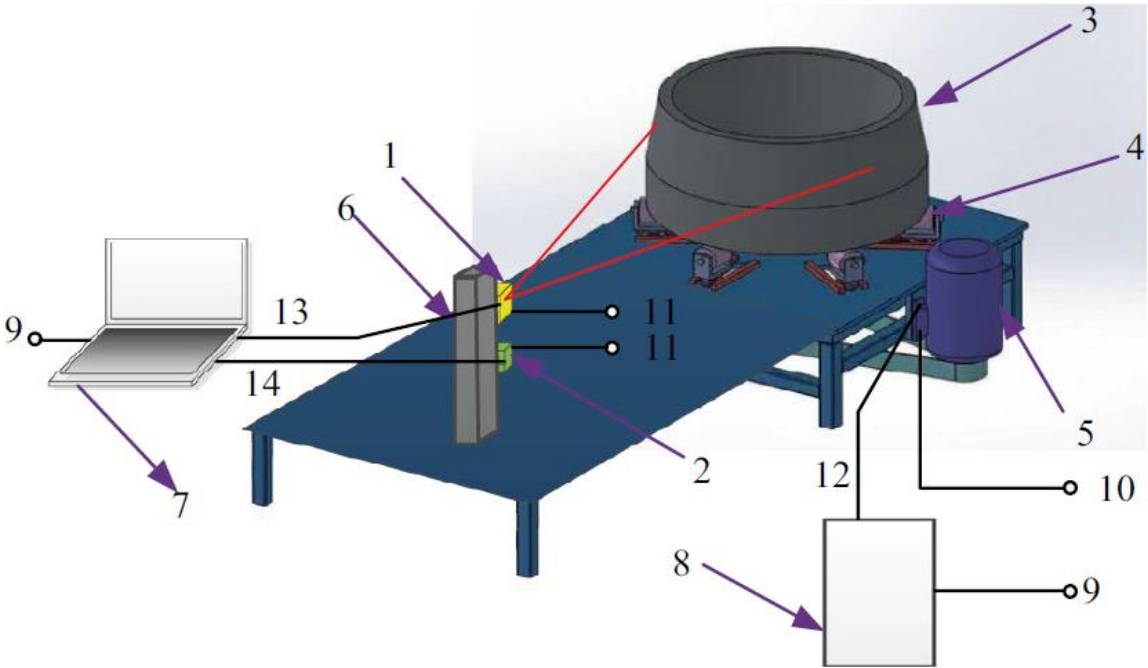


Fig. 2-23 A diagram of the measurement system based on 2D laser scanner and a CCD camera; 1 – laser scanner, 2 – camera, 3 – ring forging, 4, 5, 8, 10, 12 – manipulator, its motor, controller and supply, 6 – measurement system positioning system, 7, 9 – data processing system and its supply, 11 – measurement system supply, 13, 14 – laser scanner and camera data transmission line [40].

Laser scanning also achieved commercial application. The measurement system LaCam Forge measures the whole geometry of the forging, including the axis straightness for its correction. According to the brochure [1], the maximum forging length is limited to 28 m. The scanning time is a maximum of 15 s; however, more scans are needed to capture the complete forging geometry (1 – 4). This results in a total measurement time of 2 – 3 minutes. The standard deviation of the axis straightness or the coaxiality of the fittings is 5 mm, while the standard deviation of the measurement of length, diameter, or height is 10 mm.

### 2.3.2 Active stereo vision

A set of publications [41–46] examined the application of structured light-aided stereo vision in the measurement of forgings. A diagram of the developed system is provided in Fig. 2-24. Using the structured light source, a pattern was projected on the surface of the forging, which was triangulated by the calibrated stereo pair. A pair of calibrated cameras (REDLAKE ES4020, resolution  $2048 \times 2048$  px) was used. Zhang’s method [7] was used to calibrate the cameras. A DLP projector 3M PD80X (5000 lm) was implemented and BD 440SP, 440 nm low-cut filters were applied (spectral selective method) [41, 42, 46]. In later works, the projector was replaced with an array of blue line lasers (450-BL, Changchun Laser Optoelectronic Technology Company) and the low-cut filter was replaced with narrow bandpass filter BP450-40 TFI, with 450 nm band center [43–45]. In all cases, the authors measured only the basic dimensions of the object (length, width, or diameter).

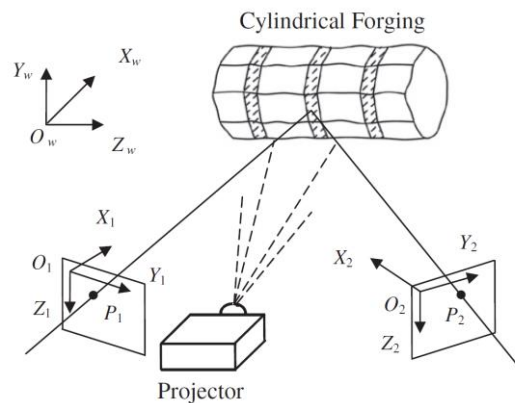


Fig. 2-24 Structured light aided stereo vision forging measurement system; camera parameters  $O$ ,  $X$ ,  $Y$ ,  $Z$  are known,  $P_1$  and  $P_2$  are the corresponding image points of an object point [42].

In the first publication of this set [41], the authors used vertical fringes projected on the surface of the forging. Only the ends of the fringes (enlightened silhouette points) were triangulated. This resulted in the forging 2D (width or diameter) measurement in the individual cross sections (Fig. 2-25). The authors developed an enlightened silhouette point detection method that achieves subpixel accuracy, based on the modified Gaussian profile of the fringe.

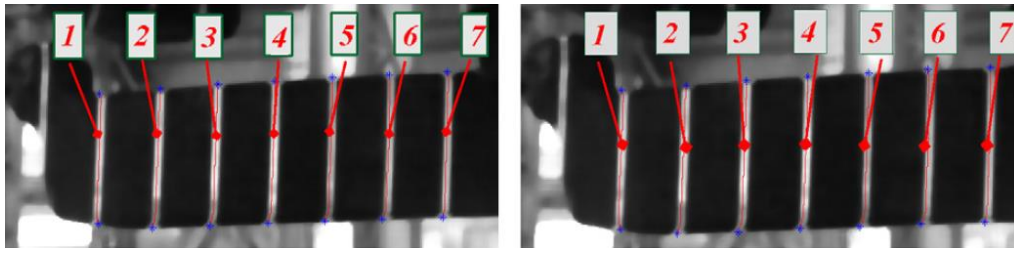


Fig. 2-25 Stereo images from the measurement system with triangulated fringe (1 - 7) end points (marked blue) [41].

The second publication [42] dealt with the 3D measurement of the forging geometry in individual cross sections. Both vertical and horizontal fringes were projected on the forging surface and their intersections were triangulated. To achieve subpixel accuracy of the detection of the fringe centers, the fringe profile model based on the Weibull distribution was used. The output of the measurement is provided in Fig. 2-26.

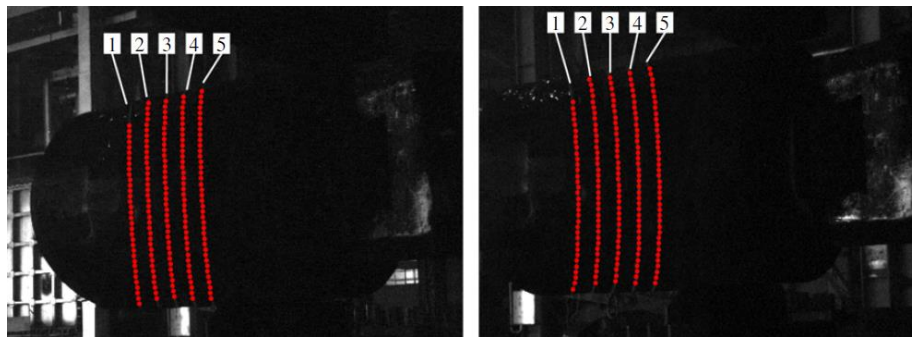


Fig. 2-26 The stereo images from the measurement system with triangulated points on the fringes 1 – 5 (marked red) [42].

In [44], the authors replaced the DLP projector with 5 blue line lasers. Laser power was regulated, based on forging temperature, to achieve an optimum signal-to-noise ratio of 10. The laser power was calculated based on the SNR prediction for forging temperatures 1050 – 1250 ° C. The distance between the measurement system and the forging was 2 m, the dimensions of the forgings were around 100 mm, and the calculated laser power for 1250 ° C was 1004 mW. The authors used the same 2D silhouette point reconstruction method as in [41]. Publication [45] introduced the accurate calibration method for this measurement system. This two-step method included the laboratory calibration of physical image center and the focal length. The calibration of exterior camera parameters and the distortion parameters was carried out using a checkerboard on-site.

Publication [43] extended the previously mentioned principle described in [44] by the application of two stereo pairs. Due to this, the measurement volume was increased to  $8.6 \times 5$  m. The distance between the object and the measurement system was 7 m. An array of 200 mW lasers was used to project fringes onto the object. Four 11 Mpx industrial grade cameras were used. The measurement system and the sample result are provided in Fig. 2-27. The camera calibration method of the measurement system was presented in [45].

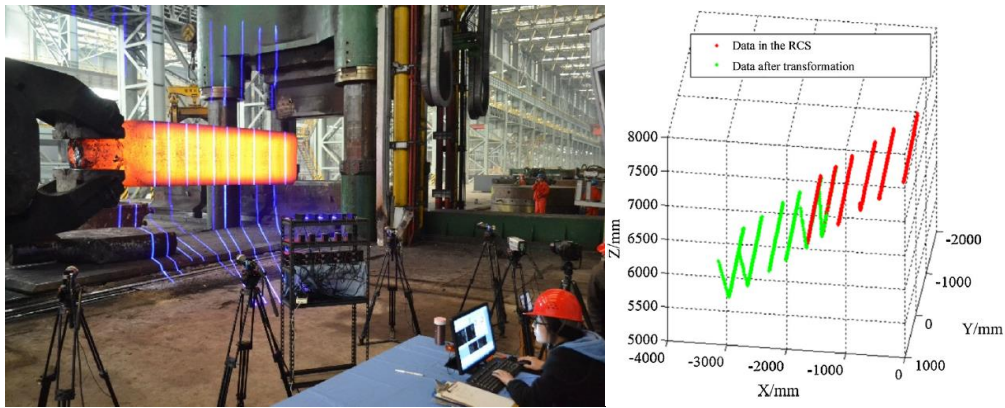


Fig. 2-27 Left – measurement system based on two stereo pairs, right – sample measurement result [43].

The function of the measurement system was demonstrated both in the laboratory and in the industrial environment. However, the accuracy of the measurement system was studied only in the laboratory environment. For systems that used a DLP projector, the accuracy of the measurement system was examined only by measuring cold objects. The measurement error ranged from 1% to 0.5% in the case of measurement of reference parts with dimensions 100 – 600 mm (sheet dimensions or diameter of the cylinder) [41, 42, 46]. Better results were achieved by using the laser array. The measurement error was less than 0.3% in case of a hot (up to 1250 ° C) 100 mm steel cube measurement [44]. In case of the measurement system based on two stereopairs, only the accuracy of the calibration was examined under laboratory conditions (average error 0.052%) [43].

### 2.3.3 Fringe projection systems

Zhao et al. [47] dealt with an application of the fringe projection system on hot forging measurement. The measurement setup consisted of a DLP projector and a camera. The system was calibrated using a set of checkerboard images (Zhang’s method [7]). The blue spectrum was used (blue pattern and blue channel of the RGB image) to enhance the signal-to-noise ratio. A three-frequency heterodyne was used for phase unwrapping to reduce the effect of nonuniform surface reflectivity of the forging (scales). A method based on a Butterworth lowpass filter was used to correct the unwrapping phase and to remove high-frequency noise. The measurement system configuration, as well as the evaluation workflow is provided in Fig. 2-28. The proposed methods were demonstrated by measuring a forging with 63 mm height and 114 mm width and a temperature of 1200 ° C. However, the accuracy was estimated only by measuring a planar object by room temperature (RMS and maximum error 0.8362 and 1.4785 mm, respectively). It was concluded that the relative error of the measurement system was less than 1:1000.

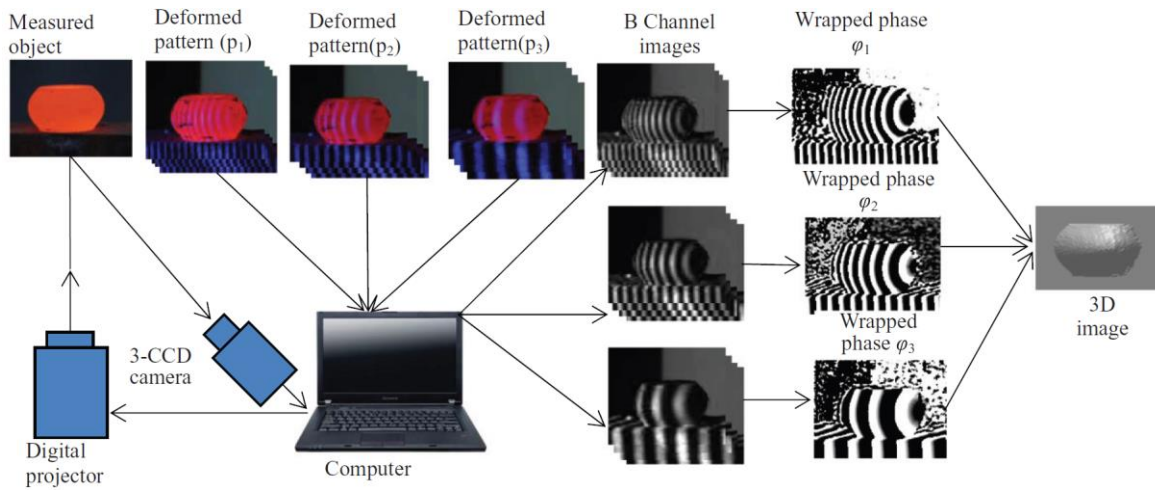


Fig. 2-28 The diagram of the fringe projection system and the result evaluation using blue image component and three-frequency heterodyne [47].

Han et al. [48] used a two-camera fringe projection system driven by a robot to automatically inspect hot forged objects on a production line. The cameras were equipped with a dual filter (IR cutoff and blue bandpass) to suppress thermal radiation. Time-division-multiplexing trigger and improved multi-frequency phase-shift sequence were used to cut the measurement time by approx. 39%. To perform the alignment, the robot positioning repeatability assumption and modified iterative closest point were used. The proposed methods were experimentally verified by repeated measurement of an axle (Fig. 2-30, 11 times). The maximum dimension of the axle (analysis provided in Fig. 2-30) was approx. 1900 mm and the maximum deviation was 0.11 mm.

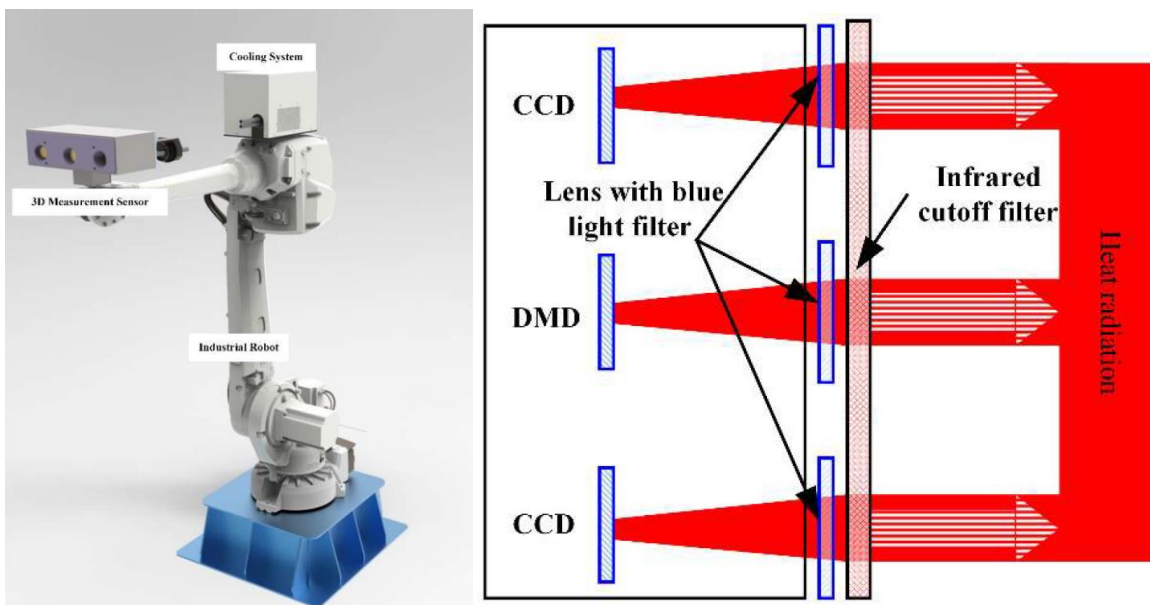


Fig. 2-29 Left - robot-driven fringe projection measurement system, right – sensor setup with a projector, 2 CCD cameras and dual optical filter [48].

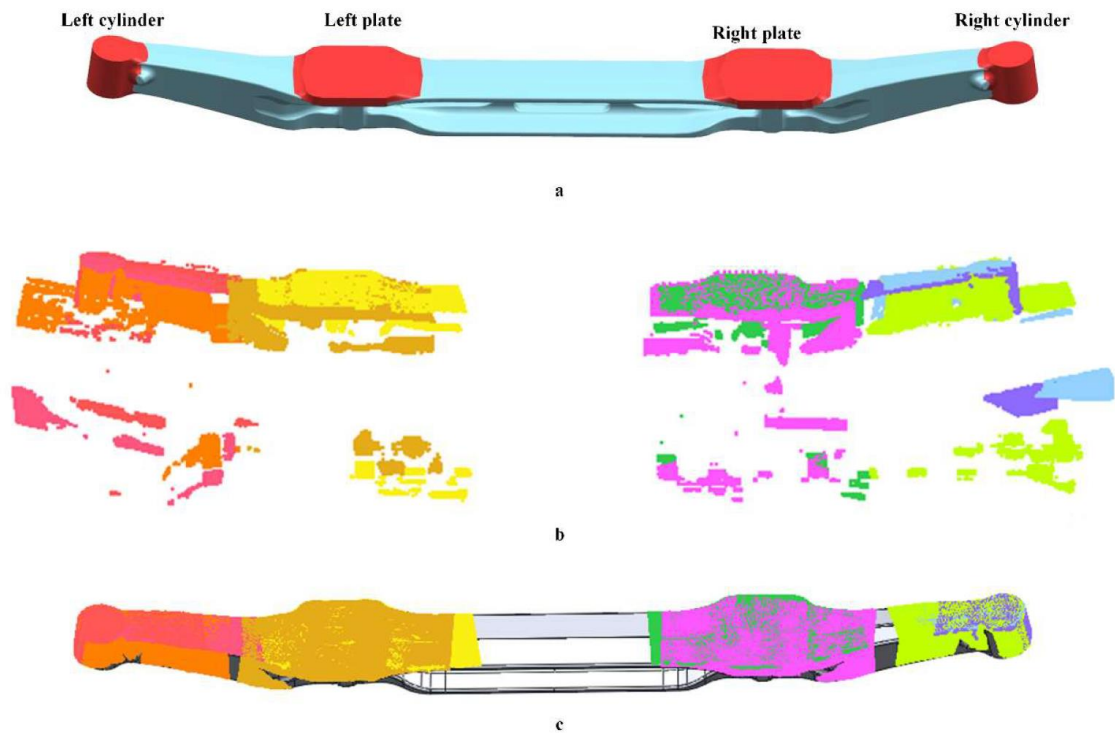


Fig. 2-30 Analysis of a forged axle [48].

The works [49, 50] dealt with the development and adaptation of phase-shift fringe projection system on the measurement of hot objects. The measurement setup used four cameras and a green LED projector. The cameras were equipped with bandpass filters. The setup is provided in Fig. 2-31.

In [49], the quality metric for a 3D geometry measurement was developed. The metric was based on the variance of a set of reconstructed, redundant points from their mean value. This method was verified both on the simulation model and also experimentally during the measurement of a hot object or a cold object behind a glass plate. In both cases, the effect of light refraction on the variance of the reconstructed point was examined, and the feasibility of the developed metric was demonstrated.

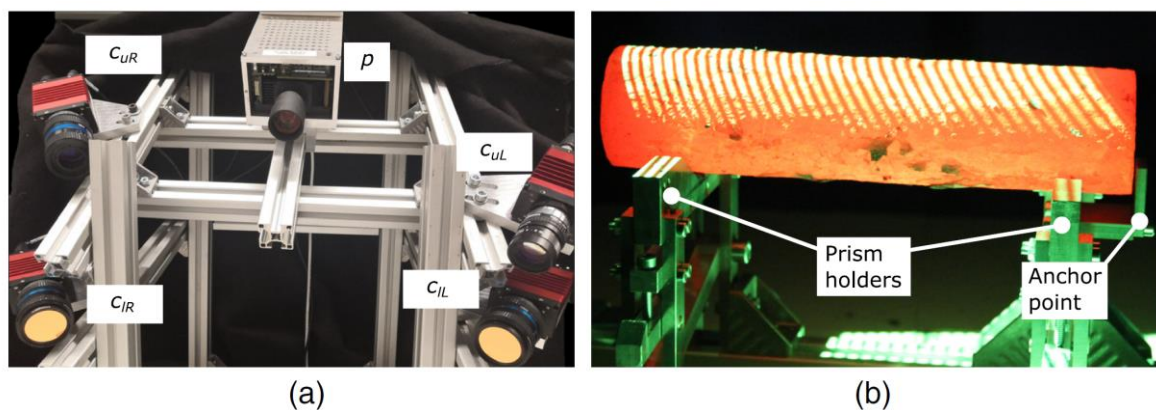


Fig. 2-31 The four-camera fringe projection setup (4 cameras C and a projector p) [49].

In [50], the authors dealt with the effect of forging radiance, which affects the phase-shift forging measurement. With the changing forging temperature, the background illumination decreases and affects the phase shift calculation. Moreover, if the air lens around the forging is physically compensated for by using a forced air flow system, the cooling effect during fringe projection could be significant. Therefore, the authors suggested two ways to suppress this effect:

- modified fringe projection sequence, minimizing the time between the corresponding images used for shape calculation
- approximation of the background intensity due to cooling (linear or quadratic).

The proposed methods were experimentally verified. A cylinder with 50 mm in diameter, 250 mm in length, and with a temperature of 1000 °C was measured. The results are provided in Fig. 2-32.

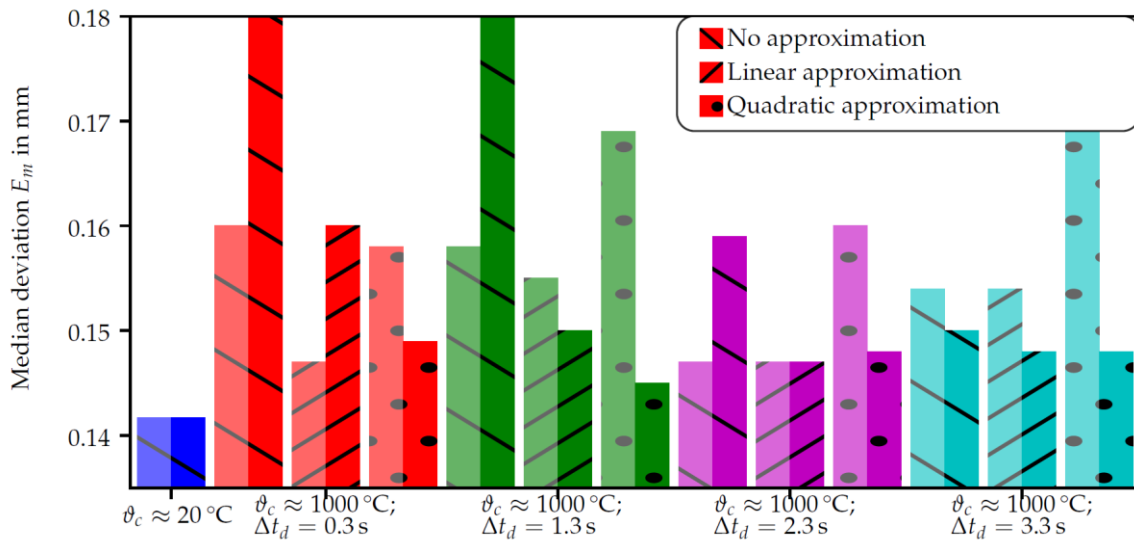


Fig. 2-32 Reconstruction quality values for different forging temperatures  $\vartheta_c$ , different time delay  $\Delta t_d$  between the activation of the air flow and the measurement, pastel colors are used for a standard sequence (air flow was not activated in this case), bright colors for the adapted sequence [50].

Based on the results, it can be stated that the combination of air flow, adapted projection sequence, and changing radiance compensation significantly improved fringe projection precision. However, the measurement time increased from 1 to 1.5 seconds due to the modified fringe projection sequence.

### 2.3.4 Laser triangulation

Zhang et al. [51] examined the feasibility of the application of line scanning (based on the laser triangulation method) to the measurement of hot objects. A green laser and narrow-bandpass green optical filter to enhance the signal-to-noise ratio (spectral selective method) were used. The device (a calibrated setup of a line laser and a camera) was placed on a linear

bearing with an accurate positioning system. The authors used a line laser MGL-III with 311 mW power, MV-VE078SM/SC camera with  $1024 \times 768$  px resolution, and a linear positioning system with  $40 \mu\text{m}$  accuracy. The angle between the optical axis of a camera and a laser plane was  $30^\circ$ . The calibration of the system was carried out using a checkerboard. The result of the individual scanning operation was a set of object points in a cross section. More scanning operations along the forging axis were carried out and compiled according to the data from the linear positioning sensor. However, the authors only measured the diameter of the object.

The same laser triangulation method was used by Bračun et al. [52] (Fig. 2-33). The developed system was capable of measuring up to 1.4 m long objects with 0.5 m diameter. The distance between the forging and the measurement system was 4.2 m. A 530 nm laser and a camera with a resolution of  $1290 \times 960$  px were used. The system was calibrated based on the reference 3D object moved by the accurate CNC positioning system ( $10 \mu\text{m}$  accuracy). The authors newly used difference imaging to enhance the signal-to-noise ratio. The method used a difference of two images taken in a short time from the same point of view. In one of the images, the line laser is switched off. The difference of images resulted in the suppression of the background and, therefore, in an enhanced of the signal-to-noise ratio.

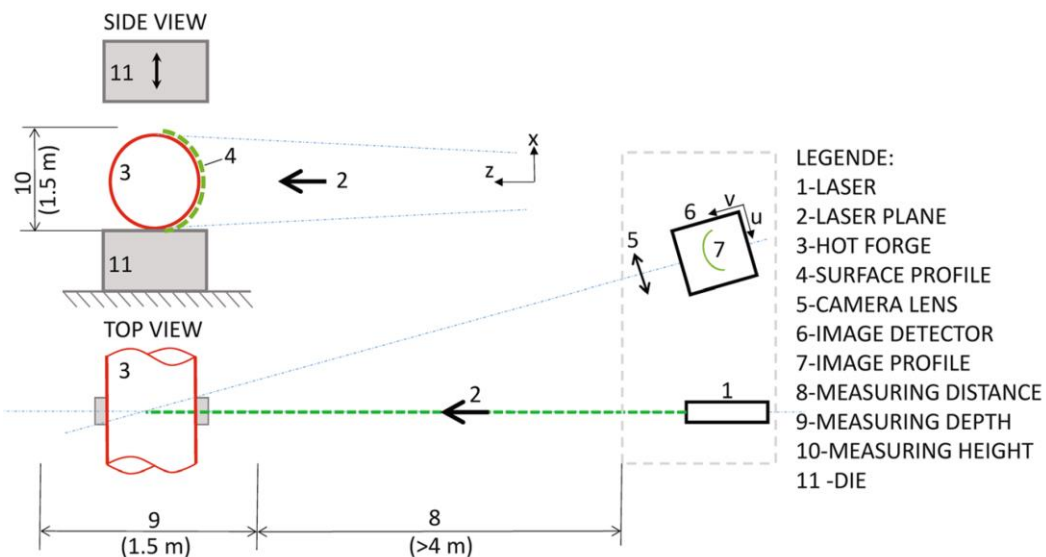


Fig. 2-33 Forging measurement using laser triangulation method [52].

Both authors experimentally verified the developed measurement systems. In case of Zhang, the largest measured dimension was 800 mm, in case of Bračun 440 mm. The surface temperature of the measured object was around  $1000^\circ \text{C}$ . In both cases, the reference dimension was measured by contact measurement techniques, although with high measurement uncertainty. Both authors reported the uncertainty of the optical measurement under 0.5%.

The authors [53] developed a specialized measurement device, integrated in a manufacturing line. The measured objects were forgings with complex shapes and high temperatures (around 600 °C). The device used two line lasers, (3 cameras total) according to Fig. 2-34. Spectral selective method was used. Blue line lasers were utilized (power 20 mW, 450 nm); bandpass optical filters were applied (transmission spectrum in interval of  $450 \text{ nm} \pm 25 \text{ nm}$ ). The calibration was carried out using a rotationally symmetric object and achieved 0.01 mm accuracy. The reference geometry was obtained using 3D scanning of a cold object. Objects of dimensions up to 162 mm were measured with an accuracy of 0.1 mm. The exact influence of the interfering effects was not examined. The developed device replaced a contact measurement method on the manufacturing line and achieved significantly faster forging measurement (1 vs. 20 minutes).

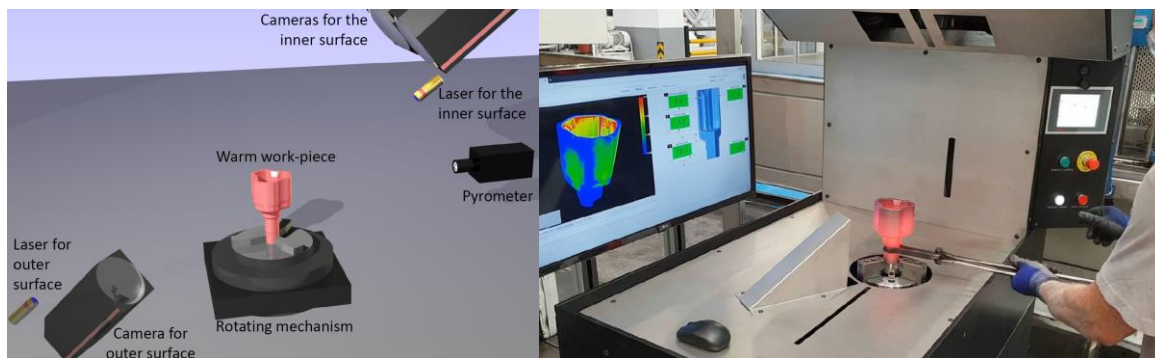


Fig. 2-34 Left – the layout of measurement system based on laser triangulation, right – on-site measurement [53].

Ghiotti et al. [54] also dealt with the design of the forging measurement system implemented in the manufacturing line. The authors used eight line lasers mounted in specialized construction. The object was moved by a motion platform. The diagram of the system is provided in Fig. 2-35. The object dimensions considered were 800 mm in length and diameter. The authors used Zumbach Electronic line scanners with a depth resolution of 0.03 mm. Spectral selective method was used. The authors dealt with the leveling of error. The thermal dilations of the frame decalibrated the system, causing a systematic error of 0.5 mm. Therefore, the whole system frame was cooled using an active water-cooling system. Thanks to this system, the error from this effect decreased to under  $50 \mu\text{m}$ . The maximum error due to the hot atmosphere around the forging was estimated to be  $30 \mu\text{m}$ . Both effects were further neglected. The developed system was experimentally verified based on the measurement of objects with known geometry and a temperature of 300 – 800 °C. The resulting uncertainty of the measurement was  $9 \mu\text{m}$ . The measurement time was less than 10 s.

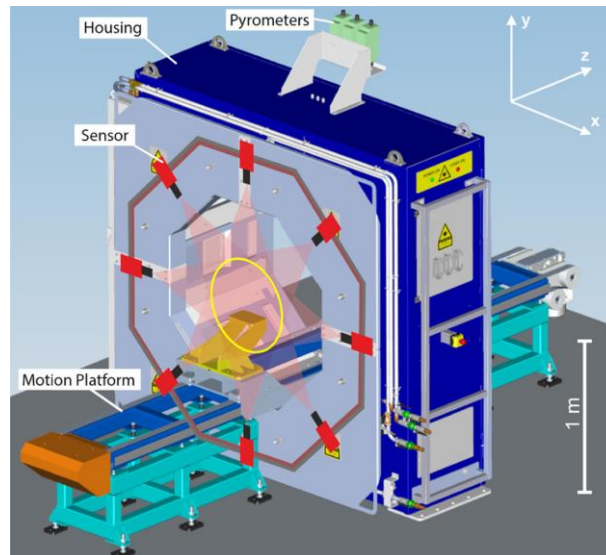


Fig. 2-35 The forging measurement system based on eight line scanners [54].

## 2.4 Passive optical forging measurement

### 2.4.1 Passive stereovision

Authors [55] dealt with the multi-image measurement of structured, deformed aluminum plate using passive stereo vision (Fig. 2-36). Triangulation of feature points obtained using the FAST feature point detector was used. Coded calibration targets were used to calibrate the cameras. The bundle adjustment was used to reconstruct the geometry of the object. The proposed method was experimentally verified. Eight images were used to measure the object. The reconstruction accuracy was dependent on the setup of the triangulation method (only points visible on four images and with a low reprojection error were used). The authors achieved an accuracy of up to 0.038 mm during a measurement of plate with 800 mm diameter (a relative accuracy of 1:21 000). The accuracy was estimated based on the distance between the skew lines used for the reconstruction of an object point.

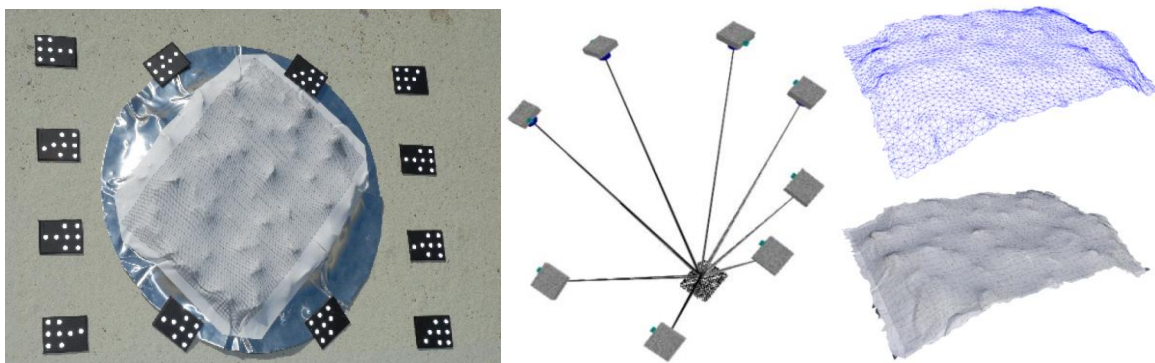


Fig. 2-36 Passive stereovision measurement; left – measured scene, center – camera positions, right – 3D object reconstruction [55].

The authors [56] examined the possibilities of the application of passive stereo vision during the measurement of hot formed parts. A proposed concept of a measurement system worked with a calibrated camera stereo pair (Fig. 2-37). The authors used a spectral selective method to remove the influence of the forging thermal radiation in the visible spectrum. The forging was illuminated using a 500 W xenon lamp and the cameras were equipped with a 450 nm low-cut filter. The measurement was based on the triangulation of the corresponding feature points. The feature points were extracted using the Harris corner operator. The authors carried out an experiment to demonstrate the measurement system; however, the accuracy of the system was not examined. The measurement images, as well as the resulting point cloud, is provided in Fig. 2-38. The measured object temperature was 1200 ° C; the dimensions were not provided.

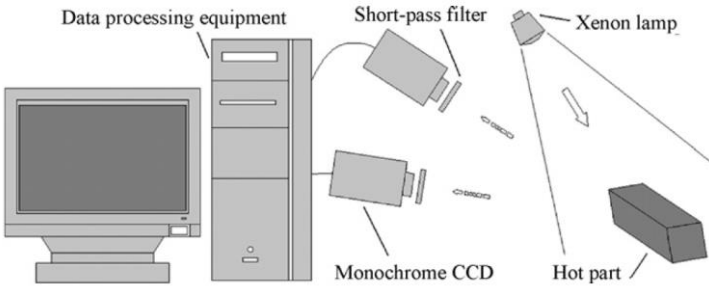


Fig. 2-37 A concept of forging measurement system based on stereo vision [56].

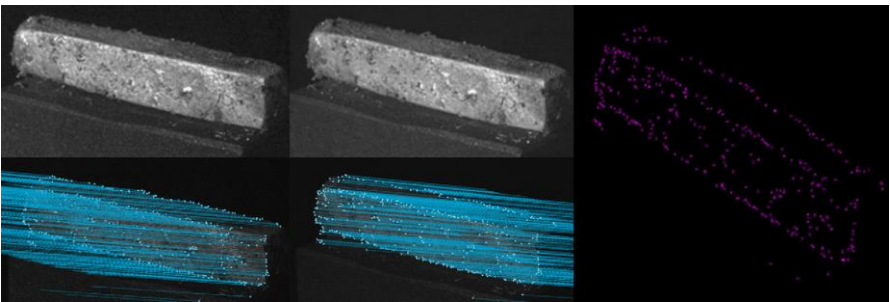


Fig. 2-38 Left – stereo images with corresponding feature points (marked blue); right – resulting 3D reconstruction of the object [56].

Lins et al. [57] proposed a six-camera measurement system based on stereo vision, for the measurement of forged crankshafts (Fig. 2-39). The object was illuminated using unspecified light sources. The corresponding feature points were found using the SIFT method. Accuracy verification of the measurement system was carried out only in a simulated environment. The estimated uncertainty of the measurement was around 0.5%.

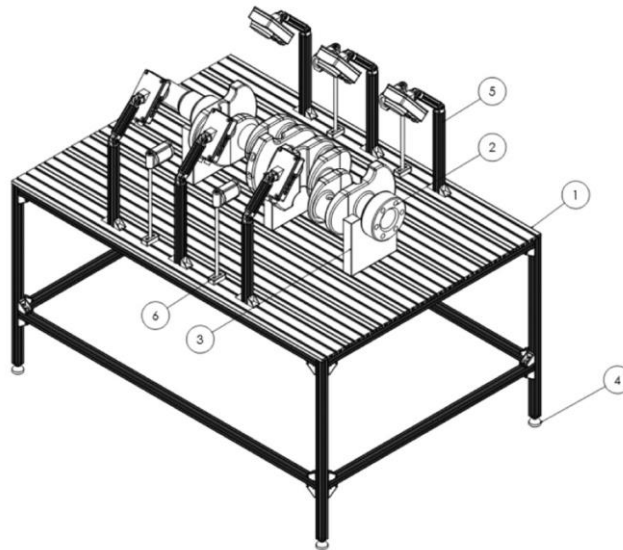


Fig. 2-39 Crankshaft measurement system based on stereo vision [57].

## 2.4.2 Measurement based on silhouettes

The authors [58] examined the possibilities of the hot object measurement based on their silhouettes, using a monocular system (Fig. 2-40). The camera was equipped with an IR cut optical filter to prevent blurring of the image. Edge detection was based on the Sobel edge detector. The internal parameters of the camera were calibrated using the Zhang method [7]. The px to mm ratio in the measurement image plane was calibrated based on calibrated objects with known dimensions. The accuracy of the system was determined based on the comparison of the measured dimensions with the known reference specimen length. The measured objects were steel cubes with dimensions of up to 60 mm. The experimental measurement of both cold and hot (1000 ° C) cubes showed an error of approximately 0.3 mm, which was considered as satisfactory.

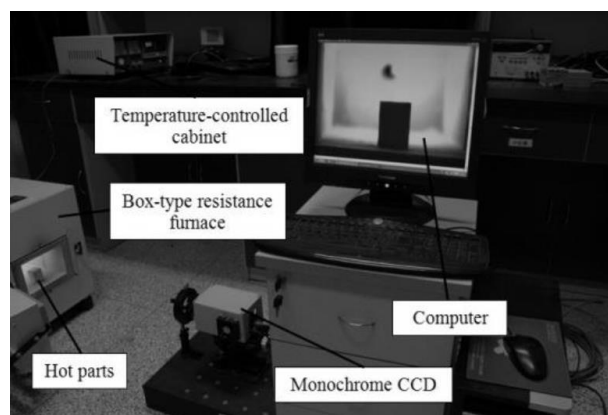


Fig. 2-40 Two-dimensional measurement setup for small forgings measurement, based on their silhouettes [58].

Zhou et al. [59] dealt with the measurement of basic object dimensions (length, width, or diameter) based on line triangulation. Image processing was based on the Hough transform, which was used to find straight lines in the image. The system was calibrated using Zhang's method [7]. The method was based on line triangulation, rather than the triangulation of individual points, to achieve high reliability. The precision of the developed system was experimentally verified in both a laboratory and an industrial environment. During laboratory experiments, the cube with an edge length of 140 mm was measured with a maximum relative error of 0.62%. During the on-site experiment, a single measurement of cylindrical forging with 115 mm in diameter (Fig. 2-41) with 0.79% relative error was carried out. From the publication, it is not clear how the reference dimension was obtained.

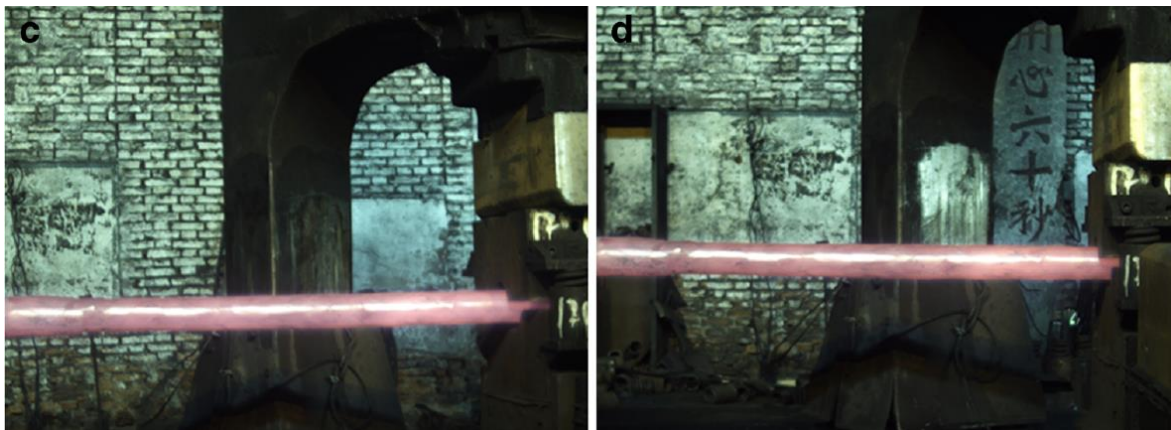


Fig. 2-41 Stereo images of hot cylindrical forging for the subsequent reconstruction using line triangulation method [59].

Wang et al. [60] developed a framework for measuring rolled bars, directly in the process of their manufacture. The framework was suitable for low-cost automation devices. The monocular measurement system was based on a GoPro® camera. The camera was calibrated using a checkerboard. The edges were found using a random forest algorithm and further denoised using morphological operations. The result can be seen in Fig. 2-42 in the upper row. The image still contained false positive edges. Based on the Moore-Neighbor algorithm, multiple potential edges were found around the expected forging boundary. Boundaries of interest were created around the potential edges (Fig. 2-42, lower row, green curves). The image was then processed using the random regression algorithm (fitting a line in the potential edge points, Fig. 2-42, lower row, black lines). This was carried out in a sliding window (Fig. 2-42, lower row; sliding windows are divided by white lines). The indicator of the level of trust ( $\Sigma$ ) in the sliding window was proportional to the diameter standard deviation in the sliding window and the area between the boundaries of interest. It was shown that if  $\Sigma$  was large, the level of trust was low and the measurement result was inaccurate (Fig. 2-42). Based on the level of trust, the corrupted measurements were deleted.

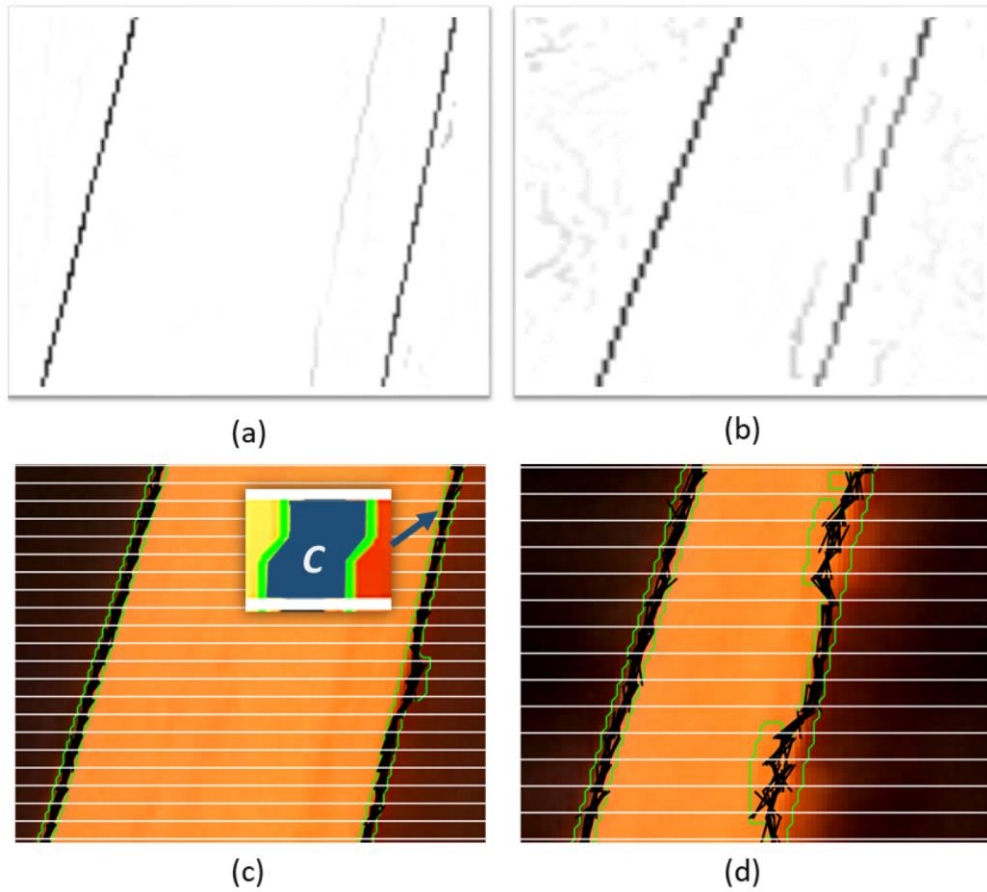


Fig. 2-42 Upper row – denoised edge maps obtained using random forest algorithm; lower row – measurement images with boundaries of interest (green) and random regression line fitting results (black) in the sliding windows (separated by white lines); the detail depicts the area C between the boundaries of interest [60].

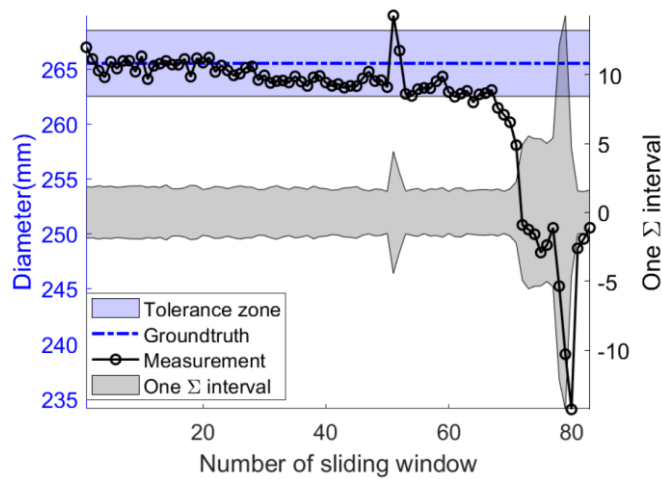


Fig. 2-43 The results of the measurement compared with the ground truth and the level of trust indicator ( $\Sigma$ ) [60].

In a set of publications [2, 61, 62], a passive 3D measurement system for the measurement of forgings, based on their silhouettes, was developed. The measurement system was limited

to cylindrical forgings, which are, however, the most common. The system worked with two calibrated cameras, whose optical axes were perpendicular and faced to the center of gravity of the forging from the radial direction (Fig. 2-44). The forging was held in V-prisms during measurement. The measurement system was able to measure the diameter, length and axis deflection of the forging. It was shown that the measurement system, based on this principle, could theoretically measure forgings up to 20 m in length and 6 m in diameter (Fig. 2-45). However, the measurement system was verified only in a laboratory environment on a small scale, in a basic two-camera configuration.

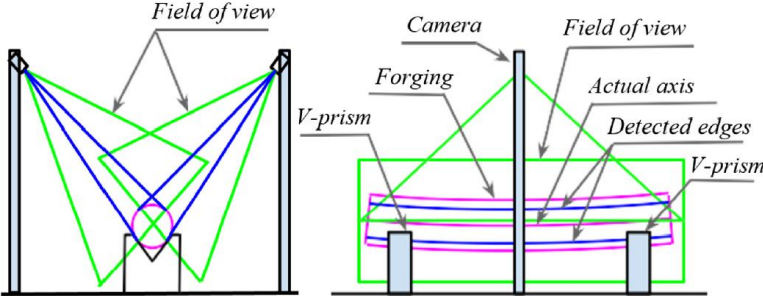


Fig. 2-44 The concept of a two-camera system for the measurement of heavy forgings [2].

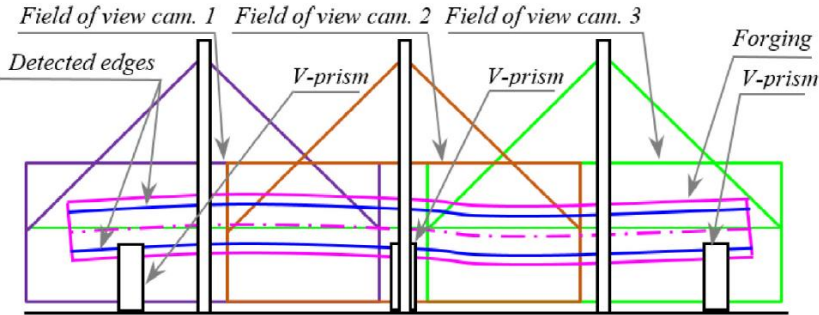


Fig. 2-45 The concept of a camera system for the measurement of forgings with extended measurement volume [2].

The camera system was calibrated based on several calibration targets (noncoded) placed in the scene. Their accurate coordinates in the space were measured using the industrial photogrammetric system TRITOP (GOM). The targets were segmented in the measurement images using thresholding, and their coordinates in the image were found using the centroid method. The camera calibration method implemented a direct linear transformation method. This method is not capable of calibrating optical setup distortion; therefore, the distortion (one-coefficient radial) was estimated by the user and removed prior to the calibration itself. The reprojection error of the calibration method was in the order of pixels.

To find the silhouettes of the object, the measurement system used the edge detection method, which worked in several steps:

- Detection of edge point candidates: The method used two rectangular windows shifted by one pixel, which scanned the image from the center of the image in the

horizontal or vertical direction. If the median values in the windows differed by a value larger than a threshold, the edge around this point was considered.

- Enhancement of edge detection accuracy: The edge point was considered as the pixel with the highest image gradient. Around the expected edge, the highest gradient was searched in a window of  $1 \times 7$  pixels (Fig. 2-46).
- Edge validation: The edges were validated based on connectivity of the edge points.

The edge detection was sensitive to the contrasting scales on the forging surface or background. The result of edge detection is provided in Fig. 2-47. However, the false positive edges were suppressed by edge validation.

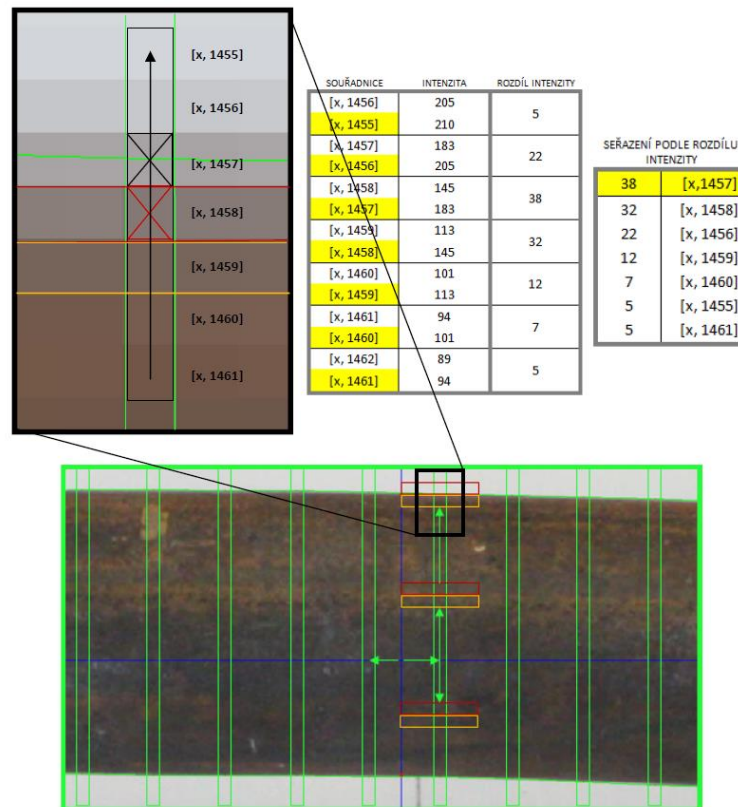


Fig. 2-46 Detection of the edge points, based on image gradient. A section of the original image with magnified edge; yellow and red windows are used to search for approximate edge; black window in the magnified image is used to search for the gradients around the edge; the table in center shows the pixel coordinates, their intensities and the difference of the intensities of neighboring pixels; the table on the right shows the intensity values from the highest to the lowest, with their coordinates, and the selected edge point marked yellow [63].

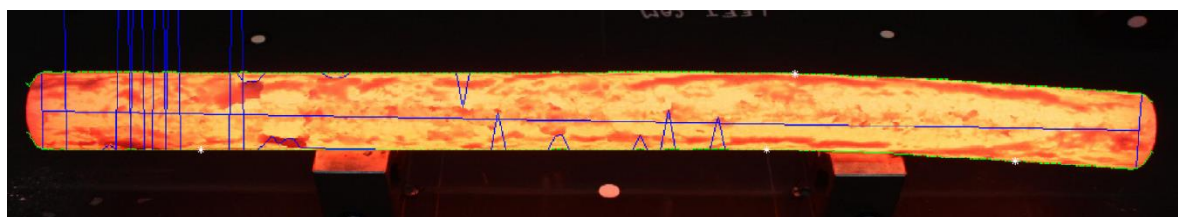


Fig. 2-47 The section of the measurement image with the edges; edges before and after the validation are marked blue and green, respectively [63].

The silhouettes from both measurement images were projected to the mutually perpendicular reference object planes, which were estimated based on the known approximate diameter of the object and the known geometry and location of the V-prisms. In regular cross sections, the circles were fitted in the silhouette points. The centers of the circles were considered as the axis points. The resulting axis and the diameters were smoothed (in the case of the axis and diameter using the Savitzki-Golay and moving average filter, respectively).

The measurement setup used two common digital single-lens reflex cameras (DSLR) with a zoom lens on tripods. The V-prisms and the calibration targets were mounted on a platform between cameras. The measurement error was determined based on the comparison of the measurement result with the reference geometry obtained using 3D scanning. The thermal dilation was compensated for.

The proposed methods were verified under laboratory conditions. Seven samples of 500 – 700 mm length, 50 mm in diameter, and a maximum deflection of 0.3 – 21.08 mm were measured. Each sample was measured 10 ×. The statistical evaluation of the results is provided in Fig. 2-48. The measurement system showed a measurement error of under 2%. However, the deflection characteristics were not evaluated in the hot state. By assuming the same relative error in different scale, the prediction of the system error in large scale, under industrial conditions, was carried out (Fig. 2-49).

Sample no.	Max. deflection (unheated)		Dimensions (unheated)		Dimensions (heated)	
	Size [mm]	Position [mm]	Length [mm]	Diameter ~ [mm]	Length [mm]	Diameter ~ [mm]
1	-0.47	-12.00	3.4	0.1	-	-
2*	0.05	0.80	0.5	0.0	-1.5	-0.3
3*	0.21	-3.28	1.0	-0.2	-3.5	-1.3
4	0.21	-8.21	6.2	0.0	-	-
5	1.28	-8.04	6.1	-0.1	-	-
6*	0.66	-5.13	-0.5	0.0	0.0	-1.6
7	2.05	6.56	-0.4	0.0	-	-
	<±2	<±12	<±6.2	<±0.2	<±3.5	Effect of scales?
	Dependent on the shape		<1%	<0.5%	<1%	

Fig. 2-48 The average error of the measurement of specimens 1 – 7 [2].

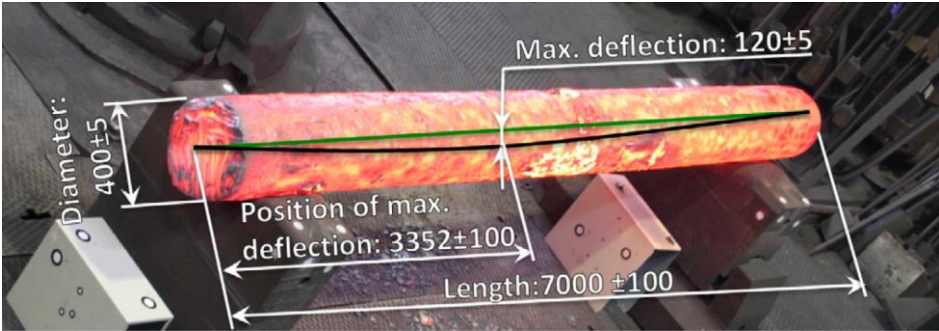


Fig. 2-49 The estimation of the accuracy of passive camera measurement system for its potential use in the industrial environment. [63].

### 3 ANALYSIS AND CONCLUSION OF LITERATURE REVIEW

During open-die forging, the shape deviations can appear and must be measured. The products (heavy forgings) are mainly cylindrical, and their dimensions could be up to 20 m in length and 6 m in diameter. Forging temperatures range between 800 – 1250 ° C [2, 37]. The measurement of these forgings is a challenge due to the influence of interfering effects or the industry environment, in general. The research can be divided into two basic approaches – active (the measurement system uses its light source, the light emitted by the forging is suppressed) and passive (these systems utilize the light emitted by the forging).

#### 3.1 Challenges during in-process forging measurement

The first interfering effect, which negatively influences the in-process measurement of heavy forgings, is thermal radiation. Forging, which is heated to the forging temperature, emits radiation in the infrared, near-infrared, and visible spectrum. The mechanism differs in the case of active and passive methods. In the case of active methods, radiation influences the signal-to-noise ratio (SNR) of the signal projected on the forging surface [17]. In the case of passive methods, the problem is the contrast between the whole forging and the background [13, 14] and the contrasting scales, making it difficult to find forging boundaries [15]. In both cases, the result can be inaccurately or false detected features (projected pattern, forging edges, surface structure) needed for the forging measurement.

Heat haze and the air lens surrounding the hot object can affect the accuracy of the measurement of the hot object due to light refraction [18–21]. All authors dealing with this effect admit that it is difficult to obtain accurate boundary conditions for the computation (air temperature, pressure, humidity, airflow, and so on). The experiment presented by [19] also showed high deviations from the developed model. Therefore, the solution to reduce this effect can be a forced airflow system [21] or a suitable placement of the measurement device [20]. However, the works show a relatively small effect of this phenomenon, on the order of tenths of a percent [19] or on the order of tens of  $\mu\text{m}$  [20, 54], depending on the situation. Therefore, in most works dealing with forging measurement, the effect of heat haze and air lens is not examined, even in the case of very accurate measurements, e.g., [48].

The calibration methods of forging measurement systems in the literature use a planar calibration field (e.g., [41, 42, 47, 59, 60]), a projected calibration field [43, 45], or various manipulators [45, 52]. These methods are difficult to use in large measurement volumes, because of the large dimensions of calibration objects or the industrial environment in general. Moreover, the external parameters of the camera can change due to thermal

dilations, leading to a significant error [54]. The solution can be a thermally controlled frame for mounting system components [54], or online calibration. For camera calibration in a large measurement volume, space resection can be used [9, 10]. This method uses a field of coded calibration targets with known location and achieves high accuracies. However, the circular coded calibration target systems used for photogrammetric measurement can fail under demanding conditions [8, 24–27, 29], where calibration targets could be damaged or occluded by scales falling from the forging surface. In various applications of machine vision, where the robustness of the target recognition is essential, this problem is solved using error correction methods [32–34]. However, different target designs are used.

## 3.2 Applicable approaches

### 3.2.1 Active measurement systems

The only measurement method that is not significantly affected by the specific environment is laser scanning [37–40]. Therefore, no special countermeasures to interfering effects were introduced in the literature. The best accuracy reported in the literature is 0.5 mm for the measurement of concentricity of cylindrical objects with up to 900 mm in diameter [39] or  $\pm 1$  mm for the measurement of the forging diameter of 2800 mm [40]. In this case, however, the scanned points were validated based on forging passive silhouettes measurement method. The laser scanning method is also commercially applied (e.g., LaCam Forge for the measurement of forgings up to 28 m long) [1]. The disadvantages of this approach are the high price of the sensor, the poorer accuracy in the case of measuring the length characteristics of the object, and the relatively long scanning times (on the order of tens of seconds [1]), during which the forging must be held still. The disadvantages of this principle motivate research in this field.

The remaining active methods are based on active close-range photogrammetry. All of the mentioned methods are affected by the thermal radiation of the forging, which resulted in the need for a spectral-selective method (used in all cases in the literature). In the case of fringe projection, many methods were developed that make this approach perform better during the measurement of hot objects. This includes the filtering method suppressing high-frequency noise [47], quality metric [49], adapted fringe projection sequences [48, 50] and prediction method to suppress unstable thermal radiation during image acquisition [50]. In the case of active stereo vision, an evaluation method was developed that uses subpixel detection of the projected feature lines based on a modified Gaussian [41] or Weibull distribution [42] function, or a specialized camera calibration method [45]. In the case of the laser triangulation technique, the difference imaging method was developed to improve SNR [52]. Both the fringe projection [48] and laser triangulation [54] methods achieved

implementation in forging lines. In these cases, the accuracy reported was 0.11 mm on a dimension of 1.9 m in the case of the fringe projection system [48] and 9  $\mu\text{m}$  in the case of 800 mm wide measurement volume (in the case of calibrated ceramic plates measurement) [54]. However, these principles have relatively small measurement volume, and therefore specimen manipulators or a robot system is needed to move the sensor. This increases the measurement time and decreases the potential for implementation of these systems in certain applications in the industrial environment, including on-site heavy forging measurement. On the other hand, a concept of active stereo vision with 8.6 m wide measurement volume was introduced [43], however, the accuracy of this system in these conditions was not verified. The system needed high-powerful light sources (1000 mW line lasers), and only a sparse point cloud was obtained. The best accuracy achieved by this method was 0.3% during the measurement of a hot object with dimensions of approx. 100 mm and a temperature of 1250 °C under laboratory conditions [44]. To conclude this section, active measurement systems are highly developed, as can be assumed from the usage of advanced methods, the accuracies achieved, and applications in the industrial environment. However, these methods still have disadvantages including limited measurement volume, longer measurement times, the need for a powerful light source, or the need for using manipulators, which can be impossible to install in many cases.

### 3.2.2 Passive measurement systems

Passive measurement methods for forging measurement include passive stereo vision and measurement based on forging silhouettes. Both methods can be used for accurate measurement of objects with contrasting surface structures or boundaries. For stereo vision, the object was illuminated by an external light source and a spectral selective method was used [56, 57]. Standard methods of detection of feature points (Harris corner detector or SIFT) were used. For forging measurements based on their silhouettes, the 2D [58, 60] and 3D [2, 59, 61, 62] systems were used. In all cases, edge detection was reported as a challenge. These methods in the literature were based on edge detectors with certain modifications [15], voting principle using the Hough transform [59], weighted variance to reveal measurement with low level of trust [60] or gradient in the image, and edge validation principles using edge point surroundings or connectivity [2]. The cameras were calibrated using Zhang's method [59] or basic space resection [2]. The 3D reconstruction method was based on the triangulation of feature lines (which can measure straight lines only) [59], or the transformation of the silhouette geometry into the object planes bounded to the positions of V-prisms [2]. The stereovision method was demonstrated in an industrial environment. However, the precision was not studied [56]. Another study examines the accuracy of stereo vision in a simulated environment, achieving a relative accuracy of 0.5% [57]. Moreover, 3D reconstruction could be sparse and depends on the forging surface texture. The accuracy of 3D silhouettes measurement varied from 0.8 (line triangulation) [59] to 2% (approach

presented in [2]). In case of line triangulation, the experiment was carried out in an industrial environment; however, in the other case, the experiment was carried out only under laboratory conditions.

To conclude this subsection, this approach showed a low level of development. Only basic methods are used, including edge detection with pixel precision, geometry reconstruction, or camera calibration. On the other hand, the approach presented in [2] is capable of measuring all the geometry characteristics of cylindrical forgings, including the axis straightness, and has the potential to overcome the disadvantages of active methods. There is a potential for rapid measurement in large volumes. However, in the literature, this method achieved a lower accuracy. The possible reason for the high error could be the application of only basic methods of optical measurement. Therefore, because of the low level of development of this method in this area and its potential for application, it was chosen as the subject of this study.

### 3.3 Summary, areas of missing knowledge

- Active forging measurement methods showed a high level of development, but also disadvantages such as limited measurement volume or relatively long scanning times. The 3D forging measurement, based on its silhouettes, is chosen as a subject of this study. This approach showed both the potential to overcome the disadvantages of active methods and a low level of development in this area.
- The passive measurement method achieved limited accuracy in the literature. It is not clear whether the reason is the implementation of basic methods in the studies dealing with this problem, or the effect of the interfering effect of the environment. Moreover, this approach was not verified in large-scale industrial conditions, where the character of the scene (scales size and contrast, background complexity, etc.) could be radically different.
- The main challenge of passive forging measurement is edge detection, which is different due to scales. It is not clear whether more advanced edge detection methods, with subpixel accuracy, would help achieve a lower measurement error or whether the potentially higher accuracy will be dominated by the negative effect of contrasting scales or forging background.
- Heat haze and air lens can have a negative effect on measurement accuracy. However, this effect is complicated to compensate for or suppress in a large measurement volume. This effect is also neglected in most works, including those in which high accuracies were achieved. However, it is not clear how this effect would affect the passive measurement method on a large scale.

- Space resection appears as the suitable camera calibration method for a large measurement volume. This method can also be performed online to compensate for the unstable environment. However, this method usually works with circular coded targets in photogrammetry applications, which recognition can fail in demanding conditions. It is not clear how to enhance their recognition robustness. A possible solution could be the error correction method used for target recognition in machine vision applications.
- Verification of the accuracy of the measurement system in an industrial environment is a challenge, which is not considered in many studies. Possible solutions to examine the precision of the measurement system used in the literature can be the analysis of the system accuracy indicators (reprojection error [10], variance of redundant measurement results [49]), measurement of objects with known dimensions [54], evaluation of measurement repeatability [48], or comparison of results with an individual measurement method [51, 52]. This can be, for example, laser scanning, which is not significantly affected by the interfering effects of the environment. However, based on the literature, it does not achieve sufficient accuracy to measure the reference dimensions.

## 4 AIMS OF THE THESIS

### 4.1 Main aim and the problems covered in thesis

During open-die forging, the shape and dimensional inaccuracies of heavy forgings need to be measured for their subsequent correction. This includes the measurement of length, diameter, and most importantly, the axis straightness. A review of the literature suggests the potential of a measurement method based on imaging of forging silhouettes in this application. However, this method showed a low level of development in this area. Therefore, the method achieved limited accuracy during the experiments. **The main goal of this thesis is to examine the properties and limits of the measurement approach based on object silhouettes in the industrial environment, during the measurement of heavy forgings. It is clear that original methods must be implemented to achieve high accuracy and reliability of the measurement system. These methods distinguish the proposed system from similar measurement systems based on the same principle. These methods and the study of their behavior represent the main novelty of the work.**

The goal is therefore achieved through the research, development, and systematic evaluation of the original or existing methods of optical measurement. The evaluation is carried out based on experimental data from both laboratory and industrial conditions. The interfering effects of the industrial environment are examined and resolved. The global contribution of this work is the original knowledge that brings the passive forging measurement method closer to implementation in the industrial environment. The work is a combination of applied research and experimental development. The specific subobjectives of research and development, based on the result of the literature review, are as follows:

- Objective 1: Research on the application of error correction method for circular coded targets used for camera calibration of the measurement system, to achieve reliable camera calibration in industrial environment.
- Objective 2: Development of calibration method for the cameras of the measurement system based on space resection, allowing on-line camera calibration to prevent the influence of dimensionally unstable environment.
- Objective 3: Research on the accurate edge detection method for the measurement of forging silhouettes, which can be corrupted by contrasting scales or background.
- Objective 4: Development of the forging silhouette measurement system, study of its precision in the industrial environment, and its comparison with independent comparative measurement method to demonstrate its feasibility.

## 4.2 Scientific question and hypotheses

As mentioned above, the thesis is a combination of applied research and experimental development. There are two research objectives (Objective 1 and Objective 3 in this order), which can be expressed using the following scientific questions and hypotheses:

- Question 1: How to implement error correction method in cyclic codes decoding of circular coded targets, used for camera calibration?
  - Hypothesis 1: The error correction method could use optimized target code library and a rotation-invariant distance between the scanned code and a code in the lookup table.
  - Reason: This error correction approach is implemented in a target system ArUco [32]. This system is used for augmented reality or machine vision applications and works with a square target design. The optimization of the target library and the error correction method during target recognition help the target system achieve high robustness, although without increasing the target confusion rate.
- Question 2: How to suppress corrupted edges during silhouette measurement?
  - Hypothesis 2: The weights, expressing the level of edge corruption, could be based on complementary information from the image, such as edge gradient magnitude and direction.
  - Reason: Based on forging images, published e.g., in [2], it can be assumed that the most correct forging edges have a strong magnitude and gradient direction perpendicular to the forging axis. On the other hand, corrupted edges have a weaker magnitude and random direction. The corrupted edges could then be suppressed using weighted edge filtering.

## 4.3 Thesis layout

The thesis is composed of three articles in journals with impact factor (Paper A, C, and D), and, in addition, one conference paper indexed in Web of Science database (Paper B). The conference paper is not a primary part of the thesis. However, it covers one of the important experimental parts and connects the individual topics covered in this thesis. The papers cover the Objectives of research and development identified in Section 4.1 via bullets. These topics are essential to resolve to achieve the main goal. In paper A, an original circular coded target system, for accurate camera calibration in demanding conditions, is proposed. The scientific Question 1, which deals with the error correction method of cyclic codes, is solved in this article. In Paper B, the camera calibration method is developed for the calibration of cameras of the system. The method uses the mentioned calibration targets and is verified under

industrial conditions, including the examination of the effect of the air lens. In paper C, the subpixel edge detection with weighted filtering is proposed, and the scientific Question 2 is answered. The Paper D deals with the development and verification of the multi-camera and multi-view measurement method, which is based on the acquired knowledge and fulfills the main goal of the thesis.

- A. J. HURNÍK, A. ZATOČILOVÁ and D. PALOUŠEK. Circular coded target system for industrial applications. *Machine Vision and Applications*. 2021, **32**(1), 1–14. ISSN 14321769. Available at: doi:10.1007/s00138-020-01159-1

Journal impact factor: 2.983 (2021, WoS), *Author's contribution 75%*.

- B. J. HURNÍK, A. ZATOČILOVÁ and D. PALOUŠEK. Camera calibration method of optical system for large field measurement of hot forgings in heavy industry. In: *Opt. Meas. Syst. Ind. Inspect. XI, Proc. SPIE*. 2019, p. 11056. Available at: doi:10.1117/12.2527693

Journal impact factor: -, *Author's contribution 65%*.

- C. J. HURNÍK, A. ZATOČILOVÁ, D. KOUTNÝ and D. PALOUŠEK. Enhancing the accuracy of forging measurement using silhouettes in images. *Measurement*. 2022, **194**(September 2021), 111059. ISSN 02632241. Available at: doi:10.1016/j.measurement.2022.111059

Journal impact factor: 5.131 (2021, WoS), *Author's contribution 60%*.

- D. J. HURNÍK, A. ZATOČILOVÁ, T. KONEČNÁ and P. ŠTARHA. Multi-view camera system for measurement of heavy forgings. *The International Journal of Advanced Manufacturing Technology*. 2022, ISSN 02683768. Available at: doi: 10.1007/s00170-022-09809-6

Journal impact factor: 3.563 (2021, WoS), *Author's contribution 50%*.

## 5 MATERIALS AND METHODS

### 5.1 Measurement system principle

The principle of forging measurement, utilized and developed in this work, was its 3D passive measurement, based on its silhouettes. The system worked with two or more cameras facing the center of gravity of the forging. The basic principle of such a system is depicted in Fig. 5-1. Based on calibrated camera projection model, the principle uses the projection rays of silhouette points from the image to space. Using 2 or more cameras, a circular object cross section can be determined. Objects with different cross sections can also be measured. However, the precondition is the convex cross section of the object.

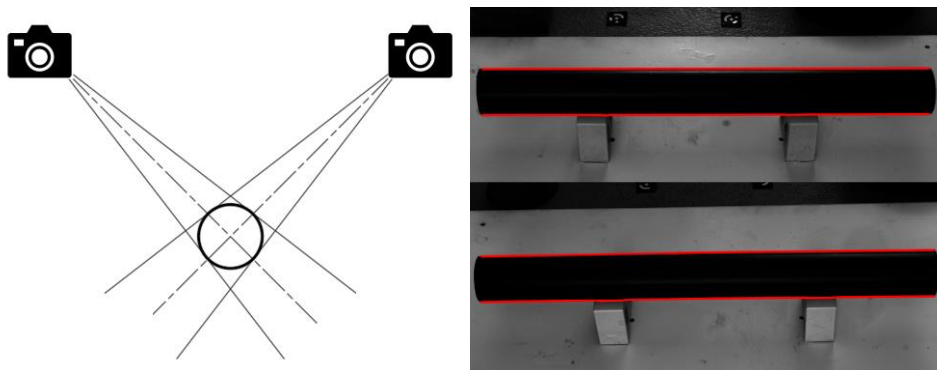


Fig. 5-1 Left - basic principle of a camera measurement system; right – example measurement images from the cameras of the system.

The measurement system workflow is provided in Fig. 5-2. The main input was the measurement images. There were two main parallel branches of the algorithm. The first was camera calibration. The first step was the coded target location in the image and their identification. Based on the target identification codes, the target coordinates in the space were associated with the target coordinates in the image. These data, together with the interior camera parameters, were the inputs to the exterior camera parameters calibration process. Both coded target coordinates in space and interior camera parameters were obtained during or before the installation of the system on-site. The other branch dealt with the silhouette extraction and object measurement itself. At first, the object was roughly segmented in the image and expected edge locations were obtained. The edges were then located using the zero-crossing subpixel edge detection method. To remove the influence of corrupted edges, the axis imprint and the edges were filtered. Based on the filtered edges and the camera parameters, the object geometry was calculated using the triangulation principle. The geometry was then aligned using two short regions on the forging ends. The geometrical characteristics of the forging, including forging length, diameter, circularity, axis straightness, maximum deflection, and its position, were then determined.

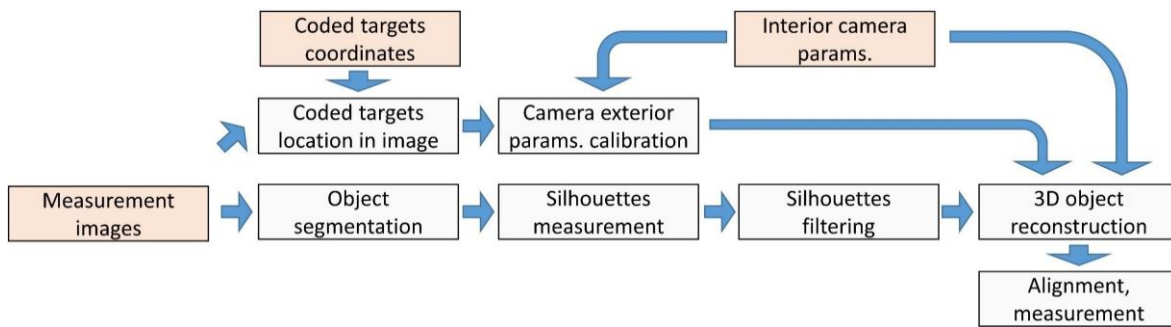


Fig. 5-2 Measurement system workflow (inputs marked red).

## 5.2 Proposed methods to enhance system robustness

To ensure the robustness of the system, the interfering effect of the industrial environment was identified, and the original countermeasures are introduced. These proposed features distinguish the proposed measurement system from the usual measurement systems based on silhouette measurement and represent the novelty in this thesis.

- Thermally and dimensionally unstable industrial environment, large measurement volume:
  - To ensure the high robustness of the target system, used for camera calibration in an industrial environment, the error correction method was introduced. The code library generator was implemented to create a code library with optimized properties. This included the rotation invariant distance between the targets in the library, to lower the target confusion rate, and the number of bit transitions, to lower the confusion rate between the targets and the objects in the environment. The error correction method then took advantage of the large distance between the codes in the library to recognize damaged codes. This was carried out based on the rotation invariant distance threshold, which was based on the distance between the codes in the code library. On the other hand, by using the target code recognition threshold, a higher confusion rate of the targets with random objects in the environment could be expected. Therefore, the similarity condition was introduced, which processed the scanned target code, based on the expected normal distribution of black and white target segments. In addition, robust target segmentation, code scanning, and accurate target location methods were implemented. These methods are described in detail in **Publication A**.
  - Camera calibration was based on the space resection method, which worked with a 3D calibration field of robust circular coded targets. Target coordinates are accurately measured using the TRITOP (GOM) professional

photogrammetric system. The method consisted of single-image, on-line camera exterior and multi-image, off-line camera interior parameters calibration. Online calibration was implemented to compensate for the dimensionally unstable environment. Moreover, to ensure stable intrinsic parameters of the camera, the cameras were placed in thermoregulated covers. The camera calibration method was described in detail in **Publication B**.

- Potentially low forging contrast in the image:
  - Based on the literature, forging contrast can be enhanced by using color filters. Red color filters were empirically chosen to enhance the forging contrast.
- Air lens and heat haze:
  - According to the literature review, the effect of air lens and heat haze cannot be easily compensated both physically (by using forced air flow, which is problematic in large measurement volume) and based on simulation (problem with boundary conditions). Therefore, in this work, the influence was minimized by suitable placement of the cameras (outside the hot air area) and by using red spectrum, to minimize the refraction.
- Forging segmentation in a complex environment:
  - Forging edges can be corrupted by contrast scales on the forging surface. Moreover, contrasting objects can appear near the forging in the scene. Major differences in brightness on the forging surface can be expected. Therefore, standard segmentation methods based on edge operators or thresholding fail. A specialized segmentation method was proposed. This segmentation method was based on the assumption that the approximate forging orientation and diameter are known. Therefore, the method worked as a filter sensitive to horizontal objects of a certain size. The method used the Sobel edge operator, morphological operations, dual threshold, and voting principle (Hough transform) to find the most probable forging axis and silhouettes in the image. The details of this method were described in **Publication C**. In the future, this method can be replaced by a more robust segmentation method based on neural networks.
- Corrupted edge points by scales on the forging surface or background:
  - According to the cylindrical forging images presented in the literature, it can be assumed that a correct edge has a strong gradient oriented perpendicular to forging axis. On the other hand, it can be assumed that the corrupted edge has a weaker gradient and an arbitrary orientation. Corrupted edges can have a major influence on measurement precision, mainly in the case of subpixel edge detection accuracy. Therefore, weighted edge filtering was implemented, based on these quality measures. Various combinations of

these quality measures were experimentally compared. The details of this method were described in **Publication C**.

- Effect of insufficient forging circularity:
  - In case of insufficient forging circularity and measurement with two cameras, major errors of the forging axis or diameter can appear. Normally, this problem is solved by using a large number of cameras; however, it is not possible in the industrial environment, where the possibilities of camera placement are limited. Therefore, a three-camera and multi-view measurement (utilizing an accurate forging press manipulator, used to accurately rotate the forging around its axis) was proposed. Details of these methods are presented in **Publication D**.

### 5.3 Measurement system hardware

The hardware of the measurement system consisted of a set-up of 2 or 3 cameras. To achieve high precision, high-resolution monochromatic cameras ZWO ASI 1600MM (Pro) were used. These cameras are equipped with a 4/3 " CMOS Panasonic MN34230 sensor. The resolution is  $4656 \times 3520$  px (16 Mpx), and the pixel size is therefore  $3.8 \mu\text{m}$ . The cameras were equipped with industrial grade Zeiss Interlock Compact objectives. Different focal lengths were used in the industrial environment to compensate for the different camera distances from the object (due to the plant layout). No special experimental stand was needed; the cameras were directly mounted on supporting constructions of the forge, or, in the laboratory, they were placed on tripods. In the laboratory, the objectives were equipped with Haida UV+IR cut filters (390 – 750 nm). In the industrial environment, the cameras were protected by specialized thermos-regulated camera covers (Fig. 5-3). The temperature in the camera covers was controlled using a Ranque-Hilsch vortex tube. Bandpass filters Schneider-Kreuznach BP 680–100 HT were chosen based on empirical findings. The camera layout in both industrial and laboratory environments (initial experiments) is provided in Fig. 5-4 and Tab. 1. The final laboratory experiment simulated the camera layout in the industrial environment; however, the dimensions were scaled (decreased) approximately  $7 \times$ . The measurement volumes were designed for 0.5 and 4 m long objects in the laboratory and industrial environment, respectively.



Fig. 5-3 Thermoregulated camera cover.

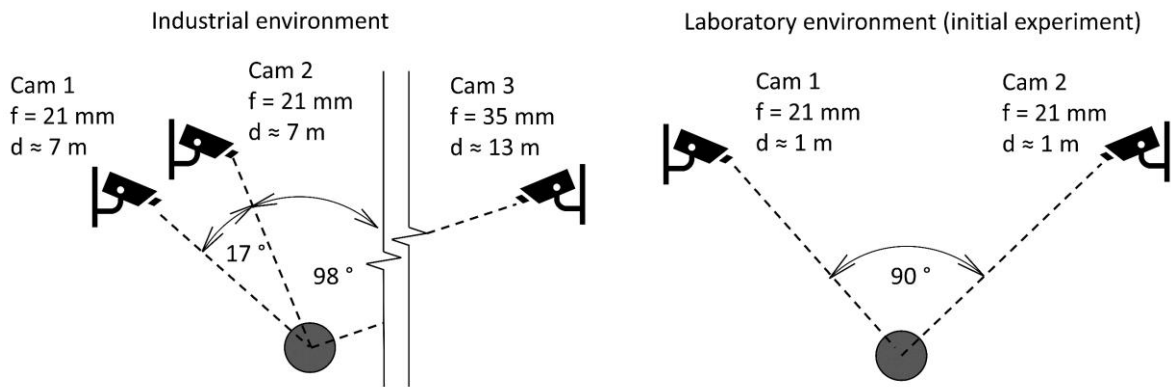


Fig. 5-4 Layout of the camera system in laboratory and industrial conditions.

Tab. 1 Detailed information about the camera system.

<b>Industrial environment</b>		
	<b>Camera 1, 2</b>	<b>Camera 3</b>
Focal length	21 mm	35 mm
Mutual field of view	Approx. $6 \times 6 \times 2$ m	
Pixel equivalent	Approx. 1.29 mm	
<b>Laboratory environment (initial experiment)</b>		
	<b>Camera 1, 2</b>	
Focal length	21 mm	
Field of view	$0.8 \times 0.8 \times 0.3$ m	
Pixel equivalent	0.17 mm	

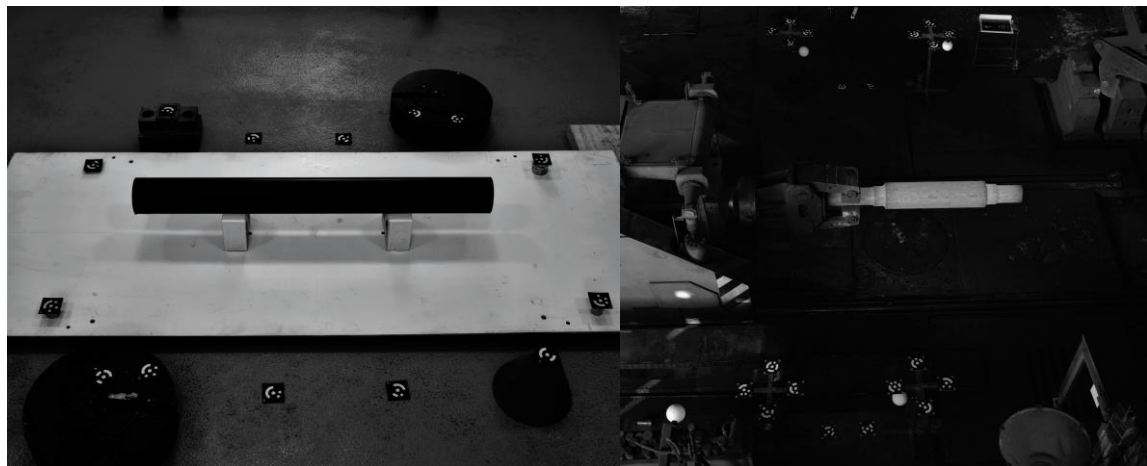


Fig. 5-5 Sample measurement image from the laboratory (left) and industrial environment (right); the images are adjusted and cropped.

The measured objects in the laboratory were steel pipes with 500 mm length, 50 mm diameter, and approx. 1 mm deflection (3 total). Repeated measurements of this object were

carried out, with arbitrary object rotation around its axis. In case of measurement in an industrial environment, the measured objects were cylindrical forgings with fittings, a length of approx. 1.9 m, a maximum diameter of approx. 300 mm, and a surface temperature around 1000 ° C.

## 5.4 Reference geometry and comparative measurement

To estimate the accuracy of the measurement system, the reference geometry of the samples in the laboratory was obtained using a professional 3D scanner ATOS III TripleScan 8M (GOM). The scanner was used in the MV560 configuration. The scanner works on the principle of fringe projection. According to VDI/VDE 2634 the measurement accuracy is in the order of thousandths of millimeters. However, in the industrial environment, a reference cannot be obtained. Therefore, to demonstrate the feasibility of the proposed methods, a comparison with independent, comparative method was used. Based on the literature, laser scanning was chosen. FARO Focus 3D S 120 professional laser scanners were used. The object was measured from both sides simultaneously. The scans were registered based on sphere targets placed in the scene. The result of both measurement methods is 3D point clouds, which were processed and evaluated using GOM Inspect software.

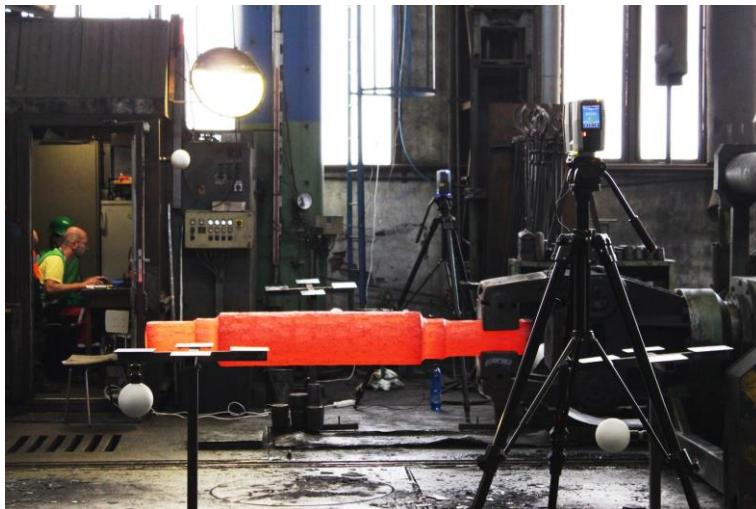


Fig. 5-6 Comparative forging measurement using laser scanners.

## 5.5 Target system benchmark

To verify the properties of the target system, a benchmark was introduced. Basic input target images were modified by image processing methods to simulate code damage and selected negative image effects, including image scale, observation angle, image noise, or image blur:

- Code damage: image scale 0.9, 0 – 7.5 bits occluded with a patch of random intensity.
- Image scale: 0.05 – 1.
- Image blur: image scale 0.9, convolution with Gaussian kernel with  $\sigma = 0 – 8$ .
- Image noise: image scale 0.9, additive noise with  $\sigma = 0 – 0.4$ .
- Observation angle: image scale 0.9, simulated angle extent 2 – 90°.

The sample cuts from the datasets are provided in Fig. 5-7. The mentioned intervals contained 100 samples. The effectiveness of the proposed methods was evaluated based on precision  $p$ , recall  $r$ , and their harmonic mean  $F$ :

$$F = 2 \frac{p \cdot r}{p + r}; p = \frac{tp}{tp + fp}; r = \frac{tp}{tp + fn} \quad (5.1)$$

Where  $tp$ ,  $fp$  and  $fn$  stand for number of true positive, false positive and false negative cases, respectively [32].

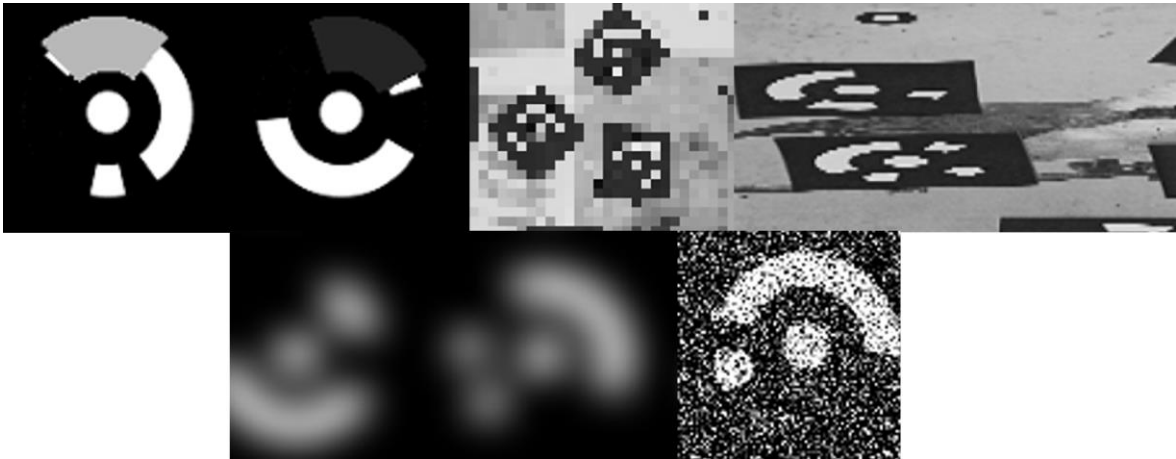


Fig. 5-7 Examples of corrupted targets from the datasets.

## 6 RESULTS AND DISCUSSION

The section Results and Discussion is arranged according to the workflow of the measurement system methods. This section mainly introduces, summarizes, and links the findings of the attached Papers A, B, C, and D. The content of the papers is as follows:

- Paper A: Enhancing the robustness of the circular coded target system for camera calibration; research on the error correction of the cyclic codes; solution of Objective 1, scientific Question 1, and Hypothesis 1.
- Paper B: Development of the camera calibration method of the forging measurement system cameras; its verification in the industrial environment; solution of Objective 2.
- Paper C: Research on the accurate forging edge detection method; Solution of Objective 3, scientific Question 2, and Hypothesis 2.
- Paper D: Development of the forging measurement system; demonstration of its feasibility in the industrial environment; solution of Objective 4.

**Paper A** dealt with the robustness of the circular coded target system. A circular coded target system for industrial applications was developed (further called ICCT, industrial circular coded target system). By using the code library generator, a library of 60 fifteen-bit target codes was generated. The minimum distance between the codes in the library was 3. Therefore, the error correction can theoretically withstand up to 1 bit completely changed or 2 bits occluded or damaged. In addition, other methods were proposed to make the system more robust to common image effects. The proposed methods were verified based on a target system benchmark and compared with the circular coded target system proposed in [27] (further SA, state-of-the-art), TRITOP (GOM) target system and ArUco [32] target system.

The experimental verification of the robustness of the target system to code occlusion up to the area equivalent of 2 bit segments was performed. The results showed excellent ICCT performance (recall over 0.9) up to an occluded area of approx. 1.5 bits equivalent, where the probability of recognition rapidly decreased. On the other hand, the precision in the whole interval was exactly 1. The results are in accordance with the assumptions because the target damage behaves likely like occlusion (unknown value); thanks to the similarity condition; the probability of code confusion is low. The advantage of this error correction method was demonstrated against the compared target systems, which ICCT overperformed. The recall of the other compared target systems began to rapidly decrease immediately. The exception was the ArUco target system, which recall decreased approximately linearly. This effect occurred despite the fact that this system used error correction. However, this was apparently the effect of using the same code occlusion path for circular coded and ArUco target systems. Moreover, the occlusion of the target code was studied up to the occlusion area of 7.5 bit segments, to study the precision of the target system. ICCT and the target

system presented in [27] showed a similar precision of approx. 0.97, while the TRITOP and ArUco did not show any target confusion at all. Although the values were close, the confusions can be problematic in some applications. However, in case of ICCT, this was compensated by a significantly higher recall compared with the other circular coded target systems. The comparison with ArUco, which achieved absolute precision despite its error correction feature, was again problematic, due to the use of the same patch for both target systems, which used a different design.

The response of ICCT on the image scale and observation angle showed that the proposed target system was capable of identifying targets with a center diameter as low as 3 px and observation angles as low as 7°. The results were comparable to those of the ArUco system in both cases. From the other circular coded target systems examined, TRITOP achieved better results and managed to recognize comparable small targets, but its observation angle limit was 27°. The proposed excellent target performance was achieved thanks to target segmentation based on Canny edge operator with upscale, to provide more smooth results, and robust sorting method based on ellipse fitting. Regarding image blur, the best results were achieved by TRITOP. ICCT and SA are both based on a Canny edge detector, which performs poorly under a high level of blur. A heavy drop in target recall was recorded around  $\sigma = 4$ . The worst result in this data set was achieved by ArUco (a heavy drop around  $\sigma = 2.5$ ). On the other hand, TRITOP target system proved to be sensitive to image noise. ICCT and SA were less sensitive and ArUco achieved the best results. However, this problem was caused by the segmentation method, based on the Canny edge operator. By increasing  $\sigma$  input of the Canny operator, the target segmentation became significantly more robust, overperforming ArUco target system.

Overall, the proposed target system was evaluated as effective, overperforming the compared target systems in occlusion up to area of 2 bits, offering great performance both on scale and observation angle datasets (comparable to ArUco and overall overperforming both SA and TRITOP) and offering great robustness to both image blur and noise (overperforming AruCo and performing comparably with SA; TRITOP system proved great results on Blur dataset, however, performed poorly under image noise). The proposed ICCT target system was also verified by application in the heavy industry environment to calibrate cameras of a forging measurement system. Future studies could include improving the target library generator, by implementing an optimization method to find an optimum set of calibration target codes (similarly to [33]), and further minor improvements in the recognition algorithm.

In **Paper B**, the calibration method for the cameras of the forging measurement system was proposed. This method was based on space resection and used a circular coded target system, presented in Paper A. The method worked in two steps, allowing the on-line camera exterior parameters calibration to compensate for small camera movements. The calibration accuracy was verified under both laboratory (meas. volume approx.  $1.5 \times 1.5 \times 0.5$  m) and industrial

conditions (meas. volume approx.  $6 \times 6 \times 1.5$  m). In both cases, the reprojection error was below 0.1 px, which was close to the value observed in [10]. The assumed error of camera calibration on silhouettes reconstruction in laboratory and industrial environment was 0.03 and 0.24 mm, respectively. This result was evaluated as satisfactory. The effect of hot atmosphere and air lens surrounding the forging was also examined. Based on the results, the reprojection error increased up to  $2.5 \times$  both in the laboratory and industrial environment. The increase in the reprojection error was approximately in agreement with the results presented in [19] (in both cases in thousandths of percent, although different air lens shapes were present). Therefore, this effect was considered as clarified and was not further studied. An alternative way of camera calibration was proposed – the cameras could be calibrated shortly before the forging is placed in the scene, to prevent the influence of air lens and heat haze. Future studies could focus on the implementation of the camera calibration method based on epipolar geometry.

The focus of **Paper C** was the development of an edge detection method for the measurement of forgings, based on their silhouettes. The main idea was to use the subpixel edge detection method and subsequent filtering based on complementary information about the edge quality measures from the image. To verify the effectiveness of the proposed methods, the developed method was compared with the method presented in [2], which used edge detection with pixel precision and uniform weight filtering. The experiment was carried out in both the laboratory and the industrial environment (two-camera system).

The first finding was the confirmation of the advantage of subpixel edge detection in both the laboratory and industrial environment. The median error decreased in both cases by approx. 50% and 30% in the case of axis straightness measurement and object diameter measurement, respectively, compared to edge detection with pixel precision. A higher improvement could be expected (the accuracy of the subpixel edge detection method utilized is up to  $1/100$  px). However, this subpixel accuracy can be achieved in an ideal image. The lower increase of accuracy can be explained as the effect of non-ideal edge contrast and object circularity in the laboratory environment, edge disturbances and heat haze in the industrial environment, and camera calibration error or minor simplification in the case of 3D geometry reconstruction method in both cases.

Regarding the filtering method, it was found that edge and axis filtering in the laboratory environment does not offer any improvements due to uniform edge contrast and no significant local edge disturbances. However, in an industrial environment, where strong local edge disturbances appeared, filtering helped reduce the axis measurement sigma error by 53% and the maximum error by 77%. The improvement was significantly lower for the diameter measurement (sigma by 7% and maximum error by 15%), due to the rapidly changing diameter along the forging axis. The advantage of the weighted filtering, based on the complementary information of the image, was then studied. It was found that in case of axis straightness, both edge gradient direction and magnitude can be used as weights,

significantly overperforming the filtering with uniform weight. The best results were achieved by using edge weights based on the direction of the edge gradient. Compared to uniform weight filtering, the sigma error decreased by 34% and the maximum error by 64%. On the other hand, for the object diameter filtering, the weight based on edge gradient magnitude turned out to be the most advantageous, overperforming the uniform weight filter by 11% in the case of both axis straightness and maximum error. The lower improvement was also explained as an effect of the rapidly changing diameter along the forging axis.

Overall, the proposed methods achieved by a 50% lower sigma and by a 63% lower maximum error compared to the state-of-the-art method [2], in the case of axis measurement in industrial environment. However, the methods performed comparably in the case of forging diameter measurement. This was explained again as the effect of rapidly changing forging diameter along its axis and the effect of a stronger diameter filter used in the case of the state-of-the-art method (moving average against weighted parabola fitting, although with windows of the same size). Finally, the precision achieved by the proposed methods in the industrial environment was  $\pm 0.5$  and  $\pm 1$  mm for the measurement of the forging axis and diameter, respectively. Based on the pixel equivalent of these values, comparable values as in case of forging measurement in laboratory were achieved thanks to the proposed methods, suppressing the interfering effects of the industrial environment (despite the higher error of forging diameter measurement).

The above-mentioned results do not include the effect of potential poor forging circularity. By studying the repeatability of the measurement with rotation around the forging axis, an approx. three-times greater measurement error was recorded. In the case of forging axis measurement, the same trend of measurement error was recorded across the compared methods. Weighted filtering with weights based on edge gradient orientation performed the best, helping to suppress less representative edge segments. In the case of the measurement of the diameter of the forging, all compared methods performed similarly, showing that the advantages of more accurate methods are dominated by the effect of circularity of the forging. Therefore, future studies included the method of assembling more observations, from different viewpoints, in one measurement, achieving a better determination of the forging cross section.

The **Paper D** dealt with the further development and feasibility demonstration of the system for forging measurement. From the method point of view, the main novelty was the introduction of three-camera and multi-view observation measurement in this application, in order to solve the above-mentioned problem of a poorly determined forging cross section. In addition, the ability of the system to measure the circularity, based on forging silhouettes, was studied. Moreover, the obtained results of the proposed measurement method were verified by comparison with those of the independent measurement system (based on laser scanning). Such experiments have not yet been carried out and demonstrate the feasibility of the proposed measurement system.

The study of repeated measurements showed a high level of outliers in the case of forging diameter and circularity measurement. These outliers are the result of a rapidly changing forging diameter along its axis and an inaccurately defined forging origin. Therefore, 10% of the outliers were removed in the case of measuring the diameter and circularity of the forging in the further analyzes. The third (added) camera decreased the measurement error by 13 – 15%. Moreover, by using the multi-view method, a decrease of the measurement error with square root of the observation number was recorded, which is in correspondence with the global assumption. However, the best results were achieved when the observations were evenly distributed around the forging axis. For the rotation of the forging around its axis by  $30^\circ$  between observations, six observations were the most effective in determining the forging geometry. This was assumed based on significant drop in the measured repeatability error. This means that forging cross section deviations were not strictly random in dependence to their polar coordinates. The cross section rather showed limited complexity, and neighboring observations can therefore show systematic similarities. However, six observation measurement offered 64 – 71% lower measurement error compared to a single observation. Overall, the precision of a six-observation measurement was  $\pm 0.5$  mm for the both forging axis straightness and diameter measurements (95% confidence interval). A different situation was recorded in the case of circularity measurement, where the result is calculated based on extremal values. Therefore, in case of low number of observations, a systematic error was observed. The systematic error was significant for up to 10 observations. However, in the case of 11 observations, the recorded error was  $\pm 0.6$  mm (95% confidence interval including systematic error).

To demonstrate the feasibility of the proposed measurement system, it was compared with the laser scanning measuring technique. The results of axis measurement showed great agreement (95% confidence intervals overlap in 98.47% cases, with a mean difference of 0.04 mm). Approx. 50% of overlap was recorded in the case of the forging diameter and circularity measurement. The mean differences were 0.5 and 0.9 mm, respectively. However, this was explained partially as the effect of the outliers and partially as the possible influence of the air lens, which affects the camera system (operating around 680 nm wavelength) more than laser scanning device (operating at 905 nm). However, these numbers were within the point cloud registration error (the mean differences were on the same order). Moreover, the proposed and comparative laser scanning systems were compared from a measurement error point of view. The proposed system surpassed the laser scanning technique in four, six, and eleven observations in the case of forging axis, diameter, and circularity measurement, respectively. From the measurement time point of view, every observation lasted around 10 s. On the other hand, the laser scan was captured in five minutes; therefore, even in case of full 12 observations, the proposed camera system achieved shorter measurement time. However, both measurement techniques could be optimized to achieve significantly lower measurement times, negligible compared to the time of forging operation.

The overall influence of the interference effects was examined. Because previous experiments did not show significant systematic errors, the effect was studied by comparing the repeatability of the measurement under industrial and laboratory conditions (considered as ideal conditions). Comparing the recorded pixel equivalent of repeatability error, the overall influence of interfering effects present in the industrial environment has a significant, but not critical, effect on the random measurement error. The error increased approx.  $5-6 \times$ ,  $3 \times$  and  $3 \times$  in the case of the measurement of axis, diameter, and circularity, respectively (considering the case without outliers of 10%). Despite the increase, the single-observation error pixel equivalent remained under 1 px in the case of axis and diameter measurement. The circularity measurement error was higher; however, it was shown that more observations were needed to measure it accurately. It is also obvious that there are fewer outliers in the results obtained under laboratory conditions. This is supported by the finding that by removing the 10% outliers, the diameter and circularity measurement error did not decrease significantly in the case of laboratory measurements (0.042 vs. 0.033 mm in the case of sigma diameter error), compared to the industrial measurements (2.070 vs. 0.833 mm in the case of the same error).

The significant relative influence was recorded as a result of the high subpixel sensitivity of the measurement system. The possible cause, instead of the influence of interference effects, was a more complex geometry of the forging surface, which contains many plastic forging press marks on its surface and also the shape of the forging itself. In addition, the circularity of the samples was not proportional.

Further studies in this case include the implementation of an accurate subpixel method of forging origin determination, which could eliminate the outliers in the case of forging diameter and circularity measurement. Another challenge is the measurement of different forging cross sections, e.g., square or rectangle, which are defined by more parameters. Another possibility is the combination of the proposed principle with different measurement principles for the determination of forging circularity, for example, laser scanning, similarly as in [40].



# Circular coded target system for industrial applications

Jakub Hurník<sup>1</sup> · Aneta Zatočilová<sup>1</sup> · David Paloušek<sup>1</sup> Received: 22 June 2020 / Revised: 9 October 2020 / Accepted: 1 December 2020 / Published online: 15 January 2021  
© The Author(s), under exclusive licence to Springer-Verlag GmbH, DE part of Springer Nature 2021

## Abstract

Coded targets are used as reference targets with a known location during camera calibration, for robust searching of corresponding features between images during various applications of machine vision like object tracking, robot navigation or 3D measurement. In this paper, a target system for industrial photogrammetric applications is outlined. The methods which have been chosen emphasize maximum robustness, along with accuracy at the expense of computational efficiency, since photogrammetric measurements are mainly evaluated offline. The outlined system combines widely used photogrammetric circular coded target design with an automatic library generator. It also utilizes robust methods of target detection and recognition with error correction (in case of 60 15-bit targets, up to 1 bit confused or 2 bits occluded) along with preserving the low false-positive or confusion rate. Any error correction method for this type of targets was not introduced before. The solution also allows for the creation of versatile target libraries or to work with the existing target libraries of a number of commercial photogrammetric systems. The properties of the target system were tested under challenging conditions (including heavy noise, blur, occlusion and geometrical image transformations) and compared to state-of-the-art systems, e.g. TRI-TOP (GOM), or ArUco, which it outperforms. The target system is already used for the camera calibration of a specialized photogrammetric system utilized in the heavy industry environment.

**Keywords** Circular coded target · CCT · Coded target · Fiducial marker · Camera calibration · Photogrammetry

## 1 Introduction

Close range photogrammetry is the science of dealing with measurement based on images. It has a wide range of applications, such as quality control and 3D object reconstruction, or object tracking. Today's technology allows us to perform the measurements automatically, quickly and accurately. Some of the main tasks of photogrammetric measurements are: determining the precise location and identification of features, as well as finding the corresponding features in the image. These features can be used for camera calibration, for the measurement itself, or both.

The camera calibration can be understood to be the estimation of the parameters of the projection from 3D coordinates in space, to 2D coordinates on the chip of the camera (or any photographic material). Camera parameters include

both intrinsic (focal length, physical centre of image, distortion) and extrinsic (camera location and orientation) parameters. There are many camera calibration or measurement methods which are suitable for different applications. Some of them utilize only natural features or textures in the image [1]. While these methods have the advantage that any modification of the environment is usually not required, methods which use calibration targets are still often used for camera calibration [2–5], or for industrial or scientific measurements [6–9]. The main decisive factors for the usage of these methods are lower computational times, better reliability (mainly in environments with less texture) and better accuracy. The artificial targets can be coded or non-coded. Coded targets are used as reference targets with a known location, or for robust searching of corresponding features between images (tie points), or object tracking.

The design of these coded targets should allow us to create a large number of unique targets whilst using minimal pattern size. The targets should be reliably identified with invariance to position, rotation, size or projective distortion. There are two main types of codes. The first are barcode-style codes (Fig. 1, upper row), which use a binary code

✉ Jakub Hurník  
Jakub.Hurnik@vut.cz

<sup>1</sup> Institute of Machine and Industrial Design, Faculty of Mechanical Engineering, Brno University of Technology, Technická 2896/2, 616 69 Brno, Czech Republic

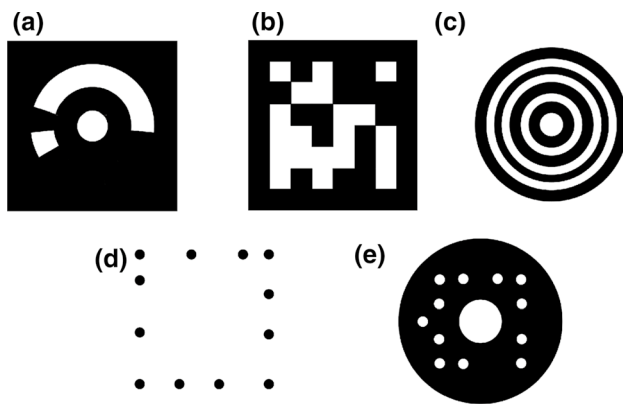


**Fig. 1** Different types of coded targets—**a** TRITOP; **b** Garrido-Jurado, 2014; **c** Calvet, 2016; **d** Bergamasco, 2013; **e** Ahn, 2001

near or around the centre of the target. The second type is the code based on the unique distribution of elements in the code area (Fig. 1, lower row, e.g. [10–12]). The barcode-style targets are mainly circular [4, 13–19] or square [20–24]—these shapes are easily detected in the image. Square targets are often used for augmented-reality applications—single detected targets provide 4 correspondence points. On the other hand, the most common target design for photogrammetric systems is circular coded. The simple circular target design with a barcode-style code (Fig. 1a, also called circular coded target, CCT) is very often used by professional photogrammetric systems including TRITOP (GOM), or scanreference (AICON). This design allows us to create large target libraries, along with fast, reliable and accurate target detection under normal conditions.

### 1.1 Related previous work

The algorithm related to the recognition of circular coded targets (Fig. 1a) is described in [4, 14–17, 19]. The authors use a similar method of the identification of coded targets with various modifications. 9–16-bit codes were used. Firstly, the binarization of the image (using thresholding or an edge operator, e.g. [25]) is carried out. The ellipses (the centres of potential targets) are detected according to certain criteria, e.g. their dimensions, contrast, the best fit of ellipse or location. The ID code is scanned (the geometry of the target is already known, so it is possible to locate and read the code). The scanned cyclic code is arbitrarily rotated—to find the starting angle, bit transition (edge) is found [14], or the code is rotated, so the sum of the variances in all bit segments is minimized [4]. The cyclic binary code is determined according to the intensity of the bit segments using thresholding (Otsu’s method [26] is used, or the threshold is set as the mean value of the mean black and the mean white values [4]), or the

code is determined according to the gradients between bit segments [19]. The cyclic code has  $n$  different forms. ( $n$  is the number of bits of the code, e.g. 4-bit cyclic code 1100 has 4 different forms—1100, 0110, 0011, 1001.) All authors consider the lowest value, after the transformation of all possible cyclic codes from binary to decimal, to be the target’s identification number. No error correction is implemented. Finally, the accuracy of the target centre coordinates is improved using a more accurate method of centre location, e.g. weighted centroid.

A different method of the recognition of circular coded targets was proposed in [18]. There are two main differences—the centre segmentation was based on radial symmetry measure, which used several oriented log Gabor filters in frequency domain. The second difference was the target recognition method, which was based on the comparison of the target code to codes in a lookup table (target library). If one of the rotations of the targets’ cyclic code exactly matched the target code in the target library, the identification number was assigned to the target.

This work was also inspired by the idea of Garrido-Jurado et al. [22]. In their work, a target system ArUco which solves the problem regarding predefined target libraries of calibration targets was developed. The predefined library could be too small or too large for some applications. If the library is too large, it could be useful to select the targets with the best properties. A simple, square barcode-type target design (Fig. 1b) was utilized. A library generator, which chooses the best set of targets with maximum inter-code distance between them (to lower the confusion rate between the targets), and the maximum number of bit transitions (to lower the confusion rate with random objects in the environment), was developed. The identification of targets in the image includes target segmentation, perspective projection removal, processing the code with Otsu’s method and code identification using the rotation-invariant distance between the scanned codes and the codes in the library (the lowest distance between the codes in the library and rotations of the square code). The target system also implements error correction, which utilizes the increased inter-code distance. If the code of the target contains errors, the closest code’s ID is assigned to the target, if the distance between the codes is lower than or equal to  $(\tau - 1)/2$ , where  $\tau$  is the minimum inter-code distance of the codes in the library. Further, the authors made improvements to the library generator; mixed integer linear programming was used to achieve optimum or sub-optimum inter-code distance of markers in the generated library [23]. The recognition algorithm was also later improved—the original bit extraction algorithm was surpassed by state-of-the-art machine learning techniques from the robustness point of view [24], at the expense of training the neural networks on large datasets (12,500 synthetic images of calibration targets, 210,000 images for negative

class). For this experiment, a library of 50 6×6 bit targets were used.

### 1.2 Problem formulation

This work is focused on the development of robust circular coded target system (target design Fig. 1a). Although this target design is often used, only basic approaches to target decoding, without error correction, are presented in the literature. The problem of circular coded target libraries generation is not examined at all. In general, the target recognition methods are not adapted to allow for high robustness. In demanding conditions, the recognition could fail.

### 1.3 Contribution

The developed target system is called ICCT (Industrial Circular Coded Target system). The inspiration is the square target system ArUco used for virtual reality applications, which use error correction to significantly improve the robustness. In this work, this approach is originally used for the system of circular coded targets. To reach maximum versatility, ICCT utilizes the common circular coded target design. With several limits, it could be used with the same targets which, for example, are used by TRITOP. On the other hand, this target system is adapted for maximum robustness and accuracy—it overcomes the disadvantages of currently available circular coded target systems. This improvement is made at the expense of computational time, which is less important, because photogrammetric measurements are evaluated mainly offline.

The main presented contribution of this work is the new approach to circular coded target library generation and their recognition in the image (highlighted part in Fig. 2). The main improvements include an error correction method (which was not introduced before for this type of targets) and automatic target library generator. The other minor improvements include an optimized, robust method of target segmentation and code scanning.

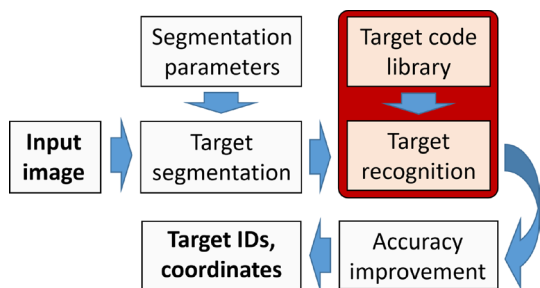


Fig. 2 General target system algorithm; the main contribution of this work is in highlighted part

The other contribution is the comparison of the proposed target system with state-of-the-art method proposed by [14], commercial solution—the TRITOP system (GOM) and the ArUco square target system [22].

The outlined target system is already being used for the camera calibration of a measurement system which is used for the quality control of heavy forgings [27–30].

## 2 Methods

- Target system design The proposed target system utilizes widely used target design, to maximize the versatility. The target design was introduced before and is displayed in Fig. 3. The main novelty is the error correction method. Error correction is enabled due to automatic target library generator, which optimizes important properties of the target codes. The target decoding with error correction is carried out based on rotation-independent distance between the cyclic code of the scanned target and the cyclic codes in the target library. In addition, we present a novel similarity condition, which is implemented to improve the performance of the recognition under occlusion. The whole recognition algorithm is based on conventional (not machine learning) methods. The key disadvantage of machine learning methods is the complicated training on large datasets. Although there is a possibility to reach more robust recognition, these methods were chosen to ensure the flexibility of target libraries (the user can make target libraries of the desired number of targets, or work with the target libraries of professional measuring systems, which use similar target designs).
- Target library generator The target library is the list of the cyclic codes of the targets. The idea of the target library generator is to adjust the library for concrete application. This includes the optimization of the rotation-independent inter-code distance in the target library to minimize the confusion rate between the targets. Second criterion is to maximize the number of bit transitions in the codes, to lower the probability of confusion of such target with

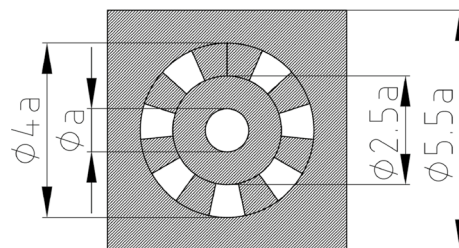


Fig. 3 Geometry of coded target, 15-bit code—0101010101010

random object in the environment. The details of this algorithm are included in Sect. 2.1.

- **Error correction method** The error correction is achieved—the identification number is assigned to the target—if the rotational-invariant distance between the target code and the code in the code library is less than the threshold. This solution allows us to take advantage of maximized inter-code distance in order to recognize codes with errors for a higher true-positive recognition rate. The details of this method are described in Sect. 2.3.8.
- **Similarity condition** Due to the error correction ability of the system, the chance of false positives may be increased. To eliminate this drawback, and to also achieve even better error correction capability of target system under occlusion, the condition of similarity between the target centre and the area of the code ring and the computation method of probabilistic code is newly introduced. The occlusion object or impurities of the code will likely have a different colour (intensity) when compared to the target. The parameters of the normal distribution of the pixel values of black and white segments are used. According to these parameters, the scanned code is quantized to obtain the probability that the certain bit segment is black, white or uncertain. The details of this method are described in Sect. 2.3.6. and 2.3.7.
- **Other minor improvements** The aforementioned approaches are combined with an improved robust target segmentation and code scanning method, which is resistant to common negative image effects (blur, noise) and allows us to identify small or distorted targets.

## 2.1 Library generation

The algorithm which creates the target library works in two phases (Fig. 4). In the first phase, all unique cyclic codes are generated (full library  $L$ , for which the user specifies the number of bits of the codes). In the second phase, a user-defined number of codes with the best properties are sorted out (user-adjusted library  $L_{adj}$ ).

### 2.1.1 Full library generation

The maximum number of unique cyclic codes (number of members in the full library) could be determined by solving the ‘necklace’ problem (Eq. 1) [31, 32].

$$N(n) = 1/n \sum_{i=1}^{\gamma(n)} \phi(d_i) 2^{n/d_i} \tag{1}$$

where  $N$  is the maximum number of unique cyclic codes,  $n$  is the number of bits of the codes,  $\gamma(n)$  is the number of divisors of the number  $n$ ,  $\phi$  is the Euler function, and  $d_i$  are the divisors of the number  $n$ . The solutions are shown in Table 1.

Generation of all unique cyclic codes could be carried out by generating all possible  $n$ -bit binary codes, and sorting all unique cyclic permutations. All possible binary codes could be generated, for example, by first converting the  $n^2$  natural decimal numbers to  $n$ -bit binary codes. From this set, unique cyclic codes could be sorted out according to the minimum rotation-independent distance  $D_L$  between this code and all codes  $m_j$ , which were already placed in the full library  $L$ .

$$D_L(m_i, L) = \min_{m_j \in L} \{D(m_i, m_j)\} \tag{2}$$

**Fig. 4** Flowchart of the code library generator algorithm

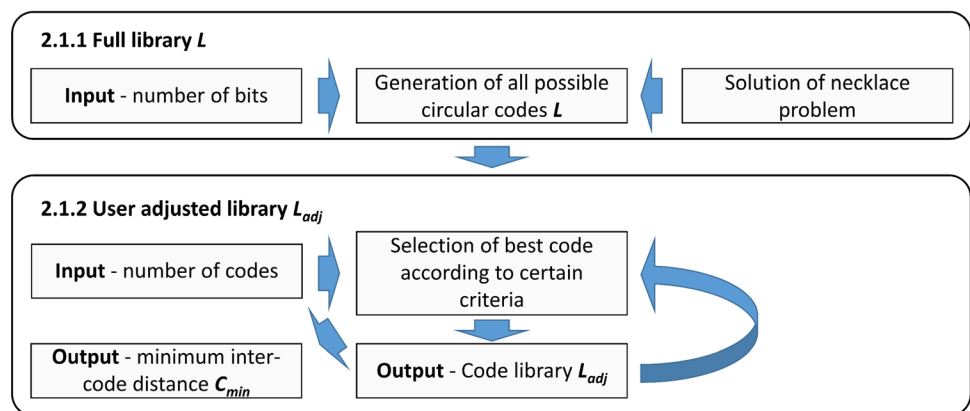


**Table 1** Solution of the necklace problem

$n$	1	2	3	4	5	6	7	8	9	10	11	12	13	14	15	16
$N(n)$	2	3	4	6	8	14	20	36	60	108	188	352	632	1182	2192	4116

The rotation-independent distance  $D$  between the codes  $m_i$  and  $m_j$  is defined as follows:

$$D(m_i, m_j) = \min_{k \in \{0, 1, \dots, n-1\}} \{H(R_k(m_i), m_j)\} \tag{3}$$

where  $R_k$  is the ‘rotation’ function which rotates the code  $k \times 360^\circ/n$  (shifts the last  $k$  elements of the code  $m_i$  at its beginning), and  $H$  is the Hamming distance between the codes.

If the distance  $D_L$  is nonzero (i.e. the cyclic code is unique), the code is put into the library—otherwise, it is rejected. This loop continues until all unique codes are generated—until the size of the library reaches the maximum number of unique cyclic codes  $N(n)$ .

### 2.1.2 User-adjusted library generation

The set of codes  $L_{adj}$  (user-adjusted library) which best fulfil criteria are sorted out from the full library  $L$ :

- Maximum number of bit transitions.
- Maximum distance between all codes in the library.

Sorting is carried out in a loop. At every step, the convenience number  $C$  (fulfilment value of the mentioned criteria) is calculated for every code  $m_j$  in full library  $L$  (the lower of the values is the most relevant in ensuring the fulfilment of both criteria at the same time):

$$C(m_j) = \min\{D_{L_{adj}}(m_j, L_{adj}); T_k(m_j)\} \tag{4}$$

where the first criterion value  $D_{L_{adj}}$  is the minimum rotation-independent distance between the code  $m_j$  and every code which has been already put into the library  $L_{adj}$ :

$$D_{L_{adj}}(m_j, L_{adj}) = \min_{m_k \in L_{adj}} \{D(m_j, m_k)\} \tag{5}$$

The second criterion value  $T_k$  is the number of bit transitions  $t$  in the code  $m_j$  divided by 2, to ensure enough bit transitions are in selected codes:

$$T_k(m_j) = t(m_j)/2 \tag{6}$$

The code  $m_j$  with the highest  $C$  is then put into the library  $L_{adj}$ . This process continues until the resulting library  $L_{adj}$  reaches the user-defined size. The identification numbers are then assigned to the codes according to their order in the library  $L_{adj}$ , which are the main output of the library generator. The second output is the convenience number  $C_{min}$  of the code, which was put into the library  $L_{adj}$  last—this number can be considered the minimum inter-code distance in the library  $L_{adj}$ .

## 2.2 Target library

Depending on the target system application, a reasonably large set of 60 targets was generated. The minimum inter-code distance in the library was examined for 14–16-bit targets. According to Fig. 5, 15-bit target codes were chosen, because for the 60 target set, they had a satisfactory inter-code distance (the same as 16-bits) while using less bits than the 16-bit variant. The minimum inter-code distance  $C_{min}$  of the codes in the generated library is 3 (a minimum of 6-bit transitions).

## 2.3 Target identification in image

The target identification method is summarized in Fig. 6. The detection of target centres is carried out in the image—which is processed by a robust edge operator. Upscaling is presented to raise the resolution of the binary image, in order to make the results of the edge operator smoother and to help find even very small targets. The ellipses are sorted out according to their geometry and local pixel values in the greyscale image. The accurate target centre coordinates in the image are calculated using the star ellipse operator, which is considered to be the most accurate method [6].

The identification code is scanned using a dense net of scanning points, in order to dampen the negative effects of image noise. The code is then divided into bit segments. The similarity condition is applied. The target is then recognized with error correction by using the rotation-invariant distance between the target code and the best-fit code in the current code library  $L_c$ .

### 2.3.1 Upscale and binarization

The greyscale input image is upscaled and pre-processed with the Canny edge operator [25]. This operator provides reliable edge detection even in noisy images or pictures with bad light conditions. The image was upscaled  $2 \times$  using bilinear interpolation. The assumption is that raising the number of edge points and smoothing the result will help to segment

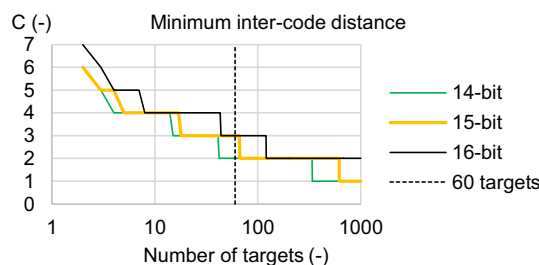


Fig. 5 Achieved minimum inter-code distance for target sets

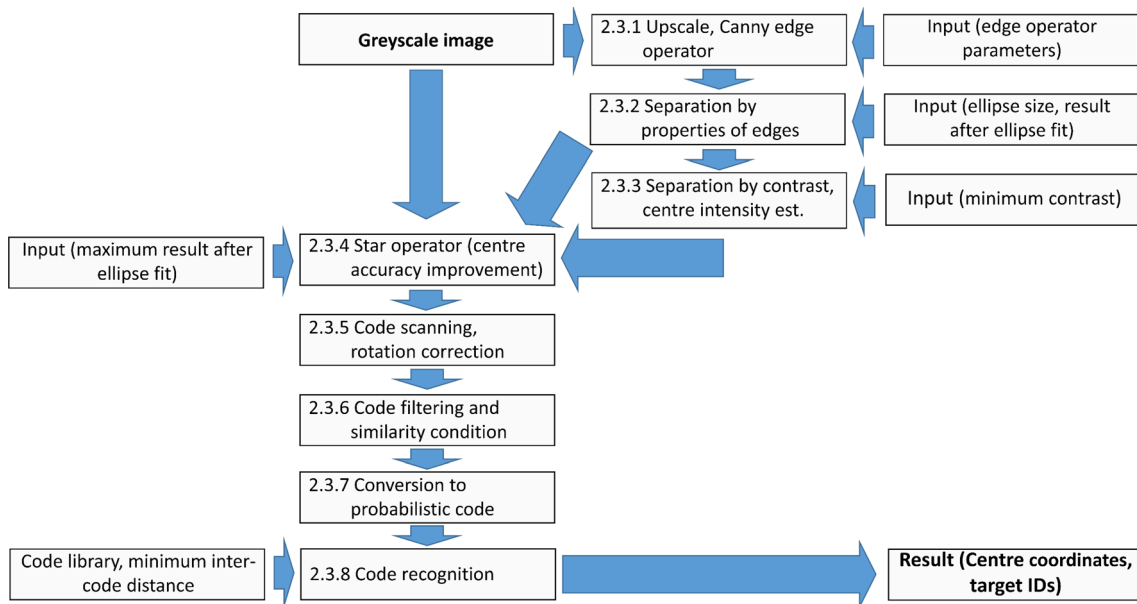


Fig. 6 Algorithm for target segmentation, identification and location

smaller targets. The sensitivity  $Sen$  and the standard deviation of the Gaussian filter of the Canny operator  $\sigma_{Canny}$  could be adjusted.

### 2.3.2 Separation by properties of edges

In the binary image of the size  $x_s \times y_s$ , a set of all connected edges  $E$  with pixel coordinates  $\{[x_i; y_i] \text{ for } i=1,2,\dots,n_s\}$ , where  $n_s$  is the number of edge pixels of the connected edge, are found. Edges of desired locations, dimensions, convexity and ellipticity are separated out according to the following properties:

- Minimum distance from the centre of mass  $[x_T; y_T]$  to the edge from the boundary of the image  $t$ , length interval  $[a_{Tmin}; a_{Tmax}]$  of the semi-major axis of the region  $a_T$ , minimum length  $b_{Tmin}$  of the semi-minor axis  $b_T$  and maximum distortion  $distor_{max}$  (maximum  $a_T/b_T$  ratio).

$$E_1 \subseteq E; E_1 = \{e \in E; 0 + t \leq x_T(e) \leq x_s - t \wedge 0 + t \leq y_T(e) \leq y_s - t \wedge a_{Tmin} \leq a_T(e) \leq a_{Tmax} \wedge b_{Tmin} \leq b_T(e) \wedge a_T(e)/b_T(e) \leq distort_{max}\} \tag{7}$$

Non-convex shapes are rejected using the maximum ratio (convar) between the area of convex envelope of the region  $Sc$  and the filled area of the region  $Sf$ :

$$E_2 \subseteq E_1; E_2 = \{e \in E_1; Sc(e)/Sf(e) \leq convar\} \tag{8}$$

- Non-elliptical objects are rejected using the maximum residual  $\epsilon_{max}$  of the fit of ellipse. The ellipse  $f$  is fitted to the normalized contour pixels with the residual  $\epsilon$ .

$$E_3 \subseteq E_2; E_3 = \{e \in E_2; \epsilon(e) \leq \epsilon_{max}\} \tag{9}$$

### 2.3.3 Separation by contrast

Using this condition, only white objects on a black background with the desired contrast are sorted out. This step is combined with the estimation of black and white centre segment intensity distribution, for further application of similarity condition. To reduce the potential negative effects of image blur on the relevance of value distributions, scanning is carried out through a set of scanning points with varied distances to the contour. (In this work, 6 paths are used, see Fig. 7.) Normal distribution of the values is used—due to its simplicity. The mean value  $m_w$  and the variance  $\sigma_w^2$  for the inner paths and the mean value  $m_b$  and the variance  $\sigma_b^2$  for the outer paths are computed. The contrast condition is expressed as follows:

$$E_4 \subseteq E_3; E_4 = \{e \in E_3; c_{min} \leq m_w/m_b\} \tag{10}$$

### 2.3.4 Centre accuracy improvement

The existing method of star ellipse operator (example in Fig. 8) was chosen because it provides the most accurate results of the methods for computation of circular target

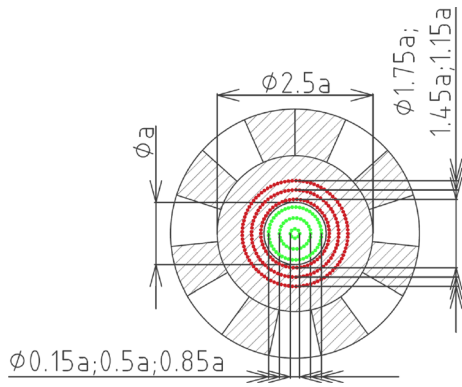


**Fig. 7** Black and white segments intensity distribution estimation

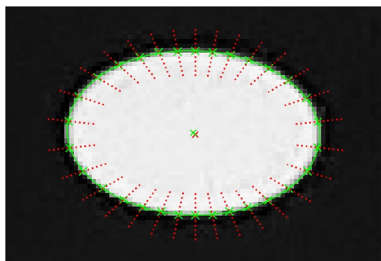


**Fig. 8** Example of star ellipse operator. Red cross—initial point, red points—scanning points, green crosses on the boundary—edge points, green line—fitted ellipse, green cross in the centre—centre of the fitted ellipse (color figure online)

centre coordinates (for the target diameter between 15 and 25 px, the expected accuracy is up to 0.005 px) and is capable of working in a wide range of target centre diameters [6]. 180 radial rays are used. On each ray, 15 points are created around the expected edge, and the pixel values on these points are interpolated using bilinear interpolation. The edge points are computed using the moment preservation method (described in [6]). The ellipse is then fitted to the edge points. According to the residual of fit  $\epsilon_s$ , only contours with accurately fitted ellipses are separated:

$$E_5 \subseteq E_4; E_5 = \{e \in E_4; \epsilon_s(e) \leq \epsilon_{s,max}\} \quad (11)$$

### 2.3.5 Code scanning and rotation correction

The code is scanned in the greyscale image (according to the geometry of the elliptical centre, Fig. 9) with a dense net of scanning points to minimize the influence of image noise—and the scanned code  $SC_a$  is obtained. In this work,  $S_n \times 360$  scanning points are used ( $S_n \times 24$  for each bit segment, due to the usage of 15-bit codes). Pixel values are calculated using bilinear interpolation. The code  $SC_a$ , which is obtained by scanning, is arbitrarily rotated. The aim of this step is to ensure the bit transitions match the segment

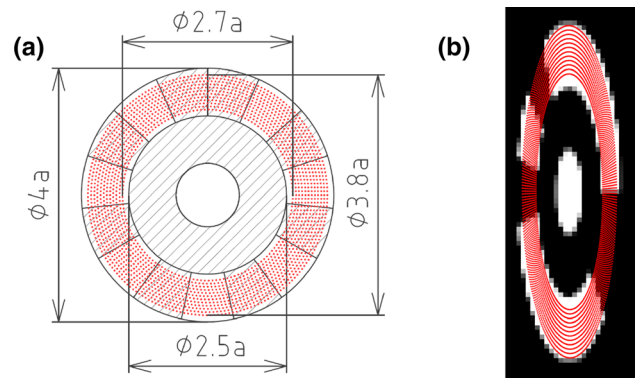


**Fig. 9** Scanning for the identification code (scanning path—red points); **a** dimensions of the scanning area, **b** scanning path in the image (color figure online)

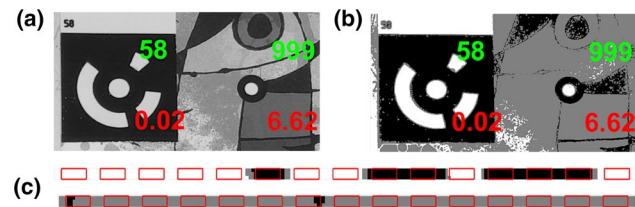


**Fig. 10** Result of quantization of coded and non-coded targets. **a** Greyscale picture, **b** quantized picture, green—target’s identification number (999=unidentified), red—rotational-independent distance from the best-fit code from the code library (explained further), **c**—scanned and quantized codes of the targets with bit segments (red) (color figure online)

boundaries. The cyclic code is rotated, so the minimum sum of mean deviations in all bit segments is obtained. The sum of mean deviations in all bit segments is used because it is less sensitive to the possible damage of bit transition than the mostly used sum of variances. To reduce the influence of irregular bit transition in the image, the irregular area around the bit transition should be neglected. In this work,  $Neg$  columns from each side of the segment are neglected. (Each bit segment is then  $S_n \times 24 - 2 \times Neg$ , see Fig. 10.) The output of this operation is the corrected code  $SC_c$ .

### 2.3.6 Code filtering and similarity condition

The corrected code  $SC_c$  is processed, so the average value of the radial scanning ray is used. The reason for this operation is empirical—for example, local impurities on the target code could appear. This step improves the tolerance during further quantization. When the code is processed using Otsu’s method, instead of the quantization method (explained further), the usage of the average value of the radial scanning ray works as a noise filter. The output of this

operation is the filtered code  $SC_{cf}$ . Every bit segment in this work is then  $1 \times 24 - 2 \times \text{Neg}$ .

Then, the similarity condition is applied. To reduce the chances of a random background—occluding objects or impurities on the target—being confused with a code ring, the code  $SC_{cf}$  is quantized using the parameters of the normal distribution of black and white segments. Values which do not belong to the interval of black or white pixel values are considered as an uncertain value (demonstrated in Figs. 10 and 11). This step should result in both a lower false-positive and a higher true-positive rate in cases of code ring occlusion or damage. The parameters of the normal distribution of black (the mean value  $m_b$  and the variance  $\sigma_b^2$ ) or white (the mean value  $m_w$  and the variance  $\sigma_w^2$ ) segments are already calculated. In this work, Gaussian distribution was used, with the interval of width  $M_\sigma \times \sigma$ :

$$g'_{(g)} = \begin{cases} 1 & \text{if } m_w - M_\sigma \times \sigma_w \leq g \leq m_w + M_\sigma \times \sigma_w \\ 0 & \text{if } m_b - M_\sigma \times \sigma_b \leq g \leq m_b + M_\sigma \times \sigma_b \\ 0.5 & \text{otherwise} \end{cases} \quad (12)$$

where  $g'$  is the quantized pixel value,  $g$  is the original value, 1 is the value of the pixel which is considered to belong to the white bit segment, 0 is the value of the pixel which is considered to belong to the black bit segment, and 0.5 is the uncertain value. To lower the sensitivity of the algorithm when dealing with certain light impurities—which can occur on the code ring—the minimum values of  $\sigma_w, \sigma_b$  should be limited. In this work, the minimum values of these variables were set to 3. In cases of low contrast or a high amount of noise, the intervals of black and white bit segments may overlap. Then, Otsu’s method [26] is used to binarize the code  $SC_{cf}$ . 1 is the value of the pixel which is considered to belong to the white bit segment, and 0 is the value of the pixel which is considered to belong to the black bit segment. In this case, the danger of false positives occurring may be increased. The output of this step is the quantized scanned code  $SC_q$ .

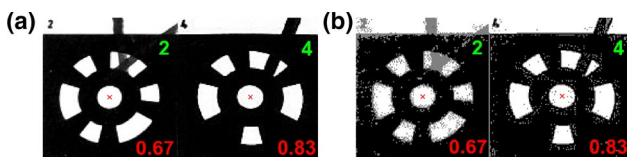


**Fig. 11** Occluded or damaged target code—**a** greyscale and **b** quantized pictures (white=1, black=0, grey=uncertain value), green—target’s identification number (999=unidentified), red—rotational-independent distance from the best-fit code from the code library (explained further)

### 2.3.7 Conversion to the probabilistic code

The quantized scanned code  $SC_q$  is transferred to the probabilistic code. The probability for each bit segment to be 1 or 0 is determined, and the probabilistic code  $PC$  is then assembled:

$$PW_i = n_{wi}/n_a, PB_i = n_{Bi}/n_a, PC = \begin{pmatrix} PW_1 & \dots & PW_n \\ PB_1 & \dots & PB_n \end{pmatrix} \quad (13)$$

where  $PW_i$  is the probability of the  $i$ -th bit segment to be 1 (white),  $PB_i$  is the probability of the  $i$ -th bit segment to be 0 (black),  $n_{wi}$  is the number of white pixels in the  $i$ -th bit segment,  $n_{Bi}$  is the number of black pixels in the  $i$ -th bit segment, and  $n_a$  is the total number of values in the bit segment (in this case  $n_a = 24 - 2 \times \text{Neg}$ ).

### 2.3.8 Code recognition and error correction

The best fitting code from the code library  $L_c$  is fitted to the probabilistic code, and its identification number is assigned to the target—if the rotation-independent distance is sufficiently low. A minimum rotation-independent distance between the probabilistic code  $PC$  and each member of the library  $L_c$  is computed:

$$D_{Lc}(PC, L_c) = \min_{m_l \in L_c} \left\{ D_2 \left[ PC, \begin{pmatrix} m_l \\ m'_l \end{pmatrix} \right] \right\} / 2 \quad (14)$$

The distance  $D_2$  is defined as follows:

$$D_2 \left[ PC, \begin{pmatrix} m_l \\ m'_l \end{pmatrix} \right] = \min_{k \in \{0, 1, \dots, n-1\}} \left\{ \sum_{i=1}^n |PC_{1,i} - R_k(m_l)(i)| + |PC_{2,i} - R_k(m'_l)(i)| \right\} \quad (15)$$

where  $R_k(m_l)(i)$  is  $i$ -th element of  $k$ -th rotation of code  $m_l$  and  $D_{Lc}$  is the rotation-independent distance between the code  $PC$  and the closest match in the library  $L_c$ ,  $m_l$  is a member of  $L_c$ ,  $m'_l$  is its complementary code, and  $R_k$  is the rotation function. If the distance is lower than  $D_{max}$ , the identification code of the closest match in the library is assigned to the target—otherwise, the potential target is rejected:

$$E_6 \subseteq E_5; E_6 = \{e \in E_5; D_{max} \leq D_{Lc}\}; D_{max} = (C_{min} - 1) / 2 \quad (16)$$

$C_{min}$  is the minimum inter-code distance between codes in the current code library  $L_c$ . When using the described 15-bit library,  $C_{min}$  is 3. The assumption here is that the target system can reach an error correction capability of up

to 1 bit fully confused, or up to 2 bits occluded or damaged while preserving the low false-positive or confusion rate.

### 2.4 Target system testing method

For the comparison of target system properties—the datasets were created. Half of the datasets were based on artificial image of the targets, with ideal contrast and no background ('synthetic'), while the second half were based on a real image of calibration targets in a complex scene ('complex'), see Fig. 12. Both images were greyscale, uncompressed and had 8-bit precision. The second half of datasets were made to examine the robustness of the target system in real conditions and to examine the precision of target recognition in a complex environment. The target size in both original images was 110×110 px. The datasets were created by applying common image effects on original images in order to test the robustness of the target systems:

- Image scale (extent of the image scale: 0.05–1).
- Image blur (image scale: 0.9; blur using convolution of the image with Gaussian kernel—sigma of the Gaussian kernel is in extent 0–8).
- Image noise (image scale: 0.9; zero-mean additive noise with Gaussian distribution and sigma in extent 0–0.4; image values are in range: 0–1).
- Observation angle (image scale: 0.9; scale transformation in one direction to simulate the observation angles; observation angles extent: 2–90°).
- Code occlusion (image scale: 0.9; 0–7.5 bits in case of circular coded targets were rewritten with a patch of arbitrary intensity value). In case of ArUco, the same patch was used to cover the target, see Fig. 13.

100 values from the each aforementioned extent were used. Geometrical transformations were carried out using bicubic convolution. The same datasets were made for the TRITOP targets—which have different codes (targets 1–60 were used) and ArUco targets (custom 6×6 bit library of 60 targets was used).

The reference target coordinates were obtained by applying the same geometrical transformations to the target coordinates, measured in original image, as were applied to the

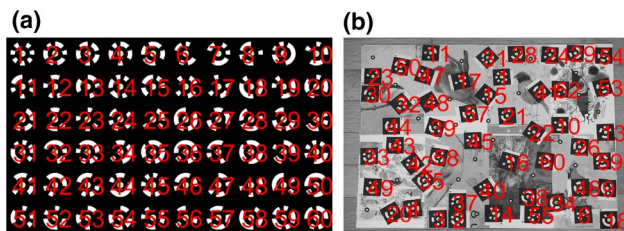


Fig. 12 Original image of synthetic (a) and complex (b) datasets

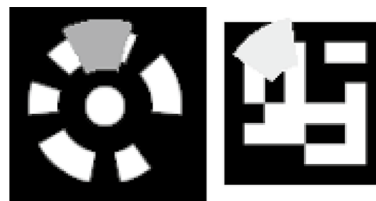


Fig. 13 Sample of targets from the occlusion dataset

image. The target coordinates were measured in the original image using the tested target system target location method itself. The accuracy of the reference coordinates should be sufficient for the quantitative analysis, considering further mentioned target classification tolerance.

The recognized target was classified as true-positive if the distance between the resulting and the reference target coordinates was less than 2 px. The recognized target was classified as false positive if the distance between the resulting and the reference target coordinates was greater than or equal to 2 px. This algorithm limits the potential number of false-positive matches in state-of-the-art systems, which were chosen for the comparison due to their significantly larger target libraries. The studied parameters were the *F*-measure (harmonic mean of *precision* and *recall*), the *precision* and *recall* (inspired by [24]):

$$F = 2 \frac{\text{precision} \cdot \text{recall}}{\text{precision} + \text{recall}} \tag{17}$$

$$\text{precision} = \frac{tp}{tp + fp}; \quad \text{recall} = \frac{tp}{tp + fn}$$

*tp* stands for true positives (correctly identified targets), *fp* for false positives (background features confused with targets), and *fn* for false negatives (non-recognized targets).

### 3 Results and discussion

The properties of the proposed target system (ICCT) were compared with TRITOP (GOM), the target system proposed in [14] (further called 'SA', 'State-of-the-Art') and ArUco system. The SA solution was programmed according to the article and adapted to the same target geometry as was used in this work. (The authors of said work have not specified the target geometry.) TRITOP was set to maximum sensitivity ('find more targets' option). SA system was set according to the recommendation of the article. (Instead of a slightly larger tolerance for ellipse segmentation, moment invariants difference was set to 0.5; correlation coefficient was set to 0.9.) ArUco system was used with default settings. ICCT was set according to the results of empirical testing (Table 2):

### 3.1 Comparison with state of the art

The results of the following comparisons are displayed in Fig. 14 and summarized in Table 3. In general, the target systems behaved similarly on synthetic and complex datasets, with the exception of lower precision (due to the complex environment) and lower recall, due to lower contrast and sharpness of the image.

#### 3.1.1 Effect of target code occlusion

Due to error correction, ICCT holds the best *recall* in the interval 0–2 occluded bits with the preservation of excellent precision, which makes this target system the best performer on this dataset. In this interval, all the competitors hold an excellent *precision*, while in case of other circular coded target systems, the *recall* was significantly lower than that of ICCT. ArUco performed better than TRITOP and SA, but still worse than ICCT.

The test further continued to a bit occlusion of up to 7.5 bits, to examine whether the systems would produce more

false positives. Although ICCT has the error correction feature, its precision was better than ‘SA’ target system. Surprisingly, TRITOP performed the best of the tested circular target systems in terms of *precision*. The perfect precision was achieved also by ArUco, which was capable to reach better recall than the circular coded target systems under heavy occlusion.

The assumption was: ICCT can reach error correction of up to 1 bit fully confused, and up to 2 bits occluded or damaged while preserving the low false-positive rate. Overall, it could be said that the error correction of ICCT is effective and the similarity condition helps to raise both *precision* and *recall*. Under light occlusions, it outperforms other tested target systems, including ArUco, while the precision does not fall significantly under heavy occlusion.

#### 3.1.2 Effect of image scale and low observation angle

Both TRITOP and ICCT were able to identify small targets of size up to  $15 \times 15$  px, and centre diameter in this case is approx. 3 px. For comparison, without the image upscaling

**Table 2** Set-up of ICCT target system

Sen	$\sigma_{\text{Canny}}$	$t$	$a_{T\text{min}}$	$a_{T\text{max}}$	$b_{T\text{min}}$	distor <sub>max</sub>
0.2	0.5	0	1.5	40	1	20
convar	$\epsilon_{\text{max}}$	$c_{\text{min}}$	$\epsilon_{s\text{max}}$	$S_N$	Neg	$M_\sigma$
1.1	3	1.2	2	12	2	3

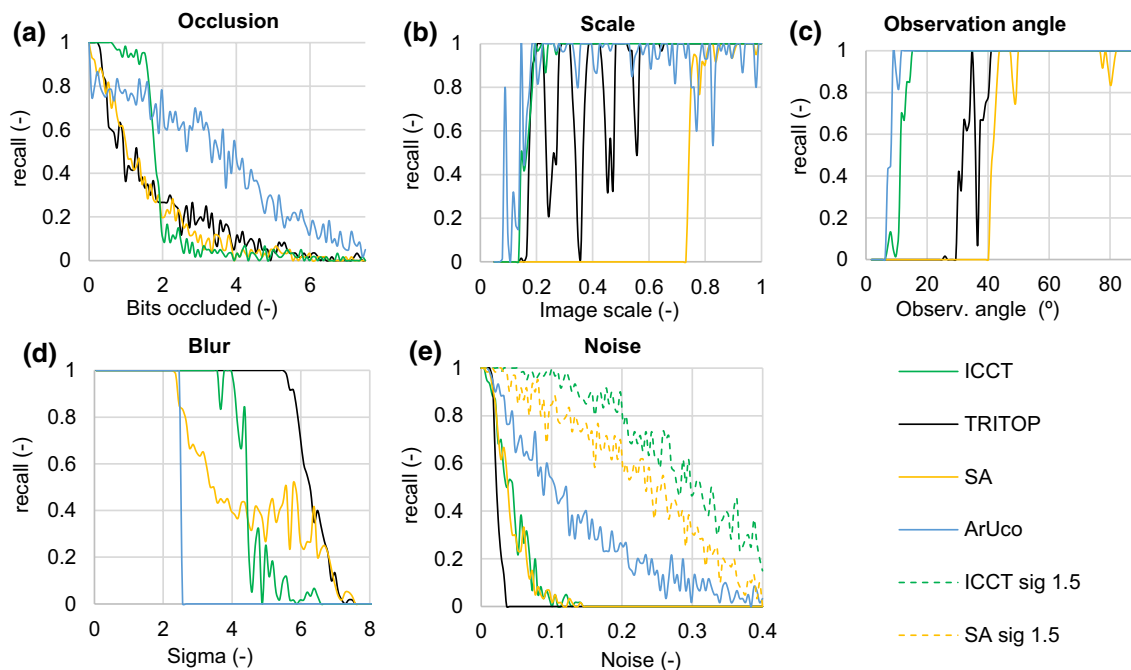


**Fig. 14** Results of target recognition on synthetic datasets—a occlusion, b scale, c obs. angle, d blur, e noise (original set-up with  $\sigma_{\text{Canny}} = 0.5$ ; set-up with  $\sigma_{\text{Canny}} = 1.5$ )

**Table 3** Target recognition results. Occlusion datasets (in brackets—up to 2 bits occluded; with brackets—up to 7.5 bits occluded)

		Synthetic dataset				Complex dataset		
		ICCT	SA	TRITOP	ArUco	ICCT	SA	TRITOP
Occlus.	Prec.	1.000 (0.970)	1.000 (0.967)	1.000 (1.000)	1.000 (1.000)	1.000 (0.991)	1.000 (0.969)	1.000 (1.000)
	Recall	0.870 (0.259)	0.577 (0.199)	0.564 (0.218)	0.767 (0.450)	0.799 (0.227)	0.519 (0.182)	0.540 (0.207)
	<i>F</i>	0.930 (0.409)	0.732 (0.329)	0.721 (0.358)	0.868 (0.621)	0.888 (0.369)	0.684 (0.306)	0.701 (0.343)
Scale	Prec.	1.000	1.000	1.000	1.000	0.999	1.000	1.000
	Recall	0.876	0.264	0.771	0.865	0.849	0.264	0.710
	<i>F</i>	0.934	0.418	0.870	0.928	0.918	0.418	0.830
Angle	Prec.	1.000	1.000	1.000	1.000	0.999	1.000	1.000
	Recall	0.885	0.540	0.633	0.926	0.843	0.517	0.600
	<i>F</i>	0.939	0.701	0.775	0.962	0.915	0.682	0.750
Blur	Prec.	1.000	1.000	1.000	1.000	1.000	0.993	1.000
	Recall	0.450	0.437	0.629	0.250	0.362	0.384	0.613
	<i>F</i>	0.620	0.609	0.772	0.400	0.532	0.553	0.760
Noise	Prec.	0.999 (1.000)	0.998 (0.999)	1.000	0.955 (1.000)	1.000 (0.997)	0.997 (1.000)	1.000
	Recall	0.723 (0.116)	0.576 (0.111)	0.063	0.327 (0.343)	0.429 (0.064)	0.303 (0.037)	0.031
	<i>F</i>	0.839 (0.208)	0.730 (0.200)	0.118	0.487 (0.511)	0.600 (0.120)	0.465 (0.071)	0.060

Noise datasets—ICCT, SA— $\sigma_{\text{Canny}} = 1.5$ ; in brackets— $\sigma_{\text{Canny}} = 0.5$  (universal set-up); ArUco—without brackets—target centre coordinates tolerance 2 px, results with target centre coordinates tolerance 8 px in brackets

during the target segmentation, ICCT would not identify smaller targets than 5.5 px. In terms of recall, ICCT performed better, because TRITOP had some problems with certain target diameters. This problem was noticed on both scale datasets. SA target system had problems with the detection of small targets in general (under  $80 \times 80$  px or 15 px in diameter), due to the target centre segmentation method, which is relatively unreliable even when the tolerance properties of the target centre were raised. According to the *F-measure*, ICCT performed best on both datasets—a slightly lower precision was compensated for with greater *recall*.

ArUco was capable to identify even smaller targets than circular target systems—up to  $10 \times 10$  px. However, ArUco achieved slightly worse or comparable results than ICCT, again because of some problems with certain target sizes.

On ‘Observation angle’ dataset, ICCT proved that a very robust ellipse segmentation and the target recognition method (it manages to recognize a target from observation angles of up to  $7^\circ$ ) achieves excellent *recall*. TRITOP started to recognize targets from  $26^\circ$ , while the SA target system started from  $40^\circ$ . ICCT achieved excellent *recall* at the cost of slightly lower precision, but according to *F-measure*, it performed significantly better than the other circular target systems.

ArUco performed here even slightly better than ICCT. It also manages to recognize a target from observation angles of up to  $7^\circ$ , but the *recall* raises more steeply.

Overall, it can be said that the combination of image upscaling for target segmentation and target segmentation

criteria (especially the ellipse fitting) with the recognition method of ICCT proved to be robust. It reaches the best results among circular target systems and comparable results with ArUco system.

### 3.1.3 Effect of image blur and noise

On the blur datasets, the best *recall* was achieved by the TRITOP target system. Both ICCT and SA target systems segmentation methods are based on the Canny edge detector, which does not achieve good results under heavy blur (Fig. 15). The disadvantage of the SA system is the lower precision, especially achieved under heavy blur. Overall, the TRITOP target system performed the best on these datasets. ICCT and SA performed similarly in terms of recall, but, nevertheless, ICCT achieved better precision. The worst results were achieved by ArUco. Although the *precision* was excellent, the *recall* was significantly lower than in case of circular coded target systems.

### 3.1.4 Effect of image noise

The TRITOP target system proved to be sensitive to image noise—in both cases, it achieved the worst *recall* (but again, the best precision). Using standard settings, both SA and ICCT performed slightly better than TRITOP. Apparently, this disadvantage was caused by the target segmentation method. When  $\sigma_{\text{Canny}}$  was raised to 1.5 (to achieve better resistance of the edge operator to noise), the *recall* was

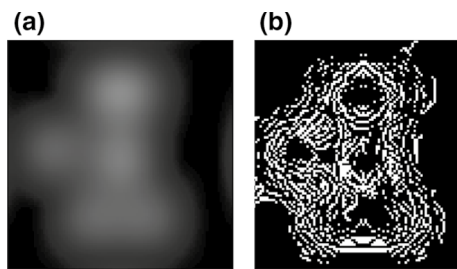


**Fig. 15** **a** Blurred image, **b** blurred image processed by the Canny edge detector ( $\sigma=10$ )

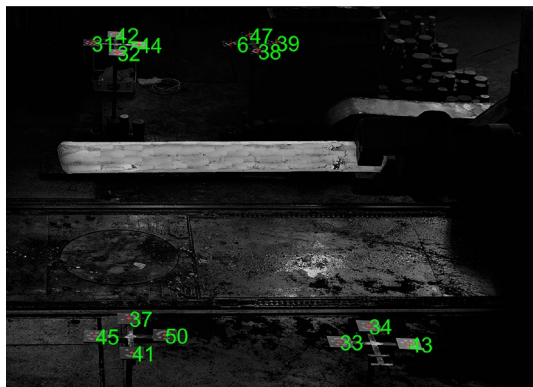


**Fig. 16** Image with calibration targets from optical measurement system for the quality control of heavy forgings

significantly raised in both cases (SA and ICCT). Suitable  $\sigma_{\text{Canny}}$  could be set by the user or it could be estimated automatically, based on image noise estimation methods.

In comparison, ArUco reached better recall than the circular target systems in standard, but significantly worse than in adjusted settings. Interestingly, the target centre coordinates were not accurately estimated in case of large amount noise in the image, due to the vertex jitter. The 2 px centre coordinates tolerance needed to be raised to 8 px, to see relevant quantitative results.

Overall, ICCT—with higher sigma—performed the best on these datasets. The combination of the target segmentation method and the proposed code scanning method proved to be robust.

#### 4 Target system application

ICCT target system is being used for the camera calibration of a multi-camera static measurement system. This system is used for the quality control of heavy forgings [30]. The calibration of this system works in two steps. First step is multi-image calibration of intrinsic camera parameters in laboratory, which is carried out only once before the installation of

the target system in the forge. Second step is a single-image calibration of the extrinsic camera parameters, which is done in the forge directly from the measuring images. Frequent calibration is needed because the dimensional instability of the environment, which could have large negative effect on the measurement accuracy.

However, calibration in the forge is challenging—the problem could be small size of target in the image or low observation angles, blur from thermally affected atmosphere around the forging and higher amount of noise due to bad light conditions. The targets could also get dirty or covered with iron scale, or other partial occlusions can appear, or the targets could be damaged. The targets could be cleaned or replaced, but only after the forging operation end, because it is dangerous to approach the forging area. Without the error correction, there is a lower probability of target recognition, or in case of lower inter-code distance in the target library, the targets could be confused with each other. It is advantageous to have higher inter-code distance and error correction, to maximize the probability of correct target recognition.

ICCT proved effectiveness in this application. It managed to recognize targets even in challenging conditions in the forge (Fig. 16). The accuracy of the target system was proved by low RMS re-projection errors, which was around or lower than 0.1 px, even in the forge.

#### 5 Conclusion

In this paper, a versatile and robust target system of circular coded targets used for demanding industrial photogrammetric tasks was developed. To reach maximum versatility, the system utilizes widely used circular coded target design, combined with an automatic library generator which is capable of creating a library of targets with the desired quantity. Moreover, the system is also capable of working with the target libraries of professional target systems (e.g. TRITOP), and since it is not based on machine learning techniques, it does not need any previous learning calculations. A very robust method of target recognition of the image was implemented, which is resistant to common negative image effects and allows for error correction. The methods were chosen in order to reach maximum robustness and accuracy at the expense of computation time, which is not critical during the usual offline evaluation of photogrammetric measurements.

The system implements multiple innovations. A target library of the desired size is created using a target library generator, which creates a set of targets with the best properties (maximum inter-code distance and maximum number of bit transitions, to ensure a low confusion rate between the targets or random objects of the environment). The targets are recognized based on a rotation-independent distance

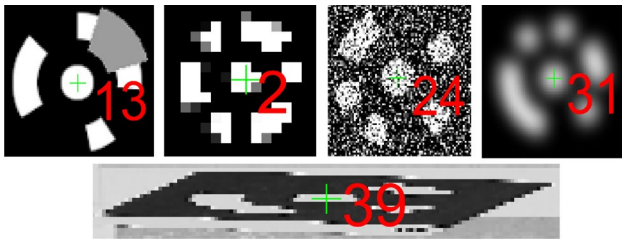


**Fig. 17** Example of target recognition in demanding conditions, using the developed ICCT target system

from the codes in the target code library—along with the large inter-code distance in the target library being utilized to achieve error correction. To detect occlusion, code damage or to refuse random objects in the background, the similarity condition is presented—target ring parts, which have different colours (intensities) than the target centre (black and white), are considered as uncertain values. We also implemented other minor improvements. For the target centre calculation, an accurate star ellipse operator is used. The target segmentation method uses the robust Canny edge operator with upscaling, and a large variety of ellipse parameters to sort out elliptical objects only—which allows us to segment very small or deformed targets (up to 3 px in diameter or up to 7° observation angle). The target code is scanned using a dense net of scanning points, in order to reach the maximum resistance to image noise. The target system allows for a wide range of library sizes and set-ups (recognition sensitivity).

To carry out the target system test, a library of 60 15-bit targets was created. The inter-code distance in this case was 3, so the target library should have the error correction capability of up to 1 bit changed or 2 bits occluded (uncertain value)—which was confirmed during the tests. The system was compared with the state-of-the-art circular target system published by [14], commercial circular target system used by TRITOP (GOM) and widely used square target system ArUco. The comparison was carried out on different datasets (image scale, low observation angles, image noise, image blur and code occlusion). Overall, the proposed methods were evaluated as effective and the ICCT target system outperformed both SA and TRITOP on almost all datasets. Comparison with ArUco showed that ICCT performed comparably on scale or observation angle dataset, but it performed better when image noise, image blur or light occlusions are present. Sample images with recognized targets can be seen in Fig. 17.

The ICCT target system has already been implemented and is being used for the camera calibration of industrial system designed for the measurement of hot forgings. In this demanding application, the target system has proved its robustness and accuracy. The next possible evolutions

include an improvement to the library generator, where the optimization method could be used to choose the best set of targets, similar to [23], or further minor optimizations of the recognition method.

**Acknowledgements** This research has received funding from Technology Agency of Czech Republic, project TREND TA1320S03000 and Faculty of Mechanical Engineering, Brno University of Technology internal specific project FSI-S-20-6296.

**Availability of data and material** Data are available on request from the authors.

## Compliance with ethical standards

**Conflict of interest** The authors declare that they have no conflict of interest.

**Code availability** Code is available on request from the authors.

## References

1. Bay, H., Ess, A., Tuytelaars, T., Van Gool, L.: Speeded-Up robust features (SURF). *Comput. Vis. Image Underst.* **110**, 346–359 (2008). <https://doi.org/10.1016/j.cviu.2007.09.014>
2. Zhang, Z.: A flexible new technique for camera calibration. *IEEE Trans. Pattern Anal. Mach. Intell.* **22**, 1330–1334 (2000). <https://doi.org/10.1109/34.888718>
3. Tsai, R.: A versatile camera calibration technique for high-accuracy 3D machine vision metrology using off-the-shelf TV cameras and lenses. *IEEE J. Robot. Autom.* **3**, 323–344 (1987)
4. Forbes, K., Voigt, A., Bodika, N.: An inexpensive, automatic and accurate camera calibration method. In: Nicolls, F. (ed.) Thirteenth Annual Symposium of the Pattern Recognition Association of South Africa. University of Cape Town, Dept. of Electrical Engineering (2002)
5. Schneider, D., Schwalbe, E., Maas, H.: Validation of geometric models for fisheye lenses. *ISPRS J. Photogramm. Remote Sens.* **64**, 259–266 (2009). <https://doi.org/10.1016/j.isprsjprs.2009.01.001>
6. Luhmann, T., Robson, S., Kyle, S., Harley, I.: *Close Range Photogrammetry*. Whittles Publishing, Scotland (2011)
7. Luhmann, T.: Close range photogrammetry for industrial applications. *Isprs J. Photogramm. Remote Sens.* **65**, 558–569 (2010). <https://doi.org/10.1016/j.isprsjprs.2010.06.003>
8. Zhang, D., Liang, J., Guo, C., Liu, J., Zhang, X., Chen, Z.: Exploitation of photogrammetry measurement system. *Opt. Eng.* **49**, 11 (2010). <https://doi.org/10.1117/1.3364057>
9. Hu, H., Liang, J., Xiao, Z., Tang, Z., Asundi, A., Wang, Y.: A four-camera videogrammetric system for 3-D motion measurement of deformable object. *Opt. Lasers Eng.* **50**, 800–811 (2012). <https://doi.org/10.1016/j.optlaseng.2011.12.011>
10. Bergamasco, F., Albarelli, A., Torsello, A.: Pi-Tag: a fast image-space marker design based on projective invariants. *Mach. Vis. Appl.* **24**, 1295–1310 (2013). <https://doi.org/10.1007/s00138-012-0469-6>
11. Bergamasco, F., Albarelli, A., Cosmo, L., Torsello, A.: An accurate and robust artificial marker based on cyclic codes. *IEEE Trans. Pattern Anal. Mach. Intell.* **38**, 2359–2373 (2016)

12. Ahn, S., Rauh, W.: Circular coded target for automation of optical 3D-measurement and camera calibration. *Int. J. Pattern Recognit. Artif. Intell.* **15**, 905–919 (2001)
13. Calvet, L., Gurdjos, P., Griwodz, C., Gasparini, S.: Detection and accurate localization of circular fiducials under highly challenging conditions. In: 2016 IEEE Conf. Comput. Vis. Pattern Recognit. 562–570 (2016). <https://doi.org/10.1109/CVPR.2016.67>
14. Li, W., Liu, G., Zhu, L., Li, X., Zhang, Y., Shan, S.: Efficient detection and recognition algorithm of reference points in photogrammetry. In: Conference on Optics, Photonics and Digital Technologies for Imaging Applications IV (2016)
15. Guo, C., Cheng, X., Cui, H., Dai, N., Weng, J.: A new technique of recognition for coded targets in optical 3D measurement. In: Optical Metrology and Inspection for Industrial Applications III (2014)
16. Xia, R.B., Zhao, J.B., Liu, W.J., Wu, J.H., Fu, S.P., Jiang, J., Li, J.: A robust recognition algorithm for encoded targets in close-range photogrammetry. *J. Inf. Sci. Eng.* **28**, 407–418 (2012). <https://doi.org/10.1688/JISE.2012.28.2.11>
17. Li, Z., Liu, M.: Research on decoding method of coded targets in close-range photogrammetry. *J. Comput. Inf. Syst.* **6**, 2699–2705 (2010)
18. Dosil, R., Pardo, X., Fdez-Vidal, X.: A new radial symmetry measure applied to photogrammetry A new radial symmetry measure applied to photogrammetry. *Pattern Anal. Appl.* **16**, 637–646 (2012). <https://doi.org/10.1007/s10044-012-0281-y>
19. Chen, R., Zhong, K., Li, Z., Liu, M., Zhan, G.: An accurate and reliable circular coded target detection algorithm for vision measurement. In: Han, S., Yoshizawa, T., Zhang, S. (ed.) *Optical Metrology and Inspection for Industrial Applications IV* (2016). <https://doi.org/10.1117/12.2245590>
20. Fiala, M.: ARTag, a fiducial marker system using digital techniques. In: IEEE Computer Society Conference on Computer Vision and Pattern Recognition, vol. 2, Proceedings (2005)
21. Romero-Ramirez, F., Muñoz-Salinas, R., Medina-Carnicer, R.: Speeded up detection of squared fiducial markers. *Image Vis. Comput.* **76**, 38–47 (2018). <https://doi.org/10.1016/j.imavis.2018.05.004>
22. Garrido-Jurado, S., Muñoz-Salinas, R., Madrid-Cuevas, F.J., Marín-Jiménez, M.J.: Automatic generation and detection of highly reliable fiducial markers under occlusion. *Pattern Recognit.* **47**, 2280–2292 (2014). <https://doi.org/10.1016/j.patcog.2014.01.005>
23. Garrido-Jurado, S., Muñoz-Salinas, R., Madrid-Cuevas, F., Medina-Carnicer, R.: Generation of fiducial marker dictionaries using mixed integer linear programming. *Pattern Recognit.* **51**, 481–491 (2016). <https://doi.org/10.1016/j.patcog.2015.09.023>
24. Mondéjar-Guerra, V., Garrido-Jurado, S., Muñoz-Salinas, R., Marín-Jiménez, M., Medina-Carnicer, R.: Robust identification of fiducial markers in challenging conditions. *Expert Syst. Appl.* **93**, 336–345 (2018). <https://doi.org/10.1016/j.eswa.2017.10.032>
25. Canny, J.: A computational approach to edge-detection. *IEEE Trans. Pattern Anal. Mach. Intell.* **8**, 679–698 (1986). <https://doi.org/10.1109/tpami.1986.4767851>
26. Otsu, N.: A threshold selection method from gray-level histograms. *IEEE Trans. Syst. ManCybern.* **9**, 62–66 (1979)
27. Zatočilova, A., Poliscuk, R., Palousek, D., Brandejs, J.: Photogrammetry based system for the measurement of cylindrical forgings axis straightness. In: Conference on Optical Measurement Systems for Industrial Inspection VIII. Spie-Int Soc Optical Engineering, Bellingham (2013). <https://doi.org/10.1117/12.2020917>
28. Zatočilova, A., Palousek, D., Brandejs, J.: Development of a photogrammetry system for the measurement of rotationally symmetric forgings. In: Conference on Optical Measurement Systems for Industrial Inspection IX. Spie-Int Soc Optical Engineering, Bellingham (2015). <https://doi.org/10.1117/12.2184916>
29. Zatočilova, A., Palousek, D., Brandejs, J.: Image-based measurement of the dimensions and of the axis straightness of hot forgings. *Measurement* **94**, 254–264 (2016). <https://doi.org/10.1016/j.measurement.2016.07.066>
30. Hurník, J., Zatočilová, A., Paloušek, D.: Camera calibration method of optical system for large field measurement of hot forgings in heavy industry. In: *Optical Measurement Systems for Industrial Inspection XI* (2019). <https://doi.org/10.1117/12.2527693>
31. Pebody, L.: The reconstructibility of finite abelian groups. *Comb. Probab. Comput.* **13**, 867–892 (2004). <https://doi.org/10.1017/S0963548303005807>
32. Pebody, L.: Reconstructing odd necklaces. *Comb. Probab. Comput.* **13**, 503–514 (2007). <https://doi.org/10.1017/S0963548306007875>

**Publisher's Note** Springer Nature remains neutral with regard to jurisdictional claims in published maps and institutional affiliations.

# PROCEEDINGS OF SPIE

[SPIDigitalLibrary.org/conference-proceedings-of-spie](https://spiedigitallibrary.org/conference-proceedings-of-spie)

## Camera calibration method of optical system for large field measurement of hot forgings in heavy industry

Hurník, Jakub, Zatocilová, Aneta, Paloušek, David

Jakub Hurník, Aneta Zatocilová, David Paloušek, "Camera calibration method of optical system for large field measurement of hot forgings in heavy industry," Proc. SPIE 11056, Optical Measurement Systems for Industrial Inspection XI, 1105635 (21 June 2019); doi: 10.1117/12.2527693

**SPIE.**

Event: SPIE Optical Metrology, 2019, Munich, Germany

# Camera calibration method of optical system for large field measurement of hot forgings in heavy industry

Jakub Hurník\*, Aneta Zatočilová, David Paloušek

Dept. of Reverse Engineering and Additive Technologies, Institute of Machine and Industrial Design, Brno University of Technology, Faculty of Mechanical Engineering, Technická 2896/2, 616 69 Brno, Czech Republic

## ABSTRACT

During the manufacturing process of heavy forgings, simple contact measuring techniques are still used to check the dimensions, therefore an optical measuring system is in demand. In this paper, a camera calibration method for the passive measuring system, which is being developed in collaboration with an industrial partner, is proposed. Our approach is based on space resection and works with robust coded targets, which are distributed in the field of view. The coordinates of targets are measured using TRITOP (GOM) measuring system. This solution allows to build a large calibration field, without a need of large calibration objects. The camera calibration works in 2 steps - at first, the intrinsic parameters of the camera, including lens distortion, are calibrated. These parameters are considered as stable, due to the use of special camera covers. Multi-image version of the calibration method and dense field of calibration targets are used. The second step is performed from every image and employs a single-image extrinsic camera parameters calibration method. Only a few coded calibration targets, mounted on stable objects in the scene, are required. The calibration method was tested in industrial conditions. The method showed great results, the average reprojection error was under 0.1 px. The effect of thermally affected zone on the calibration process is discussed.

**Keywords:** camera calibration, large field, forgings, measurement, space resection

## 1. INTRODUCTION

Heavy forgings are mainly used as semi-finished products for various shafts in energy, petrochemical and shipbuilding industry. Their dimensions are in meters, forging temperatures are around 1000 °C. During the manufacturing by open-die forging process, significant inaccuracies can occur. These inaccuracies could be corrected in the end of the manufacturing process. To provide feedback about dimensional and shape accuracy, only visual assessment or just simple contact measuring techniques are still used<sup>1</sup>. These methods are slow and inaccurate and could be dangerous. Due to the resulting inaccurate shape and dimensions of forgings, massive machining allowances (up to 15 % of the workpiece material<sup>2</sup>) must be applied. A fast, non-contact accurate and reliable measuring system is in demand. Although specialized time-of-flight systems are available, the research continues to find a cheaper and faster alternative. Researchers often propose active measuring systems – projector<sup>3,4,5</sup> or laser aided<sup>6,7</sup> stereo vision and line laser scanners<sup>2,8</sup>. The disadvantage of active systems is the need of strong light source. Zatočilová et al. proposed a passive measuring system based on forging silhouettes measurement, which proved great potential<sup>9, 10, 11</sup>.

The calibration of such systems is challenging – the field of view is large and complex, and the temperature of the environment is variable. Usually proposed calibration methods of such systems work with large 2D calibration patterns<sup>3,8</sup>, projected patterns<sup>4,7,12</sup> or various accurate manipulators<sup>2,5</sup>. These tools are not suitable for large-scale calibration or are not practical to use in industrial environment. The approaches also don't allow continuous calibration of extrinsic camera parameters. These parameters can be slightly changing in time, due to the thermal expansion of the whole environment, vibrations or other effects. Zatočilová et al.<sup>11</sup> proposed a calibration method of a static passive measuring system, which

---

\*Jakub.Hurnik@vut.cz; phone +420 54114 3255

used 3D calibration field of non-coded targets. The camera parameters were calculated using direct linear transformation (DLT) of collinearity equations. Although this approach is computationally efficient, it was not automated and therefore slow. Due to the use of DLT, the lens distortion parameters couldn't be computed, which leads to significant inaccuracies. Also, the researchers don't examine the effect of hot atmosphere around the hot forging on the calibration or whole system accuracy. The hot atmosphere has different refractive index and in certain conditions could form a lens, which could cause relative errors up to 0.35 % in measured dimensions<sup>13</sup>.

In this paper, a camera calibration method for the passive static multi-camera optical measuring system, which is being developed in collaboration with an industrial partner, is proposed. This system consists of 3 cameras, which observe the forging from radial direction. The system determines the shape and dimensions of the forging according to its silhouettes. The measuring volume is approx.  $6 \times 6 \times 2$  meters, the accuracy should be in millimetres. Our approach is based on space resection and works with a calibration field of unique, robust, coded calibration targets, which are distributed in the field of view. The coordinates of targets are measured using a commercial optical measuring system TRITOP (GOM). This solution enables to build a large and dense calibration field, without a need of huge calibration objects or 2D calibration patterns. The developed calibration method employs a rectilinear camera model with radial, tangential and affine distortion. The optimization is carried out by minimization of reprojection error using a trust-region method. Similar approaches are used e.g. for calibration of cameras with large field of view<sup>14</sup> or object tracking systems with large tracking volume<sup>15</sup>.

The developed calibration method works in 2 steps. In the first step, the intrinsic parameters of the camera are calibrated. Since the cameras are placed in thermoregulated covers and have a stable intrinsic geometry, the intrinsic parameters are constant. To achieve desired accuracy of their calibration, multi-image version of the calibration method and dense field of calibration targets are used. The first step is carried out only once, prior to the installation of the system. The second step employs a single-image method. It is carried out from every photograph taken by the system and includes the calibration of camera extrinsic parameters. For the second step, only a few coded calibration targets, mounted on stable objects in the scene are required. The proposed calibration algorithm accuracy was tested in laboratory and industrial conditions. The effects of hot atmosphere around the forging on the calibration accuracy was also examined.

## 2. MATERIALS AND METHODS

### 2.1 Equipment

The system for measurement of forgings consist of 3 cameras, which observe the forging from radial direction (Figure 1 on the left). ZWO ASI 1600 monochromatic cameras are used. The cameras are equipped with 16 MPx sensor with 3.8 μm pixel size. Zeiss Interlock Compact industrial lenses were used. The lenses are equipped with M42x1 mount and special screws to fix focus and aperture. Haida UV+IR cut filters were used to achieve sharp images. Camera 1 and 2 used 21 mm and camera 3 35 mm focal length. Camera 3 was not used during the experiments. The cameras were mounted in special thermoregulated camera covers (Figure 1 on the right), which were cooled using 29 W vortex tube – Vortec 106-2-H. The intrinsic temperature was held around 20 ° C.

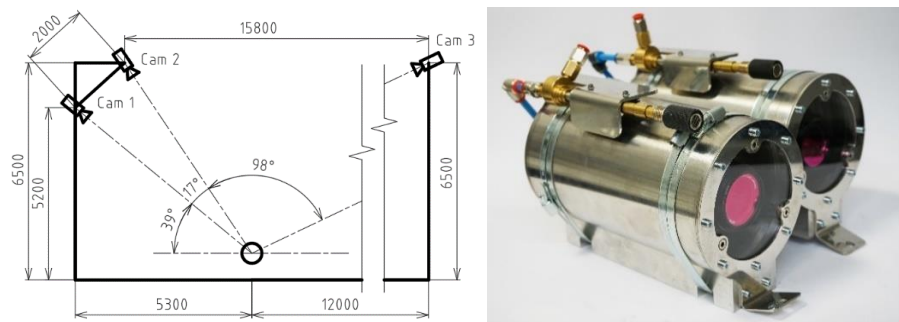


Figure 1. On the left – scheme of camera positions of measuring system, on the right – cameras in thermoregulated covers.

## 2.2 3D calibration field

In this study, the small calibration fields for testing in laboratory conditions (approx.  $1.5 \times 1.5 \times 0.5$  meters) were built from up to 50 TRITOP 5 mm coded targets. The large calibration fields (approx.  $6 \times 6 \times 2$  meters, e.g. Figure 2 on the right) were built up to 50 hybrid calibration targets. The hybrid target consists of 4 5mm TRITOP targets in the corners and 1 28mm central target with unique, specially designed robust coding (Figure 2 on the left). The central target size was designed to be at least 15 px in diameter in the image. The TRITOP targets in the corners are used by TRITOP software for image registration. These targets can also be used for automatic computation of centres of central targets. In case of big complicated projects, the central targets also could be used for image registration in TRITOP software, if the user manually assign unused codes to them in TRITOP software. The hybrid targets were manufactured using 1800 dpi direct UV printing on  $154 \times 154 \times 1.5$  mm steel plates.

The spatial coordinates of the calibration targets were measured using high precision GOM TRITOP optical 3D coordinate measuring machine (Figure 2 in the middle). The system uses 12 MPx Nikon D300s reflex camera mounted with 24 mm fixed focal length lens. A set of 2 and 1 meter GOM carbon fibre scale bars were used.



Figure 2. On the left – hybrid calibration targets, in the middle – TRITOP (GOM) measuring system with GOM CFK scale bars, on the right – an example of large calibration field.

## 2.3 Camera intrinsic parameters calibration

The intrinsic camera parameters were calibrated using a dense 3D calibration field of reference points (coded targets with known spatial coordinates). Multi-image calibration method was used, to reach maximum accuracy. Several images of the calibration field were taken from the same point of view, but different rotation of the camera around its optical axis. Using this method, sufficient spatial distribution of the targets, relatively to camera, is obtained. The reference targets were segmented and recognized using specially developed algorithm. The accurate target centre coordinates were calculated in the calibration images using star ellipse operator. According to the target codes, the spatial coordinates of the targets are automatically assigned to their image coordinates. These matching coordinates are used in the computation of camera parameters.

The camera parameters calculation could be understood as calculation of the transformation between 3D spatial coordinates and 2D image coordinates. Since both the coordinates in the space and in the image include random error, the problem was solved as minimisation of square reprojection error. Rectilinear camera model was used, which considered lens distortion<sup>16</sup>. The camera intrinsic geometry is stable, the lens setup was locked, and the cameras were kept in constant temperature in the thermoregulated covers. Therefore, the principal point coordinates, focal length and distortion coefficients were considered as constant. The image coordinates were normalized – the radius of the biggest circle, which can fit into the image, was set to 1 (the length of the shorter side of the image was 2). The optimization was carried out on all the calibration images simultaneously, the problem was defined as follows (equation 1):

$$\begin{aligned} & \underset{X_{0j}, Y_{0j}, Z_{0j}, \omega_j, \varphi_j, \kappa_j, x'_0, y'_0, c, A_1, A_2, A_3, B_1, B_2, C_1, C_2}{\operatorname{argmin}} \quad (1) \\ & \sum_{i=1}^{n_1} \sum_{j=1}^{n_2} \left( -x'_{ij} + x'_0 + \Delta x'_{ij} - c \frac{r_{11j}(X_{ij} - X_{0j}) + r_{21j}(Y_{ij} - Y_{0j}) + r_{31j}(Z_{ij} - Z_{0j})}{r_{13j}(X_{ij} - X_{0j}) + r_{23j}(Y_{ij} - Y_{0j}) + r_{33j}(Z_{ij} - Z_{0j})} \right)^2 \\ & + \left( -y'_{ij} + y'_0 + \Delta y'_{ij} - c \frac{r_{12j}(X_{ij} - X_{0j}) + r_{22j}(Y_{ij} - Y_{0j}) + r_{32j}(Z_{ij} - Z_{0j})}{r_{13j}(X_{ij} - X_{0j}) + r_{23j}(Y_{ij} - Y_{0j}) + r_{33j}(Z_{ij} - Z_{0j})} \right)^2 \\ & \text{where } r_{11j} \dots r_{33j} \text{ are elements of rotation matrix calculated from angles } \omega_j, \varphi_j, \kappa_j; \\ & \Delta x'_{ij}, \Delta y'_{ij} \text{ are functions of } A_1, A_2, A_3, B_1, B_2, C_1, C_2; x'_{ij}, y'_{ij}, X_{ij}, Y_{ij}, Z_{ij} \text{ are data} \end{aligned}$$

where  $i$  is the number of reference point ( $n_1$  total) in the  $j$ -th image,  $n_2$  is the total number of calibration images,  $X_{ij}, Y_{ij}, Z_{ij}$  are spatial coordinates and  $x'_{ij}, y'_{ij}$  are the measured image coordinates of the calibration target,  $X_{0j}, Y_{0j}, Z_{0j}$  are the spatial coordinates of camera projection centre,  $\omega_j, \varphi_j, \kappa_j$  are the rotations of camera coordinate system with respect to global (spatial) coordinate system,  $x'_0, y'_0$  are the image coordinates of principal point,  $c$  is the focal length,  $\Delta x'_{ij}, \Delta y'_{ij}$  are the distortion correction functions,  $A_1, A_2, A_3, B_1, B_2, C_1, C_2$  are the coefficients of balanced radial, tangential, and affine distortion. The distortion functions were defined as follows (equation 2):

$$\begin{aligned} \Delta x'_{ij} &= \hat{x}'_{ij} A_1 (r'^2_{ij} - r'^2_0) + \hat{x}'_{ij} A_2 (r'^4_{ij} - r'^4_0) + \hat{x}'_{ij} A_3 (r'^6_{ij} - r'^6_0) + B_1 (r'^2_{ij} + 2\hat{x}'_{ij}) + 2B_2 \hat{x}'_{ij} \hat{y}'_{ij} \quad (2) \\ &+ C_1 \hat{x}'_{ij} + C_2 \hat{y}'_{ij} \\ \Delta y'_{ij} &= \hat{y}'_{ij} A_1 (r'^2_{ij} - r'^2_0) + \hat{y}'_{ij} A_2 (r'^4_{ij} - r'^4_0) + \hat{y}'_{ij} A_3 (r'^6_{ij} - r'^6_0) + B_2 (r'^2_{ij} + 2\hat{y}'_{ij}) + 2B_1 \hat{x}'_{ij} \hat{y}'_{ij} \end{aligned}$$

where  $r'_0$  was set to  $2/3$  (universal value) and  $r'_{ij}$  is the distance of the image point from the principal point (equation 3):

$$r'_{ij} = \sqrt{\hat{x}'^2_{ij} + \hat{y}'^2_{ij}} \quad (3)$$

where  $\hat{x}'_{ij}, \hat{y}'_{ij}$  are the corrected image point coordinates, which are the approximation of the distortion-error-free image coordinates. The rotation matrix was defined as follows (equation 4):

$$\begin{aligned} \mathbf{R}_j &= \begin{bmatrix} r_{11j} & r_{12j} & r_{13j} \\ r_{21j} & r_{22j} & r_{23j} \\ r_{31j} & r_{32j} & r_{33j} \end{bmatrix} = \quad (4) \\ &= \begin{bmatrix} \cos\varphi_j \cos\kappa_j & -\cos\varphi_j \sin\kappa_j & \sin\varphi_j \\ \cos\omega_j \sin\kappa_j + \sin\omega_j \sin\varphi_j \cos\kappa_j & \cos\omega_j \sin\kappa_j - \sin\omega_j \sin\varphi_j \sin\kappa_j & -\sin\omega_j \cos\varphi_j \\ \sin\omega_j \sin\kappa_j - \cos\omega_j \sin\varphi_j \cos\kappa_j & \sin\omega_j \cos\kappa_j + \cos\omega_j \sin\varphi_j \sin\kappa_j & \cos\omega_j \cos\varphi_j \end{bmatrix} \end{aligned}$$

The mentioned optimization must be carried out iteratively, to correct the distortion, which depends on the unknown error-free image coordinates. In every following iteration, the optimization is carried out with more accurate approximation of error-free coordinates, which are calculated using values from the previous iteration (equation 5):

$$\begin{aligned} \hat{x}'_{ij} &= x'_{ij} - x'_0 - \Delta x'_{ij} \quad (5) \\ \hat{y}'_{ij} &= y'_{ij} - y'_0 - \Delta y'_{ij} \end{aligned}$$

The initial values were obtained by DLT. The initial distortion coefficients were set to 0. The optimization problem was solved using trust-region method.

## 2.4 Camera extrinsic parameters calibration

The extrinsic camera parameters were calculated using a static sparse 3D calibration field of reference points. Using this method, the camera can be calibrated from a single image. Single camera calibration method was used, because in general case, small overlap of fields of view of cameras and large difference in observation angles has to be considered. At first, the target image coordinates are obtained and matched with target spatial coordinates. The distortion effects were removed using this iteration scheme<sup>16</sup> (equation 6):

$$\hat{\mathbf{x}} = \mathbf{x}' - \Delta(\mathbf{x}' - \Delta(\mathbf{x}')) \quad (6)$$

where  $\hat{\mathbf{x}}$  is the estimation of error-free image coordinates of the target,  $\mathbf{x}'$  is the measured image coordinates of the target and  $\Delta$  is the distortion function (equation 2), which depends on already known principal point coordinates and image distortion parameters. To reach maximum accuracy, 10 iterations were used. Then, space resection is carried out. The same optimisation problem, as was presented in equation 1, is solved, but the distortion function is neglected. For the initial values computation, DLT was used.

### 3. RESULTS

#### 3.1 Calibration field accuracy

For the calibration in laboratory and industrial conditions, fields of approx.  $1.5 \times 1.5 \times 0.5$  and  $6 \times 6 \times 1.5$  m were used, respectively. The small fields contained up to 50 TRITOP coded targets, the large field up to 50 hybrid targets. TRITOP measurement projects contained from 60 to 70 images from different viewpoints. In the large projects, both small and large calibration targets were used for the image registration, to improve the reliability and accuracy of the measurement. Quality indicators of all used projects were evaluated by the TRITOP software as normal (worst cases are summarized in Table 1).

Table 1. TRITOP project quality indicators (worst cases).

	Small project	Large projects
Average image point deviation [px]	0.053	0.062
Average reference point deviation [mm]	0.023	0.037
Average scale bar deviation [mm]	0.010	0.043
Minimum number of target observations [-]	23	2
Minimum observation angle [°]	53.175	14.000

Due to the dimensions of the large calibration field, size of calibration targets and limitations of the environment, it wasn't possible to take images from positions, which are recommended in the TRITOP manual (8 images around the measured field from each of 3 height levels). For comparison, example of suitable imaging positions can be seen in Figure 3 on the left. Imaging positions of large scale project can be seen in Figure 4 on the left. The accuracy of the large calibration field was examined, to exclude potential large error of targets with low number of observations and low minimum observation angle, or large cumulative error of targets which are distant from the calibration field centre. To verify the accuracy of measurement of the large calibration field by TRITOP system, the field measurement was carried out twice. Two resulting point clouds were fitted on each other using least squares method, to compensate possible uncertainty of the coordinate systems. The repeatability of the measurement was examined and compared with the repeatability of the measurement of the small field. Only elements of the calibration field (coordinates of the centres of the large unique-coded targets) were considered. The results can be seen in Table 2, Figure 3 and Figure 4.

Table 2. Results of the repeatability test –  $N$  is the number of measured targets,  $\bar{e}$  is the mean repeatability error,  $e_{max}$  is the maximum repeatability error,  $e_{RMS}$  is the root mean square repeatability error and  $\xi_{e_{RMS}}$  is repeatability error relative to the longest distance measured in the project  $l_{max}$ .

	$N$ [-]	$\bar{e}$ [mm]	$e_{max}$ [mm]	$e_{RMS}$ [mm]	$l_{max}$ [mm]	$\xi_{e_{RMS}}$ [%]
Small field	50	0.0086	0.0200	0.0097	1523.3	0.00064
Large field	41	0.1881	0.6436	0.2372	7027.6	0.00338

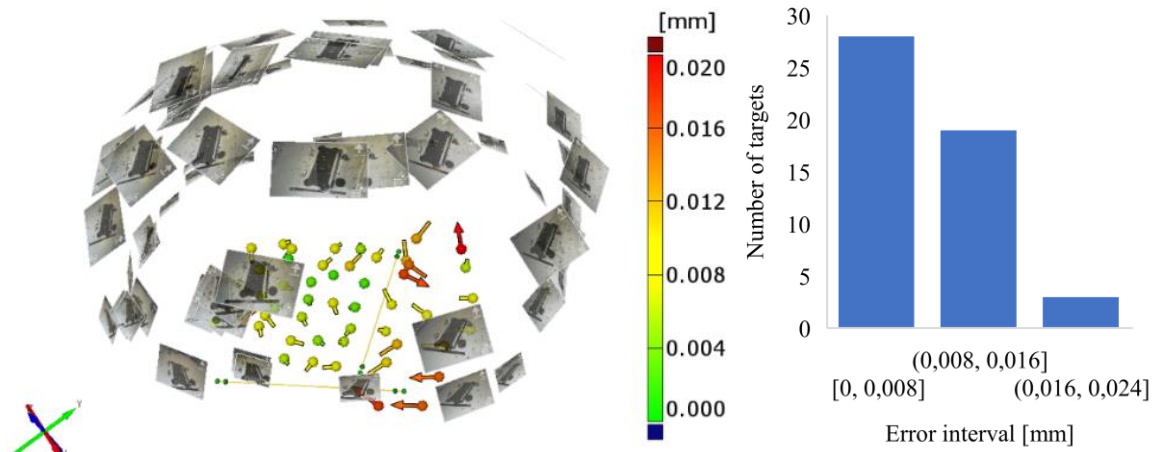


Figure 3. On the left – repeatability error distribution across the small calibration field (example of suitable imaging positions), on the right – repeatability error distribution of the targets.

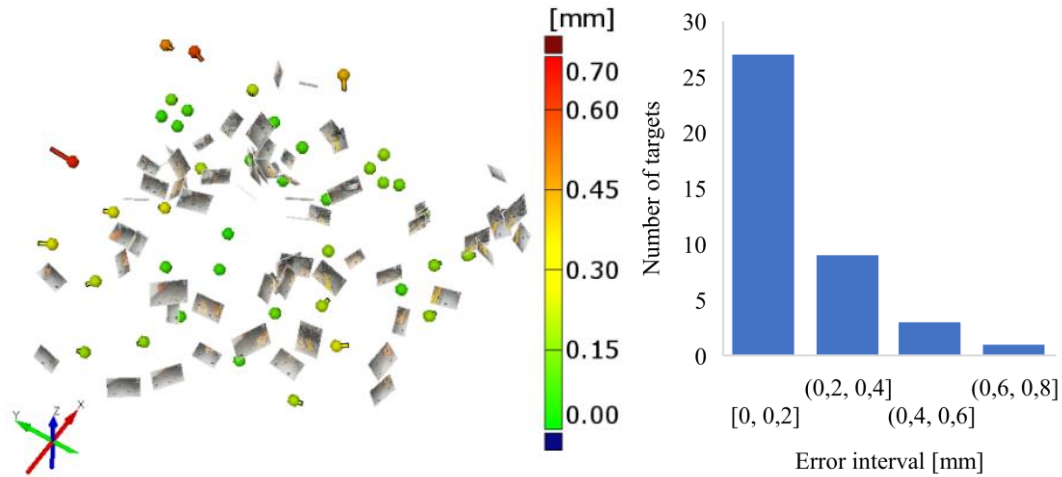


Figure 4. On the left – repeatability error distribution across the large calibration field (example of non-ideal orientation of measurement images), on the right – repeatability error distribution of the targets.

### 3.2 Camera intrinsic parameters calibration

The intrinsic parameters calibration of both cameras of the measuring system was carried out both in laboratory (small scale) and industrial (large scale) conditions. The focus and the aperture of the cameras were set to cover the necessary measuring volume with the depth of sharpness. This setup was locked using the locking screws on the lens. The cameras were then mounted in the thermoregulated covers and kept on constant temperature. Calibration fields were built and measured using TRITOP system (Figure 5 on the left). In case of large field, 41 targets were successfully measured, in case of small field, 50 targets were measured. In order to calibrate the cameras, the fields were photographed, each image was taken with different rotation angle around an optical axis of the camera, to ensure sufficient space distribution of the calibration targets in measuring volume. 7 calibration images were used in all cases. In every calibration image, around 30 calibration targets were detected, which means that around 200 targets in total were measured in the calibration volume. The distribution of targets in calibration volume can be seen in Figure 5 on the right. The intrinsic camera parameters of both cameras, with their 95 % confidence intervals, for both cases (small and large scale) were calculated, the calibration results are summarized in Table 3.

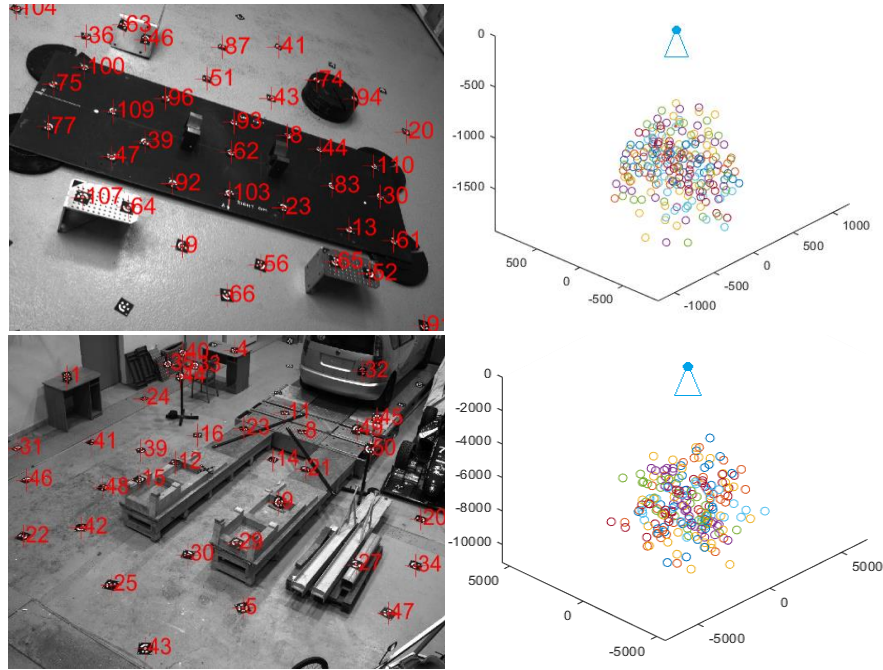


Figure 5. Left – small and large scale calibration field, right – distribution of calibration targets from a set of calibration images relative to the camera in small and large scale, both axes are in millimetres.

Table 3. Camera intrinsic parameters with 95 % confidence intervals in small and large scale ( $\overline{\Delta Res}$ ,  $\Delta RMS$  – mean and RMS reprojection error of space resection,  $N$  – total number of calibration targets in calibration volume, distortion coefficients and intrinsic parameters according to equation 1, 2).

		SMALL SCALE						
		$A1 [\cdot 10^{-3}]$	$A2 [\cdot 10^{-4}]$	$A3 [\cdot 10^{-5}]$	$B1 [\cdot 10^{-5}]$	$B2 [\cdot 10^{-5}]$	$C1 [\cdot 10^{-4}]$	$C2 [\cdot 10^{-4}]$
Cam 1		-5.984	6.696	-4.873	-8.247	6.455	1.656	0.416
		$\pm 0.105$	$\pm 0.969$	$\pm 2.448$	$\pm 1.217$	$\pm 1.086$	$\pm 0.329$	$\pm 0.317$
Cam 2		-6.212	4.220	7.669	9.953	-2.247	1.090	1.457
		$\pm 0.192$	$\pm 2.146$	$\pm 7.255$	$\pm 2.016$	$\pm 1.711$	$\pm 0.417$	$\pm 0.485$
		$x'_0 [px]$	$y'_0 [px]$	$c [mm]$	$\overline{\Delta Res} [px]$	$\Delta RMS [px]$	$N [-]$	
Cam 1		2361.17	1742.01	21.9000	0.061	0.071	217	
		$\pm 0.63$	$\pm 0.57$	$\pm 0.0009$				
Cam 2		2280.51	1737.05	21.7704	0.083	0.095	208	
		$\pm 1.00$	$\pm 0.85$	$\pm 0.0017$				
		LARGE SCALE						
		$A1 [\cdot 10^{-3}]$	$A2 [\cdot 10^{-4}]$	$A3 [\cdot 10^{-5}]$	$B1 [\cdot 10^{-5}]$	$B2 [\cdot 10^{-5}]$	$C1 [\cdot 10^{-4}]$	$C2 [\cdot 10^{-4}]$
Cam 1		-6.325	5.246	1.301	-8.541	6.500	1.231	1.216
		$\pm 0.151$	$\pm 1.439$	$\pm 3.865$	$\pm 2.150$	$\pm 1.773$	$\pm 0.378$	$\pm 0.369$
Cam 2		-6.787	6.435	-2.371	9.160	0.448	1.596	0.529
		$\pm 0.142$	$\pm 1.449$	$\pm 4.282$	$\pm 1.740$	$\pm 1.435$	$\pm 0.299$	$\pm 0.296$
		$x'_0 [px]$	$y'_0 [px]$	$c [mm]$	$\overline{\Delta Res} [px]$	$\Delta RMS [px]$	$N [-]$	
Cam 1		2367.80	1736.88	21.7466	0.085	0.103	199	
		$\pm 1.08$	$\pm 0.88$	$\pm 0.0014$				
Cam 2		2285.07	1738.14	21.5724	0.068	0.086	202	
		$\pm 0.86$	$\pm 0.68$	$\pm 0.0011$				

### 3.3 Extrinsic parameters calibration and accuracy verification

The extrinsic parameters were calibrated, and the calibration accuracy was verified both in small and large scale (directly in the forge). The cameras in camera covers were mounted on stable positions. A calibration field was built in the field of view of the cameras. The calibration field consisted of targets, which were placed on stable positions and targets, which were placed only temporary. Stable targets were further used for continuous camera calibration. Only 8 targets were chosen for continuous calibration of the extrinsic parameters of each camera (Figure 6, marked red). The temporary targets were used only for calibration accuracy evaluation and were removed further (Figure 6, marked green). The accurate spatial coordinates of both stable and temporary targets were measured using TRITOP system. The extrinsic camera parameters, with their 95 % confidence intervals were calculated, the results can be seen in Table 4.

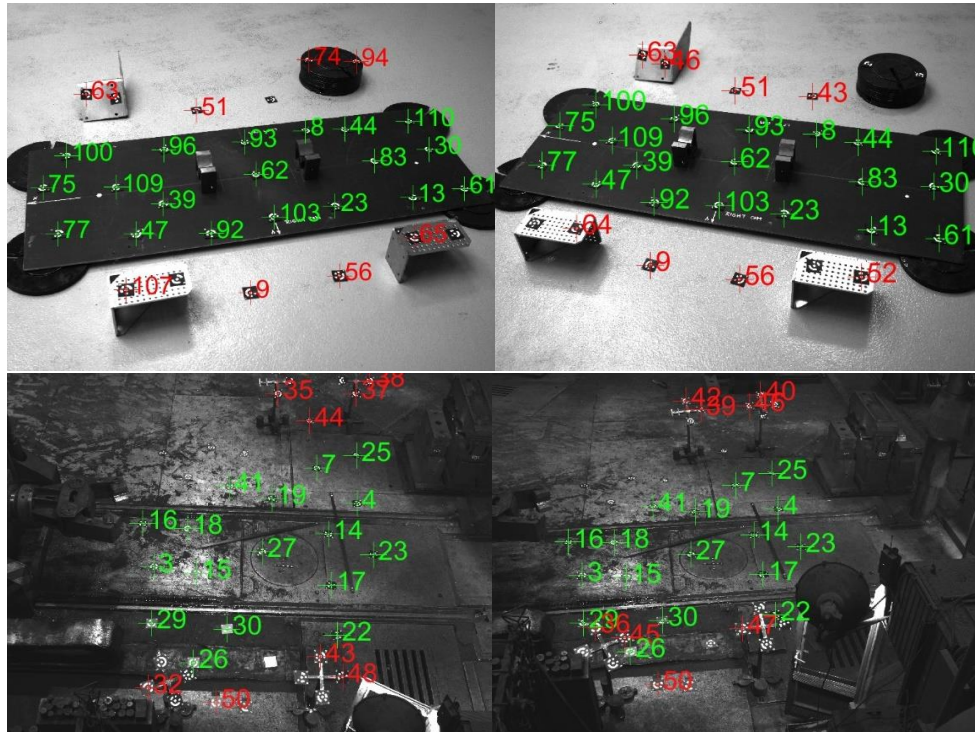


Figure 6. Images used for extrinsic parameters calibration and calibration accuracy verification in small (laboratory) and large (forge) scale; red targets – used for camera calibration, green targets – used for accuracy verification.

Table 4. Camera extrinsic parameters with 95 % confidence intervals ( $\overline{\Delta Res}$ ,  $\Delta RMS$  – mean and RMS reprojection error of space resection, extrinsic parameters according to equation 1).

SMALL SCALE								
	$X_0[mm]$	$Y_0[mm]$	$Z_0[mm]$	$\omega[rad]$	$\varphi[rad]$	$\kappa[rad]$	$\overline{\Delta Res}[px]$	$\Delta RMS[px]$
Cam 1	-952.449	-52.904	907.461	3.279928	0.778345	3.804413	0.049	0.055
	$\pm 0.041$	$\pm 0.055$	$\pm 0.062$	$\pm 0.000057$	$\pm 0.000042$	$\pm 0.000040$		
Cam 2	-486.895	-372.006	1135.220	3.480354	0.376197	3.415154	0.067	0.077
	$\pm 0.098$	$\pm 0.068$	$\pm 0.086$	$\pm 0.000064$	$\pm 0.000075$	$\pm 0.000062$		
LARGE SCALE								
	$X_0[mm]$	$Y_0[mm]$	$Z_0[mm]$	$\omega[rad]$	$\varphi[rad]$	$\kappa[rad]$	$\overline{\Delta Res}[px]$	$\Delta RMS[px]$
Cam 1	-553.64	-5503.11	6996.44	3.829816	0.014395	3.071599	0.055	0.065
	$\pm 0.70$	$\pm 0.24$	$\pm 0.60$	$\pm 0.000057$	$\pm 0.000086$	$\pm 0.000065$		
Cam 2	-508.49	-6889.15	5573.20	4.053132	0.090346	3.173747	0.040	0.051
	$\pm 0.51$	$\pm 0.19$	$\pm 0.57$	$\pm 0.000045$	$\pm 0.000063$	$\pm 0.000063$		

To verify the calibration accuracy, the spatial coordinates of temporary targets were reconstructed using calculated camera extrinsic and already known intrinsic parameters. These coordinates were compared with the reference coordinates, measured using TRITOP system. Around 20 targets, which were clearly visible in the field of view of both cameras, were used. The test was carried out both in small and large scale. The error distribution of the reconstructed spatial coordinates can be seen in Figure 7 on the left. The base of the camera stereopair (approx. 600 mm in small and 2000 mm in large scale) is short, relative to the distance between the measured targets and the stereopair (approx. 1400 mm in small and 9000 mm in large scale). Therefore, the observation angle is relatively low (around 25 ° in small and 12 ° in large scale). This leads to significant depth estimation error, mainly in case of large scale measurement. To isolate the 2D measurement error, the error vector was decomposed to 2 directions – to depth direction and to direction perpendicular to depth direction, according to this equation:  $|e_{2DS}| = \sqrt{2}|e| \sin\left(\cos^{-1}\frac{(X-X_C)\cdot e}{|X-X_C|\cdot|e|}\right)$ , where  $|e_{2DS}|$  is the 2D error of single ray,  $e$  is the coordinates error vector,  $X$  is the vector of target coordinates,  $X_C$  is the vector of stereopair centre coordinates and  $\cdot$  denotes scalar multiplication. This error could be understood as the average of 2 observations, so to obtain the estimation of error of single ray, the error was multiplied by  $\sqrt{2}$  according to central limit theorem. The 2D error distribution could be seen in Figure 7 on the right. The results of the accuracy verification can be seen in Table 5.

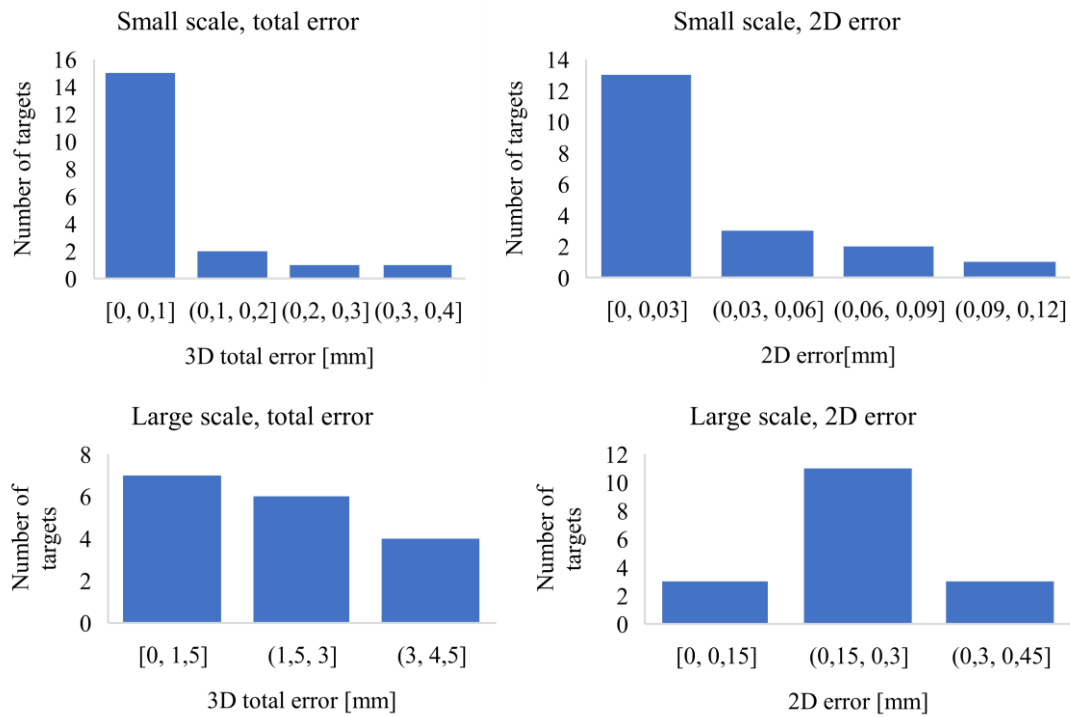


Figure 7. Error distribution of 3D and 2D measurement in small and large scale.

Table 5. 3D and 2D error characteristics of reconstructed target coordinates ( $e_{3DRMS}$  – RMS error of 3D measurement,  $\alpha$  – interval of observation angles,  $\bar{e}$ ,  $e_{max}$  and  $e_{RMS}$  – mean, maximum and RMS error of measurement in 2D,  $l_{max}$  – approximate maximum width of the field of view,  $\xi e_{RMS}$  – 2D measurement RMS error relative to maximum width of field of view).

	$e_{3DRMS}$ [mm]	$\alpha$ [°]	$\bar{e}$ [mm]	$e_{max}$ [mm]	$e_{RMS}$ [mm]	$l_{max}$ [m]	$\xi e_{RMS}$ [%]
Small s.	0.112	21.7 – 27.4	0.030	0.092	0.041	1.5	0.003
Large s.	2.303	10.3 – 14.4	0.240	0.389	0.254	6	0.004

### 3.4 Thermal influence of calibration accuracy

The influence of hot air with different refractive index on the calibration accuracy was examined both in laboratory and industrial conditions. Theoretically, the hot atmosphere might optically deform the space. This optical deformation should be noticeable on the calibration reprojection error. Camera extrinsic parameters were continuously calibrated, while the hot forging was brought to the field of view. In contrast to standard extrinsic parameters calibration, around 20 calibration targets were used, to examine the optical deformation effect more clearly. The scene with glowing hot forging (around 1000 °C) can be seen in Figure 8. The reprojection error of the calibration of the extrinsic parameters was observed – the results can be seen in Figure 9. While the RMS reprojection error without the forging in the scene was 0.10 px in laboratory and 0.11 px in industrial conditions, the maximum RMS reprojection error with the forging in the scene was 0.21 px in laboratory and 0.25 px in industrial conditions. Also, the error strongly varied between the particular images (see Figure 9).

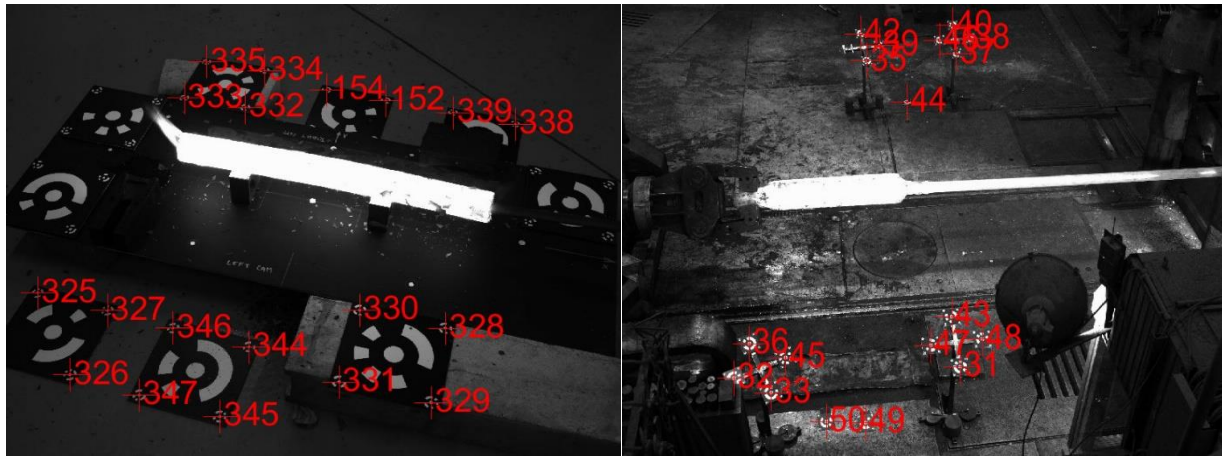


Figure 8. On the left – scene with hot forging in the laboratory, on the right – scene with hot forging in the forge, the calibration targets used for the camera calibration are marked red.

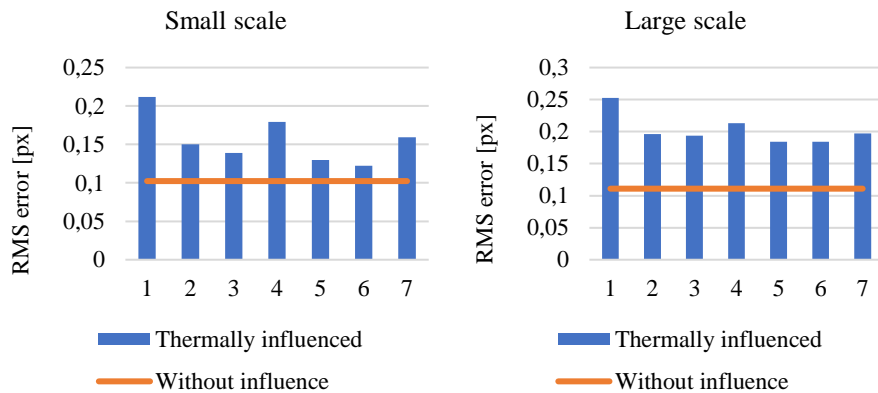


Figure 9. RMS reprojection errors of extrinsic camera parameters from particular images.

## 4. DISCUSSION

The accuracy of the large 3D calibration field was analysed. The mean square repeatability error of  $6 \times 6 \times 1.5$  m large scale calibration field was 0.24 mm, the maximum error was 0.64 mm. These results were considered as acceptable for the

camera calibration, considering the large measuring volume. The relative accuracy of the large calibration field was compared with the accuracy of small ( $1.5 \times 1.5 \times 0.5$  m) calibration field, which was captured according to the recommendations of TRITOP manual. The increase of the relative repeatability error with the field size was approx.  $5 \times$ . The increase can be explained as the effect of non-ideal optical measurement (non-ideal distribution of image positions). This problem was apparent from the TRITOP project quality indicators. The minimum number of target observation and minimum observation angle was significantly lower in case of large projects (23 vs. 2 observations,  $53$  vs.  $14^\circ$ ). Also, cumulative error can occur in coordinates of targets, which are distant from the calibration field centre. The mentioned problem could be solved by taking more images of the calibration field (only from 60 to 70 images were used). Another accuracy increase could be achieved, if aerial work platform would be used for the calibration field measurement. In the industry, such platforms are common equipment.

The camera intrinsic parameters were calibrated both in small and large scale using the proposed multi-image method. In both scales, the RMS reprojection error was under or around 0.1 px. Mean reprojection error was under 0.085 px. These values are considered as satisfactory. The residual reprojection error can be explained mainly as the influence of imperfections of optical system of the camera in camera cover, which can't be described using the distortion equations. The inaccuracies of the coordinates of the calibration field didn't have significant effect on the reprojection error – the reprojection error was similar in case of large and relatively much more accurate small calibration field. The parameters accuracy could be further improved by taking more pictures of the calibration field.

The method of continuous camera calibration of extrinsic parameters was also tested in both small and large scale and the calibration accuracy was verified. The extrinsic parameters were calibrated from only 8 targets in single image. The RMS reprojection error varied between 0.051 and 0.077 px and the mean error between 0.040 and 0.067 (less than during the intrinsic parameters calibration), due to the better distribution of random errors between less targets in image. Using the calculated camera parameters, the accuracy of the whole camera calibration was verified. Due to the relatively small base of the stereopair, the depth estimation error was dominant. The depth estimation error is not relevant for the forging measuring system which works with the silhouettes. The error in direction perpendicular to depth direction was much smaller – 0.03 mm in small and 0.24 mm in large scale. These values are, at least in case of large-scale measurement, comparable with the accuracy of the calibration field measured by commercial measuring system TRITOP. These values are considered as very accurate and sufficient, because the demands on the accuracy of the system for the measurement of large forgings are in millimetres.

The influence of the thermally affected atmosphere around the hot forging on the calibration accuracy was examined both in laboratory and industrial conditions. The reprojection error raised up to  $2.5 \times$ , from 0.1 px to 0.25 px. Also, the reprojection error strongly varied between the images, apparently due to the irregular flowing of the atmosphere. This problem could be solved by calibrating the camera extrinsic parameters shortly before the hot forging appears on the scene and then, during the measurement, considering these parameters as constant.

## 5. CONCLUSION

In this paper, a calibration method, for the calibration of cameras of passive static multi-camera system for the measurement of large hot forgings, is proposed. The method is based on space resection and works with 3D calibration field, which consists of coded targets. The spatial coordinates of the targets are measured on-site using optical measuring system TRITOP (GOM). This approach allows to calibrate the cameras with large and non-overlapping field of view, without a need of large calibration objects. Also, this approach allows continuous extrinsic camera parameters calibration. The resulting accuracy is high, the reprojection error was under or around 0.1 px. The accuracy of 2D measurement with 6 m wide field of view was in tenths of millimetre. The method was tested in laboratory as well as real industrial conditions. The negative effect of hot atmosphere with different refractive index around the forging on the calibration accuracy was examined and confirmed. The reprojection error raised up to  $2.5 \times$ , which leads to a need of calibration of the cameras shortly before the hot forging appears on the scene.

## ACKNOWLEDGEMENTS

The research leading to these results has received funding from TACR ZETA project TJ01000268 and specific project FSI-S-17-4144.

## REFERENCES

- [1] Hawryluk, M. and Ziembra J., "Possibilities of application measurement techniques in hot die forging processes," *Measurement* 110, 284-295 (2017).
- [2] Bracun, D., Skulj, G. and Kadis, M., "Spectral selective and difference imaging laser triangulation measurement system for on line measurement of large hot workpieces in precision open die forging," *Int. J. Adv. Manuf. Technol.* 90(1-4), 917-926 (2017).
- [3] Liu, W., Jia, X. H., Jia, Z. Y., Liu, S. J., et al., "Fast dimensional measurement method and experiment of the forgings under high temperature," *J. Mater. Process. Tech.* 211(2), 237-244 (2011).
- [4] Liu, W., Jia, Z. Y., Wang, F. J., Ma, X., et al., "An improved online dimensional measurement method of large hot cylindrical forging," *Measurement* 45(8), 2041-2051 (2012).
- [5] Jia, Z. Y., Liu, Y., Liu, W., Zhang, C., et al., "A spectrum selection method based on SNR for the machine vision measurement of large hot forgings," *Optik* 126(24), 5527-5533 (2015).
- [6] Liu, Y., Jia, Z. Y., Liu, W., Wang, L. L., et al., "An improved image acquisition method for measuring hot forgings using machine vision," *Sensor. Actuat. A-phys.* 238, 369-378 (2016).
- [7] Jia, Z. Y., Wang, L. L., Liu, W., Yang, J. H., et al., "A field measurement method for large objects based on a multi-view stereo vision system," *Sensor. Actuat. A-phys.* 234, 120-132 (2015).
- [8] Zhang, Y. C., Han, J. X., Fu, X. B. and Zhang, F. L., "Measurement and control technology of the size for large hot forgings," *Measurement* 49, 52-59 (2013).
- [9] Zatocilova, A., Poliscuk, R., Palousek, D. and Brandejs, J., "Photogrammetry based system for the measurement of cylindrical forgings axis straightness," *Proc. SPIE* 8788, (2013).
- [10] Zatocilova, A., Palousek, D. and Brandejs, J., "Development of a photogrammetry system for the measurement of rotationally symmetric forgings," *Proc. SPIE* 9525, (2015).
- [11] Zatocilova, A., Palousek, D. and Brandejs, J., "Image-based measurement of the dimensions and of the axis straightness of hot forgings," *Measurement* 94, 254-264 (2016).
- [12] Yang, J. H., Liu, W., Fan, C. N., Li, S. J., et al., "Improved calibration method of binocular vision measurement system for large hot forging," *ISIE* 25, 918-922 (2016).
- [13] Yamauchi, M., "Errors in optical shape measurement caused by a high-temperature atmosphere," *Opt. Eng.* 48(9), 4 (2009).
- [14] Tommaselli, A. M. G., Marcato, J., Morales, M. V. A., Silva, S. L. A., et al., "Calibration of panoramic cameras with coded targets and a 3D calibration field," *Eurocow 2014*, 137-142 (2014).
- [15] Hu, H., Liang, J., Xiao Z. Z., Tang, Z. Z., et al., "A four-camera videogrammetric system for 3-D motion measurement of deformable object.," *Opt. Laser. Eng.* 50(5), 800-811 (2012).
- [16] Luhmann, T., [Close range photogrammetry: principles, techniques and applications], Dunbeath: Whittles Publishing, 114-119, 201-214 (2011).



# Enhancing the accuracy of forging measurement using silhouettes in images

Jakub Hurník<sup>\*</sup>, Aneta Zatočilová, Daniel Koutný, David Paloušek

*Institute of Machine and Industrial Design, Faculty of Mechanical Engineering, Brno University of Technology, Technická 2896/2, 616 69 Brno, Czech Republic*

## ARTICLE INFO

### Keywords:

Forging  
Measurement  
Edge detection  
Silhouettes  
Axis straightness  
Image analysis

## ABSTRACT

In this study, a new passive camera system for heavy cylindrical forging measurement, based on silhouettes in images, is developed. New methods for making such a system more resistant to the negative effects of the industrial environment have been proposed. This includes weighted edge filtering based on complementary information about the edge quality in an image. The recorded measurement median errors were  $\pm 0.12$  mm and  $\pm 0.14$  mm. Moreover, the 95% confidence intervals were  $\pm 0.5$  mm and  $\pm 1$  mm for the forging axis and diameter measurements, respectively. Both results were achieved in a measurement volume of  $6 \times 6 \times 2$  m during the measurement of glowing hot forgings in industrial conditions. The results surpass those of the state-of-the-art method, mainly in the case of axis straightness measurement, by approximately 50%. The measurement is fast, and it provides feedback about the axis straightness for its subsequent correction.

## 1. Introduction

Heavy forgings are used as semi-finished products. Although their production is expensive, they are often used owing to their high strength. The major part of their production is cylindrical forgings, which are used for various shafts. Because of their large dimensions and small series production, they are manufactured using the open-die forging technology. This technology includes the formation of the product using flat or curved open dies on forging presses from hot pieces (temperatures between 1250 and 800 °C) of steel. Despite the high production costs, basic contact measurement techniques are still used [1,2] to provide feedback to the press operator. The lack of dimensional and shape control technologies results in large machining allowances, leading to ineffective use of material and energy. Axis straightness cannot be measured and can cause major problems during the manufacturing process owing to run-out. The shape can be corrected at the end of the forging process; however, the correction is based only on the operator's estimation. Therefore, an optical measurement system is required. Additionally, such a measurement system can become a part of an automated forging system in the future as a part of implementing Industry 4.0.

Measurement of hot forgings in the manufacturing process is a challenge. The environment is unstable owing to rapidly changing temperatures (thermal dilations) and vibrations. This can cause major problems for adjusting [3] or calibrating [4] measurement systems. Another problem is the hot atmosphere around the forging, which

affects the accuracy of every optical system [5,6]. Although there are studies on simulating the error to compensate for it [7], the studies admit that this simulation can be inaccurate owing to probable turbulent air flow. This error can be on the order of tenths of a percent [6]. There may also be other problems connected to the radiation of hot forging in the visible spectrum [8] or contrasting scales on the surface [9]. Therefore, standard optical measurement systems cannot be directly used.

Hot forgings can be measured, for example, using laser scanning technology (time-of-flight). Studies have shown that the environment does not have a significant effect on this method [10–13]. However, laser scanning has disadvantages, including long scanning times on the order of seconds. During this period, the forging has to be held still. Another disadvantage is the limited accuracy on the order of millimeters. Another method for hot forging measurement is active photogrammetry. These methods (e.g., line scanning [14–17], structured light aided stereovision [18–21], or laser-aided stereovision [22–24]) can achieve high accuracies (e.g., 0.2 mm ( $4\sigma$ ), considering the case of >400 mm diameter measurement [15] or a 0.27% maximum error, [23] respectively). The disadvantage is the signal-to-noise ratio owing to the light emissions of hot forging. Although the spectrum selection method [21] or difference imaging [15] is used to enhance the ratio, these methods limit the measurement volume. The third main approach is passive photogrammetry, which is usually based on 2D [9,25,26] or 3D forging silhouettes [27–30]. This approach is complicated to implement because of the need for camera calibration and the specialized image

<sup>\*</sup> Corresponding author.

E-mail address: [Jakub.Hurnik@vut.cz](mailto:Jakub.Hurnik@vut.cz) (J. Hurník).

processing owing to the contrasting scales. However, because the absence of a structured light source and the ability to achieve low measurement times, it can overcome the disadvantages of the other approaches.

### 1.1. State-of-the-art method

Hurník et al. [4] examined the influence of a hot atmosphere around hot forging in an industrial environment (measurement volume  $6 \times 6 \times 1.5$  m) on camera calibration error. The camera calibration method was based on spatial resection and the original robust target system [31]. The reprojection error, due to the thermal influence, increased up to  $2.5 \times$  from 0.1 px to 0.25 px, with a pixel resolution of 1.3 mm, which was satisfactory.

Hu et al. [9] developed a specialized edge operator for forging silhouette detection. The operator was based on the Canny edge detector [32]. The author used image preprocessing with histogram equalization and post-processing for edge validation. Edge validation was implemented directly in the Canny edge operator. The edge weights were modified based on the resistance of the edge to Gaussian blurring with a large kernel, which proved to be effective.

Bi et al. [25] introduced a 2D monocular measurement system for measuring small hot cubical workpieces. Edge detection was based on the Sobel edge operator, further fitting the line to edge pixels. The system was verified on cold workpieces with maximum dimensions of 60 mm and hot workpieces with temperatures of approximately 1000 °C and maximum dimensions of 40 mm. The measurement error was less than 0.5 mm in both cases. Thereafter, the authors investigated the effect of color filters on the contrast of forging silhouettes [26], which is crucial for their measurement. They observed that different filters should be used to obtain the optimum contrast for different temperatures.

Wang et al. [33] developed a 2D monocular system for steel bar diameter measurement during their manufacturing using high temperature rolling. The edge detection was based on the structured forest algorithm. The authors suggested the weighted edge variance as a level of trust in individual diameter measurements for further decision-making. This suppresses measurements on low level of trust. The proposed methods were verified in an industrial environment on glowing hot steel bars with a diameter of approximately 260 mm. The recorded diameter error of measurements that were classified as acceptable was approximately  $\pm 2.5$  mm.

Zhou et al. [30] introduced a method for measuring the basic dimensions of heavy forgings (diameter) in 3D. The system works with a stereo-pair of calibrated cameras. Instead of single points, the system uses whole lines to achieve better reliability. Image processing is based on the Hough transformation. The line was reconstructed using the triangulation method. The method achieved a 0.79% error in an industrial environment on hot forging with a diameter of 115 mm.

Publications [27–29] presented a system for measuring the length, diameter, and axis straightness of cylindrical forgings based on two cameras. The forgings are observed from the radial direction. The shape of the object is determined based on silhouettes in mutually perpendicular planes. These are bounded to the v-prisms in which the forging is placed. The measurement system uses only basic optical measurement or image analysis methods, including the non-iterative camera calibration method, edge detection with pixel precision (multistep method with edge validation), and object reconstruction. The experiments were conducted in a laboratory environment on both cold and heated (approximately 1150 °C) samples with a maximum length of 700 mm, diameter of 50 mm, and deflection size from 0.3 to 21 mm. Considering the measurement in the cold state, the maximum length and diameter measurement errors were approximately 2% (1% median) and 1% (0.5% median) [29], respectively. The maximum measured deflection error varied from less than  $\pm 1$  mm ( $\pm 0.2$  mm median) to approximately 3 mm for some samples. In the hot state, only the length and diameter of

forgings were measured. Significantly larger errors (even more than 2 mm) were observed due to the contrasting scales on the forging surface.

### 1.2. Scope of the study

This study focused on measuring 3D cylindrical forgings based on their silhouettes in images from a pair of cameras (Fig. 1). Using this method, it is possible to quickly obtain the data for axis straightness correction without major disadvantages. However, this method has not been tested in industrial conditions. Moreover, laboratory measurements of hot steel rods suggested limited accuracy of this method (on the order of percentages [29]). The achieved accuracy is relatively low compared to formed pipeline inspection systems [34–36] based on the same principle.

We assume that this is caused by the implementation of basic optical measurement methods in the literature. This study aims to use more advanced optical measurement methods to examine the measurement accuracy limits in industrial environments, including methods for accurate calibration and subpixel silhouette detection. It is not clear if these methods can significantly improve accuracy despite the interfering effects of the industrial environment.

Moreover, ways to make this system more robust to interferences are presented. Instead of providing several engineering solutions, we present an originally developed specialized edge filtering method. The edges can be partially corrupted by contrasting scales on the forging surface. Our aim was to use edge quality indicators from an image to determine edge point quality. We suggest the use of these indicators for weighted silhouette filtering to effectively suppress inaccurately detected edges.

The following are the main hypotheses of the study.

- Calculating silhouettes in an image with subpixel accuracy can help to achieve better measurement accuracy.
- Gradient magnitude and direction can be used as edge quality indicators for weighted edge smoothing to effectively suppress incorrect or inaccurate edges.
- The interfering effects of the industrial environment will not significantly affect the measurement accuracy.

This study also verifies the measurement method in industrial conditions, which has not been done before. Furthermore, the proposed method is compared to the state-of-the-art method [29].

## 2. Materials and methods

### 2.1. Proposed measurement system

Normally, the geometric characteristics of a convex object can be determined from tangent lines. Considering a camera's central projection model, the tangents are the projection rays of the silhouette points in the image. These silhouettes can be determined using image analysis methods as shown in Fig. 2.

Considering most common cylindrically-shaped forgings, the center position and diameter of an approximately circular cross-section can be determined from three or more tangent lines. A set of these cross-section center positions and diameters along the forging axis approximately forms the cylindrical forging geometry (Fig. 3). Considering that two cameras observe the object from the radial direction, the lowest error can be achieved if the optical axes are perpendicular.

This method is flexible, the forging can be arbitrarily placed in the measurement volume, and the measurement results are not sensitive to the accuracy of the camera mounting positions. The advantage of the flexibility is that the forging is measured while it is held by a forging press manipulator directly on the forging press site. The disadvantage is the assumption of a regular (circular) cross-section. The factors critical to the accuracy of such a system are camera calibration and silhouette

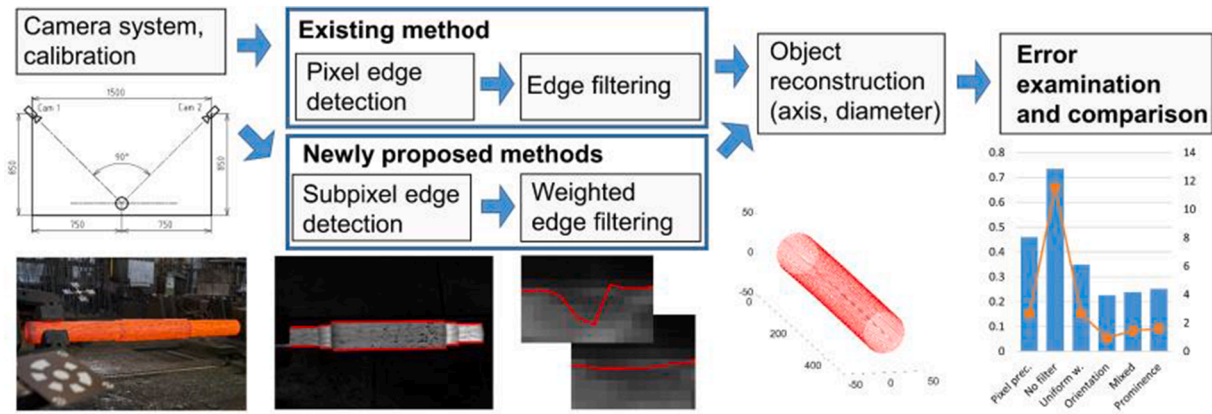


Fig. 1. Workflow of the scientific work.

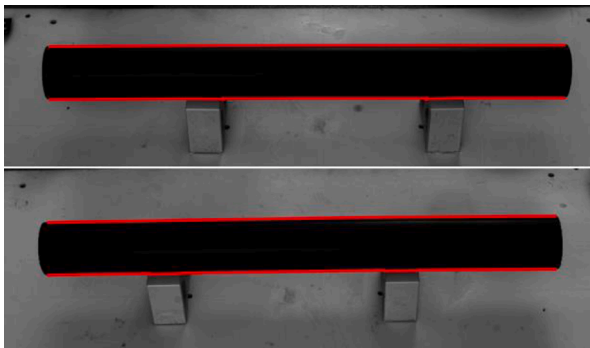


Fig. 2. Detected object silhouettes for tangent ray reconstruction.

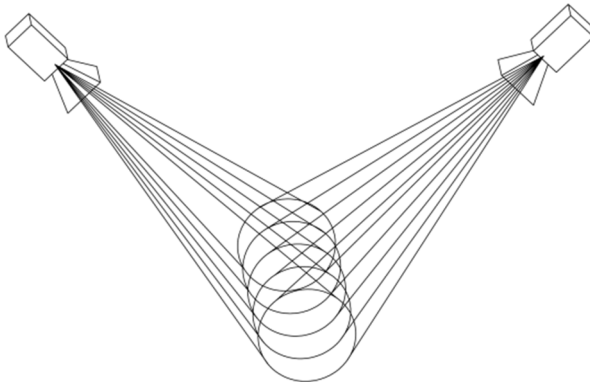


Fig. 3. Measurement system principle – circular cross sections delimited by tangent rays.

calculation. To achieve maximum accuracy, we used high resolution cameras, accurate camera calibration based on spatial resection, and the subpixel edge calculation method.

The measurement system is designed to provide feedback to the forging press operator. A measurement output is demonstrated in Fig. 4.

### 2.2. Robustness to the industrial environment

Robustness of the measurement system method to the interfering effects of the industrial environment is critical. We introduce the negative effects and our implemented countermeasures. These solutions distinguish our measurement system from common 3D pipeline inspection systems. The details of these methods are presented in Section 2.3.

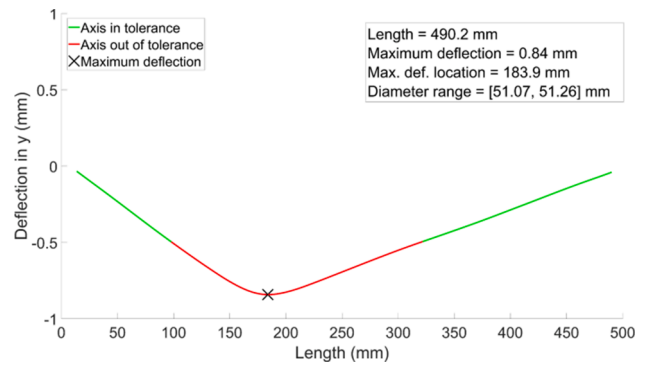


Fig. 4. Output of the forging measurement for subsequent axis straightness correction.

- **Dimensionally and thermally unstable environment:** It is impossible to ensure stable camera positions. Therefore, we used an on-line camera calibration method. Nevertheless, we ensured a stable camera intrinsic geometry.
- **Heat haze, air lens:** To prevent image blurring, we placed the cameras on the sides, relative to the forging. This is to minimize the distance travelled by light rays in the hot atmosphere. Moreover, we used red bandpass optical filters which minimize the refraction.
- **Low object contrast:** A forging emits light mainly in the red spectrum. Therefore, red bandpass optical filters are also advantageous.
- **Edge interferences (scales):** We implemented a robust forging segmentation method and developed a specialized weighted edge filter based on edge quality measures. We assumed that the ideal forging edge gradient has high magnitude, and its direction is approximately perpendicular to the forging axis. By contrast, the gradient of the edge corrupted by scales on the forging surface or false edge has probably lower magnitude and random direction.

### 2.3. Measurement system details

For repeatability, we present the details of the measurement system

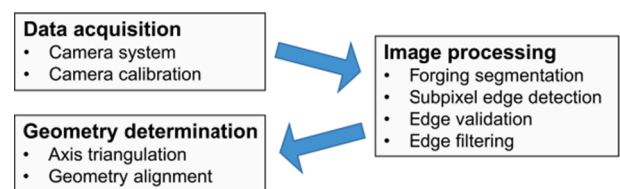


Fig. 5. Measurement system workflow.

sequentially based on the workflow depicted in Fig. 5.

### 2.3.1. Data acquisition

#### Camera system.

The measurement setup includes two cameras, which capture the silhouettes of an object from the radial direction. The camera locations are provided in Fig. 6. In the industrial environment, the cameras are protected against thermal shocks using special thermo-regulated camera covers to ensure their stable intrinsic geometry (Fig. 7 left). These covers are made from stainless steel, and the window is from borosilicate glass. Cooling is performed using a 117 W vortex tube controlled by a temperature sensor. The protected cameras are mounted on supporting constructions of the industrial hall. The difference in the camera locations is because of the environmental arrangement in the forge and is compensated by different focal lengths. The approximate measurement volume is  $6000 \times 6000 \times 2000$  mm. The maximum expected forging length is 4000 mm.

A sample image from the measurement system camera is shown on the right-hand side of Fig. 7, showing the forging held by the press manipulator during the measurement and the calibration targets used for camera calibration.

Sixteen Mpx ZWO ASI 1600 MM/ZWO ASI 1600 MM PRO monochromatic cameras were used in this study. These cameras use a 4/3" CMOS Panasonic MN34230 camera sensor with  $3.8 \mu\text{m}$  pixel size. The cameras are fitted with Zeiss Interlock Compact objectives (both with a 21 mm focal length) during the laboratory experiments. During the experiments in an industrial environment, the camera closer to the forging had a 21 mm (focal length) lens, and the other camera used a 35 mm lens. Considering this case, the cameras were equipped with Schneider-Kreuznach BP 680–100 HT red bandpass filters to ensure high contrast of the forging.

#### Camera calibration

The calibration method is based on spatial resection. The method employs robust calibration targets. This target system implements a widely used circular coded target design, where the bit code is stored in a ring around the target center. In contrast to similar target systems, a bit correction method is implemented. A library of 60 15-bit targets is used. In this setup, the target identification is performed accurately up to 2 bits of code damage. A high accurate star ellipse operator is applied to compute the target centers in the images. The details of the target system are presented in [31].

The calibration method includes two individual steps. First, the intrinsic camera parameters, such as the focal length, physical center of the image, and image distortion parameters (three-parameter radial, tangential, and affine), are calculated only once before the installation of the measurement system. These parameters are calculated based on imaging a dense calibration field. Seven images with different rotations of the camera around its optical axis are used.

The second step of the camera calibration includes single-image calibration of the extrinsic parameters (camera projection center and orientation). This step is performed from every measurement image to compensate for possible small camera movements. Twenty targets placed in the measurement volume on stable positions are used. Their

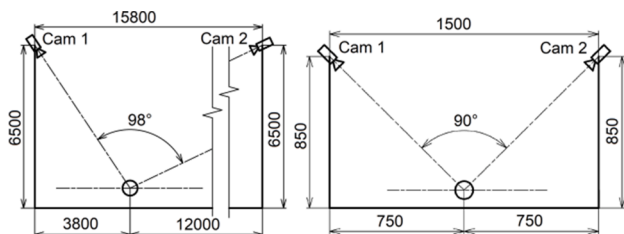


Fig. 6. Camera arrangement; left: industrial environment, right: laboratory environment.

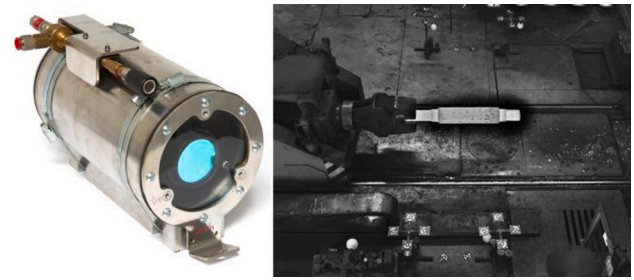


Fig. 7. Left: thermo-regulated camera cover; right: sample image from the measurement system camera. The image has been adjusted.

accurate coordinates are measured during the system installation using the TRITOP (GOM) measurement system. The error of the camera calibration method in the laboratory environment is below 0.1 px. The effect of the hot air surrounding the measured forging increases the error; however, it remains on the order of tenths of pixel. The details of the camera calibration method and its performance in industrial conditions are introduced in [4].

### 2.3.2. Image processing

Further steps are applied to the images from both cameras of the measurement system.

#### Forging segmentation

The forging segmentation method is based on the assumption that the forging is in an approximately horizontal orientation and its approximate diameter in the image is known. This is to build a robust image filter that passes only such objects in the image.

The method (Fig. 8) first downscales the image by half for better computational efficiency (only for segmentation purposes), and the image is smoothed with a  $3 \times 3$ ,  $\sigma = 0.5$  Gaussian kernel to remove image noise. Thereafter, the image is processed with the Sobel edge operator with the resulting image gradient magnitude map **Gmag** and gradient direction map **Gdir**. The magnitude map contains several imprints of false edges. These edges belong to the background or scales on the forging surface. The false edges are usually smaller isolated objects with random orientations and often strong gradient magnitudes. By contrast, true edges are often weak. The subsequent steps are inspired by the Canny edge detector, which is robust because of the dual threshold method.

The dual threshold is used (strong magS and dirS and weak magW and dirW) for both the gradient and direction maps. This results in four binary maps: **GmagS**, **GmagW**, **GdirS**, and **GdirW**. Thereafter, strong and weak maps are created by multiplying the corresponding magnitude and direction map, resulting in the map **GS**, where the nonzero points are pixels with strong magnitudes and are strictly correct orientations. Moreover, equivalently, map **GW** includes pixels with weaker gradient

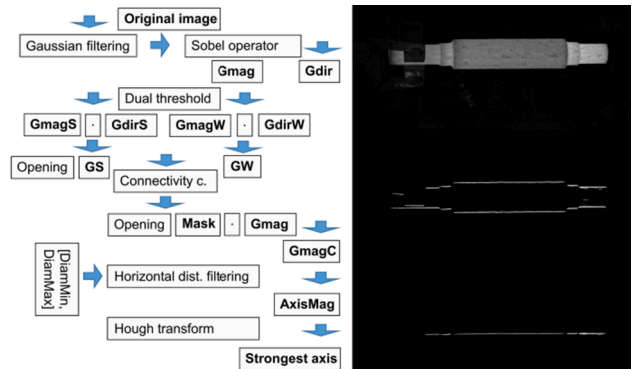


Fig. 8. Segmentation workflow. The images on the right are the original image, clean magnitude map **GmagC**, and axis probability map **AxisMag**, respectively.

magnitudes and less strict orientations. False isolated edges are removed in the strong mask **GS** using a morphological opening with a kernel of rectangular shape along the horizontal direction. Subsequently, **Mask** is assembled based on the connectivity of the nonzero connected regions of **GW** with nonzero elements of **GS**. Nonzero weak elements with no connectivity to the strong elements are erased in this step. Considering this phase, **Mask** still contains the imprints of false isolated edges; therefore, they are removed using morphological opening.

Subsequently, **Gmag** is multiplied by **Mask**, resulting in the clean magnitude map **GmagC**. This cleaned magnitude map still contains false edges in the form of horizontal lines. A filter that passes only nonzero elements of **GmagC** and has a certain horizontal distance [**DiamMin DiamMax**] is built. A new image **AxisMag** is assembled. The filter forms a virtual axis point between each nonzero element of **GmagC**, which has a given distance. The axis probability at that point is the result of the multiplication of the values in **Gmag**. Thereafter, the Hough transform is applied to this image, and the strongest line is considered as the forging axis.

Although the forging segmentation method is fast and robust during the testing, the segmentation method based on neural networks will be implemented after gathering sufficient image data for the training. These methods offer several advantages over the classic methods, considering the robustness [37].

**Subpixel edge detection**

After the rough segmentation, subpixel edge detection is performed. The principle is shown in Fig. 9. The scanning points with 0.5 px spacing are assembled around the expected edge (Fig. 10 top left), and their values are interpolated using the bilinear interpolation. We assume that the potential edge can be at every peak of the first derivative, with a certain minimum width. Accurate edge coordinates are calculated using the “zero-crossing” subpixel edge detection method. This method searches the zero crossing in the second central derivative. To reduce the effect of noise, line fitting is applied to the approximately linear slope of the second derivative, and the zero-crossing of this fitted line is considered as the edge point [38].

**Edge validation and axis computation**

The subpixel edge detection method often finds more edges. The connectivity of the edges is used to filter out the invalid ones. First, the pixel coordinates are divided into regions that have the maximum allowed horizontal gaps and vertical jumps. Only regions with high strengths are considered as valid. If more regions overlap, the stronger region is considered as valid. The axis imprint in the image is then computed as the center of the upper and lower edge points in the vertical direction (Fig. 10 on the right).

**Edge and axis filtering**

It is considered that the validated edges differ in accuracy owing to the contrasting scales on the forging surface near the edge or background objects. It is also possible that a minor number of invalid edges

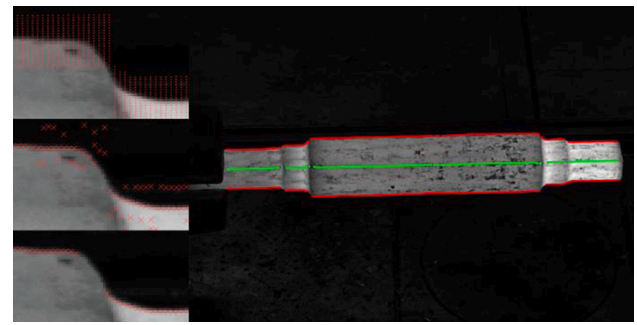


Fig. 10. Left: Edge detection workflow – scanning rays, potential edges, and validated edges; right: Resulting edges and expected axis.

can pass the edge validation algorithm. To reduce the effects of these inaccuracies, a weighted edge filtering method based on the complementary image information is applied. Two characteristics in the accurate edge location are computed using the Sobel kernel (the **gradient direction** relative to axis direction and its **magnitude**). Thereafter, we compute the edge point weights based on these characteristics. The Gaussian function  $w$  is used to compute the weights of both quantities, which are further expressed as  $x$  (Eq. (1)):

$$w(x) = ae^{-\frac{(x-\mu)^2}{2\sigma^2}}; \sigma = \left( -\frac{(E(x) - \mu)^2}{2 \cdot \log\left(\frac{hw}{a}\right)} \right)^{0.5}$$

$$a = 1; hw = 0.5; \mu = \begin{cases} \max(x) & \text{in case of grad. mag.} \\ 90^\circ & \text{in case of grad. dir.} \end{cases} \quad (1)$$

The maximum value of the function was set to 1 ( $a = 1$ ). The width of the peak was set such that the weight of the mean value of the population was 0.5 ( $hw = 0.5$ ), and the center was set to the maximum gradient magnitude, considering the gradient magnitudes. Moreover, it was  $90^\circ$  in the case of gradient directions (perpendicular to the approximate forging axis). An example of Gaussian weighting functions is shown in Figs. 11 and 12.

Three variants of the output were examined.

**Orientation:** Only the direction weight is used.

**Combined:** The mean value of the direction and magnitude weight is used.

**Magnitude:** Only the magnitude weight is used.

Considering the axis imprint, the lower weights of the upper and lower edges are used. The edges and the axis are smoothed using the weighted parabola fitting, which keeps the edge or axis trend on the short section. The filter window length is set to ten for the edge filtering

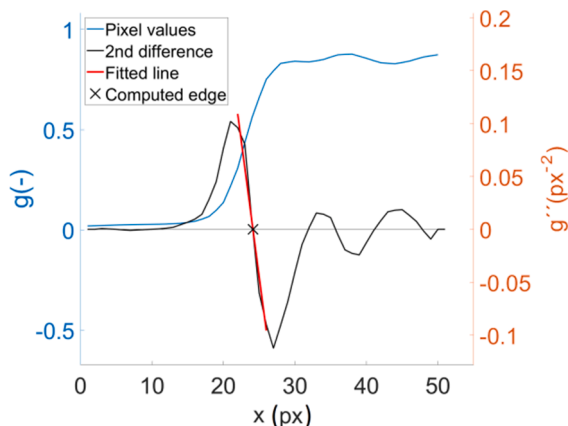


Fig. 9. Zero-crossing subpixel edge detection method.

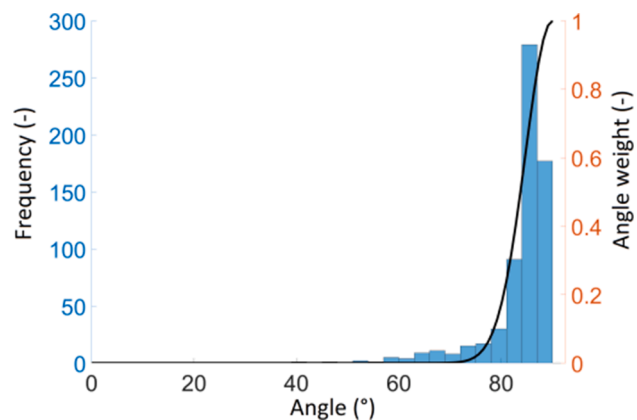


Fig. 11. Sample edge orientation histogram with its weighting function (black line) for subsequent edge filtering.

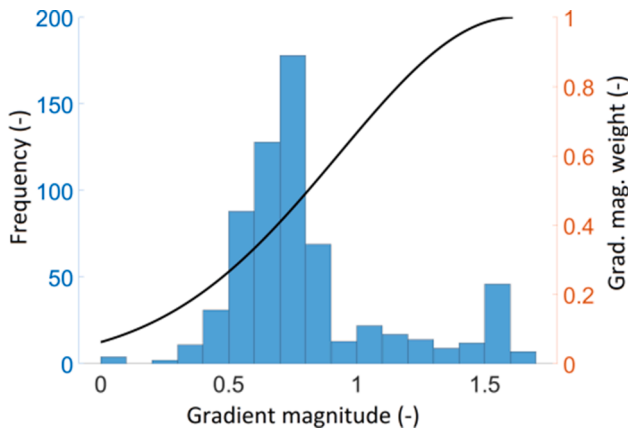


Fig. 12. Sample magnitude histogram with its weighting function (black line) for subsequent edge filtering.

to retain the details of the varying diameter, and the filter window length for axis smoothing is set to 40. The edge filtering comparison is demonstrated in Fig. 13.

### 2.3.3. Geometry determination

#### Geometry reconstruction.

First, the image distortion is compensated to obtain error-free image coordinates of both the axes and edges. The distortion removal method is related to the camera calibration method, and the details are in [4]. The axis is reconstructed based on the triangulation principle (Fig. 14). Using camera intrinsic and extrinsic coordinates, considering every axis point in the image, a ray in the space is reconstructed (Eq. (2)):

$$Y_1 = X_1 + k_1 \cdot \begin{bmatrix} x_{a1} \\ y_{a1} \\ f_1 \end{bmatrix} \cdot R_1; \quad Y_2 = X_2 + k_2 \cdot \begin{bmatrix} x_{a2} \\ y_{a2} \\ f_2 \end{bmatrix} \cdot R_2, \quad k_1, k_2 \in R. \quad (2)$$

where  $X_1$  and  $X_2$  are the projection centers of the cameras, and  $R_1$  and  $R_2$  are the rotation matrices expressing the orientation of the cameras. Moreover, points  $A_1 [x_{a1}; y_{a1}]$  and  $A_2 [x_{a2}; y_{a2}]$  are error-free axis coordinates in the image with the coordinate origin in the physical image center, and  $f_1$  and  $f_2$  are the camera focal lengths in pixels. The axis points are considered as the intersection of the rays. Because the rays do not intersect, the “intersection” is calculated between every two closest rays from the opposite cameras as a center of the skew lines axis (Eq. (3)). The skew line axis is the shortest line section between the skew lines:

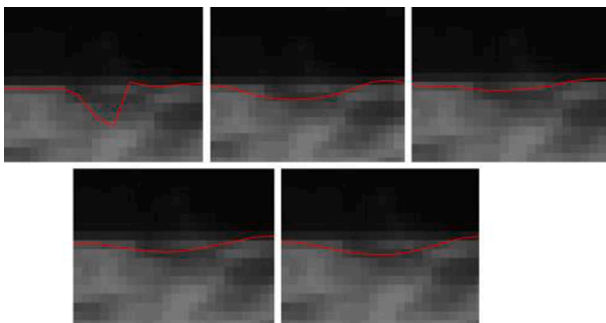


Fig. 13. Impact of edge filtering using different methods on the problematic edge section. From up left: Originally detected edge with no filter applied, smoothing using uniform edge weight, and “Orientation,” “Combined,” and “Magnitude” weighting methods, respectively.

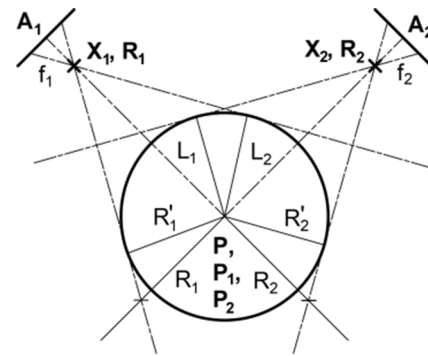


Fig. 14. Cross-section reconstruction diagram.

$$P_1 = X_1 + t_1 \cdot \begin{bmatrix} x_{a1} \\ y_{a1} \\ f_1 \end{bmatrix} \cdot R_1; \quad P_2 = X_2 + t_2 \cdot \begin{bmatrix} x_{a2} \\ y_{a2} \\ f_2 \end{bmatrix} \cdot R_2.$$

$$P = \frac{(P_1 + P_2)}{2}; \quad r = |P_1 - P_2|. \quad (3)$$

Line parameters  $t_1$  and  $t_2$ , which form the closest points  $P_1$  and  $P_2$  on the skew lines, can be computed using the analytic geometry or the ordinary least squares method. The intersection point  $P$  is the center of this line. Parameter  $r$  is the distance between the rays. A threshold for the mutual ray distance  $r$  is set to eliminate the possible inaccurate results. This situation can be caused by missing the axis points in one image, for example, owing to scales.

Considering the simplest case, using the known parameters  $t_1$  and  $t_2$ , the forging edges can be transformed from the image to space using the ray equation equivalent to Eq. (3). The diameters  $R$  are computed as the distances between the edge points and the axis curve. However, the edges spotted by the camera are not at the same distance from the camera as the axis because of the perspective. Therefore, we introduce the corrected radius  $R'$  (Eq. (4)):

$$R' = L \cdot \sin \left( \tan^{-1} \left( \frac{R}{L} \right) \right) \quad (4)$$

The variables are depicted in Fig. 14.

#### Geometry alignment

The forging geometry is arbitrarily placed in the space, and the origin is dependent on camera calibration data. Thereafter, the geometry is rotated; therefore, the ideal axis matches the x-axis of a coordinate system. The ideal axis of the forging is determined as a mutual axis of the short axis sections on both ends of an object. Regarding the laboratory experiments with 500 mm long samples, the axis section was 15 mm long. Nonetheless, considering the experiments in an industrial environment with a 1900 mm long sample, the axis section was 80 mm long. These numbers were assessed based on the holder size during the heavy forging matching procedure. Subsequently, the object is shifted to the origin of the coordinate system (result in Fig. 15).

### 2.4. Experimental design

The experiments were designed to verify the correctness of the proposed methods and to compare them to each other and to the state-of-the-art methods [29] in both the laboratory and industrial environments. Comparatively, we used the following edge detection and filtering method combinations:

- “Pixel precision”: Highest gradient edge detection, Savitzki-Golay/moving average filter. This state-of-the-art [29] method implements edge detection with pixel precision. The pixel with the highest gradient is considered as the edge. This method uses the

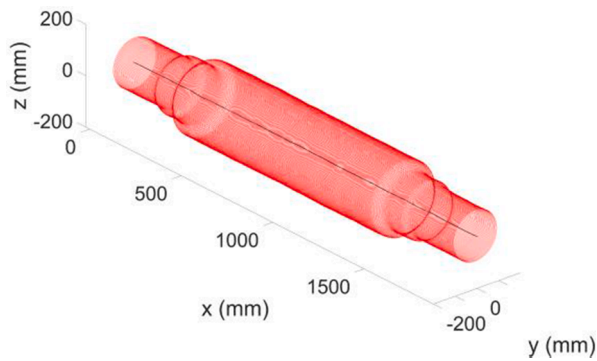


Fig. 15. Reconstructed and aligned forging geometry.

Savitzki-Golay axis filtering method, and it filters the diameter values using the moving average. The sizes of the filter windows were the same as those of the other compared newly proposed methods.

- **“No filter”:** Subpixel edge detection, no filter. This method was implemented to show the significance of data filtering.
- **“Uniform weight”:** Subpixel edge detection, filter with uniform edge weight. This method was implemented to verify whether the proposed edge quality measures are useful to obtain better accuracy than using the uniform edge weight.
- **“Orientation”:** Subpixel edge detection, filter with edge weights based on their gradient direction.
- **“Combined”:** Subpixel edge detection, filter with edge weights based on both the edge gradient direction and its magnitude.
- **“Magnitude”:** Subpixel edge detection, filter with edge weights based on their magnitude.

Each measurement was evaluated by each examined experimental method, resulting in the axis error, which was computed as the deviation of the axis points from the reference axis in 3D. The diameter measurement error is again computed as the difference of the measured diameters from the reference diameters along the object axis. The results were evaluated using standard statistical methods.

#### 2.4.1. Laboratory experiment

To verify the correctness of the proposed methods, small scale laboratory experiments were conducted. The measured and reference geometries were compared. The measured objects were three steel tubes with a length of 500 mm and a diameter of 50 mm. The tube deflection was approximately 1 mm, which was considered as being proportional to the deflection of the heavy cylindrical forgings. For the purpose of comparison, the conditions were the same as in [29], which included holding the forging in v-prisms. The area where the forging was held by the v-prisms was neglected. More than 20 measurements of each sample were made. The tube was arbitrarily rotated in each measurement to change the viewpoint.

##### Reference geometry

The reference geometry in the laboratory environment was obtained using a GOM ATOS III Triple Scan 8 M optical 3D scanner. This scanner was used in the MV560 configuration (measurement volume  $560 \times 420 \times 420$  mm). The measurement point span was 0.17 mm. Considering the acceptance tests (VDI/VDE 2634), the measurement error is in the thousandth of millimeters.

The scanned geometry was processed, and important data for comparison with the measured data were evaluated using GOM Inspect. The scanned surface was aligned based on two cylinders, which were fit to both ends of the cylinder. The height of each cylinder was set to 15 mm. The mutual axis of these two cylinders was considered as the ideal axis. The origin was placed on one end of the forging. The results of the alignment are provided in Fig. 16. This method is considered as being

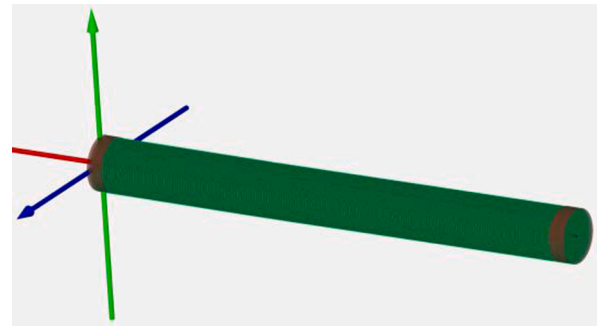


Fig. 16. Reference object geometry aligned using the red fitted cylinders on both ends.

equivalent to the alignment method used during the proposed measurement. A cross-section was made every 2 mm, and a circle was fitted to the cross-section geometry using the best-fit method. The reference geometry was the axis coordinates and the diameters of the fitted circles in the cross-sections. Subsequently, both the measured and reference geometries were arbitrarily rotated around the ideal axis. For comparison, the resulting axis of each measurement was rotated around the ideal axis to match the reference using the least squares method.

#### 2.4.2. Experiment in the industrial environment

A single 1900 mm hot (approximately 1000 °C) forging with a maximum diameter of approximately 300 mm was repeatedly measured. The measurement was performed directly after the forging manufacturing operation on the forging press site. During the measurement, the forging was held by the forging press manipulator. The manipulator works with positioning accuracy in millimeters or degrees.

The measurement consisted of two parts. First, the measurement was conducted ten times to verify the repeatability of the measurement system. The forging was not rotated around its axis between the measurements to eliminate the effect of the circularity deviation. This could affect both the axis and diameter measurements. Second, the forging was measured 12 times with different rotations around its axis. The forging in the subsequent measurements was rotated around its axis by 30°. This experiment was conducted to examine whether the forging geometry can be accurately determined using a single measurement. The entire procedure was performed in less than 2 min.

##### Reference geometry

In this experiment, a direct reference geometry is impossible to obtain because of the lack of an accurate measurement method capable of measuring hot heavy forgings. Instead of comparing the measurement results with the reference geometry, we examined the repeatability of the measurement. The mean axis from the measurements in both experimental parts was used as a reference. Considering the forging measurement with rotation around its axis, the different forging rotations between the measurements were compensated based on the known rotation angle.

### 3. Results and discussion

Using the described methods, we conducted laboratory experiments and experiments in an industrial environment (on-site). We assume a Gaussian distribution of the errors; therefore, we examined the parameters of this distribution, including the mean and sigma. We also investigated the medians and maximum errors. Considering the measurement of the three samples in the laboratory, we assumed that the error is equivalent to different samples. Therefore, we summarize the results to one set, which represents all the measurements of all samples. The characteristics of the experiments are summarized in Table 1.

**Table 1**  
Measurement characteristics.

	Laboratory	On-site
Measurement volume	0.8 × 0.8 × 0.3 m	6 × 6 × 2 m
Pixel resolution	0.17 mm	1.29 mm
Num. of measurements	21 + 22 + 26	10 + 12

3.1. Laboratory experiments

In this section, we introduce and discuss the measurement results obtained in the laboratory environment. Moreover, Figs. 17 and 18 display the measured geometry of one of the three dimensionally tested steel rods. Furthermore, Table 2, Table 3, and Fig. 19 display the characteristics of the measurement error.

The first finding is that when using the subpixel edge detection method, the measurement error significantly decreased. The measured axis geometry error in the laboratory environment decreased by approximately 50%. Sigma decreased from 0.05 to 0.025 mm, and the median error decreased from 0.04 to 0.02 mm (Table 2). Considering the diameter measurement, sigma decreased from 0.06 to 0.04, and the median error was approximately the same (0.06 – 0.07 mm in both cases, Table 3). These results show the 30% improvement in measurement repeatability using the subpixel method. However, the non-negligible systematic error seems to be present owing to the equality of the median and median absolute error. This error is the result of comparing the results with the reference values obtained using the “best-fit” method of circles fitting the cross sections of the reference geometry. The measurement principle using the tangent lines matches the more likely (theoretically) “minimum circumscribed” method. The difference between these methods is shown in Fig. 18 and is caused by the imperfect circularity of the measured samples. The measured values using the proposed methods mostly fluctuate between the reference values obtained using these two methods owing to imperfect circularity of the sample.

Another finding is that data filtering (smoothing) in the laboratory environment, where no significant noise or edge disturbances are present, is not needed. This finding is supported by the fact that the error characteristics, with or without filtering (even weighted), are similar.

To summarize the findings, direct comparisons show that the newly proposed methods were more accurate than the state-of-the-art methods in the laboratory environment [29]. Considering the reason described above, no significant systematic error was recorded. Therefore, the newly proposed methods are considered as valid. Considering the axis measurement, the achieved median error was under ±0.02, and the 95% confidence interval of the result was approximately ±0.05 mm. Regarding the diameter measurement, the median error was ±0.06 mm. This included the “systematic” part of the error, and the 95% confidence

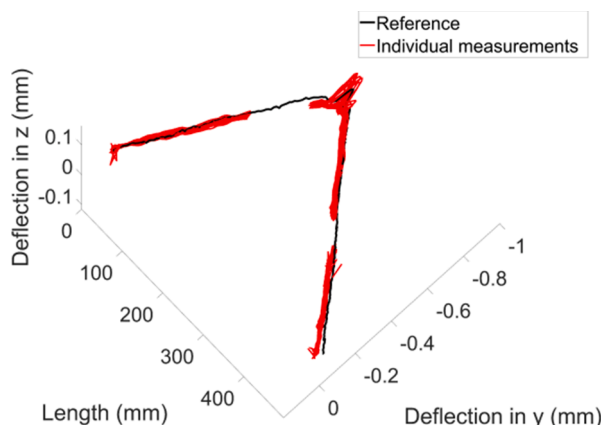


Fig. 17. Measured and reference object axis geometry.

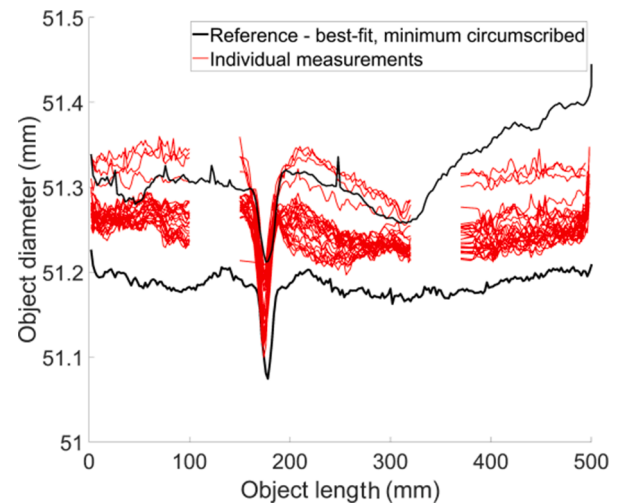


Fig. 18. Measured and reference object diameters.

interval of the result was approx. ±0.08 mm.

3.2. Experiments in an industrial environment

In this section, we introduce and discuss the measurement results obtained in the industrial environment. Figs. 20 and 21 demonstrate the measured geometry of the specimen. Moreover, Table 4, Table 5, and Fig. 22 show the measurement method error characteristics in an industrial environment with no rotation around the forging axis.

The measurements in the industrial environment also confirm the advantage of implementing the subpixel edge detection method. This can be observed from the median error in both the axis geometry and diameter measurements (Table 4 and 5). The median error decreased by 50% for the axis measurement and by 35% for the diameter measurement (decreases from 0.30 to 0.15 mm and from 0.22 to 0.14 mm, respectively), compared with pixel edge detection. These values approximately match the accuracy improvement in the laboratory conditions.

Contrary to the laboratory environment, the sigma error is heavily influenced by strong edge disturbances. Therefore, edge filtering (smoothing) is necessary. The edge filter helps to decrease both the maximum and sigma repeatability errors, especially considering the axis geometry measurements (Fig. 22). Considering this case, the filter with a uniform weight helps to reduce the sigma by 53%, and the maximum error is reduced by 77% (from 0.74 to 0.35 mm and from 11.54 to 2.67 mm, respectively). Considering the diameter measurement, the decrease was insignificant. Sigma decreased by 7%, and the maximum error decreased by 15% (from 0.69 to 0.64 mm and from 20.24 to 17.03 mm, respectively). This is because the diameter of the measured sample rapidly changes along the forging axis (Fig. 21).

Based on the results of the axis geometry measurement, it is apparent that complementary image information for weighted filtering is effective for obtaining significantly more accurate results. Filtering using all the three proposed weighting methods (“orientation,” “combined,” and “magnitude”) perform better than the method that uses uniform weight. The weighting method based on the edge orientation performed the best. Compared with the uniform weight filtering method, this method achieved a 34% lower sigma and a 64% lower maximum error (from 0.35 to 0.23 mm and from 2.67 to 0.96 mm, respectively). The obtained results surpass the state-of-the-art method by 50% for the sigma and by 64% for the maximum error (from 0.46 to 0.23 mm and from 2.66 to 0.96 mm, respectively). However, regarding the diameter measurements, the “magnitude” and “combined” methods performed better than “orientation”. The improvement against the uniform weight was not as significant as in the case of axis geometry measurement. Considering the

**Table 2**  
Axis error characteristics during the laboratory measurement.

Error	Pixel prec.	No filter	Uniform w.	Orientation	Combined	Magnitude
Max. (mm)	0.2908	0.2393	0.2398	0.2398	0.2401	0.2402
Median (mm)	0.0374	0.0189	0.0185	0.0185	0.0185	0.0185
Sigma (mm)	0.0469	0.0250	0.0247	0.0246	0.0247	0.0247
Sigma eq. (px)	0.2758	0.1472	0.1453	0.1449	0.1450	0.1452

**Table 3**  
Diameter error characteristics during the laboratory measurement.

Error	Pixel prec.	No filter	Uniform w.	Orientation	Combined	Magnitude
Range (mm)	0.3797	0.3286	0.3312	0.3283	0.3296	0.3310
Median (mm)	0.0664	0.0624	0.0623	0.0621	0.0623	0.0623
Median abs. (mm)	0.0670	0.0625	0.0624	0.0621	0.0623	0.0624
Sigma (mm)	0.0569	0.0411	0.0410	0.0411	0.0410	0.0410
Sigma eq. (px)	0.3347	0.2420	0.2414	0.2415	0.2414	0.2414

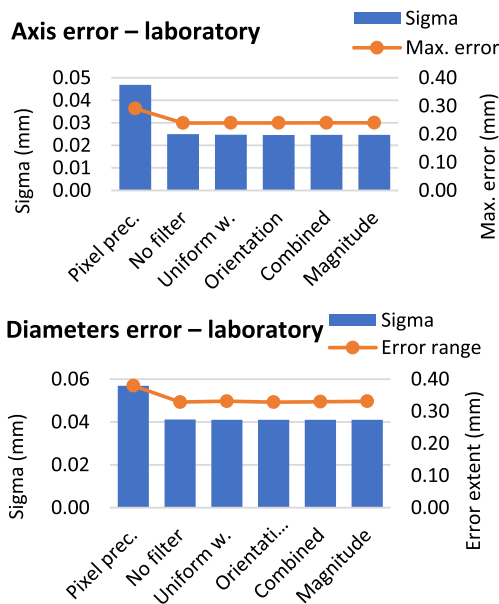


**Fig. 19.** Measurement error characteristics in the laboratory environment.

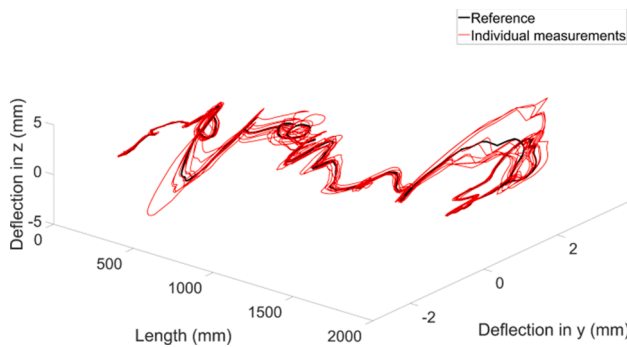


**Fig. 20.** Axis measurement in the industrial environment with no rotation around the forging axis.

“magnitude” method, the sigma and maximum error are both lower by 11% (from 0.64 to 0.57 mm and from 17.03 to 15.12 mm, respectively). These values are comparable with the “state-of-the-art” method, which even reaches a lower maximum error despite the higher median error. These results may be caused by the rapidly changing diameter along the forging axis. It may also be because the “state-of-the-art” method uses a

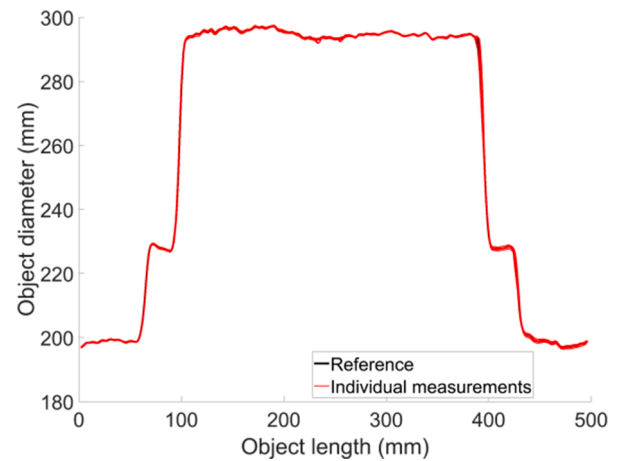


**Fig. 21.** Diameter measurement in the industrial environment with no rotation around the forging axis.

stronger filter (moving average against the weighted parabola fitting). Using the pixel equivalents, the relative system accuracy in the laboratory and industrial conditions can be compared without the effect of the irregular forging cross-section, considering the industrial environment. Considering the axis geometry measurement, the pixel equivalent of the sigma was comparable (0.15 vs. 0.18 px). The achieved median error was  $\pm 0.12$  mm, and the 95% confidence interval of the result was  $\pm 0.5$  mm. Regarding the diameter measurement, the resulting sigma was significantly larger; however, it was still less than  $2 \times$  (0.24 vs. 0.44 px). This error was caused by the rapidly changing forging diameter along its axis. The achieved median error was  $\pm 0.14$  mm, and the 95% confidence interval of the result was approximately  $\pm 1$  mm.

**3.2.1. Experiments with forging rotation around its axis**

In this section, we introduce and discuss the measurement results obtained when the forging was rotated around its axis between the individual measurements. Specifically, Table 6, Table 7, and Fig. 23 display the measurement method error characteristics.

In the case of forging measurement in industrial conditions with rotation around its axis, the irregularity of cross-sections strongly influenced the results. It is shown mainly in the case of diameter measurement (Fig. 23 and Table 7). The irregularities were larger than the measurement resolution. Therefore, the performances of all the methods in all the indicators were similar, excluding the slightly worse results obtained without the use of any edge filter.

Regarding the axis measurement, the effect of the irregular cross-section geometry resulted in a similar median error for all the

**Table 4**  
Axis error characteristics during on-site measurement with no rotation around the forging axis.

Error	Pixel prec.	No filter	Uniform w.	Orientation	Combined	Magnitude
Max. (mm)	2.6592	11.543	2.6701	0.9572	1.4623	1.6195
Median (mm)	0.2961	0.1453	0.1362	0.1220	0.1227	0.1257
Sigma (mm)	0.4609	0.7352	0.3492	0.2267	0.2386	0.2526
Sigma eq. (px)	0.3573	0.5699	0.2707	0.1757	0.1849	0.1958

**Table 5**  
Diameter error characteristics during on-site measurement with no rotation around the forging axis.

Error	Pixel prec.	No filter	Uniform w.	Orientation	Combined	Magnitude
Range (mm)	11.007	20.237	17.026	21.392	14.956	15.122
Median abs. (mm)	0.2249	0.1435	0.1373	0.1370	0.1370	0.1367
Sigma (mm)	0.5751	0.6932	0.6359	0.7865	0.5926	0.5726
Sigma eq. (px)	0.4458	0.5373	0.4929	0.6097	0.4594	0.4439

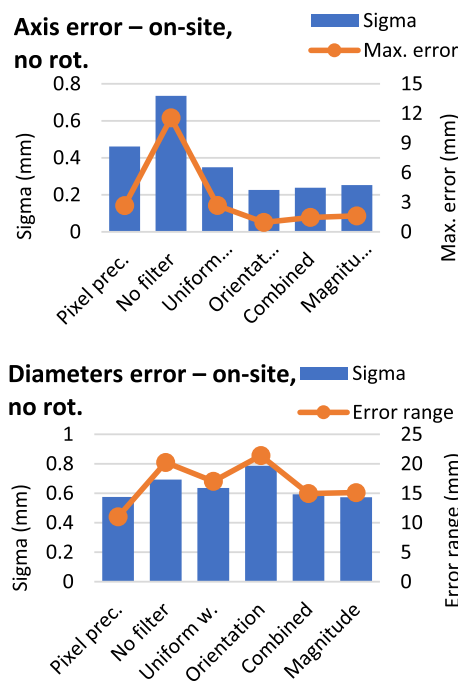


**Fig. 22.** Measurement method error characteristics in an industrial environment with no rotation around the forging axis.

**Table 6**  
Axis error characteristics during on-site measurement with rotation around the forging axis.

Error	Pixel prec.	No filter	Uniform w.	Orientation	Combined	Magnitude
Max. (mm)	5.0916	14.163	6.2614	2.4261	3.1901	4.0884
Median (mm)	0.6863	0.7267	0.6728	0.6203	0.6403	0.6593
Sigma (mm)	1.1052	1.6005	1.1449	0.8105	0.8825	0.9751
Sigma eq. (px)	0.8568	1.2407	0.8875	0.6283	0.6841	0.7559

**Table 7**  
Diameter error characteristics during the on-site measurement with rotation around the forging axis.

Error	Pixel prec.	No filter	Uniform w.	Orientation	Combined	Magnitude
Range (mm)	26.378	35.312	28.482	26.107	26.244	26.157
Median abs. (mm)	0.9579	0.9787	0.9626	0.9572	0.9550	0.9612
Sigma (mm)	1.7038	1.8031	1.7236	1.7359	1.7074	1.7087
Sigma eq. (px)	1.3208	1.3977	1.3361	1.3457	1.3236	1.3245

methods (Table 6). However, the results show the same trends, similar to the forging measurement without rotation around its axis. Filtering helps to significantly reduce the measurement error by 29% in the case of sigma and by 56% in the case of error ranges (from 1.60 to 1.14 and from 14.16 to 6.26, respectively). Moreover, the proposed weighted edge filtering methods offer an improved accuracy over a uniform weight filter. The best performing method was again the “orientation” method. It helped to lower the sigma by 29% and the maximum error by 61% (from 1.14 to 0.81 mm and from 6.26 to 2.43 mm, respectively). Therefore, the weights help to suppress irrelevant parts of the forging to achieve better repeatability, even in the case of forgings with poor circularity.

Overall, the axis deflection trend is measurable using the proposed “orientation” method. Moreover, considering the measurement volume, the results of a  $\pm 0.6$  mm median error and  $\pm 1.6$  mm 95% confidence interval of the results are acceptable. The diameters were measured with a  $\pm 1$  mm median error and a  $\pm 3.4$  mm 95% confidence interval of the results. The repeatability error increased by approximately 3 $\times$ , compared with the measurement without forging rotation. However, more measurements from different angles could be combined to gather more information about the cross-sections.

### 3.3. Future studies

Although the developed weighted filtering methods helped to achieve better repeatability even despite insufficient forging circularity, the error in this case increased approximately three times. This indicates that complete geometry, including circularity, cannot be measured using only one measurement with two cameras (four silhouettes). More information about forging cross-sections is needed. Therefore, a future

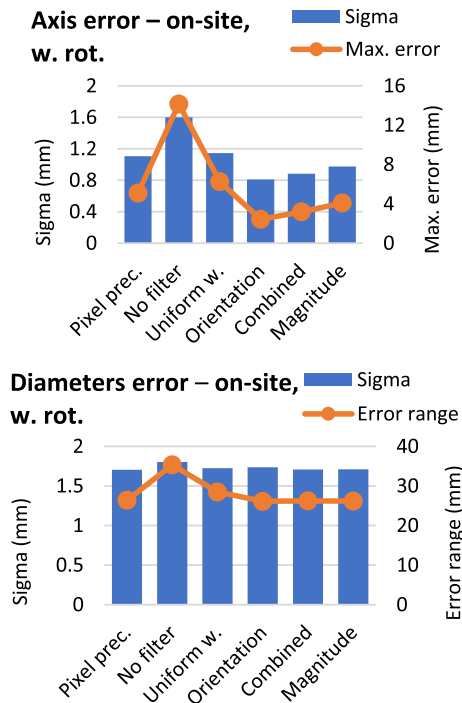


Fig. 23. Measurement method error characteristics in an industrial environment with rotation around the forging axis.

study can include the development of an assembly method for more measurements with different forging rotations around the forging axis. Consequently, it may be possible to extend the measurable shapes to rods of different convex cross-sections (e.g., square or rectangular). Instead, we plan to focus on further tuning the methods: evaluating the effect of the edge contrast on the edge detection method reliability and accuracy, the influence of bandpass color filters on the forging contrast, verifying the repeatability on larger datasets, and implementing the segmentation or edge validation methods based on neural networks when large datasets are available.

#### 4. Conclusion

In this study, a new forging measurement method using silhouettes in images was developed. The proposed method was verified through more than 90 measurements in laboratory and industrial environments. We made the following major observations.

- The implementation of subpixel edge detection method contributes to the accuracy of silhouettes measurement. This method lowers the median error during measurements in laboratory and industrial conditions by approximately 50%.
- Weighted filtering based on complementary information about the silhouette quality from the image can be used to suppress the inaccurately detected forging edges in industrial environment. Edge gradient direction weights lower the axis measurement sigma error by approximately 30%.
- The accuracy and reliability of the measurement system is not critically influenced by the negative effect of industrial environment. The 95% confidence interval was  $\pm 0.5$  mm and  $\pm 1$  mm for the forging axis and diameter measurements, respectively, in a measurement volume of  $6 \times 6 \times 2$  m.
- The proposed measurement system surpasses the state-of-the-art method mainly in terms of axis-straightness measurement. Without considering forging cross-section irregularities, the performance was better by 50%, considering the sigma error.

- The assumption of regular forging cross-sections was the weak point of the proposed measurement system. Therefore, the repeatability error of the measurement increased by approximately three times. However, we suggest a solution to suppress this effect as a future research direction.

Generally, the proposed measurement system can be applied to the forging manufacturing process. The measurement can provide feedback to the press operator, or in the future, it can become a part of the automated Industry 4.0 forging complex.

#### CRedit authorship contribution statement

**Jakub Hurník:** Conceptualization, Methodology, Software, Validation, Formal analysis, Writing – original draft, Writing – review & editing, Visualization. **Aneta Zatočilová:** Investigation, Resources, Data curation, Project administration, Funding acquisition. **Daniel Koutný:** Supervision, Funding acquisition, Writing – review & editing. **David Paloušek:** Supervision, Funding acquisition.

#### Declaration of Competing Interest

The authors declare that they have no known competing financial interests or personal relationships that could have appeared to influence the work reported in this paper.

#### Acknowledgments

This research has received funding from the Technology Agency of Czech Republic project TREND FW01010098, and Faculty of Mechanical Engineering, Brno University of Technology internal specific project FSI-S-20–6296. We would like to thank Editage ([www.editage.com](http://www.editage.com)) for English language editing. We also acknowledge ZDAS company for allowing the research team to conduct the experiment in their factory.

#### References

- [1] M. Hawryluk, J. Ziemba, P. Sadowski, A review of current and new measurement techniques used in hot die forging processes, *Meas. Control.* 50 (2017) 74–86, <https://doi.org/10.1177/0020294017707161>.
- [2] M. Hawryluk, J. Ziemba, Possibilities of application measurement techniques in hot die forging processes, *Measurement* 110 (2017) 284–295, <https://doi.org/10.1016/j.measurement.2017.07.003>.
- [3] A. Ghiotti, A. Schöch, A. Salvadori, S. Carmignato, E. Savio, Enhancing the accuracy of high-speed laser triangulation measurement of freeform parts at elevated temperature, *CIRP Ann. Manuf. Technol.* 64 (2015) 499–502, <https://doi.org/10.1016/j.cirp.2015.04.012>.
- [4] J. Hurník, A. Zatočilová, D. Paloušek, Camera calibration method of optical system for large field measurement of hot forgings in heavy industry, in: *Opt. Meas. Syst. Ind. Inspect. XI, Proc. SPIE*, 2019, p. 11056, <https://doi.org/10.1117/12.2527693>.
- [5] P.E. Ciddor, Refractive index of air: New equations for the visible and near infrared, *Appl. Opt.* 35 (1996) 1566–1573, <https://doi.org/10.1364/AO.35.001566>.
- [6] M. Yamauchi, Errors in optical shape measurement caused by a high-temperature atmosphere, *Opt. Eng.* 48 (2009) 4, <https://doi.org/10.1117/1.3212674>.
- [7] R. Beermann, L. Quentin, G. Stein, E. Reithmeier, M. Kästner, Full simulation model for laser triangulation measurement in an inhomogeneous refractive index field, *Opt. Eng.* 57 (2018) 1, <https://doi.org/10.1117/1.OE.57.11.114107>.
- [8] S.B. Dworkin, T.J. Nye, Image processing for machine vision measurement of hot formed parts, *J. Mater. Process. Technol.* 174 (2006) 1–6, <https://doi.org/10.1016/j.jmatprotec.2004.10.019>.
- [9] C.H. Hu, B. Liu, X.X. Song, A novel edge detection approach used for online dimensional measurement of heavy forging, in: S. Ye, G. Zhang, J. Ni (Eds.), *Proc. SPIE Vol. 7160 (2009) International Conference on Optical Instruments and Technology: Optoelectronic Measurement Technology and Applications 2008*, n.d., <https://doi.org/10.1117/12.807046>.
- [10] Y. Zhang, Y. Wang, Y. Liu, D. Lv, X. Fu, Y. Zhang, J. Li, A concentricity measurement method for large forgings based on laser ranging principle, *Measurement* 147 (2019), 106838, <https://doi.org/10.1016/j.measurement.2019.07.066>.
- [11] Z.C. Du, Z.Y. Wu, J.G. Yang, 3D measuring and segmentation method for hot heavy forging, *Measurement* 85 (2016) 43–53, <https://doi.org/10.1016/j.measurement.2016.02.004>.

- [12] X. Fu, Y. Zhang, K. Tao, S. Li, The outer diameter detection and experiment of the circular forging using laser scanner, *Optik* 128 (2017) 281–291, <https://doi.org/10.1016/j.ijleo.2016.09.118>.
- [13] Z.S. Tian, F. Gao, L.Z. Jin, X.C. Zhao, Dimension measurement of hot large forgings with a novel time-of-flight system, *Int. J. Adv. Manuf. Technol.* 44 (2009) 125–132, <https://doi.org/10.1007/s00170-008-1807-8>.
- [14] Y.C. Zhang, J.X. Han, X.B. Fu, F.L. Zhang, Measurement and control technology of the size for large hot forgings, *Measurement* 49 (2014) 52–59, <https://doi.org/10.1016/j.measurement.2013.11.028>.
- [15] D. Bračun, G. Škulj, M. Kadiš, Spectral selective and difference imaging laser triangulation measurement system for on line measurement of large hot workpieces in precision open die forging, *Int. J. Adv. Manuf. Technol.* 90 (2017) 917–926, <https://doi.org/10.1007/s00170-016-9460-0>.
- [16] Y.C. Zhang, C. Luo, X.B. Fu, Y.M. Chen, Automatic measurement method for the size of large forgings based on scattering on rough surface, *IET Sci. Meas. Technol.* 11 (2017) 118–124, <https://doi.org/10.1049/iet-smt.2016.0283>.
- [17] D. Mejia-Parra, J.R.J.R. Sánchez, O. Ruiz-Salguero, M. Alonso, A. Izaguirre, E. Gil, J. Palomar, J. Posada, In-line dimensional inspection of warm-die forged revolution workpieces using 3D mesh reconstruction, *Appl. Sci.* 9 (2019) 1–21, <https://doi.org/10.3390/app9061069>.
- [18] W. Liu, X.H. Jia, Z.Y. Jia, S.J. Liu, B.G. Wang, J.A. Du, Fast dimensional measurement method and experiment of the forgings under high temperature, *J. Mater. Process. Technol.* 211 (2011) 237–244, <https://doi.org/10.1016/j.jmatprotec.2010.09.015>.
- [19] B. Wang, W. Liu, Z. Jia, X. Lu, Y. Sun, Dimensional measurement of hot, large forgings with stereo vision structured light system, *Proc. Inst. Mech. Eng.* 225 (2011) 901–908, <https://doi.org/10.1177/2041297510393513>.
- [20] W. Liu, Z.Y. Jia, F.J. Wang, X. Ma, W.Q. Wang, X.H. Jia, D. Song, An improved online dimensional measurement method of large hot cylindrical forging, *Measurement* 45 (2012) 2041–2051, <https://doi.org/10.1016/j.measurement.2012.05.004>.
- [21] Z.Y. Jia, Y. Liu, W. Liu, C. Zhang, J.H. Yang, L.L. Wang, K. Zhao, A spectrum selection method based on SNR for the machine vision measurement of large hot forgings, *Optik* 126 (2015) 5527–5533, <https://doi.org/10.1016/j.ijleo.2015.09.110>.
- [22] Z.Y. Jia, L.L. Wang, W. Liu, J.H. Yang, Y. Liu, C.N. Fan, K. Zhao, A field measurement method for large objects based on a multi-view stereo vision system, *Sens. Actuators, A* 234 (2015) 120–132, <https://doi.org/10.1016/j.sna.2015.08.024>.
- [23] Y. Liu, Z.Y. Jia, W. Liu, L.L. Wang, C.N. Fan, P.T. Xu, J.H. Yang, K. Zhao, An improved image acquisition method for measuring hot forgings using machine vision, *Sens. Actuators, A* 238 (2016) 369–378, <https://doi.org/10.1016/j.sna.2015.11.035>.
- [24] J. Yang, W. Liu, R. Zhang, Z. Jia, F. Wang, S. Li, A method for measuring the thermal geometric parameters of large hot rectangular forgings based on projection feature lines, *Mach. Vis. Appl.* 29 (2018) 467–476, <https://doi.org/10.1007/s00138-017-0900-0>.
- [25] B.i. Chao, Q.u. Xinghua, L. Yong, L. Yaping, L. Jingliang, Dimensional Measurement of Small Hot Pieces Based on a Monochrome CCD, *Procedia Eng.* 99 (2015) 1158–1163.
- [26] C. Bi, J.G. Fang, D. Li, X.H. Qu, Study on application of color filters in vision system of hot forgings, in: S. Han, J. Tan (Eds.), *Optical Measurement Technology and Instrumentation*, Proc. SPIE Vol. 10155, 2016. <https://doi.org/10.1117/1.2.2246795>.
- [27] A. Zatočilová, R. Poliščuk, D. Paloušek, J. Brandejs, Photogrammetry based system for the measurement of cylindrical forgings axis straightness, in: Proc. SPIE Vol. 8788. *Spie-Int Soc Optical Engineering Conference on Optical Measurement Systems for Industrial Inspection VIII*, Bellingham, 2013. <https://doi.org/10.1117/12.2020917>.
- [28] A. Zatočilová, D. Paloušek, J. Brandejs, Development of a photogrammetry system for the measurement of rotationally symmetric forgings, in: Proc. SPIE Vol. 9525. *Spie-Int Soc Optical Engineering Conference on Optical Measurement Systems for Industrial Inspection IX*, Bellingham, 2015. <https://doi.org/10.1117/12.2184916>.
- [29] A. Zatočilová, D. Paloušek, J. Brandejs, Image-based measurement of the dimensions and of the axis straightness of hot forgings, *Measurement* 94 (2016) 254–264, <https://doi.org/10.1016/j.measurement.2016.07.066>.
- [30] Y. Zhou, Y. Wu, C. Luo, A fast dimensional measurement method for large hot forgings based on line reconstruction, *Int. J. Adv. Manuf. Technol.* 99 (2018) 1713–1724, <https://doi.org/10.1007/s00170-018-2551-3>.
- [31] J. Hurník, A. Zatočilová, D. Paloušek, Circular coded target system for industrial applications, *Mach. Vis. Appl.* 32 (2021) 1–14, <https://doi.org/10.1007/s00138-020-01159-1>.
- [32] J. Canny, A computational approach to edge detection, *IEEE Trans. on Pattern Anal. Mach. Intell.* 8 (1986) 679–698, <https://doi.org/10.1109/tpami.1986.4767851>.
- [33] P. Wang, Y. Lin, R. Muroiwa, S. Pike, L. Mihaylova, A weighted variance approach for uncertainty quantification in high quality steel rolling, in: Proc. 2020 23rd Int. Conf. Inf. Fusion, Fusion 2020. (2020). <https://doi.org/10.23919/FUSION45008.2020.9190527>.
- [34] P. Jin, J. Liu, S. Liu, X. Wang, A new multi-vision-based reconstruction algorithm for tube inspection, *Int. J. Adv. Manuf. Technol.* 93 (2017) 2021–2035, <https://doi.org/10.1007/s00170-017-0664-8>.
- [35] T. Zhang, J. Liu, S. Liu, C. Tang, P. Jin, A 3D reconstruction method for pipeline inspection based on multi-vision, *Measurement* 98 (2017) 35–48, <https://doi.org/10.1016/j.measurement.2016.11.004>.
- [36] J. Hu, S. Liu, J. Liu, Z. Wang, H. Huang, Pipe pose estimation based on machine vision, *Measurement* 182 (2021), 109585, <https://doi.org/10.1016/j.measurement.2021.109585>.
- [37] L. Liu, W. Ouyang, X. Wang, P. Fieguth, J. Chen, X. Liu, M. Pietikäinen, Deep learning for generic object detection: A survey, *Int. J. Comput. Vis.* 128 (2020) 261–318, <https://doi.org/10.1007/s11263-019-01247-4>.
- [38] T. Luhmann, S. Robson, S. Kyle, I. Harley, *Close Range Photogrammetry*, Whittles Publishing, Scotland, UK, 2011.



# Multi-view camera system for measurement of heavy forgings

Jakub Hurník<sup>1</sup> · Aneta Zatočilová<sup>1</sup> · Tereza Konečná<sup>1</sup> · Pavel Štarha<sup>1</sup> · Daniel Koutný<sup>1</sup>

Received: 4 March 2022 / Accepted: 18 July 2022

© The Author(s), under exclusive licence to Springer-Verlag London Ltd., part of Springer Nature 2022

## Abstract

Open-die forging is used to manufacture heavy durable parts such as shafts. In-process measurements are required for shape correction. The passive 3D measurement method is based on forging silhouettes in images and has demonstrated its advantages in this application. However, when using two cameras, only four tangents are available to determine the cross-section. In this paper, we propose a novel multi-camera multi-observation method for forging measurements; it increases the number of tangent lines used to determine the forging cross-section. The results suggest a decrease in measurement error proportional to the square root of the observation number. The six-observation precision is  $\pm 0.5$  mm in a measurement volume of  $6 \times 6 \times 2$  m for axis straightness and diameter measurements (95% confidence interval). However, many outliers remain in case of diameter measurement. In addition, the forging circularity can be measured. The proposed system shows good agreement with the laser scanning measurement method. Overall, the system has considerable potential for forging manufacturing applications.

**Keywords** Axis · Diameter · Edge detection · Forging · Measurement · Laser scanner · Silhouettes

## 1 Introduction

Obtaining forging measurements (during fabrication from a glowing hot piece of steel in an open-die forging press) represents a challenge. The dimensions of the forgings and their shape characteristics are used for final corrections directly after forging, or, in the future, to control the forging process [1]. However, common optical measurement systems are unsuitable in this application because of the large dimensions of the forgings (on the order of meters), their high temperatures (up to 1200 °C), and the challenging environments of heavy industry in general. Heat haze and air lens around the forging also affect the measurement, causing potential measurement errors of the order of tenths of percent [2, 3]. Therefore, primitive contact-measurement methods remain in use [4, 5].

In the literature, several optical methods have been used for forging geometry measurements [6]. The laser scanning measurement method can be applied in the desired

measurement volumes and is not significantly affected by the negative effects of the heavy industry environment [7–9]. The disadvantages include the long scanning times and the high prices of the sensors. However, this measurement principle has been applied in commercial applications, including systems such as the LaCam® Forge developed by Ferrotron. Other approaches are based on active photogrammetry. Using these methods (e.g., line scanners [10–13], fringe projection systems [14, 15], structured-light, or laser-aided stereovision [16–21]), high accuracies of the order of tenths of millimeters can be achieved. However, a strong light source is required to achieve a high signal-to-noise ratio [19]; this limits the measurement volume.

On the other hand, the passive measurement method based on forging silhouettes offers fast measurements without the need for a light source. However, numerous difficulties are involved in the application of this principle. Problems arise in the imaging of hot objects, owing to the light radiation, which leads to blurred images [22]. Another problem is the low silhouette contrast, which can be improved using an appropriate bandpass filter [23]. Silhouettes are also corrupted by contrasting image scales on the forging surface; hence, it is difficult to correctly identify the edges. This problem has been solved in various ways in the literature, including the use of a customized edge detection method [24], trust levels for the individual edge points [25],

✉ Jakub Hurník  
Jakub.Hurnik@vut.cz

<sup>1</sup> Faculty of Mechanical Engineering, Brno University of Technology, Technická 2896/2, 616 69 Brno, Czech Republic

the Hough transform (as a robust tool for finding straight forging edges) [26], and detected-edge-point validation [27]. A 3D passive optical measurement system capable of measuring the straightness of a cylindrical forging axis and its diameter has been presented in [27–29]. There, two cameras (whose optical axes were perpendicular and oriented towards the center of gravity of the forging) were used. Ref. [30] developed this principle by applying more accurate methods, including online camera calibration, subpixel edge detection, and edge filtering (based upon complementary edge quality information obtained from the image). The achieved repeatability in this case was  $\pm 0.5$  mm for axis straightness and  $\pm 1$  mm for diameter measurements, both in a measurement volume of  $6 \times 6 \times 2$  m.

The disadvantage of the silhouette-based forging measurement method is the limited number of tangent lines used to determine the cross-sections. For the two-camera measurement method, only four tangent lines are used (two silhouette imprints per image). Higher errors can be observed in the case of poor forging circularity. For example, in a study [30], the measurement error due to this reason increased three times. A straightforward way to solve this problem is to use more cameras, to thereby increase the number of tangent lines when determining the cross-section. However, this solution is not fully suitable to heavy industry environments. The possibilities for camera placement are limited by the layout of the forge and the hot air above the forging. Another option was introduced in [31], where the authors suggested using monocular forging silhouette measurements combined with laser scanning.

Various measurement principles are used for in-process forging measurements. The passive silhouette-based 3D measurement of forgings offers many advantages over other principles. However, the cross-section is poorly defined. Therefore, in this article, we present a multi-camera, multi-observation system for measuring heavy forgings. We used three cameras and further observations taken from various angles around the forging perimeter, to maximize the measurement accuracy. These methods reduce the measurement error in the case of a potentially poor forging circularity. Regarding the verification of the proposed measurement system, it is not possible to obtain the accurate reference geometry due to the forging high temperature and large dimensions. Therefore, to verify the proposed measurement system, the measurement results were directly compared with those obtained using an independent comparative measurement method. Laser scanning was used as the comparative method because it is not significantly affected by the interfering effects. The measurements were performed directly in an industrial environment upon heavy, glowing hot forgings during manufacturing. The novelty of this study is the application of the multi-camera, multi-observation measurement system, in the area of forging measurement.

Although the principles are known in general, their purposeful modifications and combinations, to achieve high measurement accuracy and reliability, are original. Moreover, the statistical verification of such a measurement system against an independent comparative method in the industrial environment was not carried out yet.

## 2 Materials and methods

### 2.1 Proposed measurement system overview

The measurement system was designed to measure forgings with a circular cross-section. Such objects can be approximately represented by a cylinder featuring varying diameters and minor axis deviations. The geometry of such objects can be perceived as a set of cross-sections, varying in terms of diameter and location. Each cross-section is reconstructed using three or more tangents. These tangent lines represent the projection lines of the forging edges (silhouettes) in the image, as shown in Fig. 1.

The workflow of the measurement system is shown in Fig. 2. It includes the image extraction process, their processing (to produce accurate forging silhouette coordinates), and a geometry determination method, which reconstructs the forging geometry from the silhouettes and camera calibration data. However, each silhouette is heavily affected by the potentially poor circularity of the object cross-section, leading to large random deviations. This means that the measurement repeatability (in the case of forging measurements taken from different angular positions around the forging axis and for a limited number of tangent lines determining the forging cross-section) can be heavily impacted.

The basic idea of the novel method proposed and examined in this study is to strongly overdetermine every

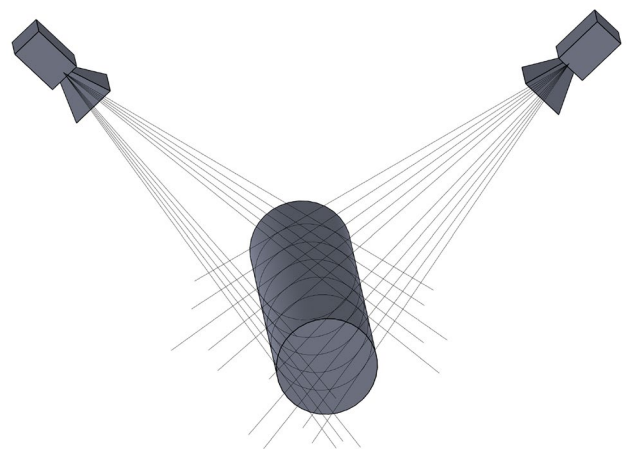


**Fig. 1** General measurement system principle (basic, two-camera configuration)

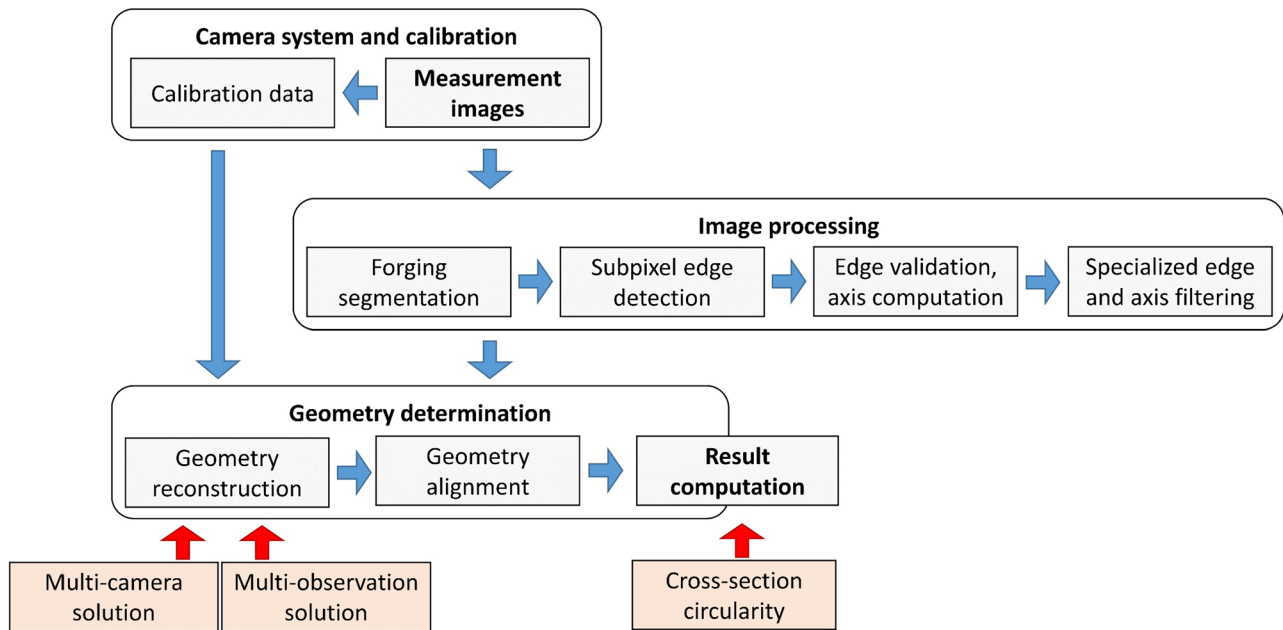
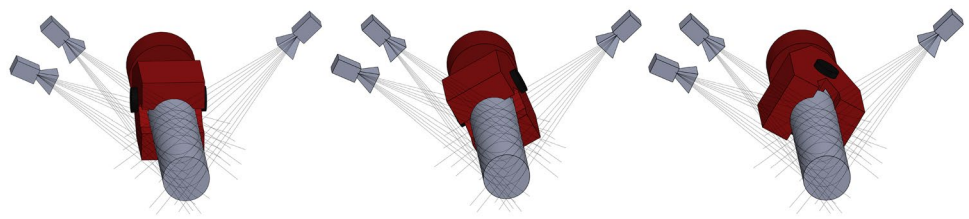


**Fig. 2** Measurement system workflow. The main areas of focus are marked in red

cross-section using numerous tangent lines taken from various directions. This solution should statistically reduce the cross-sectional error. This means increasing the number of tangent lines which define each cross-section. One solution is to use more cameras and image the forging from different perspectives. However, the possibilities for camera placement in forges are usually limited because of the forging equipment arrangement and the hot airflow above the forging. Therefore, we present a method that uses more observations to reduce the measurement error. During manufacturing, the forging is typically held and moved using an accurate forging press manipulator capable of rotating the forging around its axis. We suggest taking advantage of the manipulator and using more observations taken from certain angles to determine the forging geometry. Moreover, we present a new method that uses three images from three cameras to produce six forging silhouettes per observation, to maximize the measurement efficiency. By considering the large number of tangent lines defining the cross-section, it is possible to reliably compute the cross-section's circularity. This concept is depicted in Figs. 3 and 4.

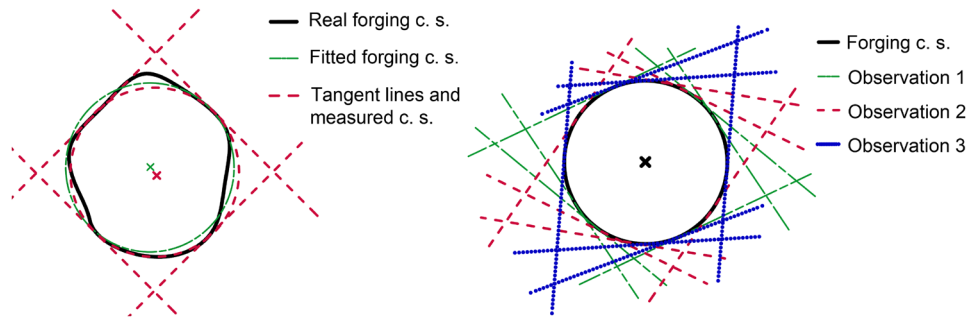
**Fig. 3** Basic concept for multi-camera, multi-observation measurement



### 2.1.1 Camera system

In this study, the measurement system consisted of three cameras oriented towards the center of gravity of the forging, approximately perpendicular to the forging axis. The mutual field-of-view of the cameras was approximately  $6 \times 6 \times 2$  m. The camera positions were chosen primarily according to the limited possibilities of the forge environment. The detailed camera positions are shown in Fig. 5. The measurement system used ZWO ASI 1600MM (PRO) 16 MPx monochromatic cameras equipped with Zeiss Interlock Compact objectives and Schneider-Kreuznach BP 680–100 HT red color filters to enhance the contrast of the forging edges. A secondary advantage of bandpass filters is the reduction of the spectral extent of the scene and forging radiance, which prevents image blur. The objective focal length is displayed in Fig. 5 and varied because of the different camera distances from the forging. The cameras were protected by special thermoregulated covers (Fig. 5); these were required to protect the cameras and maintain a constant intrinsic camera geometry. The

**Fig. 4** Left: single-observation measurement of irregular forging cross-section and error of the measured cross-section with respect to fitted cross-section. Right: multi-camera, multi-observation measurement



temperature in the camera covers was controlled using a Ranque-Hilsch vortex tube Vortec 106–2-H.

The cameras were calibrated using the space resection method. The interior camera parameters' (including distortion parameters) calibration was conducted in the laboratory using a set of images of a 3D calibration field containing targets with known locations. The interior camera parameters were calibrated only once prior to mounting. The camera exterior parameters (i.e., the perspective center and rotation of the image plane) were calibrated using all measurement images. This was based upon 20 calibration targets with known locations in the forge. Calibration in both laboratory and industrial environments is based upon a unique system of circular-coded targets with error corrections. The locations of the targets were measured using a professional photogrammetric system TRITOP (GOM). A detailed description of this calibration method and the employed target system are presented in [32, 33]. The mean reprojection error during interior camera calibration was less than 0.1 px. In the case of exterior camera parameter calibration, the mean reprojection error increased because of the air lens around the forging, though the maximum mean error identified was 0.56 px. The median value of these mean calibration errors was 0.16 px.

**2.1.2 Image processing**

The measurements were based on digital images obtained from the calibrated cameras. First, the forging was roughly

segmented within the image. Segmentation operates as a filter that is sensitive to horizontal objects of a defined size. The algorithm was based on the Sobel edge operator. Information regarding the orientation and magnitude of the edge points was obtained. Dual thresholding was then applied to produce two binary images. A strong threshold was used to obtain correctly oriented (horizontal) strong edges, and a weak threshold extended the pass criterion to less strictly oriented edges of smaller magnitudes. The strong and weak edges were merged into a binary image according to the connectivity criterion. This means that weak edges were considered valid only when connected to strong edges. To filter out isolated edges, a morphological opening with a horizontal rectangular kernel was used, and a binary mask was obtained. The edge map created using the Sobel edge operator was multiplied by this binary mask. Therefore, only the horizontal edges remained in the image, as shown in Fig. 6. The potential axis points of objects with the desired diameter were computed in vertical cross-sections (Fig. 6, red). The Hough transform was used to find the strongest line, which was taken as the object axis. Approximate object silhouettes were considered as points that formed the object axis (Fig. 6, green dots).

Furthermore, the forging edges (silhouettes) were located with subpixel precision. A set of image values was interpolated in the vertical direction around every segmented edge point (Fig. 7, green dots). Accurate edge coordinates were interpolated using the second derivation zero-crossing edge interpolation method (Fig. 7, red crosses).

**Fig. 5** Left: camera setup and placement (focal length, distance from object). Right: specialized thermoregulated camera cover

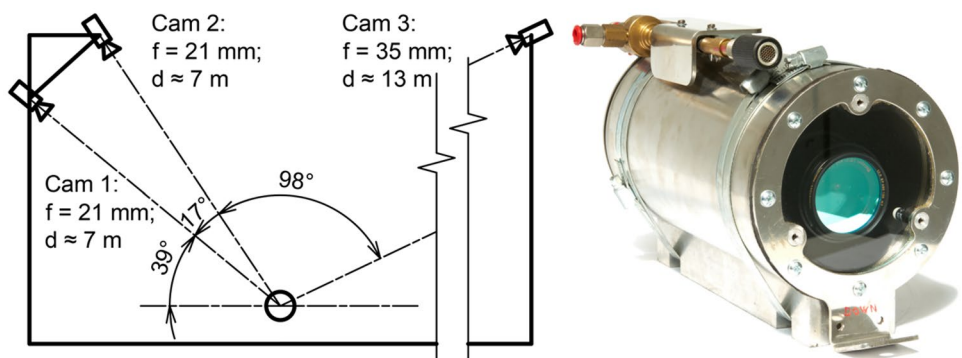
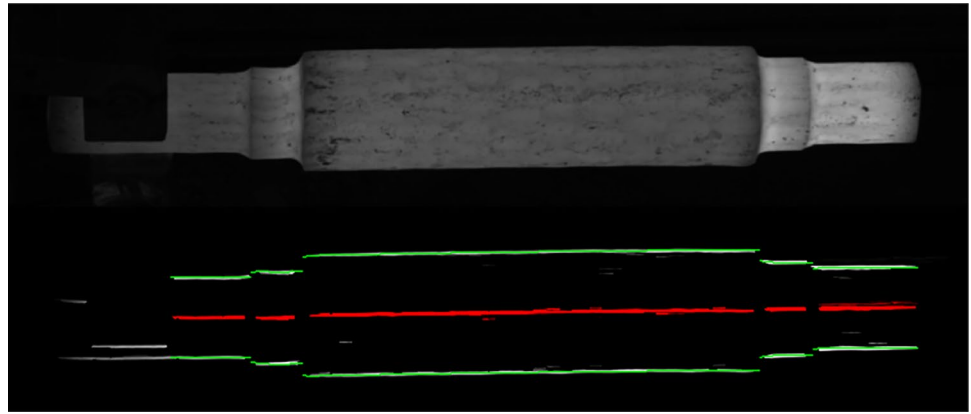


**Fig. 6** Segmentation method: upper: original greyscale image; lower: greyscale image processed by Sobel edge operator and cleaned using binary mask; red: potential axis points; green: estimated edge



The axis imprint in the image was calculated as the center between the upper and lower edges. Both edges and axis imprints were smoothed using weighted filtering. We assume that the correct edges (which were not affected by the scales on the forging surface) were edges with a strong magnitude and a gradient direction perpendicular to the approximate forging axis. On the other hand, the corrupted edges were likely to have smaller magnitudes with random directions. Therefore, the weights were based on complementary information in the image, in terms of the forging edge quality, gradient magnitude, and direction. Optimal results are obtained using the gradient direction weight for axis filtration and gradient magnitude weight for edge filtration. Thus, smoothing was performed according to these weights using weighted parabola fitting. The window width was set to 40 and 10 values for axis and diameter filtering, respectively. Finally, based on the camera calibration parameters, image distortion was compensated for. The resulting edge and axis imprints are shown in Fig. 8.

This method was applied to all three images (or 6, 9, 12, ... in the case of 2, 3, 4, ... observations, respectively). The image processing algorithm outputted the axis imprint and upper and lower silhouettes in each of the measurement images. Each of these curves was composed of 500 error-free (image distortion removed) image points.

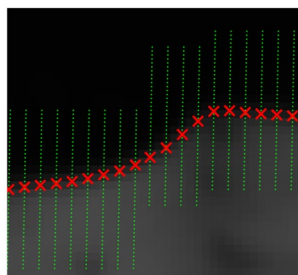


**Fig. 7** Subpixel edge interpolation: green: interpolated image points around the expected edge; red: subpixel edge points

For details of the entire image processing workflow used in this study, please refer to [30].

### 2.1.3 Geometry determination and alignment

As can be seen in Fig. 2, the geometry was determined in three main stages: geometry reconstruction, geometry alignment, and result computation. Geometry reconstruction included two main stages. First, the partial forging geometry was computed from a single multi-camera observation (three images). Next, the joint geometry was computed using more observations and the known rotation between observations, as set by an accurate forging manipulator. The detailed geometry determination workflow is shown in Fig. 9.

**Multi-camera solution** Based on the central projection model of the camera, the axis imprint in every measurement image can be used to create a set of rays in space (Fig. 10). If we consider a three-camera system, arbitrary rays  $r$  from cameras 1, 2, and 3 can be written as.

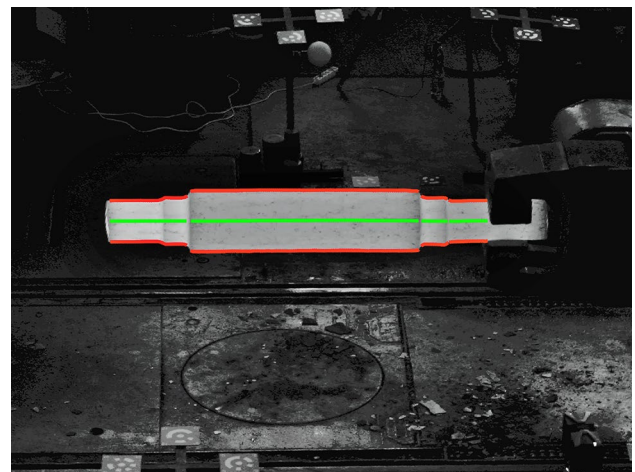


**Fig. 8** Example of evaluated measurement image (edited and cropped): red: silhouettes; green: axis imprint

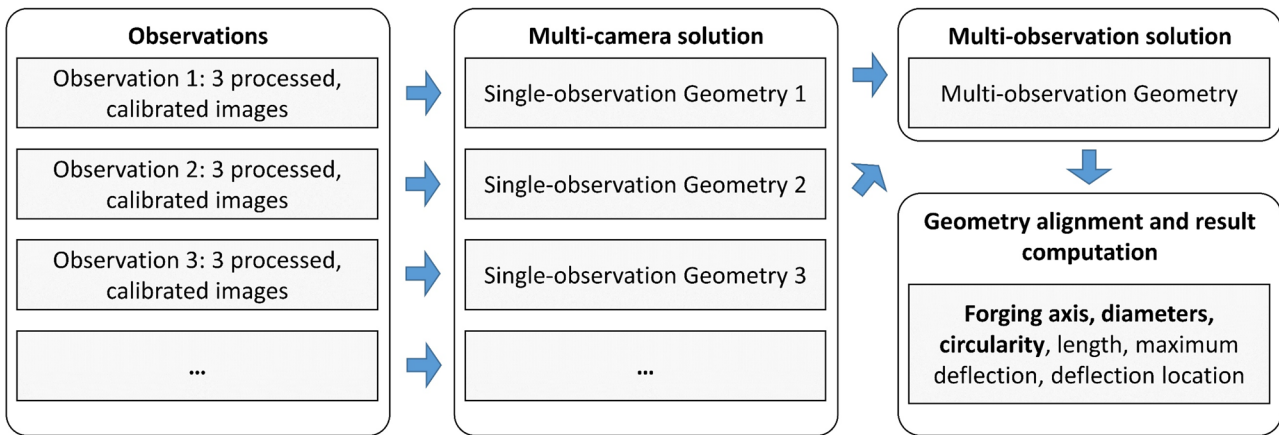


Fig. 9 Geometry determination workflow

$$r_1 : Y_1 = X_1 + k_1 \cdot v_1; r_2 : Y_2 = X_2 + k_2 \cdot v_2; r_3 : Y_3 = X_3 + k_3 \cdot v_3;$$

$$v_1 = \begin{bmatrix} x'_{ax1} \\ y'_{ax1} \\ f_1 \end{bmatrix} \cdot R_1; v_2 = \begin{bmatrix} x'_{ax2} \\ y'_{ax2} \\ f_2 \end{bmatrix} \cdot R_2; v_3 = \begin{bmatrix} x'_{ax3} \\ y'_{ax3} \\ f_3 \end{bmatrix} \cdot R_3; k_1, k_2, k_3 \in R \quad (1)$$

where  $X_1, X_2,$  and  $X_3$  are the camera projection centers;  $R_1, R_2,$  and  $R_3$  are the camera rotation matrices, obtained from the camera calibration procedure;  $Y_1, Y_2,$  and  $Y_3$  are the arbitrary points on the projection rays;  $k_1, k_2,$  and  $k_3$  are the parameters;  $v_1, v_2,$  and  $v_3$  are the directional vectors of the rays;  $[x'_{ax1}, y'_{ax1}], [x'_{ax2}, y'_{ax2}],$  and  $[x'_{ax3}, y'_{ax3}]$  are the coordinates of the corresponding axis imprint points in the image; and  $f_1, f_2,$  and  $f_3$  are the camera focal distances in pixels. The indexes denote the camera numbers, and the apostrophes denote coordinates in the camera coordinate system.

By considering the forging imaging from the radial direction and from different angular positions, each axis point in space was triangulated using the corresponding (closest) image rays from separate cameras. The closest corresponding rays were assigned to each other according to the minimum distance between them. Because the rays from

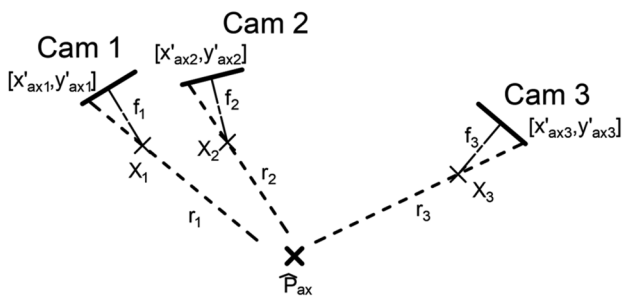


Fig. 10 Axis triangulation scheme

the cameras do not intersect, they are skew lines, and their distance can therefore be computed via

$$|r_t, r_u| = \frac{\left| \overline{[X_t X_u \overline{v_t v_u}]} \right|}{|\overline{v_t} \times \overline{v_u}|} \quad (2)$$

where the indices  $t$  and  $u$  denote different camera indices. After grouping the rays, groups with maximum inter-ray distances  $|r_t, r_u|_{max}$  that exceeded a certain limit were removed.

In every group (i.e., cross-section), the axis point was defined as the nearest point to these three skew lines, measured in terms of least squares. This problem can be computed by solving the overdetermined system of equations in Eq. (1) using the ordinary least-squares method, by setting

$$\widehat{P}_{ax} = Y_1 = Y_2 = Y_3 \quad (3)$$

where  $\widehat{P}_{ax}$  denotes the axis point. When the axis point is reconstructed, it is possible to calculate the image scale  $m_t$ . In general, the forging is not parallel to the image plane; therefore,  $m_t$  varies between cross-sections. The image scale was used to transform the upper and lower object silhouettes ( $\widehat{S}_{Ut}$  and  $\widehat{S}_{Ltp}$ , respectively) from the image to the space; it was calculated using

$$m_t = \frac{|\widehat{P}_{ax} - X_t|}{f_t}; \widehat{S}_{Ut} = X_t + \begin{bmatrix} x'_{Uet} \\ y'_{Uet} \\ f_t \end{bmatrix} \cdot m_t; \widehat{S}_{Ltp} = X_t + \begin{bmatrix} x'_{Let} \\ y'_{Let} \\ f_t \end{bmatrix} \cdot m_t \quad (4)$$

where  $[x'_{Uet}, y'_{Uet}]$  and  $[x'_{Let}, y'_{Let}]$  are the upper and lower image edge points, respectively. The proposed method can be used for an arbitrary number of cameras. The outputs are the axis and (in the case of three-camera measurement) six silhouettes, which form the output of a single forging observation. Both the axis and silhouettes are formed of discrete points in space. The discrete curves were reduced to 500

points. Despite the silhouettes and axis filtering, these results were too complex for axis straightness or other shape corrections; thus, they were smoothed using a Savitzki–Golay second-order filter.

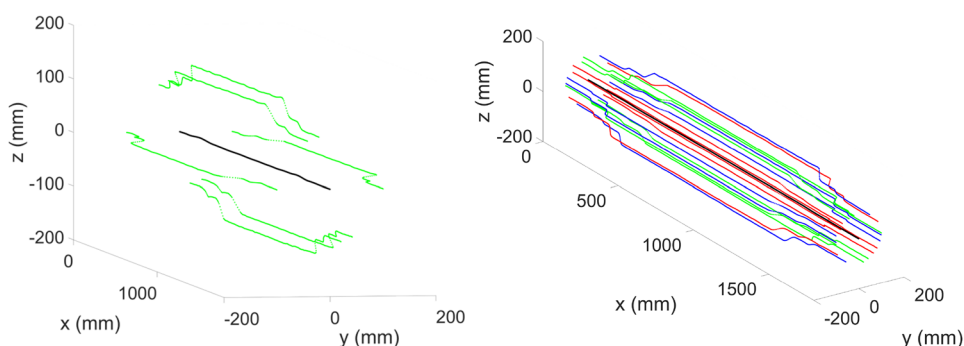
**Multi-observation solution** This section describes the computation of the mean geometry from two or more individual observations. The primary (first) and secondary (one or more) observations were distinct. The individual observations were transformed according to the known rotation around their axis and the best-fit method (for matching), and the mean axis was computed. The basic assumption is that the rotation angle around the forging axis between the individual observations is known, and the forging circularity errors are random (in both size and direction) along the forging axis. The algorithm operates in three stages: pre-alignment, best-fit transformation (with forging rotation compensation), and joint-axis computation.

Pre-alignment was performed individually for every observation (both primary and secondary observations). The purpose of the pre-alignment was to set the measured geometry and thereby correct the orientation. The forging was rotated and translated in space according to the criteria defined in the “Geometry alignment and result computation” section. The output was the measured forging geometry translated to the origin and rotated such that the forging axis matched the *x* axis.

Next, different forging rotations between individual observations were compensated for, and the individual observations were translated in the *y* and *z* directions for matching, using the best-fit method. The assumption here is that the measured forging lengths in all measurements were similar, and the forging orientation was determined during pre-alignment to a sufficient accuracy. The translation parameters  $t_y$  and  $t_z$  were computed based on the least-squares fitting method, where the problem was defined as

$$\underset{t_y, t_z}{\operatorname{argmin}} \sum_{\text{Axis}} |P_{pi} - P_{si}|; P_{si} = \begin{bmatrix} x_i \\ y_i \cdot \cos(\varphi) - z_i \cdot \sin(\varphi) + t_y \\ y_i \cdot \sin(\varphi) + z_i \cdot \cos(\varphi) + t_z \end{bmatrix} \tag{5}$$

**Fig. 11** Single observation and multi-observation geometries; color lines denote measured forging boundaries—green: observation 1; red: observation 2; blue: observation 3; black: (joint) axis



where  $P_p$  is the primary (pre-aligned) observation axis point,  $P[x;y;z]$  is the secondary (also pre-aligned) observation axis point,  $P_s$  is the translated (shifted) secondary axis point, and  $\varphi$  is the known forging rotation during observation. The transformation was performed on both the axis and silhouettes. The joint axis was then computed as the mean of the primary and translated secondary axes, as obtained from individual observations:

$$P_m = \operatorname{mean}(P_p, P_{s1}, P_{s2}, \dots, P_{sj-1}) \tag{6}$$

Here, the index *j* denotes the number of observations. The results of this method were the joint axis and individually transformed silhouettes obtained from the included observations. A graphical representation of the resulting geometries obtained using single- and multi-observation methods is shown in Fig. 11 (three observations).

**Geometry alignment and result computation** The resulting geometry was aligned such that the *x*-axis formed the mutual axis of two 80-mm-long lines fitted to either end of the measured axis, and the origin was set at the start of the measured forging axis by the manipulator. With the geometry aligned, the results of the forging axis geometry, its maximum deflection and location, the forging diameters (the effect of possible deviation between the forging axis direction and cross-section normal is corrected), and forging circularity were measured as follows:

- Forging length: computed as the length of the forging axis.
- Maximum forging deflection and its position: computed from the aligned axis geometry as the maximum distance between the actual measured axis and the ideal axis, as well as its position along the forging axis.
- Forging diameter: computed as the mean Cartesian distance of the silhouette points from the joint axis point in every cross-section.
- Cross-section circularity: computed as the difference between the maximum and minimum measured individual diameters in a specific cross-section, divided by two.

## 2.2 Comparative measurement

### 2.2.1 Laser scanning system

For comparison purposes, we measured the forging using a commercial laser scanning system, the FARO Focus 3D 120. The laser scanner employed the phase shift principle and was capable of measurement in a 0.6–120 m range with a minimum step size of  $0.009^\circ$  in both vertical and horizontal directions. The scanner was fitted with a 20 mW 905 nm laser. The reported ranging error was  $\pm 2$  mm; however, this depended on the measured distance and reflectivity of the object.

Two laser scanning devices were used to capture the entire forging geometry. The scanners were placed on tripods  $\sim 2.2$  m above the floor level. The scanners were placed on each side  $\sim 4$  m from the forging. Four spherical reference targets were placed in the scene for point cloud registration. The scanning resolution at the distance of forging was 3–3.5 mm. In this setup, each measurement lasted  $\sim 5$  min.

### 2.2.2 Point cloud processing and evaluation

First, the point cloud pairs from the laser scanners were aligned using spherical reference targets in the scene. The mean registration accuracy was less than 1.0 mm for all samples. GOM Inspect software was used for further data processing. The point clouds were polygonized using the parameters provided in Fig. 12. To remove the strong noise effect, the mesh was smoothed using the parameters shown in Fig. 13.

Furthermore, the geometry was aligned similarly to that for camera system measurements. The alignment was performed using two cylinders fitted to either end of the forging (three-sigma Gaussian best-fit method). The approximate length of the cylinder was 80 mm. The ideal forging axis was found by fitting the line to the four endpoints of the cylinder axes. The origin was taken as the intersection of the ideal forging axis and the front plane of the manipulator clamp, as shown in Fig. 14. The forging geometry characteristics were evaluated for a dense array of cross-sections perpendicular

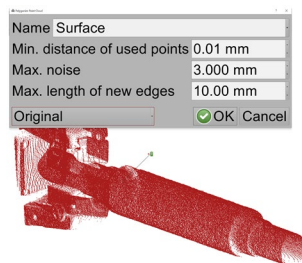


Fig. 12 Polygonize point cloud function parameters

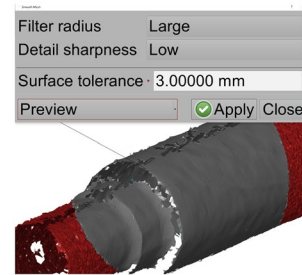


Fig. 13 Smooth mesh function parameters

to the ideal forging axis. These cross-sections were regularly generated along the forging axis with a spacing of 2 mm. The diameter was taken as the diameter of the fitted circle (three-sigma Gaussian best-fit, Fig. 14). The axis deflection was taken as the distance between the center of the fitted circle and the ideal axis. The circularity was also evaluated.

The discrete forging geometry data were further processed. For comparison, the sampling was reduced to 500 samples along the forging axis. A Savitzki–Golay filter was applied to smooth the forging axis geometry. In the same way, this filter was used to smoothen the forging diameter and circularity. The window sizes were chosen to produce the same level of data filtering as the camera system results. The axis geometry was rotated to compensate for the known difference of forging rotations thereabout between individual measurements. Based on these results, the forging length, maximum forging deflection, and maximum deflection position were also computed.

## 2.3 Experimental plan

Experiments in the laboratory and industrial environment were carried out. Multiple specimens were measured. The measurement of a single specimen included 12 observations. The forging was turned about its axis by  $30^\circ$  between

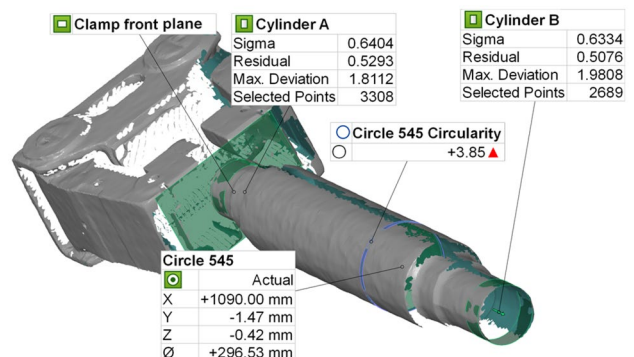


Fig. 14 Laser scanning system data evaluation: cylinders A and B and clamp front plane used for geometry alignment. Geometric characteristics evaluated in random cross-section 545

individual observations to capture the entire forging geometry. To verify the feasibility of the proposed forging measurement system, a comparison with an independent measurement method, based on different principles, was carried out. For comparison, we considered only the following measurement results: forging diameter, circularity along the forging axis, and forging axis geometry. Other complementary measurement results (including forging length and maximum axis deflection) were not examined, because they were dependent on the abovementioned results. The results were evaluated using standard statistical methods.

### 2.3.1 Industrial environment

In the industrial environment, the experiments were conducted directly at the forging press site. The experimental setup is provided in Fig. 15 on the right. The forging was measured while glowing hot ( $\sim 800$  °C) immediately after manufacturing. During this phase, the forging was held in the press manipulator, offering a positioning accuracy within 1 mm and  $0.5^\circ$ . First, a set of measurements (12 measurements) was performed using the camera system. The total measurement time was less than 2 min. Immediately thereafter, a set of laser scanner measurements was performed. Eleven scans were acquired. The forging was again turned around its axis between individual scanning operations. Five scans were taken at  $0^\circ$ , and three scans were performed at  $120^\circ$  and  $240^\circ$  positions. In this case, the total measurement time was less than 60 min. Three forged samples were measured, resulting in 36 individual camera system measurements and 33 laser scans.

Regarding the experiments in the industrial environment, we found that both measurement methods (the proposed camera system and laser scanner system) provided measurement accuracies of the same order. Therefore, instead of taking one of the methods as the reference, the results and repeatability of both methods were compared.

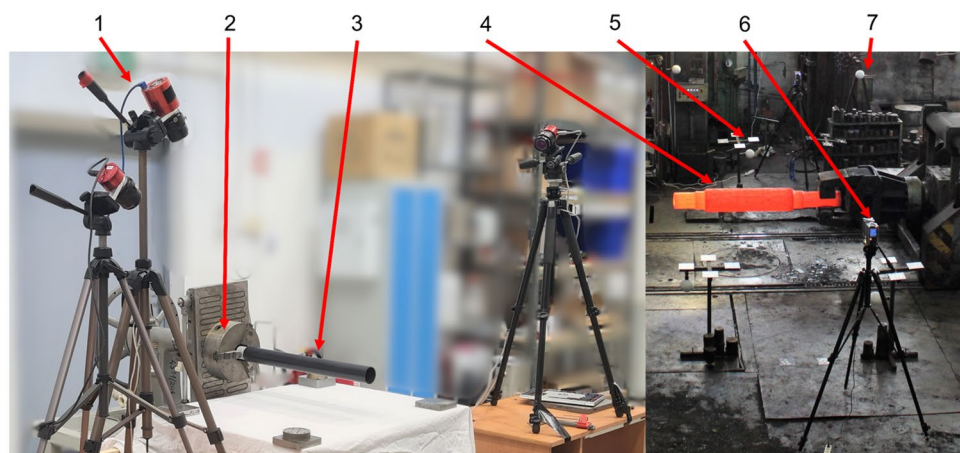
### 2.3.2 Laboratory conditions

The measurement system was also tested under laboratory conditions, to examine the measurement system accuracy without the influence of interfering effects. In this case, the measurement system configuration was scaled approx. 7 times, with respect to the configuration in the industrial environment (the angles were kept the same; however, the distances between the cameras and the object were divided by 7). The cameras were placed on tripods. The measured object was a black steel tube on a white contrasting background with 500 mm length, 50 mm diameter, and a deflection of approx. 1 mm. The positioning of the specimen was carried out using a manual system with precision on the order of minutes of arc. Following changes were made due to the absence of interfering effects of the industrial environment. In this case, the cameras were not mounted on the camera covers and were equipped with UV-IR cut filters instead of red bandpass filters. Online camera calibration was not used in this case; the extrinsic camera parameters were calibrated shortly before the experiment. The experiment layout is provided in Fig. 15 on the left. The image processing and geometry determination methods were the same as presented for the measurement in the industrial environment. The only modification was the size of the fitting cylinders used for the geometry alignment method. In this case, these were 15 mm long, instead of 80 mm, proportionally to the smaller general object size. Three different specimens were measured, resulting in 36 individual camera system measurements total.

### 2.3.3 Mean forging geometry

Because the reference forging geometry in the industrial environment was not available, the mean geometry was used to evaluate the repeatability and correspondence between the developed camera measurement system and the laser

**Fig. 15** Experimental setup—left: laboratory experiment; right: experiment in industrial environment; 1: calibrated measurement system cameras; 2: manual positioning system; 3: object of measurement; 4: measured forging; 5: calibration targets for online camera calibration; 6: laser scanners; 7: targets for point cloud data registration (obtained using laser scanning)



scanning one. In the case of the camera system measurement, the mean geometry of every forging was calculated using the method described in the “Multi-observation solution” section. All 12 measurements of each specimen were included. To evaluate the laser scanner system measurement error, the mean axis of each forging was calculated from all 11 individual scans. The individual axis geometries were fitted using the least-squares method. The mean geometry was then calculated and further aligned using the same method as that used to align the camera system measurements. Furthermore, the mean diameter and circularity were calculated as the mean of the measurements. In both cases, the deviations from the mean geometry were evaluated.

A similar evaluation method was used during the evaluation of the laboratory experiment. However, only the

repeatability of the proposed camera measurement system was evaluated.

### 3 Results and discussion

#### 3.1 Measurement method comparison

The correspondence between measurements obtained using the proposed camera system and the comparative laser scanning system was analyzed. Mean geometric characteristics and their 95% confidence intervals, obtained using both measurement methods, are compared in Fig. 16. Axis deflection was calculated as the distance between the axis points and the ideal forging axis, for depiction purposes. The 95%

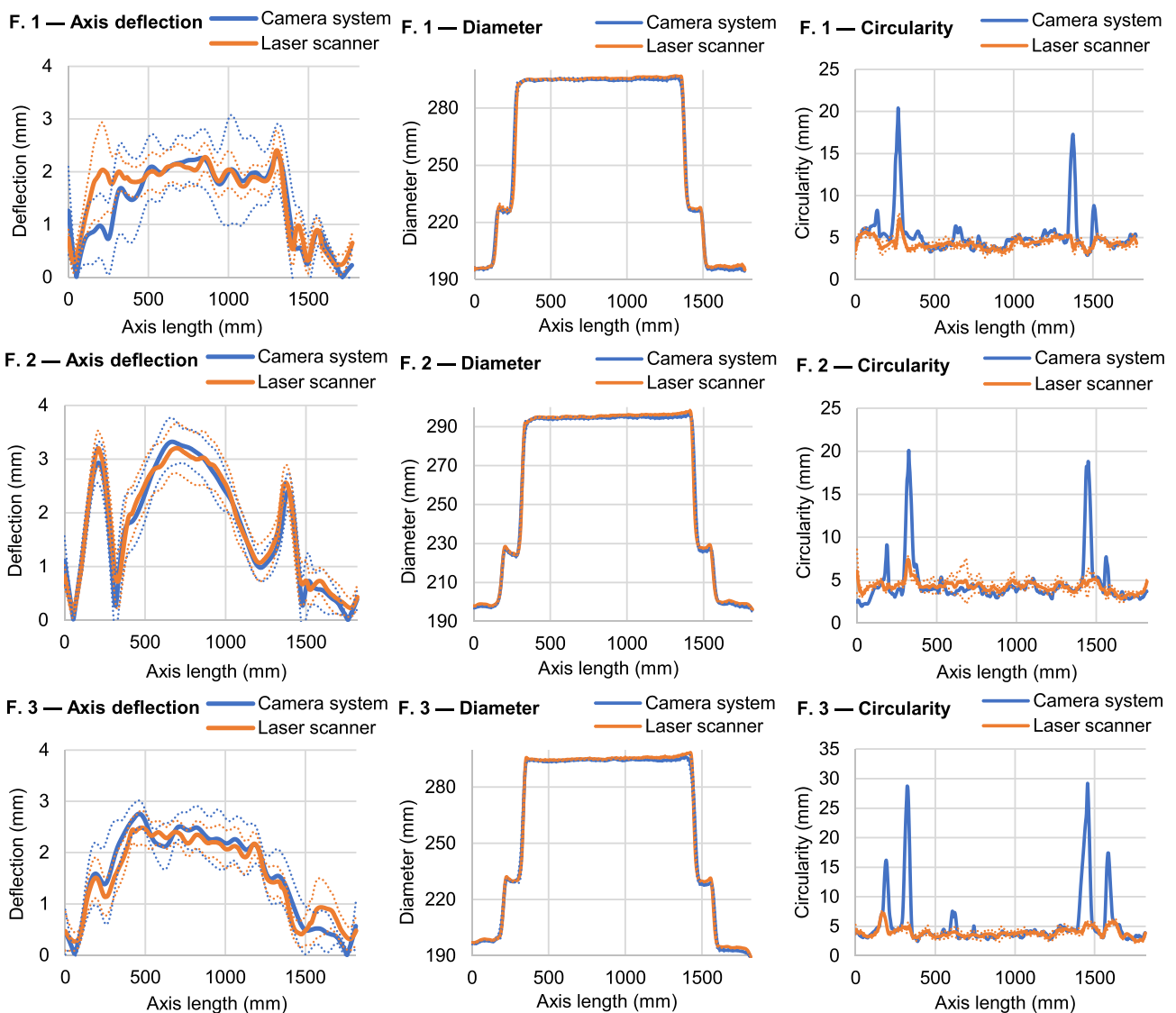


**Fig. 16** Forgings 1–3 mean geometry characteristics obtained using both the camera system and laser scanner measurement methods. Dotted lines delineate the 95% confidence interval of the mean geometry

confidence interval in this case was the confidence interval of the 3D axis geometry. The mean and median differences between the results (and their overlaps) are provided in Table 1. Overlap is defined as the percentage of sample points for which the 95% confidence intervals of the camera and laser measurements have at least one common point. The mean and median differences were computed from the differences between the results of the compared measurement methods (*Camera system measurement – laser scanner measurement*). The results are presented in Table 1.

In the results, the axis geometry measurement showed good agreement between the methods, as shown in the left column of Fig. 16. The 95% intervals overlapped in almost all cases, though with a few local exceptions. The mean and median differences between the methods were also negligible ( $-0.0402$  and  $0.0043$  mm, respectively).

Regarding the circularity measurement, many outliers were present in the camera system forging measurement results, as shown in the right column of Fig. 16. This is also supported by the fact that the mean difference was relatively high ( $0.9041$  mm), while the median difference was relatively low ( $0.0720$  mm). The circularity 95% confidence intervals overlapped in  $\sim 50\%$  of the sample points. This occurred because of the more uncertain forging origin in the camera system measurement compared to the laser scanning one. For a rapidly changing diameter along the forging axis, high local peaks occurred, as can be seen in the right column of Fig. 16. The mean difference in the measured circularity between methods was therefore caused by this effect (in the laser scanner measurement, the forging origin was more accurately defined). The second reason was the laser scanner point cloud processing method, which implements stronger bidirectional smoothing. In comparison, the camera system only performed smoothing along the forging axis. This filtering method did not smooth the local diameter extremes measured in the individual cross-sections. Moreover, it increased the width of the outliers.

The outliers in the circularity measurements also imply outliers in the diameter measurements, owing to the computational method. However, the effect of the inaccurate forging origin was not as strong in this case; this was mainly shown via the widening of the confidence intervals around the areas with high diameter changes. Although

**Table 1** Comparison of the measurement results obtained using camera system and laser scanning. In the case of mean and median differences, the positive number denotes larger values measured by the proposed camera system

	Axis def.	Diameter	Circularity
<b>Overlap</b>	98.47%	50.27%	51.20%
<b>Mean difference</b>	$-0.0402$	$-0.5027$	$0.9041$
<b>Median difference</b>	$0.0043$	$-0.7755$	$0.0720$

the trends of the measured values matched (according to Fig. 16), the diameter measured using the camera system was systematically lower (mean error:  $-0.5027$  mm; median error:  $-0.7755$  mm). Our hypothesis is that this error was caused by imprecise point cloud registration. The error value was within the point cloud registration error. Moreover, a possible explanation is also the influence of the air lens surrounding the forging, which affects the camera images (taken around  $680$  nm wavelength) more than the laser scanning device (operating on  $905$  nm).

### 3.2 Multi-view optical measurement

In this section, the effects of the multi-camera, multi-observation measurement method were analyzed. The methods were evaluated from a repeatability perspective and compared with the laser scanning method. The error parameter sigma was considered a representative parameter of the measurement method's precision. The exception was the circularity measurement obtained using a camera system, in which the representative parameter was considered as the sum of the mean error and sigma. The mean error was a significant parameter in this case, because circularity was evaluated as the difference between the extremal diameters measured in a single cross-section. In the case of the camera system measurement, a relatively low number of measurement points were obtained from a single observation. This produced significant systematic (mean) errors.

The results are presented in Table 2. However, in the case of the camera system's diameter and circularity measurement, the results were influenced by numerous outliers. Therefore, 10% of the outliers were removed. The results without this influence of outliers are presented in Table 3 and Fig. 17. Moreover, the results were compared with the assumption that the error decreased with  $\sqrt{n}$ , where  $n$  is the number of measurements (Fig. 17, "prediction" curve).

From these results, it is clear that better repeatability can be obtained using the multi-camera measurement method than the two-camera method. This method provides more information about the forging cross-section. By adding one camera to a two-camera measurement system, the measurement repeatability error can be decreased by 15% (sigma  $0.889$  vs.  $0.752$  mm), 13% (sigma  $0.963$  to  $0.833$  mm), and 15% (mean + sigma  $4.444$  vs.  $3.797$  mm) in the case of axis, diameter, and circularity, respectively.

The general assumption that the sigma measurement error decreases in approximate proportion to  $\sqrt{n}$  (where  $n$  is the number of measurements) was partially confirmed. As shown in Fig. 17, the measurement error fluctuated around the prediction. However, it is apparent from both the axis and diameter measurements that evenly distributed observations produce a lower error. Therefore, observations should

**Table 2** Multi-camera, multi-observation measurement method repeatability error, compared with the two-camera and laser scanning measurement methods

	1 obs.	2 obs.	3 obs.	4 obs.	5 obs.	6 obs.	7 obs.	8 obs.	9 obs.	10 obs.	11 obs.	1 obs., 2 cam.	Laser sc.
<b>Axis (sigma)</b>	0.752	0.577	0.554	0.445	0.405	0.243	0.343	0.315	0.320	0.259	0.227	0.889	0.522
<b>Diameters (sigma)</b>	2.070	2.010	1.950	1.841	1.703	1.548	1.439	1.301	1.126	0.899	0.624	2.318	0.848
<b>Circularity (sigma + mean)</b>	6.061	5.315	5.101	4.779	4.507	4.180	3.855	3.475	3.108	2.603	1.836	6.643	0.848 (sigma)

be evenly distributed around the forging perimeter. This means that, in this case (30° rotation between the individual observations), six observations are optimal. The measurement error decreased by 68% (sigma 0.752 vs. 0.243 mm), 71% (sigma 0.833 vs. 0.245 mm), and 64% (sigma + mean 3.797 vs. 1.379 mm) for the axis, diameter, and circularity, respectively. However, if a higher accuracy is required, the rotation angle between the single measurements can be lowered; thus, more observations can be used.

The proposed camera measurement system was compared with a comparative measurement using laser scanning from a repeatability perspective. The results suggest that the proposed camera measurement system is effective for measuring the forging axis geometry and diameter. In the case of axis straightness and diameter measurements, the proposed camera system surpassed the laser scanning solution in four and six observations, respectively. However, the circularity measured using the proposed camera system exhibited a larger error, which decreased to values comparable with laser scanning for 11 observations. A lower number of observations also showed a large mean error, indicating that diameter extremes were not captured. The reason for this is the limited number of measurement points that determine the forging cross-section. Therefore, the circularity could only be accurately measured using a large number of observations, which in this case was at least 11.

Moreover, the methods can be compared from a measurement time perspective. The camera system observation was very fast (a fraction of a second). Therefore, the measurement time depended primarily on the forging positioning speed. During our experiments, both the forging press manipulator and camera measurement system were manually controlled by the operators. Therefore, the time between observations was ~10 s. This was much lower than that of the laser scanning comparative system, where the measurement

time was ~5 min. However, both methods could achieve much shorter measurement times. Considering the automatically controlled forging production line, the camera system observation time can be significantly shortened to an order of seconds. On the other hand, the laser scanning system measurement volume can be further optimized to achieve lower scanning times; alternatively, a faster sensor can be used to reduce the measurement times to a fraction of that recorded during the experiment. Therefore, both measurement principles (camera multi-observation system and laser scanning system) can achieve low measurement times on the order of several seconds, which is acceptable for manufacturing processes.

### 3.3 Influence of interfering effects

The overall influence of the interfering effects could result in both systematic and random errors. Significant systematic errors were not observed during the comparison of the proposed measurement system with the independent comparative system. To study the influence of the interfering effect on the random measurement errors, the experiment in the laboratory, under nearly ideal conditions, was carried out. The overall influence of the interfering effects was shown based on the comparison of the measurement repeatability in the laboratory and the industrial environment. The different scale (measurement volume) was eliminated by using the pixel equivalent of the repeatability error for comparison. Only a single observation measurement was examined, because the multi-observation measurement error is dependent on the single observation error. The measurement results of specimen 1 (out of 3 measured specimens) are provided in Fig. 18. The comparison of the repeatability errors in the laboratory and industrial environment is provided in Table 4.

**Table 3** Multi-camera, multi-observation measurement method repeatability error compared with the two-camera and laser scanning measurement methods. Ten percent of outliers were removed from the statistical sets

	1 obs.	2 obs.	3 obs.	4 obs.	5 obs.	6 obs.	7 obs.	8 obs.	9 obs.	10 obs.	11 obs.	1 obs., 2 cam.	Laser sc.
<b>Diameters (sigma)</b>	0.833	0.633	0.585	0.488	0.442	0.245	0.373	0.345	0.337	0.283	0.251	0.963	0.438
<b>Circularity (sigma + mean)</b>	3.797	2.772	2.334	1.921	1.650	1.379	1.216	1.035	0.837	0.597	0.307	4.444	0.503 (sigma)

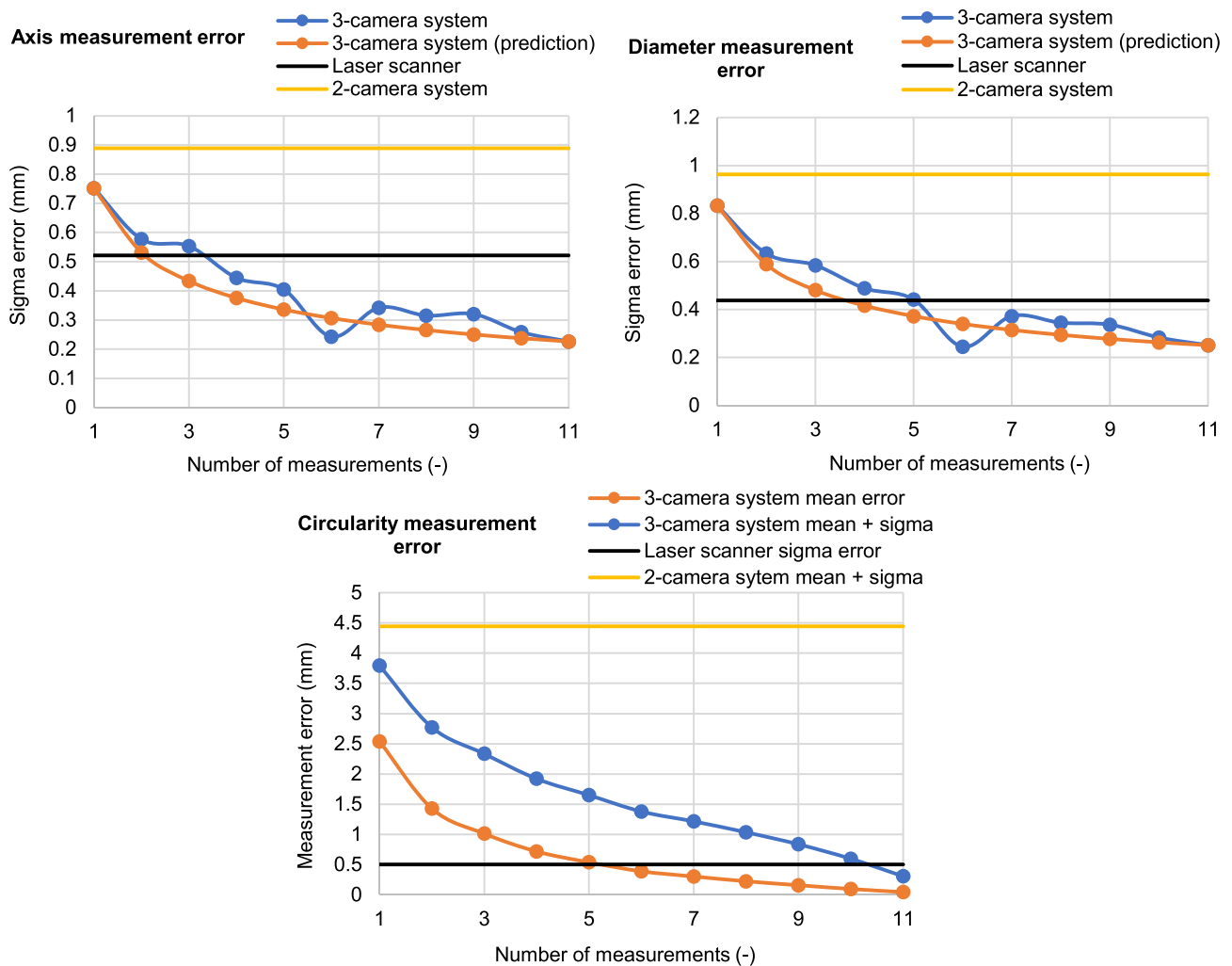


**Fig. 17** Multi-observation method error compared with its prediction for the two-camera measurement and laser scanning measurement methods. Ten % of outliers were removed from the diameter and circularity results

From Table 4, it is obvious that the influence was significant, however not critical. Two main effects were noticeable. First, the error increased approx. 5–6× in case of axis, 3× in case of diameter, and 3× in case of circularity measurement (considering the case without 10% outliers). However, the pixel equivalent error was below one pixel in case of axis and diameter measurement. The error of circularity measurement was in the order of pixels; however, like it was shown, more observations are needed to obtain accurate circularity. The significant relative influence of the axis and diameters measurement was recorded thanks to the high subpixel sensitivity of the system. The cause, instead of the influence of the interfering effects, was more complex forging surface geometry, which contains many plastic forging press marks on its surface, compared to the smooth steel tube measured in the laboratory. Moreover, the circularity of the forging was higher and not proportional to the objects measured

in the laboratory environment (forging – under 300 mm in diameter and approx. 5 mm circularity; laboratory specimen – approx. 50 mm in diameter and approx. 0.3 mm circularity). The second main effect is that there are outliers present in the results obtained during measurement in industrial conditions. Removal of outliers in laboratory conditions causes a relatively small decrease in the measurement errors in the laboratory conditions, while in the industrial conditions, the error decreased significantly. The occurrence of the outliers was discussed earlier.

### 3.4 Future studies

During the forging diameter and circularity measurements, outliers arose because of inaccurate forging origin determination. The forging origin was determined during the forging segmentation process as the beginning of the forging edge.

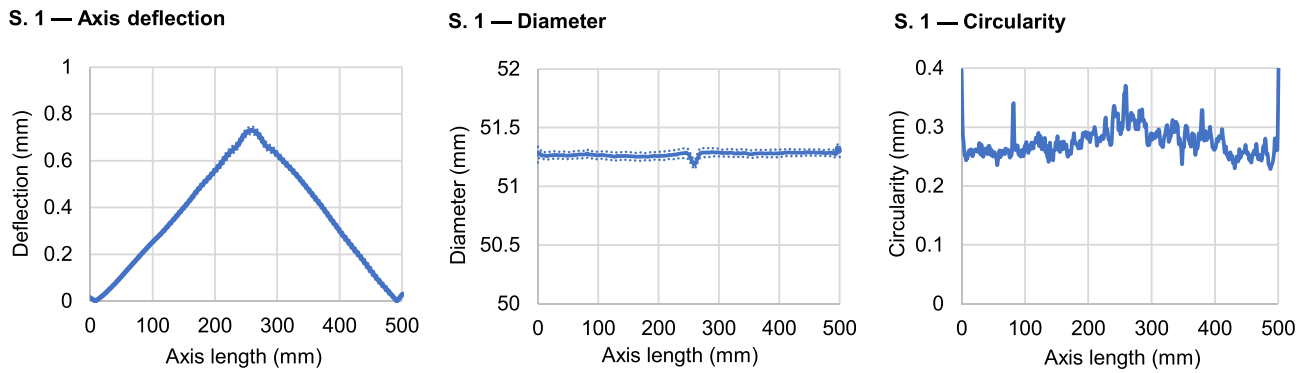


**Fig. 18** Specimen 1 mean geometry characteristics measured in the laboratory environment. Dotted lines delineate the 95% confidence interval of the mean geometry

**Table 4** Comparison of repeatability error of single observation measurement in laboratory and industrial conditions (m.+sig. means mean + sigma error)

	Axis (sigma)	Diam. (sigma)	Circ. (m. + sig.)		Diam. (sigma)	Circ. (m. + sig.)
<b>Laboratory (mm)</b>	0.018	0.042	0.164	Without 10% of outliers	0.033	0.149
<b>Laboratory (px)</b>	0.106	0.247	0.963		0.194	0.876
<b>Industry (mm)</b>	0.752	2.070	6.061		0.833	3.797
<b>Industry (px)</b>	0.583	1.605	4.698		0.646	2.943

This process only approximates the accuracy of pixels. The method can be further improved by subpixel detection of the end of the curve or the manipulator clamp silhouette. This countermeasure should result in more accurate forging diameter and circularity measurements in the case of rapid forging diameter changes along the forging axis. Moreover, further work will include optimization of image processing methods (e.g., forging segmentation and edge verification methods) using neural networks. The measured shapes will be extended to rods of various convex cross-sections (e.g., square and rectangular). Furthermore, the measurement system will be verified using a larger dataset of forgings of various dimensions and the systematic difference between the proposed and laser scanning method will be examined. As a possibility for future study, the proposed measurement method can be combined with different principles (e.g., laser scanning or line scanning), to obtain more data about the forging cross-section.

## 4 Conclusion

In this study, we introduced a 3D forging measurement system that measures an object via its silhouettes. This system can be used to extract information regarding the forging shape for in-process correction. The innovations suggested in this work include multi-camera and

multi-observation solutions. The results obtained using the proposed camera measurement system were also directly compared with an independent comparative measurement system based on the laser scanning principle. The experiment included the measurement of 3 individual forgings. A total of 36 individual measurements were performed using the proposed camera system, and 33 individual comparative measurements were performed using the comparative laser scanning system. The key findings were as follows:

- The negative impact of cross-sectional irregularities on the measurement accuracy is significantly reduced using the proposed multi-camera multi-observation solution. The measurement error for the axis geometry and diameter decreases in approximate proportion to the square root of the measurement number.
- The proposed measurement method proves to be effective for axis straightness and diameter forging measurements. The method can also be used to measure the forging circularity; however, numerous individual observations are required to be evenly distributed around the entire forging perimeter (11 observations or more).
- Although the high relative influence of the interfering effects present in the industrial environment on the single-observation measurement repeatability was recorded (3–6× higher error), the absolute accuracy is acceptable

and can be further improved using the multi-observation method.

- In the case of six observations, the precision in a measurement volume of  $6 \times 6 \times 2$  m is 0.243 mm (sigma), 0.245 mm (sigma), and 1.379 mm (sum of sigma and mean error) for the axis geometry, diameter, and circularity, respectively. Ten % of outliers were deleted in the case of diameter and circularity measurements, owing to the rapidly changing forging diameter.
- The compared independent measurement methods achieved good agreement, which demonstrates the feasibility of the proposed camera measurement system.
- The measurement method is fast, accurate, and practical for use in industrial environments, and it shows potential for application in the manufacturing of heavy forgings.

**Acknowledgements** We thank the ZĎAS company for allowing the research team to conduct experiments in their factory. We would like to thank Editage ([www.editage.com](http://www.editage.com)) for English language editing. Special thanks belong to the Institute of Geodesy, Faculty of Civil Engineering, Brno University of Technology, namely Ing. Tomáš Volařík, Ph.D., for the laser scanning measurement.

**Author contribution** Jakub Hurník was responsible for conceptualization, methodology, software, and writing of an original draft. Material preparation and data collection were performed by Aneta Zatočilová, Pavel Štarha, and Jakub Hurník. The analysis of the data was carried out by Jakub Hurník and Aneta Zatočilová. Aneta Zatočilová and Daniel Koutný were responsible for project administration and funding acquisition. Tereza Konečná was responsible for the formal analysis. Daniel Koutný was performing the supervision. All authors read and approved the final manuscript.

**Funding** This research was funded by the Technology Agency of the Czech Republic (Project: TREND FW01010098) and the Faculty of Mechanical Engineering, Brno University of Technology (Internal Specific Projects: FSI-S-20–6296 and FSI-S-20–6187).

## Declarations

**Competing interests** The authors declare no competing interests.

## References

1. Quentin L, Beermann R, Brunotte K et al (2020) Concept of a control system based on 3D geometry measurement for open die forging of large-scale components. In de Groot PJ, Leach RK, Picart P (eds) *Optics and Photonics for Advanced Dimensional Metrology*. SPIE, p 12
2. Yamauchi M (2009) Errors in optical shape measurement caused by a high-temperature atmosphere. *Opt Eng* 48:4. <https://doi.org/10.1117/1.3212674>
3. Beermann R, Quentin L, Stein G et al (2018) Full simulation model for laser triangulation measurement in an inhomogeneous refractive index field. *Opt Eng* 57:1. <https://doi.org/10.1117/1.OE.57.11.114107>
4. Hawryluk M, Ziemia J (2017) Possibilities of application measurement techniques in hot die forging processes. *Measurement* 110:284–295. <https://doi.org/10.1016/j.measurement.2017.07.003>
5. Hawryluk M, Ziemia J, Sadowski P (2017) A review of current and new measurement techniques used in hot die forging processes. *Meas Control* 50:74–86. <https://doi.org/10.1177/0020294017707161>
6. Wen X, Wang J, Zhang G, Niu L (2021) Three-dimensional morphology and size measurement of high-temperature metal components based on machine vision technology: a review. *Sensors*. <https://doi.org/10.3390/s21144680>
7. Tian ZS, Gao F, Jin LZ, Zhao XC (2009) Dimension measurement of hot large forgings with a novel time-of-flight system. *Int J Adv Manuf Technol* 44:125–132. <https://doi.org/10.1007/s00170-008-1807-8>
8. Du ZC, Wu ZY, Yang JG (2016) 3D measuring and segmentation method for hot heavy forging. *Measurement* 85:43–53. <https://doi.org/10.1016/j.measurement.2016.02.004>
9. Zhang Y, Wang Y, Liu Y et al (2019) A concentricity measurement method for large forgings based on laser ranging principle. *Measurement*. <https://doi.org/10.1016/j.measurement.2019.07.066>
10. Zhang YC, Han JX, Fu XB, Zhang FL (2014) Measurement and control technology of the size for large hot forgings. *Measurement* 49:52–59. <https://doi.org/10.1016/j.measurement.2013.11.028>
11. Ghiotti A, Schöch A, Salvadori A et al (2015) Enhancing the accuracy of high-speed laser triangulation measurement of free-form parts at elevated temperature. *CIRP Ann Manuf Technol* 64:499–502. <https://doi.org/10.1016/j.cirp.2015.04.012>
12. Bračun D, Škulj G, Kadiš M (2017) Spectral selective and difference imaging laser triangulation measurement system for on line measurement of large hot workpieces in precision open die forging. *Int J Adv Manuf Technol* 90:917–926. <https://doi.org/10.1007/s00170-016-9460-0>
13. Mejia-Parra D, Sánchez JR, Ruiz-Salguero O et al (2019) In-line dimensional inspection of warm-die forged revolution workpieces using 3D mesh reconstruction. *Appl Sci* 9:1–21. <https://doi.org/10.3390/app9061069>
14. Quentin L, Beermann R, Reinke C et al (2021) Adapted fringe projection sequences for changing illumination conditions on the example of measuring a wrought-hot object influenced by forced cooling. *Sensors* 21:1–17. <https://doi.org/10.3390/s21051599>
15. Quentin L, Reinke C, Beermann R et al (2020) Design, setup, and evaluation of a compensation system for the light deflection effect occurring when measuring wrought-hot objects using optical triangulation methods. *Metals (Basel)* 10:1–15. <https://doi.org/10.3390/met10070908>
16. Liu W, Jia XH, Jia ZY et al (2011) Fast dimensional measurement method and experiment of the forgings under high temperature. *J Mater Process Technol* 211:237–244. <https://doi.org/10.1016/j.jmatprotec.2010.09.015>
17. Liu W, Jia ZY, Wang FJ et al (2012) An improved online dimensional measurement method of large hot cylindrical forging. *Measurement* 45:2041–2051. <https://doi.org/10.1016/j.measurement.2012.05.004>
18. Jia ZY, Wang LL, Liu W et al (2015) A field measurement method for large objects based on a multi-view stereo vision system. *Sens Actuators A* 234:120–132. <https://doi.org/10.1016/j.sna.2015.08.024>
19. Jia ZY, Liu Y, Liu W et al (2015) A spectrum selection method based on SNR for the machine vision measurement of large hot forgings. *Optik (Stuttg)* 126:5527–5533. <https://doi.org/10.1016/j.jleo.2015.09.110>
20. Liu Y, Jia ZY, Liu W et al (2016) An improved image acquisition method for measuring hot forgings using machine vision. *Sens*

- Actuators A 238:369–378. <https://doi.org/10.1016/j.sna.2015.11.035>
21. Yang J, Liu W, Zhang R et al (2018) A method for measuring the thermal geometric parameters of large hot rectangular forgings based on projection feature lines. *Mach Vis Appl* 29:467–476. <https://doi.org/10.1007/s00138-017-0900-0>
  22. Dworkin SB, Nye TJ (2006) Image processing for machine vision measurement of hot formed parts. *J Mater Process Technol* 174:1–6. <https://doi.org/10.1016/j.jmatprotec.2004.10.019>
  23. Bi C, Fang J, Li D, Qu X (2016) Study on application of color filters in vision system of hot forgings. *Opt Meas Technol Instrum* 10155:1015522. <https://doi.org/10.1117/12.2246795>
  24. Hu CH, Liu B, Song XX (2009) A novel edge detection approach used for online dimensional measurement of heavy forging. In Ye S, Zhang G, Ni J (eds) 2008 International Conference on Optical Instruments and Technology: Optoelectronic Measurement Technology and Applications
  25. Wang P, Lin Y, Muroiwa R et al (2020) A weighted variance approach for uncertainty quantification in high quality steel rolling. *Proc Int Conf Inf Fusion (FUSION 2020)*. <https://doi.org/10.23919/FUSION45008.2020.9190527>
  26. Zhou Y, Wu Y, Luo C (2018) A fast dimensional measurement method for large hot forgings based on line reconstruction. *Int J Adv Manuf Technol* 99:1713–1724. <https://doi.org/10.1007/s00170-018-2551-3>
  27. Zatočilová A, Paloušek D, Brandejs J (2016) Image-based measurement of the dimensions and of the axis straightness of hot forgings. *Measurement* 94:254–264. <https://doi.org/10.1016/j.measurement.2016.07.066>
  28. Zatočilová A, Paloušek D, Brandejs J (2015) Development of a photogrammetry system for the measurement of rotationally symmetric forgings. In Lehmann P, Osten W, Albertazzi Gonçalves A (eds) *Proc SPIE Vol. 9525, Optical Measurement Systems for Industrial Inspection IX*
  29. Zatočilová A, Poliščuk R, Paloušek D, Brandejs J (2013) Photogrammetry based system for the measurement of cylindrical forgings axis straightness. In Lehmann P, Osten W, Albertazzi Gonçalves A (eds) *Proc SPIE Vol. 8788, Optical Measurement Systems for Industrial Inspection VIII*
  30. Hurník J, Zatočilová A, Koutný D, Paloušek D (2022) Enhancing the accuracy of forging measurement using silhouettes in images. *Measurement* 194:111059. <https://doi.org/10.1016/j.measurement.2022.111059>
  31. Fu X, Zhang Y, Zhang W et al (2021) Research on the size of ring forgings based on image detection and point cloud data matching method. *Int J Adv Manuf Technol*. <https://doi.org/10.1007/s00170-021-08268-9>
  32. Hurník J, Zatočilová A, Paloušek D (2019) Camera calibration method of optical system for large field measurement of hot forgings in heavy industry. In Lehmann P, Osten W, Albertazzi Gonçalves A (eds) *Proc SPIE 11056, Optical Measurement Systems for Industrial Inspection XI*
  33. Hurník J, Zatočilová A, Paloušek D (2021) Circular coded target system for industrial applications. *Mach Vis Appl* 32:1–14. <https://doi.org/10.1007/s00138-020-01159-1>

**Publisher's note** Springer Nature remains neutral with regard to jurisdictional claims in published maps and institutional affiliations.

## 7 CONCLUSIONS

The thesis deals with the problem of in-process open-die forged rod measurement. This is a challenge due to the more interfering effects present in the industrial environment. Therefore, common available measurement systems cannot be used without major limitations. Research in this area aims to find a solution. Although the 3D passive measurement method based on forging silhouettes in images potentially offers many advantages in this application, only a little attention was paid to this approach. It is not clear how to implement this method, how to deal with the interfering effects present in the environment, and how it performs. Therefore, in this work, original methods on how to make such a system accurate and reliable under industrial conditions are proposed and examined. This knowledge could be used during the development of a professional optical measurement system for this application in the future.

The thesis begins with a review of the state-of-the-art in this area. The first part of this section is an overview of studies focused on the interfering effects expected in the industrial environment. The second part includes studies on various measurement approaches applied in this area. Based on the review, the interfering effects and ways to deal with them were summarized and evaluated. The measurement approaches are critically compared. Passive 3D optical measurement, based on object silhouettes in images, is evaluated as the best approach for further research, due to its numerous advantages over other approaches and its low level of development in this application. Moreover, such a system has not been examined in the industrial environment. Therefore, the main goal is to examine the properties and limits of this measurement approach in the industrial environment, during the measurement of heavy forgings. The problem is then divided into four main domains: research on calibration targets robustness enhancement, camera calibration method development, research on subpixel edge detection, and feasibility verification of the proposed measurement system. The thesis consists of three journal articles. Moreover, a conference paper was added that covers one of the important topics and connects the publications. Each publication deals primarily with one of the mentioned domains.

The sections Materials and Methods and Results and Discussion are the primary focus of the attached publications. Therefore, both sections are presented briefly. The Materials and Methods section introduces the methods used to achieve high accuracy of the measurement as well as the measurement system robustness to the interfering effects. The original methods providing the robustness of the measurement system and their verification are the focus of this work. These include the robust calibration target recognition method to recognized targets under occlusion, camera calibration method allowing online camera calibration to deal with the dimensionally unstable environment, and robust forging edge detection with subpixel accuracy. Moreover, the hardware setup and verification methods of the experimental system are provided. The Results and Discussion section then summarizes and

connects the findings of the studies. The work is a combination of experimental development and applied research. The research topics are presented using the two scientific questions and hypotheses. The main findings of the thesis are as follows:

- The error correction method for circular coded targets can be based on rotation-invariant distance, target code generator, and similarity condition. The assumption was that the 15-bit target library of 60 targets can achieve error correction of up to 1 bit changed or 2 bits occluded. The results confirm this assumption. Moreover, the results prove that the number of false positives or the number of target confusions is comparable to the target recognition method without the error correction. The target system achieves stable results under different negative image effects, such as noise or blur. Therefore, the proposed methods are evaluated as effective. **Therefore, Hypothesis 1 is not falsified in this thesis.**
- Space resection allows accurate camera calibration in industrial environment, including on-line exterior camera parameters. The influence of air lens surrounding the forging on reprojection error is significant, however, the cameras can be calibrated shortly before the hot forging appears on the scene.
- Subpixel edge detection proves the advantage over edge detection method with pixel precision, however, local edge disturbances appear during the measurement in industrial environment. To take advantage of the higher accuracy, edge filtering is needed. The assumption that correctly identified edges have high gradient magnitude and their direction is perpendicular to forging axis, while corrupted edges have lower gradient magnitude and random direction, is confirmed. Weighted edge filtering proves to be a significant improvement over uniform weight filtering in case of axis straightness measurement. **Therefore, Hypothesis 2 is not falsified in this thesis.** The weight based on the edge direction proved to be the most efficient in the case of axis filtering. On the other hand, the weight based on gradient magnitude proved to be more efficient in the case of forging diameter filtering.
- The major error of the forging geometry can appear when there is insufficient forging circularity. To solve this problem, a multi-view measurement method is proposed, achieving accuracy in  $\pm 0.5$  mm for both forging axis straightness and diameter measurements (95% confidence interval, however, in case of diameter measurement, 10% of outliers were removed). This is achieved in a measurement volume of approx.  $6 \times 6 \times 2$  m. Therefore, the feasibility of the forging measurement principle, based on its silhouettes in images, is confirmed.

Although current measurement methods are limited to cylindrical forgings, they can be generalized to other common forging shapes, including rods with square or rectangular cross sections. The system could be used to provide feedback about the dimensional accuracy, for its in-process correction (e.g., axis straightness). This will help to achieve better dimensional accuracy of the forgings and prevent problems during machining due to run-out. In addition,

the machining allowances could be minimized, to save material and energy. In the future, this measurement system could become a part of the fully automated manufacturing line, in accordance with industry 4.0 trends.

## 8 LIST OF PUBLICATIONS

### 8.1 Papers published in journals with impact factor

HURNÍK J., A. ZATOČILOVÁ and D. PALOUŠEK. Circular coded target system for industrial applications. *Machine Vision and Applications*. 2021, **32**(1), 1–14. ISSN 14321769. Available at: doi:10.1007/s00138-020-01159-1

*IF 2.983; Q2 (by JIF; Engineering, electrical & electronic)*

*AIS 0.475, Q3 (by AIS; Computer science, artificial intelligence); according to WoS, 2021.*

HURNÍK J., A. ZATOČILOVÁ, D. KOUTNÝ and D. PALOUŠEK. Enhancing the accuracy of forging measurement using silhouettes in images. *Measurement*. 2022, **194**, 111059. ISSN 02632241. Available at: doi:10.1016/j.measurement.2022.111059

*IF 5.131; Q1 (by JIF; Engineering, multidisciplinary)*

*AIS 0.643; Q2 (by AIS; Engineering, multidisciplinary); according to WoS, 2021.*

MICHALEC, M., V. POLNICKÝ, J. FOLTÝN, P. SVOBODA, P. ŠPERKA and J. HURNÍK. The prediction of large-scale hydrostatic bearing pad misalignment error and its compensation using compliant support. *Precision Engineering*. 2022, **75**, 67–79. ISSN 01416359. Available at: doi:10.1016/j.precisioneng.2022.01.011

*IF 3.315; Q2 (by JIF; Engineering, multidisciplinary)*

*AIS 0.624; Q2 (by AIS; Engineering, multidisciplinary); according to WoS, 2021.*

J. HURNÍK, A. ZATOČILOVÁ, T. KONEČNÁ and P. ŠTARHA. Multi-view camera system for measurement of heavy forgings. *The International Journal of Advanced Manufacturing Technology*. 2022, ISSN 02683768. Available at: doi: 10.1007/s00170-022-09809-6

*IF 3.563; Q2 (by JIF; Automation & control systems)*

*AIS 0.450; Q3 (by AIS; Automation & control systems); according to WoS, 2021.*

MICHALEC, M., J. HURNÍK, J. FOLTÝN and P. SVOBODA. Contactless measurement of hydrostatic bearing lubricating film using optical point tracking method. *Proceedings of the Institution of Mechanical Engineers Part J-Journal of Engineering Tribology*. 2022, ISSN 13506501. Available at: doi: 10.1177/13506501221108138

*IF 1.818; Q3 (by JIF; Engineering, mechanical)*

*AIS 0.279; Q3 (by AIS; Engineering, mechanical); according to WoS, 2021.*

## 8.2 Papers in conference proceedings

VRÁNA, R., VAVERKA, O., ČERVINEK, O., PANTĚLEJEV, L., HURNÍK, J., KOUTNÝ, D., PALOUŠEK, D. Heat treatment of the SLM processed lattice structure made of AlSi10Mg and its effect on the impact energy absorption. In: *Euro PM2019 Proceedings*. 2019.

*Indexed in Scopus*

J. HURNÍK, A. ZATOČILOVÁ and D. PALOUŠEK. Camera calibration method of optical system for large field measurement of hot forgings in heavy industry. In: *Opt. Meas. Syst. Ind. Inspect. XI, Proc. SPIE*. 2019, p. 11056. Available at: doi:10.1117/12.2527693

*Indexed in WoS*

## REFERENCES

- [1] FERROTRON. LaCam Forge. *LaCamForge* [online]. 2015 [accessed. 2019-06-30]. Available at: [https://www.mineralstech.com/docs/default-source/refractories-documents/ferrotron/lacam-forge---presentation.pdf?sfvrsn=6daf9d8b\\_0](https://www.mineralstech.com/docs/default-source/refractories-documents/ferrotron/lacam-forge---presentation.pdf?sfvrsn=6daf9d8b_0)
- [2] ZATOČILOVÁ, A., D. PALOUŠEK and J. BRANDEJS. Image-based measurement of the dimensions and of the axis straightness of hot forgings. *Measurement* [online]. 2016, **94**, 254–264. ISSN 0263-2241. Available at: doi:10.1016/j.measurement.2016.07.066
- [3] QUENTIN, L., R. BEERMANN, K. BRUNOTTE, B. A. BEHRENS, M. KÄSTNER and E. REITHMEIER. Concept of a control system based on 3D geometry measurement for open die forging of large-scale components. In: Peter J. DE GROOT, Richard K. LEACH and Pascal PICART, eds. *Optics and Photonics for Advanced Dimensional Metrology* [online]. B.m.: SPIE, 2020, p. 12. ISBN 9781510634763. Available at: doi:10.1117/12.2554720
- [4] LUHMANN, Thomas. Close range photogrammetry for industrial applications. *ISPRS Journal of Photogrammetry and Remote Sensing* [online]. 2010, **65**(6), 558–569. ISSN 09242716. Available at: doi:10.1016/j.isprsjprs.2010.06.003
- [5] LUHMANN, T., S. ROBSON, S. KYLE and I. HARLEY. *Close Range Photogrammetry*. Scotland, UK: Whittles Publishing, 2011. ISBN 978-184995-057-2.
- [6] TSAI, R. A Versatile Camera Calibration Techniaue for High-Accuracy 3D Machine Vision Metrology Using Off-the-shelf TV Cameras and Lenses. *IEEE Journal of Robotics and Automation*. 1987, **3**(4), 323–344.
- [7] ZHANG, Z. Y. A flexible new technique for camera calibration. *IEEE Transactions on Pattern Analysis and Machine Intelligence* [online]. 2000, **22**(11), 1330–1334. ISSN 0162-8828. Available at: doi:10.1109/34.888718
- [8] FORBES, K., A. VOIGHT and N BODIKA. An Inexpensive, Automatic and Accurate Camera Calibration Method. In: *Thirteenth Annual Symposium of the Pattern Recognition Association of South Africa*. 2002, p. 1–7. ISBN 0799221473.
- [9] SCHNEIDER, D., E. SCHWALBE and H. MAAS. Validation of geometric models for fisheye lenses. *ISPRS Journal of Photogrammetry and Remote Sensing* [online]. 2009, **64**(3), 259–266. ISSN 0924-2716. Available at: doi:10.1016/j.isprsjprs.2009.01.001
- [10] HU, H., J. LIANG, Z. Z. XIAO, Z. Z. TANG, A. K. ASUNDI and Y. X. WANG. A four-camera videogrammetric system for 3-D motion measurement of deformable

- object. *Optics and Lasers in Engineering* [online]. 2012, **50**(5), 800–811. ISSN 0143-8166. Available at: doi:10.1016/j.optlaseng.2011.12.011
- [11] BADRINARAYANAN, V., A. KENDALL and R. CIPOLLA. SegNet: A Deep Convolutional Encoder-Decoder Architecture for Image Segmentation. *IEEE Transactions on Pattern Analysis and Machine Intelligence* [online]. 2017, **39**(12), 2481–2495. ISSN 01628828. Available at: doi:10.1109/TPAMI.2016.2644615
- [12] LIU, L., W. OUYANG, X. WANG, P. FIEGUTH, J. CHEN, X. LIU and M. PIETIKÄINEN. Deep learning for generic object detection: A survey. *International Journal of Computer Vision* [online]. 2020, **128**(2), 261–318. ISSN 15731405. Available at: doi:10.1007/s11263-019-01247-4
- [13] DWORKIN, S. B. and T. J. NYE. Image processing for machine vision measurement of hot formed parts. *Journal of Materials Processing Technology* [online]. 2006, **174**(1–3), 1–6. ISSN 0924-0136. Available at: doi:10.1016/j.jmatprotec.2004.10.019
- [14] BI, C., J. G. FANG, D. LI and X. H. QU. Study on application of color filters in vision system of hot forgings. In: S. HAN and J. TAN, eds. *Optical Measurement Technology and Instrumentation, Proc. SPIE Vol. 10155* [online]. 2016. Proceedings of SPIE. ISBN 978-1-5106-0769-9. Available at: doi:10.1117/12.2246795
- [15] HU, C. H., B. LIU and X. X. SONG. A novel edge detection approach used for online dimensional measurement of heavy forging. In: S. YE, G. ZHANG and J. NI, eds. *Proc. SPIE Vol. 7160 (2009) International Conference on Optical Instruments and Technology: Optoelectronic Measurement Technology and Applications 2008* [online]. no date. Proceedings of SPIE-The International Society for Optical Engineering. ISBN 978-0-8194-7404-9. Available at: doi:10.1117/12.807046
- [16] CANNY, J. A computational approach to edge detection. *IEEE Trans. on Pattern Anal. Mach. Intell.* [online]. 1986, **8**(6), 679–698. ISSN 0162-8828. Available at: doi:10.1109/tpami.1986.4767851
- [17] JIA, Z. Y., Y. LIU, W. LIU, C. ZHANG, J. H. YANG, L. L. WANG and K. ZHAO. A spectrum selection method based on SNR for the machine vision measurement of large hot forgings. *Optik* [online]. 2015, **126**(24), 5527–5533. ISSN 0030-4026. Available at: doi:10.1016/j.ijleo.2015.09.110
- [18] CIDDOR, P. E. Refractive index of air: New equations for the visible and near infrared. *Applied Optics* [online]. 1996, **35**(9), 1566–1573. Available at: doi:https://doi.org/10.1364/AO.35.001566
- [19] YAMAUCHI, M. Errors in optical shape measurement caused by a high-temperature atmosphere. *Optical Engineering* [online]. 2009, **48**(9), 4. ISSN 0091-3286. Available at: doi:10.1117/1.3212674

- [20] BEERMANN, R., L. QUENTIN, G. STEIN, E. REITHMEIER and M. KÄSTNER. Full simulation model for laser triangulation measurement in an inhomogeneous refractive index field. *Optical Engineering* [online]. 2018, **57**(11), 1. ISSN 1560-2303. Available at: doi:10.1117/1.OE.57.11.114107
- [21] QUENTIN, L., C. REINKE, R. BEERMANN, M. KÄSTNER and E. REITHMEIER. Design, setup, and evaluation of a compensation system for the light deflection effect occurring when measuring wrought-hot objects using optical triangulation methods. *Metals* [online]. 2020, **10**(7), 1–15. ISSN 20754701. Available at: doi:10.3390/met10070908
- [22] BERGAMASCO, F., A. ALBARELLI, L. COSMO and A. TORSELLO. An Accurate and Robust Artificial Marker Based on Cyclic Codes. *IEEE Transactions on Pattern Analysis and Machine Intelligence*. 2016, **38**(12), 2359–2373.
- [23] BERGAMASCO, F., A. ALBARELLI and A. TORSELLO. Pi-Tag: A fast image-space marker design based on projective invariants. *Machine Vision and Applications* [online]. 2013, **24**(6), 1295–1310. Available at: doi:10.1007/s00138-012-0469-6
- [24] LI, Z. and M. LIU. Research on Decoding Method of Coded Targets in Close-range Photogrammetry. *Journal of Computational Information Systems*. 2010, **6**(8), 2699–2705.
- [25] XIA, R. B., J. B. ZHAO, W. J. LIU, J. H. WU, S. P. FU, J. JIANG and J. Z. LI. A Robust Recognition Algorithm for Encoded Targets in Close-range Photogrammetry. *Journal of Information Science and Engineering* [online]. 2012, **28**, 407–418. Available at: doi:10.1688/JISE.2012.28.2.11
- [26] GUO, C. Y., X. S. CHENG, H. H. CUI, N. DAI and J. P. WENG. A new technique of recognition for coded targets in optical 3D measurement. In: *Optical Metrology and Inspection for Industrial Applications III*. 2014.
- [27] LI, W. M., G. LIU, L. C. ZHU, X. F. LI, Y. H. ZHANG and S. Y. SHAN. Efficient detection and recognition algorithm of reference points in photogrammetry. In: *Conference on Optics, Photonics and Digital Technologies for Imaging Applications IV*. 2016.
- [28] CALVET, L., P. GURDJOS, C. GRIWODZ and S. GASPARINI. Detection and Accurate Localization of Circular Fiducials under Highly Challenging Conditions. *2016 IEEE Conference on Computer Vision and Pattern Recognition* [online]. 2016, 562–570. Available at: doi:10.1109/CVPR.2016.67
- [29] DOSIL, R., X. M. PARDO and X. R. FDEZ-VIDAL. A new radial symmetry measure applied to photogrammetry A new radial symmetry measure applied to photogrammetry. *Pattern Analysis and Applications* [online]. 2012, **16**(4), 637–646. Available at: doi:10.1007/s10044-012-0281-y

- [30] FIALA, M. ARTag, a fiducial marker system using digital techniques. In: *IEEE Computer Society Conference on Computer Vision and Pattern Recognition, Vol 2, Proceedings*. 2005.
- [31] ROMERO-RAMIREZ, F. J., R. MUÑOZ-SALINAS and R. MEDINA-CARNICER. Speeded up detection of squared fiducial markers. *Image and Vision Computing* [online]. 2018, **76**, 38–47. ISSN 0262-8856. Available at: doi:10.1016/j.imavis.2018.05.004
- [32] GARRIDO-JURADO, S. Automatic generation and detection of highly reliable fiducial markers under occlusion. *Pattern Recognition* [online]. 2014, **47**(6), 2280–2292. ISSN 0031-3203. Available at: doi:10.1016/j.patcog.2014.01.005
- [33] GARRIDO-JURADO, S., R. MUÑOZ-SALINAS, F. J. MADRID-CUEVAS and R. MEDINA-CARNICER. Generation of fiducial marker dictionaries using Mixed Integer Linear Programming. *Pattern Recognition* [online]. 2016, **51**, 481–491. ISSN 0031-3203. Available at: doi:10.1016/j.patcog.2015.09.023
- [34] MONDÉJAR-GUERRA, V., S. GARRIDO-JURADO, R. MUÑOZ-SALINAS, M. J. MARÍN-JIMÉNEZ and R. MEDINA-CARNICER. Robust identification of fiducial markers in challenging conditions. *Expert Systems With Applications* [online]. 2018, **93**, 336–345. Available at: doi:10.1016/j.eswa.2017.10.032
- [35] OTSU, N. A Threshold Selection Method from Gray-Level Histograms. *IEEE Trans. Syst. Man Cybern.* 1979, **9**(1), 62–66.
- [36] WEN, X., J. WANG, G. ZHANG and L. NIU. Three-dimensional morphology and size measurement of high-temperature metal components based on machine vision technology: A review. *Sensors* [online]. 2021, **21**(14). ISSN 14248220. Available at: doi:10.3390/s21144680
- [37] TIAN, Z. S., F. GAO, L. Z. JIN and X. C. ZHAO. Dimension measurement of hot large forgings with a novel time-of-flight system. *International Journal of Advanced Manufacturing Technology* [online]. 2009, **44**(1–2), 125–132. ISSN 0268-3768. Available at: doi:10.1007/s00170-008-1807-8
- [38] DU, Z. C., Z. Y. WU and J. G. YANG. 3D measuring and segmentation method for hot heavy forging. *Measurement* [online]. 2016, **85**, 43–53. ISSN 0263-2241. Available at: doi:10.1016/j.measurement.2016.02.004
- [39] ZHANG, Y., Y. WANG, Y. LIU, D. LV, X. FU, Y. ZHANG and J. LI. A concentricity measurement method for large forgings based on laser ranging principle. *Measurement* [online]. 2019, **147**. ISSN 02632241. Available at: doi:10.1016/j.measurement.2019.07.066
- [40] FU, X., Y. ZHANG, W. ZHANG, Q. LI and T. KONG. Research on the size of ring forgings based on image detection and point cloud data matching method.

- International Journal of Advanced Manufacturing Technology* [online]. 2021. ISSN 14333015. Available at: doi:10.1007/s00170-021-08268-9
- [41] LIU, W., X. H. JIA, Z. Y. JIA, S. J. LIU, B. G. WANG and J. A. DU. Fast dimensional measurement method and experiment of the forgings under high temperature. *Journal of Materials Processing Technology* [online]. 2011, **211**(2), 237–244. ISSN 0924-0136. Available at: doi:10.1016/j.jmatprotec.2010.09.015
- [42] LIU, W., Z. Y. JIA, F. J. WANG, X. MA, W. Q. WANG, X. H. JIA and D. D. SONG. An improved online dimensional measurement method of large hot cylindrical forging. *Measurement* [online]. 2012, **45**(8), 2041–2051. ISSN 0263-2241. Available at: doi:10.1016/j.measurement.2012.05.004
- [43] JIA, Z. Y., L. L. WANG, W. LIU, J. H. YANG, Y. LIU, C. N. FAN and K. ZHAO. A field measurement method for large objects based on a multi-view stereo vision system. *Sensors and Actuators A: Physical* [online]. 2015, **234**, 120–132. ISSN 0924-4247. Available at: doi:10.1016/j.sna.2015.08.024
- [44] LIU, Y., Z. Y. JIA, W. LIU, L. L. WANG, C. N. FAN, P. T. XU, J. H. YANG and K. ZHAO. An improved image acquisition method for measuring hot forgings using machine vision. *Sensors and Actuators A: Physical* [online]. 2016, **238**, 369–378. ISSN 0924-4247. Available at: doi:10.1016/j.sna.2015.11.035
- [45] YANG, J. H., W. LIU, C. N. FAN, S. J. LI, F. J. WANG, Z. Y. JIA, H. Y. YAN and X. LI. Improved calibration method of binocular vision measurement system for large hot forging. In: *Proceedings 2016 Ieee 25th International Symposium on Industrial Electronics* [online]. 2016, Proceedings of the IEEE International Symposium on Industrial Electronics, p. 918–922. ISBN 978-1-5090-0873-5. Available at: %3CGo
- [46] YANG, J., W. LIU, R. ZHANG, Z. JIA, F. WANG and S. LI. A method for measuring the thermal geometric parameters of large hot rectangular forgings based on projection feature lines. *Machine Vision and Applications* [online]. 2018, **29**(3), 467–476. ISSN 14321769. Available at: doi:10.1007/s00138-017-0900-0
- [47] ZHAO, X., J. LIU, H. ZHANG and Y. WU. Measuring the 3D shape of high temperature objects using blue sinusoidal structured light. *Measurement Science and Technology* [online]. 2015, **26**(12). ISSN 13616501. Available at: doi:10.1088/0957-0233/26/12/125205
- [48] HAN, L., X. CHENG, Z. LI, K. ZHONG, Y. SHI and H. JIANG. A robot-driven 3D shape measurement system for automatic quality inspection of thermal objects on a forging production line. *Sensors* [online]. 2018, **18**(12). ISSN 14248220. Available at: doi:10.3390/s18124368
- [49] QUENTIN, L., R. BEERMANN, M. KÄSTNER and E. REITHMEIER. Development of a reconstruction quality metric for optical three-dimensional

- measurement systems in use for hot-state measurement object. *Optical Engineering* [online]. 2020, **59**(06), 1. ISSN 15602303. Available at: doi:10.1117/1.oe.59.6.064103
- [50] QUENTIN, L., R. BEERMANN, C. REINKE, P. KERN, M. KÄSTNER and E. REITHMEIER. Adapted fringe projection sequences for changing illumination conditions on the example of measuring a wrought-hot object influenced by forced cooling. *Sensors* [online]. 2021, **21**(5), 1–17. ISSN 14248220. Available at: doi:10.3390/s21051599
- [51] ZHANG, Y. C., J. X. HAN, X. B. FU and F. L. ZHANG. Measurement and control technology of the size for large hot forgings. *Measurement* [online]. 2014, **49**, 52–59. ISSN 0263-2241. Available at: doi:10.1016/j.measurement.2013.11.028
- [52] BRAČUN, D., G. ŠKULJ and M. KADIŠ. Spectral selective and difference imaging laser triangulation measurement system for on line measurement of large hot workpieces in precision open die forging. *International Journal of Advanced Manufacturing Technology* [online]. 2017, **90**(1–4), 917–926. ISSN 0268-3768. Available at: doi:10.1007/s00170-016-9460-0
- [53] MEJIA-PARRA, D., J. R. SÁNCHEZ, O. RUIZ-SALGUERO, M. ALONSO, A. IZAGUIRRE, E. GIL, J. PALOMAR and J POSADA. In-line dimensional inspection of warm-die forged revolution workpieces using 3D mesh reconstruction. *Applied Sciences* [online]. 2019, **9**, 1–21. ISSN 20763417. Available at: doi:10.3390/app9061069
- [54] GHIOTTI, A., A. SCHÖCH, A. SALVADORI, S. CARMIGNATO and E. SAVIO. Enhancing the accuracy of high-speed laser triangulation measurement of freeform parts at elevated temperature. *CIRP Annals - Manufacturing Technology* [online]. 2015, **64**(1), 499–502. ISSN 17260604. Available at: doi:10.1016/j.cirp.2015.04.012
- [55] FRASER, C. S., I. JAZAYERI and S. CRONK. A Feature-based matching strategy for automated 3D model reconstruction in multi-image close-range photogrammetry. In: *ASPRS 2010 Annual Conference San Diego, California*. 2010.
- [56] JIA, Z. Y., B. G. WANG, W. LIU and Y. W. SUN. An improved image acquiring method for machine vision measurement of hot formed parts. *Journal of Materials Processing Technology* [online]. 2010, **210**(2), 267–271. ISSN 0924-0136. Available at: doi:10.1016/j.jmatprotec.2009.09.009
- [57] LINS, R. G. Mechatronic system for measuring hot-forged automotive parts based on image analysis. *Transactions of the Institute of Measurement and Control* [online]. 2018, **40**(13), 3774–3787. Available at: doi:10.1177/0142331217731619
- [58] BI, C., X. H. QU, Y. LIU, Y. P. LIU and J. L. LIU. Dimensional measurement of small hot pieces based on a monochrome CCD. In: H. HAIYAN, ed. *Procedia Eng.*

- Asia Pacific International Symposium on Aerospace Technology, Apisat2014* [online]. 2015, p. 1158–1163. *Procedia Engineering*. Available at: doi:10.1016/j.proeng.2014.12.698
- [59] ZHOU, Y., Y. WU and C. LUO. A fast dimensional measurement method for large hot forgings based on line reconstruction. *International Journal of Advanced Manufacturing Technology* [online]. 2018, **99**, 1713–1724. ISSN 14333015. Available at: doi:10.1007/s00170-018-2551-3
- [60] WANG, P., Y. LIN, R. MUROIWA, S. PIKE and L. MIHAYLOVA. A weighted variance approach for uncertainty quantification in high quality steel rolling. *Proceedings of 2020 23rd International Conference on Information Fusion (FUSION 2020)* [online]. 2020, (c). Available at: doi:10.23919/FUSION45008.2020.9190527
- [61] ZATOČILOVÁ, A., R. POLIŠČUK, D. PALOUŠEK and J. BRANDEJS. Photogrammetry based system for the measurement of cylindrical forgings axis straightness. In: *Proc. SPIE Vol. 8788. Spie-Int Soc Optical Engineering Conference on Optical Measurement Systems for Industrial Inspection VIII* [online]. 2013. Proceedings of SPIE. ISBN 978-0-8194-9604-1. Available at: doi:10.1117/12.2020917
- [62] ZATOČILOVÁ, A., D. PALOUŠEK and J. BRANDEJS. Development of a photogrammetry system for the measurement of rotationally symmetric forgings. In: *Proc. SPIE Vol. 9525. Spie-Int Soc Optical Engineering Conference on Optical Measurement Systems for Industrial Inspection IX* [online]. 2015. Proceedings of SPIE. ISBN 978-1-62841-685-5. Available at: doi:10.1117/12.2184916
- [63] ZATOČILOVÁ, Aneta. *Measurement and evaluation of axis straightness of rotary forgings using photogrammetry and image analysis*. B.m., 2014. Thesis. b.n.

## LIST OF SYMBOLS AND ABBREVIATIONS

CCD	coupled charge device
CMOS	complementary metal-oxide-semiconductor
CNC	computer numeric control
DLP	digital light processing
DSLR	digital single-lens reflex camera
FAST	features from accelerated segment test
ICCT	industrial circular coded target system
IR	infrared
NIR	near infrared
RGB	red-green-blue
RMS	root mean square
SA	state-of-the-art circular coded target system
SIFT	scale-invariant feature transform
SNR	signal-to-noise ratio
TOF	time-of-flight
UV	ultraviolet
$c$	focal length
$D(m_i, m_j)$	rotation invariant distance between the binary codes $m_i, m_j$
$F$	harmonic mean of recall and precision
$H$	Hamming distance
$H'[x'_0, y'_0]$	physical image center
$M_n$	noise intensity
$M_p$	projected signal intensity

$\mathbf{P}[X, Y, Z]; \mathbf{P}'[x', y']$	arbitrary point in space and its image in an image plane respectively
$r$	recall
$r_{11} \dots r_{33}$	components of image plane rotation matrix
$r_l$	radius of the air lens
$R_k$	rotation function (by $k \cdot 90^\circ$ )
$p$	precision
$n$	refractive index
$S$	area
$SNR$	signal-to-noise ratio
$tp, fp, fn$	true positive, false positive, false negative cases, respectively
$V_O; V_B$	image intensities of the object and background respectively
$\mathbf{X}_0[X_0, Y_0, Z_0]$	camera projection center
$z'$	camera optical axis
$\Delta V$	object contrast
$\Delta x', \Delta y'$	image distortion
$\eta_f$	transmissivity of the optical filter
$\eta_s$	camera sensor efficiency
$\lambda$	wavelength
$\rho$	reflectivity
$\Sigma$	level of trust in individual measurement
$\tau$	minimum rotation invariant distance in the code library
$\phi_p$	radiation flux
$\omega, \varphi, \kappa$	orientation of image plane

## LIST OF FIGURES AND TABLES

Fig. 1-1	Correction of axis straightness using LaCam® Forge by Ferrotron; 1) measurement of forging, 2) forging segmentation, 3) evaluation of axis-straightness, 4) three-point bending axis correction, 5), 6) repeated measurement [1].	11
Fig. 2-1	Basic representation of central projection model (image formation) [5].	13
Fig. 2-2	Image without use of color filter and the result of forging segmentation using thresholding [13].	15
Fig. 2-3	Image taken using NIR color filter and the result of forging segmentation using thresholding [13].	15
Fig. 2-4	Forging images taken by using (from left): red, green, blue, and IR-cut color filter [14].	16
Fig. 2-5	Dependency of forging contrast on the forging temperature [14].	16
Fig. 2-6	Comparison of the forging image processed by Canny edge operator (left), and the proposed segmentation method (right) [15].	16
Fig. 2-7	Structured light aided stereo vision experimental setup [17].	17
Fig. 2-8	Comparison of the measurement images without (a) and with (b) the usage of the spectral selective method [17].	18
Fig. 2-9	The layout of the experiment verifying the derived air lens model (Vivid 9i is the laser range finder by Konica-Minolta) [19].	19
Fig. 2-10	The results of the measurement affected by air lens compared to the prediction [19].	19
Fig. 2-11	Air lens simulation layout ( $n$ is a local refractive index of air) [20].	20
Fig. 2-12	Simulated measurement error due to air lens; left – the effect of different forging temperatures, right – the effect of different measurement device location [20].	20
Fig. 2-13	The resulting simulated atmosphere surrounding the hot object in dependence on the compensator air flow velocity $v_{ff}$ – (a) $0.0 \text{ ms}^{-1}$ ; (b) $0.2 \text{ ms}^{-1}$ ; (c) $0.55 \text{ ms}^{-1}$ ; (d) $1.0 \text{ ms}^{-1}$ [21].	21
Fig. 2-14	The experimentally measured mean reconstruction error $E_m$ in dependence on the compressed air pressure ( $p_{ff}$ ), time from flow activation of the flow to the measurement ( $t_d$ ). The hatched columns denote the measurement with activated air flow [21].	21

Fig. 2-15	Left – videogrammetric system camera layout; right – calibration object [10]. 22	
Fig. 2-16	Hemispherical calibration room for calibrating the cameras equipped with fisheye lenses [9].....	23
Fig. 2-17	Different designs of coded targets (schematic) – a) TRITOP (GOM); b) Calvet, 2016; c) Garrido-Jurado 2014; d) Ahn, 2001; e) Bergamasco, 2013.....	23
Fig. 2-18	Sample design of circular coded target often used in industrial photogrammetric applications; in the center - contrasting circle for target segmentation and location; annulus around – the unique code ring (9-bit in this case) [8].....	24
Fig. 2-19	The response of Gabor filter and Laplacian of Gaussian filter for comparison on different objects in an input image; the result of sum and multiplication of the images [29].....	25
Fig. 2-20	ArUco square coded targets (5, 6, and 8-bit) [32]. .....	25
Fig. 2-21	The timeline of advances in 3D hot objects measurement [36].....	27
Fig. 2-22	Left – the measurement result presented by Tian [37] and Du [38]. .....	27
Fig. 2-23	A diagram of the measurement system based on 2D laser scanner and a CCD camera; 1 – laser scanner, 2 – camera, 3 – ring forging, 4, 5, 8, 10, 12 – manipulator, its motor, controller and supply, 6 – measurement system positioning system, 7, 9 – data processing system and its supply, 11 – measurement system supply, 13, 14 – laser scanner and camera data transmission line [40].....	28
Fig. 2-24	Structured light aided stereo vision forging measurement system; camera parameters O, X, Y, Z are known, $P_1$ and $P_2$ are the corresponding image points of an object point [42].....	29
Fig. 2-25	Stereo images from the measurement system with triangulated fringe (1 - 7) end points (marked blue) [41].....	30
Fig. 2-26	The stereo images from the measurement system with triangulated points on the fringes 1 – 5 (marked red) [42]. .....	30
Fig. 2-27	Left – measurement system based on two stereo pairs, right – sample measurement result [43].....	31
Fig. 2-28	The diagram of the fringe projection system and the result evaluation using blue image component and three-frequency heterodyne [47].....	32
Fig. 2-29	Left - robot-driven fringe projection measurement system, right – sensor setup with a projector, 2 CCD cameras and dual optical filter [48]. .....	32

Fig. 2-30	Analysis of a forged axle [48].	33
Fig. 2-31	The four-camera fringe projection setup (4 cameras C and a projector p) [49].	33
Fig. 2-32	Reconstruction quality values for different forging temperatures $\vartheta_c$ , different time delay $\Delta t_d$ between the activation of the air flow and the measurement, pastel colors are used for a standard sequence (air flow was not activated in this case), bright colors for the adapted sequence [50].	34
Fig. 2-33	Forging measurement using laser triangulation method [52].	35
Fig. 2-34	Left – the layout of measurement system based on laser triangulation, right – on-site measurement [53].	36
Fig. 2-35	The forging measurement system based on eight line scanners [54].	37
Fig. 2-36	Passive stereovision measurement; left – measured scene, center – camera positions, right – 3D object reconstruction [55].	37
Fig. 2-37	A concept of forging measurement system based on stereo vision [56].	38
Fig. 2-38	Left – stereo images with corresponding feature points (marked blue); right – resulting 3D reconstruction of the object [56].	38
Fig. 2-39	Crankshaft measurement system based on stereo vision [57].	39
Fig. 2-40	Two-dimensional measurement setup for small forgings measurement, based on their silhouettes [58].	39
Fig. 2-41	Stereo images of hot cylindrical forging for the subsequent reconstruction using line triangulation method [59].	40
Fig. 2-42	Upper row – denoised edge maps obtained using random forest algorithm; lower row – measurement images with boundaries of interest (green) and random regression line fitting results (black) in the sliding windows (separated by white lines); the detail depicts the area C between the boundaries of interest [60].	41
Fig. 2-43	The results of the measurement compared with the ground truth and the level of trust indicator ( $\Sigma$ ) [60].	41
Fig. 2-44	The concept of a two-camera system for the measurement of heavy forgings [2].	42
Fig. 2-45	The concept of a camera system for the measurement of forgings with extended measurement volume [2].	42
Fig. 2-46	Detection of the edge points, based on image gradient. A section of the original image with magnified edge; yellow and red windows are used to search for approximate edge; black window in the magnified image is used to search for	

	the gradients around the edge; the table in center shows the pixel coordinates, their intensities and the difference of the intensities of neighboring pixels; the table on the right shows the intensity values from the highest to the lowest, with their coordinates, and the selected edge point marked yellow [63].	43
Fig. 2-47	The section of the measurement image with the edges; edges before and after the validation are marked blue and green, respectively [63].	43
Fig. 2-48	The average error of the measurement of specimens 1 – 7 [2].	44
Fig. 2-49	The estimation of the accuracy of passive camera measurement system for its potential use in the industrial environment. [63].	44
Fig. 5-1	Left - basic principle of a camera measurement system; right – example measurement images from the cameras of the system.	53
Fig. 5-2	Measurement system workflow (inputs marked red).	54
Fig. 5-3	Thermoregulated camera cover.	56
Fig. 5-4	Layout of the camera system in laboratory and industrial conditions.	57
Fig. 5-5	Sample measurement image from the laboratory (left) and industrial environment (right); the images are adjusted and cropped.	57
Fig. 5-6	Comparative forging measurement using laser scanners.	58
Fig. 5-7	Examples of corrupted targets from the datasets.	59
Tab. 1	Detailed information about the camera system.	57